# Comprehensive Analysis of Divertor W Erosion and C Deposition during and between ELMS for Mixed Material Environments on DIII-D

**A Dissertation Presented for the**

**Doctor of Philosophy**

**Degree**

**The University of Tennessee, Knoxville**

**Alec Meeh Cacheris**

**May 2026**

**Copyright © 2026 by Alec M. Cacheris**

**All rights reserved.**

***This work is an expression of the ongoing struggle to accurately define the truth, fix challenging problems in today's society, and provide a meaningful contribution to the future.***

## Acknowledgements

Special thanks are given to Dr. Tyler Abrams and Dr. David Donovan, the DIII-D team, and the University of Tennessee at Knoxville for their collaboration. Without the patience and support granted from my colleagues, the work at task would have been an unobtainable journey. Additional thanks are given to my mom and dad, Sean Kosslow, Brandon Connor, and Harrison Reisinger for their motivational support. Lastly, I thank my committee members, Jun Ren, Stuart Loch, and Maik Lang for their academia expertise.

# Table of Contents

**Chapter 1 Introduction** ..... **1**

**1.1 The Call for Carbon-Free Reliable Energy** ..... **1**

**Chapter 2 Motivation** ..... **6**

**Chapter 3 Background** ..... **8**

**3.1 Plasma-Material Interactions** ..... **8**

**3.2 $D_2$ Pellet & Gas Injection** ..... **14**

**3.3 Open & Closed Divertor Configurations** ..... **16**

**Chapter 4 Modelling** ..... **19**

**4.1 Free Stream plus Recycling Model (FSRM)** ..... **19**

**4.2 C/W Mixed Material Model** ..... **22**

**Chapter 5 Experimental Procedure** ..... **25**

**5.1 Metal Rings Campaign** ..... **25**

**5.2 Small Angle Slot** ..... **28**

**Chapter 6 Experimental Results** ..... **37**

**6.1 Metal Rings Campaign** ..... **37**

**6.2 Small Angle Slot** ..... **59**

**Chapter 7 SAS-VW Surface Analysis** ..... **85**

**7.1 Energy Dispersive X-ray Spectroscopy** ..... **85**

**7.2 Profilometer Topographical Data** ..... **90**

**Chapter 8 RustBCA Modelling ..... 95**

**8.1 Single Ion-Target Sputtering Yields and Reflection Coefficients ..... 95**

**8.2 Multi Ion-Target Sputtering Yields and Reflection Coefficients ..... 103**

**Chapter 9 Conclusions and Key Takeaways ..... 108**

**9.1 Overview ..... 108**

**9.2 Key Findings from Experimental Campaigns ..... 108**

**9.2.1 ELM-resolved tungsten erosion trends ..... 108**

**9.2.2 Influence of divertor geometry (open vs. closed configurations) ..... 109**

**9.2.3 Carbon-induced erosion, deposition, and mixed-material layer formation ..... 110**

**9.2.4 Heat flux measurements and implications for melting risk ..... 112**

**9.3 Modeling Insights and Validation ..... 113**

**9.3.1 FSRM performance and limitations ..... 113**

**9.3.2 RustBCA contributions ..... 115**

**9.3.3 Predictive limits of current erosion models ..... 116**

**9.4 Future Work ..... 116**

**9.5 Final Remarks ..... 117**

**References ..... 118**

**Appendix ..... 123**

**Vita ..... 209**

# List of Figures

**Figure 1. World Electricity Energy Source Distribution since 1900 [1]. ..... 2**

**Figure 2. Capacity Factor by Energy Source in 2020 [2]. ..... 2**

**Figure 3. Tokamak Fusion Reactor [3]. ..... 4**

**Figure 4. Plasma electron (a) pressure, (b) temperature, and (c) density as a function of plasma radius [4]. ..... 4**

**Figure 5. Illustration of the complex surface plasma-material interactions [6]. ..... 9**

**Figure 6. Cartoon diagram of W divertor PMI adapted from [7]. ..... 9**

**Figure 7. Physical Sputter Yield (Y) of D, C, and Be ions on W as a function of ion energy [8]. ..... 11**

**Figure 8. W Physical Sputtering by incident C and D ions as a function of impact angle (θ) relative to the divertor surface normal [9]. ..... 11**

**Figure 9. C and D ion species fractional contribution to W gross erosion as a function of the pedestal and divertor temperature [9]. ..... 13**

**Figure 10. Average divertor (a) ELM deposited energy and (b) ELM peak heat flux as a function of $D_2$ pellet frequency [11]. ..... 15**

**Figure 11. Comparison of the DIII-D upper, closed divertor (blue) and lower, open divertor (red) [14]. ..... 18**

**Figure 12. Illustrated overview of the FSRM with magnetic field lines mapped into a 2D plane [8]. ..... 20**

**Figure 13. Overview of the diagnostics used to perform ELM-resolved measurements during the MRC. Figure adapted from [8]. ..... 26**

**Figure 14. Overview of the diagnostics used to perform ELM-resolved measurements during the SAS-VW campaign adapted from [13]. The red line indicates the outer strike point (OSP) position for the analyzed plasma shots. The orange spectroscopic lines of sight include the WI, $D_\alpha$, and CIII filterscopes. LP and SETCs indicated by blue and red dots, respectively, were installed along the W surface shown by the grey line. Spectroscopy, LPs, and SETCs are at different toroidal locations within the SAS divertor [14]. ..... 31**

**Figure 15. Comparison between SETC and IR camera intra-ELM heat flux [30]..... 33**

**Figure 16. Calibrated two-filter filterscope WI photon intensity versus the calibrated MDS WI photon intensity integrated for the analyzed time range of each plasma shot. ..... 35**

**Figure 17. Mass injection rate as a function of $D_2$ nominal injection frequency. ..... 39**

**Figure 18. Time history of the $D_2$ mass injection rate and divertor electron density and temperature in DIII-D discharge 167351. Y-axis values represent $D_2$ mass injection rate and divertor electron density and temperature. Normalized plasma pressure ($\beta_N$), the ratio of the plasma pressure to the poloidal magnetic pressure ($\beta_p$), the ratio of measured confinement time over predicted confinement time (H98), and the total plasma energy measured at a rapid frequency (wmhdf) plasma confinement are also overlaid. ..... 41**

**Figure 19. Measured divertor and pedestal electron temperature and density just before the ELM crash as a function of $D_2$ mass injection rate for all cases listed in Table 1. The partially transparent data points represent the pellet pacing frequency sweep, shot 167351. ..... 42**

**Figure 20. Measured average W gross erosion rate per ELM during DIII-D discharge 167351 for the time ranges indicated in Table 1. Each time range corresponds to a $D_2$ mass injection rate averaged over the respective time range. ..... 44**

**Figure 21. Average gross W erosion rate per ELM measured experimentally (purple), calculated by the FSRM with no mixed-material model (green), and with the mixed-material model (gold), as a function of plasma electron inter-ELM (a) density and (b) temperature. Linear trendlines are overlaid in all cases. 46**

**Figure 22. MRC experiment vs. predicted inter-ELM W erosion. 48**

**Figure 23. MRC experiment vs. predicted inter-ELM W erosion. 49**

**Figure 24. Fractional concentration of W at the divertor surface during an ELM with respect to $D_2$ mass injection rate. 51**

**Figure 25. Measured total intra-ELM gross W erosion rate (blue) and predicted gross W erosion rate in the absence of a C/W mixed material layer (red) vs. plasma electron inter-ELM (a) density and (b) temperature. Linear fits are overlaid in both cases. 53**

**Figure 26. ELM frequency and average pedestal stored energy drop per ELM as a function of $D_2$ mass injection rate. 53**

**Figure 27. Average peak intra-ELM heat flux vs. $D_2$ mass injection rate. 54**

**Figure 28. MRC intra-ELM experimental heat flux as a function of FSRM heat flux. 56**

**Figure 29. Mass injection rate as a function of inter-ELM $n_e$ for shots at 2.6 MW of heating power. $D_2$ midplane gas puff plasma shot data points interpolated by the linear trendline are shown in orange diamonds while $D_2$ pellet injection plasma shots are displayed in blue circles. A black trendline for the data is displayed. 61**

**Figure 30. $D_2$ pellet shots inter-ELM density as a function of $D_2$ mass injection rate. 62**

**Figure 31. $D_2$ gas shots inter-ELM density as a function of gas puff rate in Torr-L/s. 62**

**Figure 32. Plasma shot 191009 parameters vs time for (a) Injected Power in blue, (b) $D_2$ Midplane Gas Puff Rate in orange, (c) OSP Position in green for r-axis and purple for z-axis, (d) Line Average Density in red, and (e) Divertor $D_\alpha$ Intensity in brown. ..... 64**

**Figure 33. Experiment vs. predicted inter-ELM W erosion at θ=45°. $D_2$ gas puffing plasma shots are displayed in orange diamonds, $D_2$ pellet injection plasma shots are displayed in blue circles, and plasma shots with neither are displayed in green triangles. ..... 67**

**Figure 34. Measured divertor and pedestal electron temperature and density just before the ELM crash as a function of $D_2$ injection frequency for all cases listed in Table 2. Linear trendlines are shown in all cases. ..... 69**

**Figure 35. Average large intra-ELM W erosion as a function of inter-ELM. ..... 69**

**Figure 36. SAS-VW intra-ELM experimental ion flux as a function of FSRM ion flux. ..... 71**

**Figure 37. Fractional surface concentration of W as a function of inter-ELM density. ..... 72**

**Figure 38. Experiment vs. predicted intra-ELM W erosion at θ=45°. $D_2$ gas puffing plasma shots are displayed in orange diamonds, D2 pellet injection plasma shots are displayed in blue circles, and plasma shots with neither are displayed in green triangles. ..... 73**

**Figure 39. Experiment intra-ELM W Erosion vs. inter-ELM $n_e$ shown in orange diamonds for the MRC and in blue circles for the SAS-VW campaign. ..... 75**

**Figure 40. Experiment (SETC) vs. predicted (FSRM) intra-ELM peak heat flux. $D_2$ gas puffing plasma shots are displayed in orange diamonds, $D_2$ pellet injection plasma shots are displayed in blue circles, and plasma shots with neither are displayed in green triangles. . 79**

**Figure 41. Total W intra- and inter-ELM erosion rates shown in solid. ..... 81**

**Figure 42. Large ELM frequency and pedestal stored energy drop as a function of inter-ELM density with dashed linear trendlines. ..... 81**

**Figure 43. Average large ELM peak heat flux as a function of inter-ELM density with a linear dashed trendline. ..... 83**

**Figure 44. SAS-VW intra-ELM experimental heat flux as a function of FSRM heat flux.. 83**

**Figure 45. SAS-VW tile cut positions are indicated by the red lines (a) side view of entire tile (b) exposed tile sample positions (c) unexposed tile sample positions. ..... 86**

**Figure 46. EDS profiles for exposed tiles. Dark colored areas represent C concentration while light colored areas represent W concentration. (a) large sample 1 (b) small sample 1 (c) large sample 2 (d) small sample 2 (e) large sample 3 (f) small sample 3. ..... 87**

**Figure 47. Secondary electron image scan taken from sample 1. The lighter color represents C while the darker color represents W, contrary to the EDS profile. The C layer thicknesses are approximated in red. ..... 87**

**Figure 48. 5 kV EDS spectrum for (a) Unexposed representative large sample 1 (b) Exposed representative large sample 1. ..... 89**

**Figure 49. Schematic of how surface roughness affects ion impact angle (θ) on the target. θ' represents the rough surface θ [39]. ..... 91**

**Figure 50. LIAD for exposed SAS-VW tile sample. ..... 91**

**Figure 51. Theoretically smooth surface IAD at $E_i$ = 1200 eV determined by LPTMC. ..... 93**

**Figure 52. Theoretically smooth surface IAD at $E_C$ = 800 eV (blue) and $E_C$ = 1700 eV (orange) determined by LPTMC. ..... 93**

**Figure 53. Sputtering Yield (Y) vs. Ion Impact Energy ($E_i$) for RustBCA and 2002 Eckstein (a) $Y_{D\text{-}C}$ (b) $Y_{C\text{-}C}$ (c) $Y_{D\text{-}W}$ (d) $Y_{C\text{-}W}$. ..... 96**

**Figure 54. Reflection Coefficient (R) vs. Ion Impact Energy ($E_i$) for RustBCA and 2002 Eckstein (a) $R_{C\text{-}C}$ and (b) $R_{C\text{-}W}$. ..... 98**

**Figure 55. Sputtering Yield (Y) vs. Ion Impact Energy ($E_i$) for RustBCA and 2002 Eckstein (a) $Y_{D-W}$ (b) $Y_{C-W}$. ..... 98**

**Figure 56. (a) $Y_{D-C}$ at $E_D$ = 200 eV and (b) $Y_{C-C}$ at $E_C$ = 300 eV. ..... 99**

**Figure 57. $Y_{C-W}$ at $E_C$ = 300 eV. ..... 99**

**Figure 58. (a) $R_{C-C}$ and (b) $R_{C-W}$ at $E_C$ = 300 eV. ..... 100**

**Figure 59. (a) $Y_{D-C}$ and (b) $Y_{C-C}$ at $E_i$ = 1200 eV. ..... 100**

**Figure 60. (a) $Y_{D-W}$ and (b) $Y_{C-W}$ at $E_i$ = 1200 eV. ..... 101**

**Figure 61. (a) $R_{C-C}$ and (b) $R_{C-W}$ at $E_i$ = 1200 eV..... 101**

**Figure 62. RustBCA $Y_W$ comparison between W and homogenous 1:1 C:W targets for a 97% D and 3% C ion flux at θ = 45°. ..... 104**

**Figure 63. The ratio of 0.5*$Y_W$ to the homogenous 1:1 C:W $Y_W$ vs. Ion Impact Energy ($E_i$). ..... 106**

**Figure 64. (a) RustBCA $Y_W$ comparison between homogenous 1:1 C:W and a monolayer of C atop homogenous 1:1 C:W for a 97% D and 3% C ion flux at θ = 45° (b) The ratio of $Y_W$ for a monolayer of C atop homogenous 1:1 C:W to homogenous 1:1 C:W vs. Ion Impact Energy ($E_i$). ..... 106**

**Figure 65. $C^{2+}$ distribution probability at $T_e$ = 20 eV and $E_C$ = 1 keV as a function of θ for τ = 0.5 (blue), τ = 1.0 (red), τ = 1.5 (green), and τ = 2.0 (orange) determined by LPTMC. .. 114**

# Chapter 1

# Introduction

## 1.1 The Call for Carbon-Free Reliable Energy

Every year the world's energy demand increases due to growing populations and usage of technological devices. In conjunction, fossil fuels comprise most of the world's energy production and harm the environment through pollution and toxic waste. Likewise, the world's electricity energy source distribution since 1985 is shown in Figure 1 [1]. Notably, fossil fuels (coal, gas, and oil) still account for about 60% of the world's energy distribution. Demand for energy continues to rise, while environmentally friendly sources are not expanding quickly enough to reduce fossil fuel usage. Nuclear fission and renewable sources together make up the remaining 40%, but both have shortcomings. Nuclear fission poses risks of fuel proliferation, requires radioactive waste storage, and carries the potential for reactor meltdowns. In contrast, wind, hydropower, and solar are limited by the availability of wind, water, and sunlight, respectively. The fraction of time an energy source can reliably supply the grid is known as its capacity factor. Thus, Figure 2 shows an estimation of the capacity factor for each energy source type below [2]. It is apparent that renewable sources such as wind, hydroelectric, and solar cannot alone sustain our energy demands given their capacity factors. Moreover, each is only optimal in specific locations for high efficiency. Theoretically, fusion energy avoids nearly all the drawbacks of fission while reliably providing carbon-free power. The primary fusion reaction is shown in Equation 1.1 below.

$$D + T \rightarrow He + n + 17.6\,MeV \qquad 1.1$$

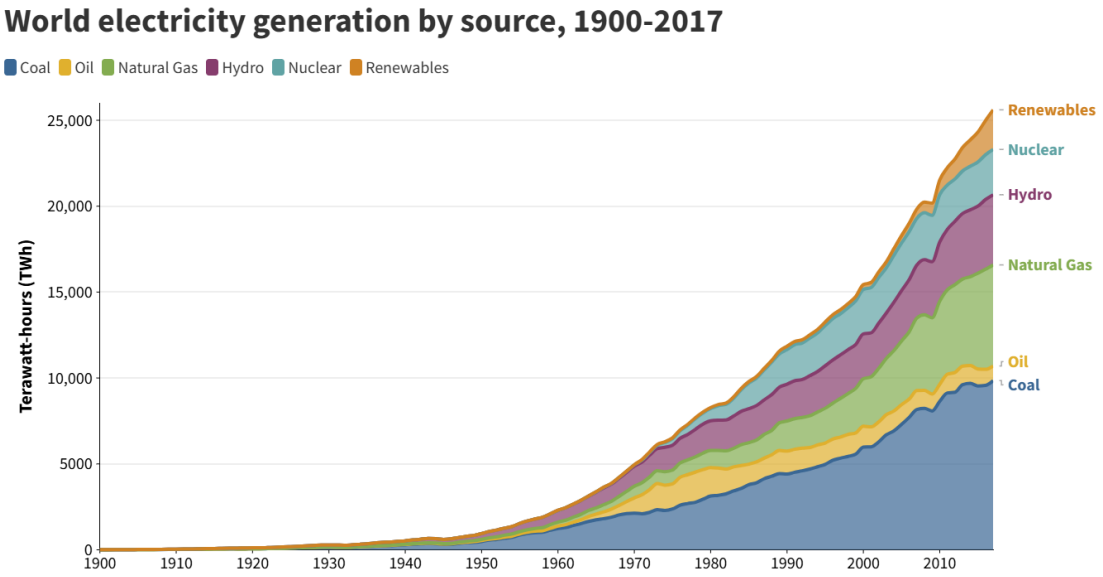



*Figure 1. World Electricity Energy Source Distribution since 1900 [1].*

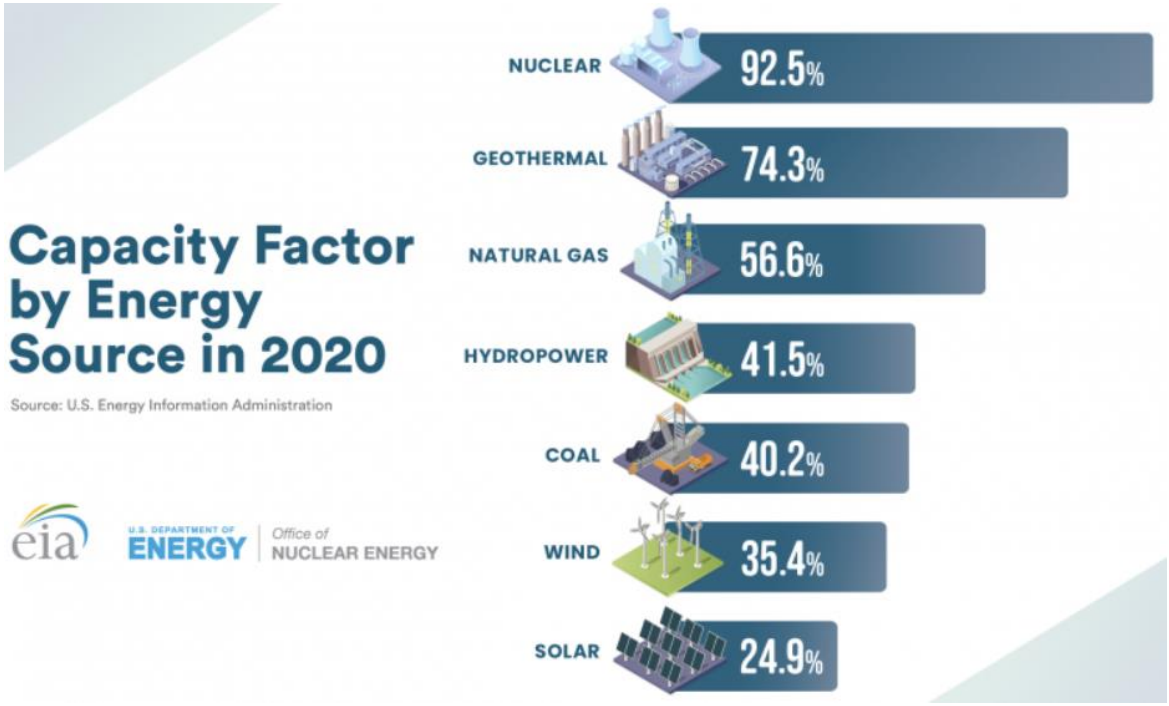



*Figure 2. Capacity Factor by Energy Source in 2020 [2].*

Deuterium (D) and tritium (T) are hydrogen isotopes that serve as the primary fuel for fusion energy. Currently, one of the leading candidates for achieving fusion power is the tokamak reactor. The tokamak reactor uses toroidal and poloidal magnetic fields to confine the D-T plasma in a torus as seen in Figure 3 [3]. Currently, many engineering challenges remain unresolved in tokamak reactors. Among the most daunting is ensuring the survival of reactor walls under plasma–material interactions. Dating back to 1982, tokamak plasma confinement persisted in what is now known as low-confinement mode, also called L-mode. Then, a new confinement regime was discovered when a certain power threshold was breached. This new high-power mode was termed high-confinement mode, also known as H-mode. H-mode plasmas were defined by an increase in plasma pressure, density, and temperature, the three key variables that must be optimized to drive fusion power. H-mode plasma led to a steep pressure, temperature, and density gradient on the plasma edge known as the pedestal, as depicted below in Figure 4. Unfortunately, the transition to H-mode was also characterized by a loss of particle confinement at the pedestal, known as an edge-localized mode (ELM). During ELMs (intra-ELM), intense bursts of particle flux are released from the pedestal and follow magnetic field lines to the divertor, a region of the plasma-facing wall built to withstand the highest particle and heat fluxes. Depending on the fusion device operating design parameters, ELMs or other similar periodic particle bursts can vary substantially in frequency and magnitude. While many ELM mitigation techniques exist, this study utilized $D_2$ injection in attempt to mitigate ELMs, to be further discussed. Some tokamak regimes are optimized to eliminate ELMs all together but contain their own drawbacks limiting the operating parameter space. By nature, divertor erosion is difficult to assess and ELMs complicate predictions of PFC lifetime. Thus, a key part of this study aims to assess divertor erosion during ELMs, and between ELMs (inter-ELM). Even

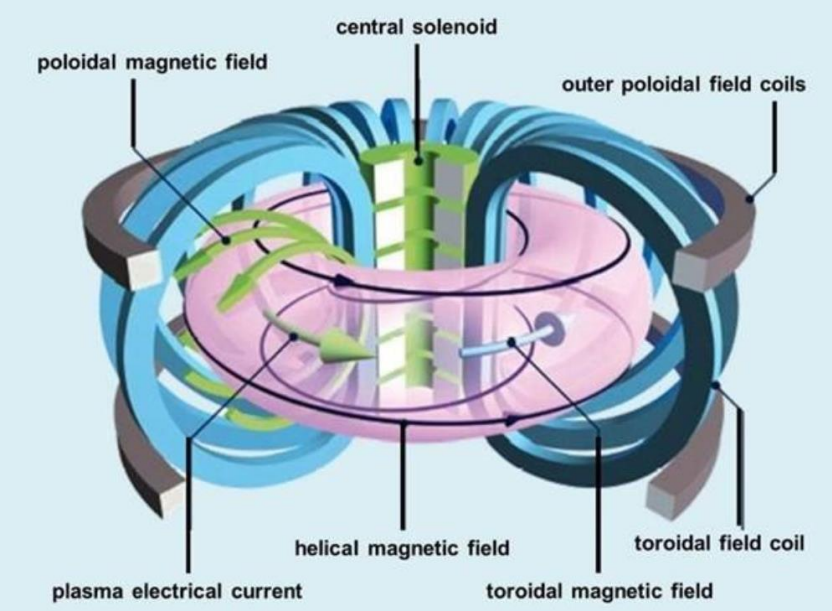



*Figure 3. Tokamak Fusion Reactor [3].*

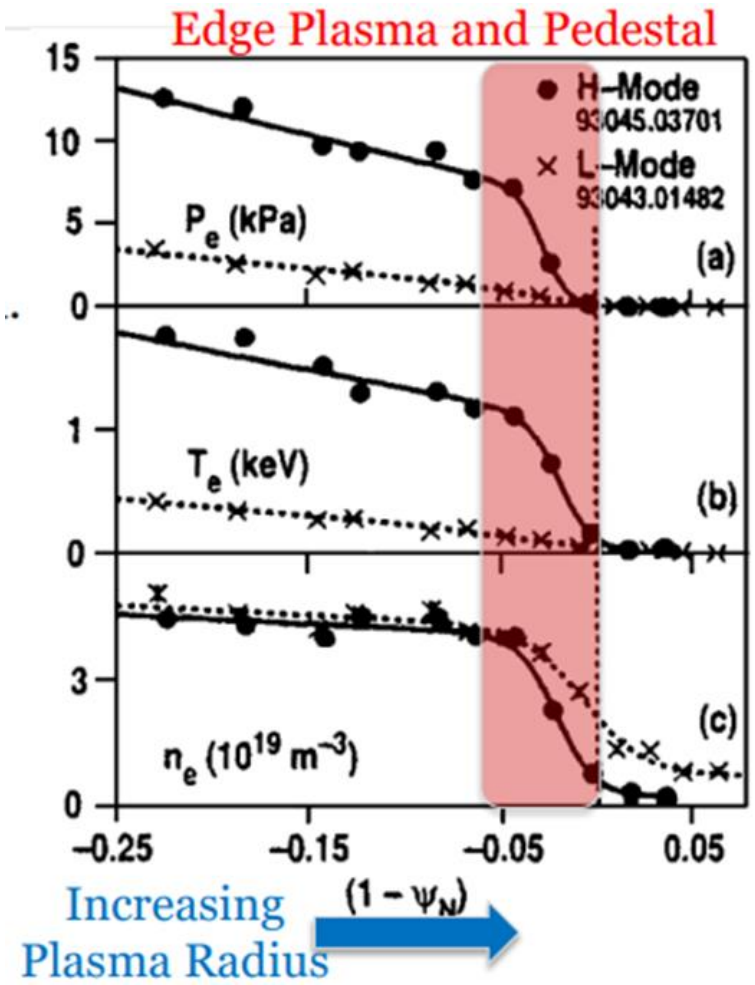



*Figure 4. Plasma electron (a) pressure, (b) temperature, and (c) density as a function of plasma radius [4].*

without ELMs, plasma impurities complicate predictions of divertor erosion by implanting in and on the PFC surface. Essentially, an impurity is defined as any particle that does not comprise the D-T fuel reaction. Mixed material environments, such as those studied here, are quite complex and will be further detailed in this manuscript.

# Chapter 2

## Motivation

To commercialize fusion tokamak energy, we must accurately predict and understand the lifetime of plasma-facing components (PFCs). PFCs degrade through mechanisms including melting, sputtering, bubble and blister formation, embrittlement, and loss of structural integrity. This study focuses primarily on divertor damage through physical sputtering while also monitoring heat flux profiles related to divertor melting. The MRC and SAS-VW experiments used in this study employed midplane outboard $D_2$ mass injection as an ELM mitigation technique for H-mode plasmas. While ELM-free regimes and alternative mitigation methods exist, each has drawbacks that may limit practicality under design constraints. Regardless of the mitigation approach, predictive models for intra-ELM divertor erosion and heat flux must be improved to ensure viability for many tokamak designs. Both intra- and inter-ELM divertor erosion predictions are jeopardized by mixed material environments. A substantial piece of this thesis aims to decouple the presence of C impurities in the DIII-D tokamak and its impact on the divertor erosion, studying C implantation and sputtering of the W-coated DIII-D divertor surface. Moreover, this mixed material analysis gives critical insight to future fusion materials research that may utilize mixed material environments.

This dissertation addresses two overarching goals:

1. **Divertor Erosion Modelling Validation and Improvement**

   This work validates and improves an ELM erosion model known as the Free Stream Recycling Model (FSRM) by incorporating the effects of C impurity deposition and implantation in the DIII-D divertor across the Metal Rings Campaign (MRC) and Small Angle Slot V-Shaped Tungsten (W) Divertor (SAS-VW) campaign. Assessment of C

impurity deposition is conducted in a similar manner between ELMs to predict inter-ELM W erosion. Associated physical sputtering yield (Y) and reflection coefficient (R) used in the modelling were computed with RustBCA, a binary collision model for ion-material interactions [5]. Moreover, RustBCA has been utilized to assess the effect of mixed material concentrations at the divertor surface on $Y_W$. Comparisons of intra- and inter-ELM W erosion between experiments and model predictions were made for both campaigns. Intra-ELM erosion predictions showed better agreement in the open MRC divertor than in the baffled SAS-VW divertor. The discrepancies in SAS-VW are primarily linked to an expected increase in C deposition and insufficient analysis of ion–material Y and R values for C–W mixed divertor targets. Other possible contributors include uncertainties in the Langmuir probe (LP) plasma electron temperature ($T_e$) measurements, divertor ion-to-electron temperature ratio ($\tau$), low-Z redeposition physics, ion impact angle ($\theta$), and atom-to-photon ionization (S/XB) coefficients.

2. **Effectiveness of $D_2$ mass injection**

   This work also analyzes the effectiveness of $D_2$ mass injection in mitigating intra-ELM divertor heat flux and erosion. The MRC experiment examined Type-I ELM erosion and heat flux in an open divertor configuration, while the SAS-VW campaign studied faster, lower-magnitude Type-I ELMs in a closed divertor configuration with lower plasma collisionality.

To support these goals, substantial background information and preliminary results are provided in the following sections.

# Chapter 3

# Background

## 3.1 Plasma-Material Interactions

Many plasma–material interactions threaten the survival of PFCs during tokamak operation. This study focuses on ELM-induced physical sputtering (Y) from ion impact and material recycling, along with heat flux measurements. Y, also referred to as erosion, is used interchangeably in this study. Ion implantation, reflection, and redeposition directly influence Y. Ions lacking sufficient energy may reflect without sputtering; implanted ions can shield the surface and reduce subsequent sputtering; and reflected or sputtered atoms may redeposit, contributing to additional erosion or reducing erosion through deposition. Implantation refers to both embedment and deposition. Embedment occurs when atoms or ions implant beneath the material surface, whereas deposition occurs when they settle on the surface. A cartoon of these three plasma-material interactions relevant to the experimental data in this manuscript is depicted in Figure 6 [7]. The cartoon illustrates that when an ion strikes the divertor, it may reflect, sputter the target, or deposit on the surface. Although plasma–material interactions (PMI) are more complex, these three mechanisms are most relevant for this study. In DIII-D, D and carbon (C) ions cause the greatest damage to PFCs because the reactor fuel is D and the main wall is C, resulting in the highest particle and heat fluxes of these ions to the divertor. The incident D flux is several orders of magnitude higher than the C flux; however, D ions are more likely to reflect from the W surface and less likely to sputter the W surface than C due to their lower mass per atom. In the background (non-transient) plasma, C ions have sufficient energy to sputter the surface as well as deposit on or implant into it. In these experiments, sputtered W also recycles and re-strikes the divertor, but due to its low energy and short mean free path relative to

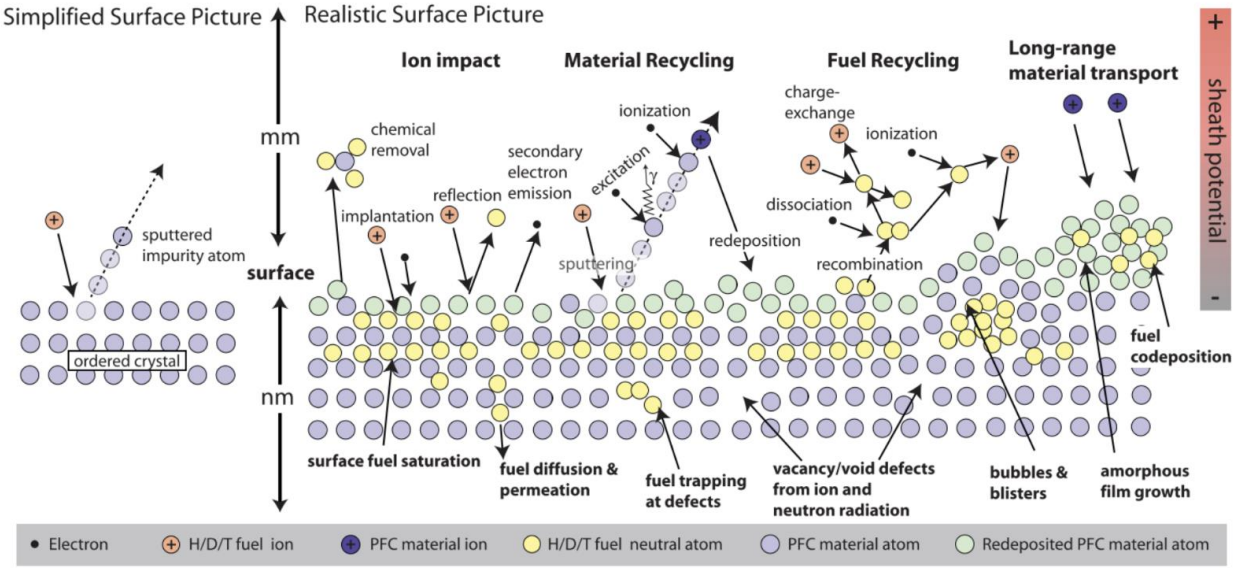



*Figure 5. Illustration of the complex surface plasma-material interactions [6].*

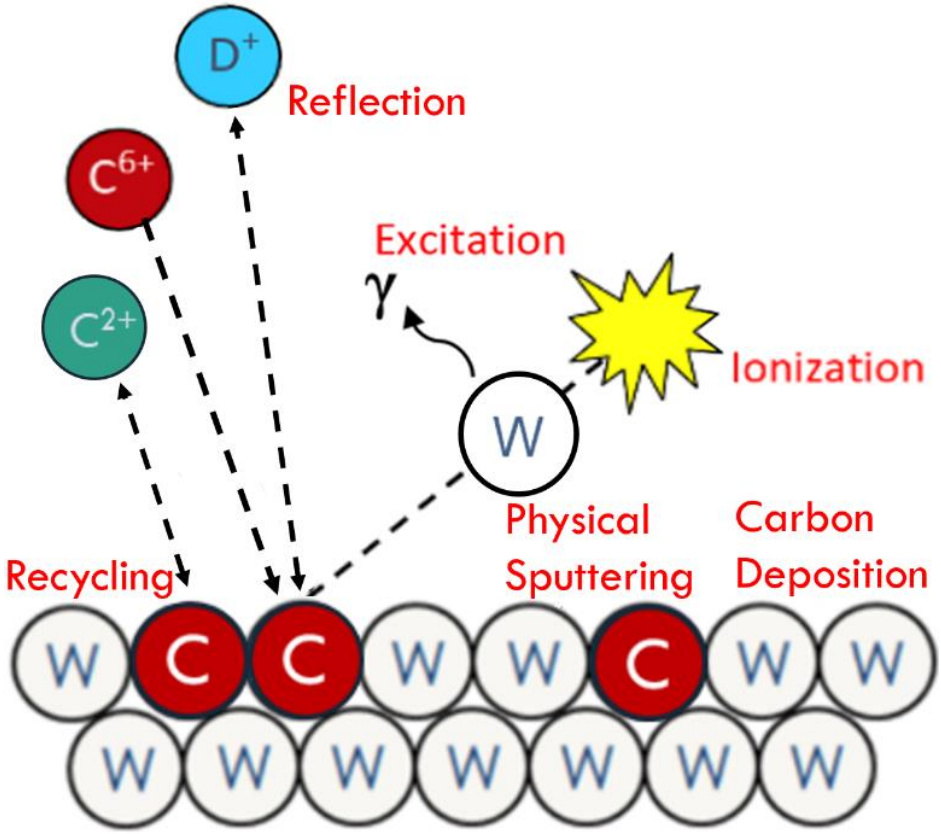



*Figure 6. Cartoon diagram of W divertor PMI adapted from [7].*

the $W^+$ gyro-radius, most sputtered W is promptly redeposited rather than causing significant additional sputtering. Accordingly, Figure 7 shows the Y for D, C, and Beryllium (Be) ions on W assuming a 45° angle of incidence to the surface, determined from a couple of past studies referenced here [7, 8]. Notably, the Y of C on W and Be on W are scaled to 2% and 0.5%, respectively, of their actual values. C ions with higher charge states carry greater energy than those with lower charge states, resulting in increased Y and deposition. When ions strike the divertor, some or all their charge is transferred to the target upon collision. Consequently, D and C particles primarily reflect or scatter as neutral D atoms or as low charge states of C. These reflected or scattered atoms are then re-ionized through electron-impact ionization as they move into the Debye sheath. If they lack sufficient energy to escape the sheath and return to the main plasma, they are repelled by the positively charged sheath and restrike the divertor [9]. Thus, recycling ions contribute significantly to erosion and the near-surface deposition layer. However, the current Y and R values for the SAS-VW campaign may inaccurately estimate W divertor erosion. A sharper magnetic field incidence angle ($\alpha$) relative to the divertor surface in the SAS-VW configuration compared to the MRC may reduce the average $\theta$. Variations in $\theta$ can either increase or decrease W erosion depending on the ion impact energy ($E_i$). Figure 8 shows the calculated $Y_W$ due to incident C and D ions as a function of $\theta$ [10]. As shown, variations in the $\theta$ have a non-negligible effect on the $Y_W$ and, consequently, on overall W erosion. The results in Figure 9 show 1 keV C and D ions, representative of the intra-ELM conditions in the MRC. In the SAS-VW campaign, however, higher $E_i$ values are expected due to an increased pedestal electron temperature ($T_{e,ped}$), averaging closer to 1.2 KeV for the plasma shots studied herein. In the inter- ELM regime, the average $D^+$ impact energy is much lower and contributes negligibly to W divertor erosion. On average, ions are expected to strike the divertor at an angle of

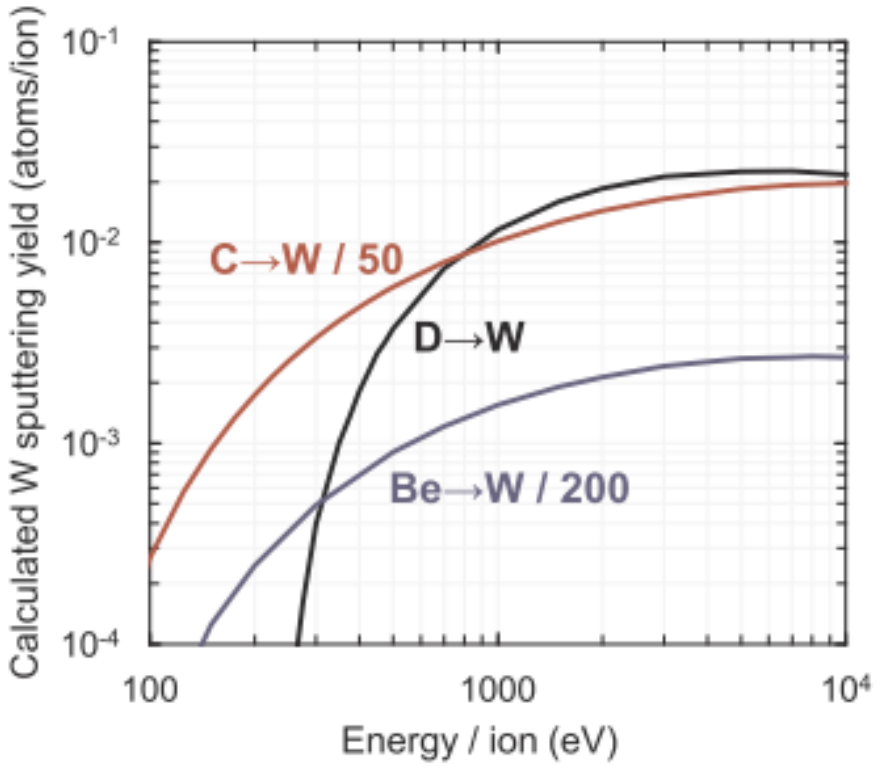



***Figure 7. Physical Sputter Yield (Y) of D, C, and Be ions on W as a function of ion energy [8].***

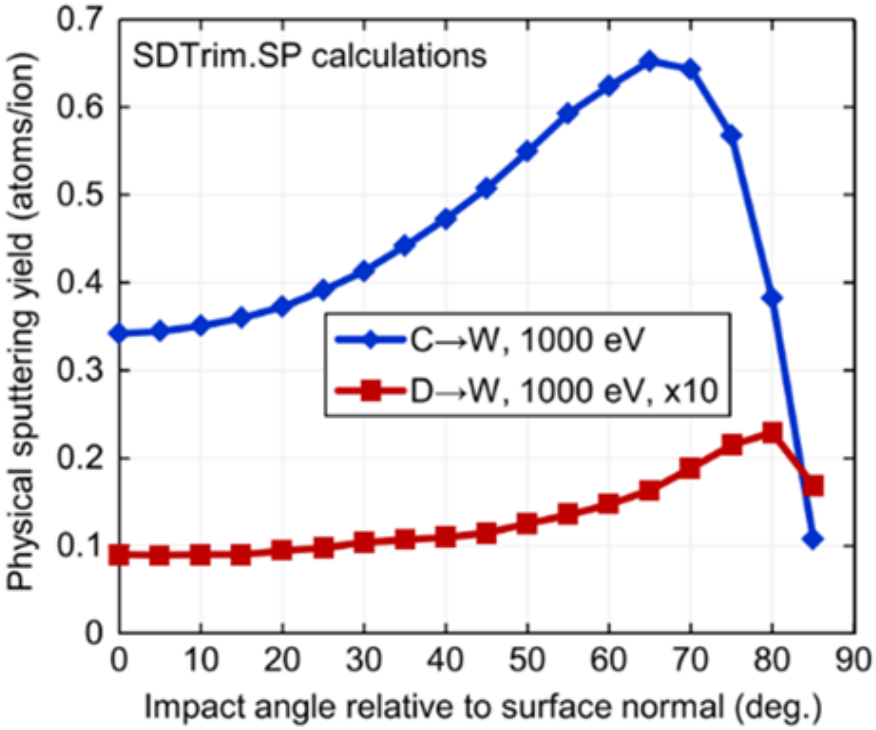



***Figure 8. W Physical Sputtering by incident C and D ions as a function of impact angle (θ) relative to the divertor surface normal [9].***

approximately 45° due to gyro-orbit motion and surface roughness effects. As discussed later, improved estimations of Y and R values enhance the accuracy of W erosion predictions. Furthermore, Figure 9 presents the fractional contribution to gross W erosion from various ion species in DIII-D as a function of pedestal and divertor electron temperature ($T_e$). These results assume an average $\theta = 45°$ relative to the surface and are computed using the FSRM, described in detail in the following section and in reference [9]. Clearly, the total and fractional contributions to W gross erosion depend strongly on the pedestal electron temperature ($T_{e,ped}$), divertor electron temperature ($T_{e,div}$), and the role of recycling lower charge states of C, which cannot be neglected. In all cases, recycling $D^+$ ions lack sufficient impact energy ($E_i$) to sputter W atoms. In contrast, the fractional contribution to W gross erosion from recycling $C^{2+}$ ions increase with higher $T_{e,div}$ and lower $T_{e,ped}$. A higher $T_{e,div}$ enhances the $C^{2+}$ contribution because the $C^{2+}$–W Y increases more rapidly with increasing divertor temperature than that of $C^{6+}$–W Y or $D^+$–W Y. Conversely, higher $T_{e,ped}$ results in a larger $D^+$ contribution to gross W erosion due to a proportionally greater rise in $D^+$–W Y relative to $C^{6+}$–W or $C^{2+}$–W Y. Additionally, the impact of C deposition on the W divertor surface must be considered when predicting $Y_W$, as discussed in the next section. While Y dominates PFC damage in DIII-D operation, material melting caused by intense heat fluxes is the primary concern for many future tokamak reactors. Melting risks outweigh Y in many future devices because their much hotter plasmas will produce stronger intra-ELM heat fluxes and associated surface damage. Importantly, these elevated temperatures will also influence the Y of various ions on divertor materials. Crucially, $T_{e,div}$ measurements are comparable between the SAS-VW campaign and the MRC shots analyzed here, but $T_{e,ped}$ values are significantly higher for the SAS-VW divertor. Therefore, we expect C to contribute even less to W erosion relative to deuterium in the SAS-VW campaign than in the

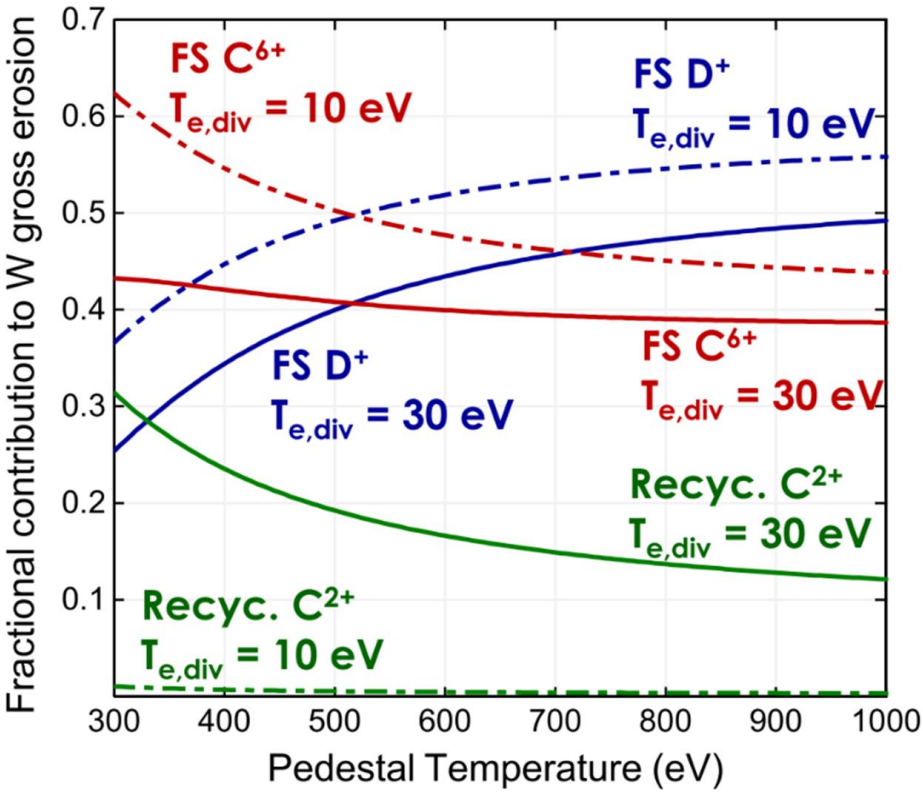



***Figure 9. C and D ion species fractional contribution to W gross erosion as a function of the pedestal and divertor temperature [9].***

MRC, assuming similar fractional C impurity concentration ($f_C$) in the divertor region. However, variations in θ will also influence these trends. While various divertor configurations and damage-mitigation techniques exist, this work initially focused on $D_2$ pellet injection as an ELM mitigation strategy across two major DIII-D experiments. However, $D_2$ injection also altered $f_C$ in the W divertor, thereby affecting W erosion predictions. The next section provides background on the $D_2$ pellet injection technique used to mitigate divertor damage from intense particle and heat fluxes.

## 3.2 $D_2$ Pellet & Gas Injection

$D_2$ pellets injected at thermal velocities (100-200 m/s) near the low-field side midplane of the tokamak, where instabilities are significant, have been demonstrated to mitigate ELM effects by triggering more frequent lower magnitude ELMs. $D_2$ pellet injection destabilizes the pedestal, perturbing the ballooning stability boundary associated with ELMs [11, 12]. Smaller ELMs result in a lower energy deposited in the divertor per ELM, providing a mechanism to remain below the damage threshold of impacted PFMs. Through past studies on DIII-D, $D_2$ pellet injection has proved to reduce divertor peak ELM heat flux while the impact on W divertor is nonmonotonic [9, 11, 12]. Figure 10 shows the ELM deposited energy and peak ELM heat flux on the divertor as a function of pellet frequency from the 2016 MRC. As shown, the average divertor ELM deposited energy and ELM peak heat flux decreases as a function of the $D_2$ pellet frequency. Moreover, $D_2$ pellet injection can help induce plasma detachment from the divertor by lowering the divertor $T_e$ sufficiently ($T_e$ <5 eV). Low $T_e$ values result in reduced ion temperatures ($T_i$) and impact energies ($E_i$) to the divertor target. This lowers the D and C induced $Y_W$ to lessen W erosion. However, increasing the amount of injected $D_2$ generally increases the

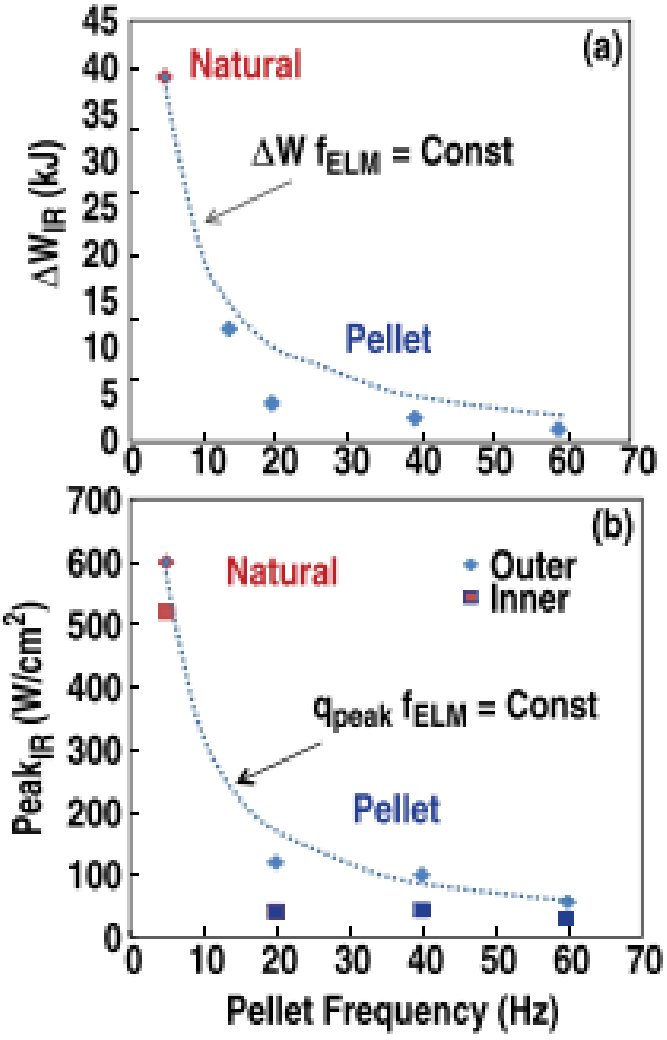



***Figure 10. Average divertor (a) ELM deposited energy and (b) ELM peak heat flux as a function of $D_2$ pellet frequency [11].***

divertor incident $D^+$ ion flux, potentially increasing W erosion if a sufficiently low divertor $T_e$ is not achieved. $D_2$ injection also affects pedestal conditions. As in the divertor, pedestal $T_e$ may decrease and plasma electron density ($n_e$) may increase with larger frequencies of injected $D_2$ pellets. The ideal $D_2$ pellet injection frequency must avoid significantly increasing the collisionality of the pedestal to maintain adequate plasma confinement and performance. It is worth noting that in the SAS-VW campaign our $n_{e,ped}$ is lower than in the MRC, so $D_2$ mass injection may have a greater impact on this lower collisionality plasma. Notably, $D_2$ gas puffing also affects ELM characteristics and plasma parameters like $D_2$ pellet injection. However, $D_2$ gas puffing is thought to have less of an effect on ELM triggering due to less localized pedestal perturbations [11, 12]. $D_2$ mass injection refers to either $D_2$ gas puffing or $D_2$ pellet injection. Part of this study aims to compare the effect $D_2$ mass injection rate has on intra-ELM and inter-ELM W erosion and peak ELM heat fluxes, and whether differences exist between $D_2$ gas or $D_2$ pellets inserted at a similar $D_2$ mass injection rate. Moreover, this study compares results from two experimental campaigns, one with an open divertor configuration from the MRC in 2016 and the other with a closed divertor configuration from the Small Angle Slot (SAS-VW) in 2022. The differences between an open and closed divertor configuration is discussed in the next subsection.

## 3.3 Open & Closed Divertor Configurations

Notable differences exist between the MRC open, and SAS-VW closed divertor configuration. Increased divertor baffling characterizes a more closed divertor. The trapping of recycling neutrals near the divertor due to greater baffling increases divertor neutral pressure and improves divertor power and particle exhaust to mitigate melting and sputtering, respectively [13-15]. Effects of C impurity trapping on the SAS-VW divertor are not directly accounted for in

our current C/W mixed material model and may need to be incorporated. This study includes heat flux and erosion results from single-null, ELMy H-mode discharges with the strike point either on the open lower or closed upper divertor on DIII-D with similar plasma shape and parameters. Likewise, Figure 11 illustrates the open and closed divertor configurations on DIII-D. As seen, the upper divertor contains a much narrower slot than the lower divertor. This design traps impurities produced by divertor and first wall damage to help prevent impurity leakage into the core. Crucially, this helps sustain plasma performance, since impurities in the core lead to large radiative power losses. In addition, increased closure is designed to induce plasma detachment at a lower line-averaged plasma density. In fact, past studies on DIII-D report a ~20% reduction in the density required for partial detachment in H-mode discharges for the upper divertor compared to the lower divertor [14, 16]. Therefore, closure grants the ability for upper divertor plasma discharges to operate at a hotter pedestal electron temperature ($T_{e,ped}$) and lower pedestal electron density ($n_{e,ped}$) while resulting in similar divertor electron temperature ($T_{e,div}$). As a result, the plasma discharges studied here are attached plasmas at the outer strike point (OSP) position with similar $T_{e,div}$ compared to the MRC despite the hotter SAS-VW $T_{e,ped}$. Lastly, it is important to consider α. Another effect of increased baffling in the upper divertor geometry is a smaller α. Presumably, this results in more glancing θ, impacting $Y_W$. Though after considering sheath and ion pyro-orbit effect, the difference is largely diminished [17, 18]. Potentially, it could reduce heat flux but increase divertor erosion when taking a closer look into intra-ELM $Y_W$ peaking around ~65° from the surface normal. Further details regarding the lower, open MRC and upper, closed SAS-VW divertor configurations will be discussed in the experimental procedure and preliminary results sections.

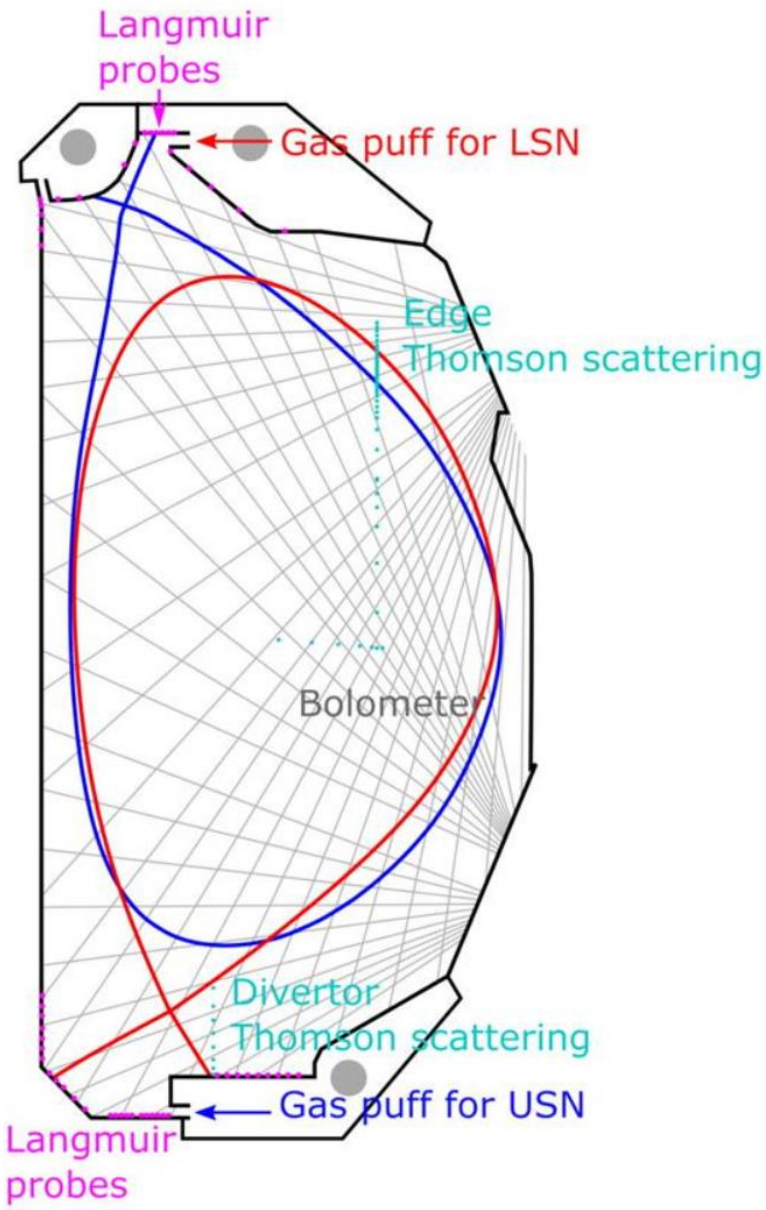



***Figure 11. Comparison of the DIII-D upper, closed divertor (blue) and lower, open divertor (red) [14].***

# Chapter 4

# Modelling

## 4.1 Free Stream plus Recycling Model (FSRM)

The analytic "free-streaming model (FSM)" treats ELMs as a 1D plasma filament that detaches from the pedestal into the scrape-off layer (SOL), where particles rapidly (<1 ms) stream to strike the divertor target [8, 9, 19, 20]. A conception of this model is imaged in Figure 12. The plasma filament is transported from the core plasma and streams quickly along magnetic field lines in the SOL to the divertor target. Sputtered and reflected ions often ionize near the target and re-accelerate back to the divertor to cause particle recycling, as discussed previously. The particles undergo repeated recycling, interacting with the divertor target numerous times. This is the general conception for the FSRM, a relatively simple 1D model used to predict the divertor erosion during ELMs [9, 19, 20]. The FSRM predicts intra-ELM erosion based off plasma parameters that are assumed to be relatively constant during the inter-ELM phase but fluctuate over the duration of an ELM. The inputs to the FSRM include the peak characteristic $n_e$ and $T_e$ at the pedestal top and the divertor, impurity concentrations at the pedestal top or divertor, the effective recycling coefficient ($R_{eff}$), the parallel length of the ELM filament ($L_{ELM}$), the parallel intra- ELM magnetic connection length ($L_{||}$), and $\alpha$. It is worth noting that the divertor $n_e$ and $T_e$ inputs are coherently averaged from measurements over many ELMs, spanning times up to 1 ms after the ELMs start (just before the ELM crash). Meanwhile, the pedestal $n_e$ and $T_e$ inputs are taken approximately 0.5 ms before the ELMs start. Contrary, all other inputs are averaged values over the whole-time frame of the shot analyzed. Then, expressions are derived for the ion flux ($\Gamma_{||,FS}$), and heat flux ($q_{||,FS}$) to the divertor target. Likewise, the following

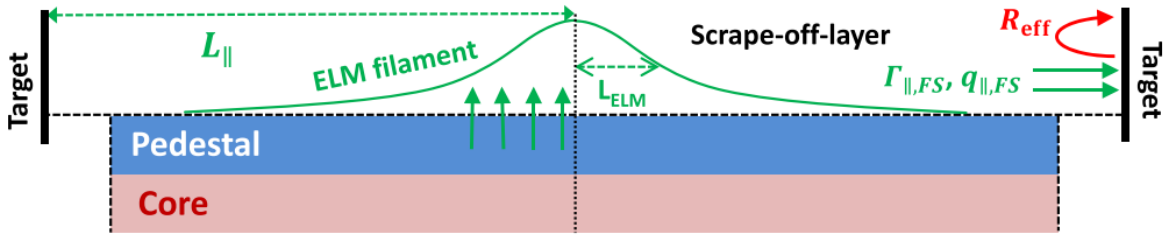



***Figure 12. Illustrated overview of the FSRM with magnetic field lines mapped into a 2D plane [8].***

equations show the correlation between $\Gamma_{||,FS}$, $q_{||,FS}$, predicted W erosion, and several of the key various input parameters discussed.

$$\Gamma_{||,FS} \propto ne,ped * (Te,ped)^{.5} \quad 4.1$$

$$q_{||,FS} \propto ne,ped * (Te,ped)^{1.5} \quad 4.2$$

$$FSRM\ W\ ELM\ Erosion = \Gamma_{||,FS} * Y_W \quad 4.3$$

As discussed previously, $Y_W$ is a function of the ion's $E_i$ and $\theta$ on the W divertor surface. Intra-ELM $E_i$ is directly proportional to the pedestal $T_e$. Additionally, both $q_{||,FS}$ and $\Gamma_{||,FS}$ are roughly proportional to $L_{ELM}$*$L_{||}$ and each other. The full mathematical expressions for the ion and heat flux and further discussion of the FSRM can be found in [19, 20]. Another potential nuisance of the FSRM are the required manual inputs for $L_{ELM}$ and $L_{||}$. Thus far, the parameters are assumed to be the same as the MRC, but are impacted by ion sound speed ($c_s$) and ELM signal decay time ($\tau_n$). Some FSRM incorporation of $L_{||}$ ELM parameters may improve intra-ELM erosion estimates. Equation 5 shows the relation between $L_{||}$, $\tau_n$, $c_s$, adapted from Equation 4.4 in [20].

$$L_{||} \sim c_s * \tau_n \quad 4.4$$

Equation 4.4 incorporates the effect of collisions when the plasma filament cools with a fluid model description for parallel losses. Though, parallel ELM filament losses are seen to be roughly similar between the MRC and SAS-VW campaign when comparing ELM signal decay time and ion speed values. Prominently, the FSRM does not take C deposition onto the W divertor surface into account, which can screen the divertor from incoming ions and reduce erosion. To account for this, we use a C/W mixed material model to predict the C and W

fractional divertor surface coverage during an ELM, which is also applied to inter-ELM W erosion predictions. Thus, this C/W mixed material model is discussed in the next subsection below.

## 4.2 C/W Mixed Material Model

Importantly, C ions interacting with the divertor surface not only physically sputter W but may deposit on or embed in the W surface. Previous modeling work has indicated that a higher percentage of C deposition results from a larger impurity percentage of C in the background plasma [21]. Additionally, a lower $T_{e,div}$ will result in a lower C $E_i$ to the divertor, leading to a decreased chance of W sputtering due to C ion impact and an increased chance of C deposition. Moreover, lower energy C ions are less likely to overcome the sheath potential to reach the main plasma and increase the chance of C recycling back to the divertor target. In this paper, it is postulated that C deposition on the W surface acts as a barrier protecting the W target from direct interactions with incoming ions, reducing $Y_W$. Here we present an analytic model for the fraction of W ($\sigma_W$) and C ($\sigma_C$) present in the deposition layer and incorporate such effects into the FSRM.

Consider, in steady-state, a near-surface mixed-material C/W layer with normalized C and W fractional divertor surface coverage concentrations $\sigma_C$ and $\sigma_W$, respectively. No other impurities are assumed present such that $\sigma_C + \sigma_W = 1$. The total gross erosion yield of C ($Y_{C,tot}$) and W ($Y_{W,tot}$) are thus given by the following set of equations, modified from Abrams (2021) [22]:

$$Y_{C,tot} = \Gamma_D \sigma_C (f_C Y_{C\to C} + (Y_{D\to C} + X_{D\to C})) \quad 4.5$$

$$Y_{W,tot} = \Gamma_D \sigma_W (f_C Y_{C\to W} + Y_{D\to W}) \quad 4.6$$

Where $f_C$ is the carbon impurity flux fraction, $\Gamma_C/\Gamma_D$ and $X_{D\rightarrow C}$ is the D-induced C chemical sputtering yield. As discussed previously, we assume self-sputtering by tungsten flux to the surface, $\Gamma_W = f_W\Gamma_D$, is negligible. For inter-ELM and recycling conditions, we assume $Y_W$ by $D^+$ is negligible because the average $E_i$ for $D^+$ is below the threshold energy for this process to occur. Accounting additionally for the R, the total flux ($\Gamma$) of material leaving the surface is given by:

$$\Gamma_{C,out,tot} = Y_{C,tot} + R_{C\rightarrow C}\sigma_C f_C\Gamma_D + R_{C\rightarrow W}\sigma_W f_C\Gamma_D \quad 4.7$$

$$\Gamma_{W,out,tot} = Y_{W,tot} + R_{W\rightarrow C}\sigma_C f_W\Gamma_D + R_{W\rightarrow W}\sigma_W f_W\Gamma_D \quad 4.8$$

The carbon impurity flux fraction, $f_C$, is assumed to be equal to the value at the pedestal top and is thus a known quantity provided by charge exchange spectroscopy (CER) diagnostics on DIII-D [23] for the MRC while $f_C$ is inferred directly from CIII filterscopes present in SAS-VW. In steady-state, the values of $\sigma_C$ and $\sigma_W$ do not change. We assume the net erosion regime for carbon, where $0 < \sigma_C < 1$. Steady-state implies that the amount of material leaving the mixed-material layer is equal to the amount of material entering the layer, for both species (C and W). For C, this can be expressed as follows:

$$f_C\Gamma_D = \Gamma_{C,out,tot} \quad 4.9$$

$$f_C = \sigma_C(f_C Y_{C\rightarrow C} + Y_{D\rightarrow C} + X_{D\rightarrow C}) + R_{C\rightarrow C}\sigma_C f_C + R_{C\rightarrow W}(1-\sigma_C)f_C \quad 4.10$$

Solving for $\sigma_C$:

$$\sigma_C = \frac{f_C(1-R_{C\rightarrow W})}{f_C(Y_{C\rightarrow C}+R_{C\rightarrow C}-R_{C\rightarrow W})+Y_{D\rightarrow C}+X_{D\rightarrow C}} \quad 4.11$$

After solving the normalized C concentration, $\sigma_C$, the FSRM simulated intra-ELM W erosion can account for the effects of a mixed C/W material to an extent. Currently, it is assumed that W erosion only stems from the concentration of $\sigma_W$, with negligible PMI beyond the several-nanometer thick mixed material layer. Hence, the intra-ELM W erosion simulated by the FSRM is multiplied by the normalized W concentration, $\sigma_W$, to correct for a C/W mixed material effect. Y and R values have been analyzed more closely using RustBCA, to be discussed later. R have been made $E_i$-dependent for better prediction of $\sigma_C$ and particle recycling.

# Chapter 5

# Experimental Procedures

## 5.1 Metal Rings Campaign

The experiments described here were performed during the DIII-D Metal Rings Campaign (MRC), in which two toroidally symmetric rows of W-coated tiles were installed in the DIII-D lower divertor where the W coating thickness varied from 10-15 micron [13, 24]. In the plasma discharges analyzed in this work, 1.3 mm diameter, 0.9 mm length cylindrical $D_2$ pellets were injected at frequencies up to nominally 60 Hz near the low-field side midplane of the tokamak using two pellet guns capable of injection up to 30 Hz each [11]. These $D_2$ pellets were injected during H-mode, attached plasma conditions. In-situ experimental W divertor erosion estimations were obtained via visible light spectroscopy. WI (400.9 nm) filterscopes [9] obtained photon emission intensity rates from sputtered neutral W atoms while Langmuir probes (LP) and Thomson scattering (TS) were used to obtain $T_e$ and $n_e$ at the divertor surface and pedestal top, respectively. Langmuir probes used V-I scanning with a spatiotemporal resolution of 4 mm width LP tips to capture the time resolution of the transient $T_e$ caused by ELMs by coherently averaging numerous peak ELM $T_e$ inputs [8, 25]. Figure 13 gives an overview of the diagnostics used in this study, as well as a typical magnetic equilibrium during this experiment. In Figure 13a and Figure 13b, the MRC filterscopes in red contain the WI filterscope chords, each viewing several radial positions of the W-coated tiles installed in both the divertor floor and shelf. Notably, this image is a poloidal projection of views that are not parallel to the poloidal plane. This causes the viewing chords to look "bent." The location of the Thompson Scattering views to measure pedestal plasma conditions are also overlaid. For this experiment, the outer strike point (OSP) position resided at approximately a major radius of R=1.42 m on the divertor

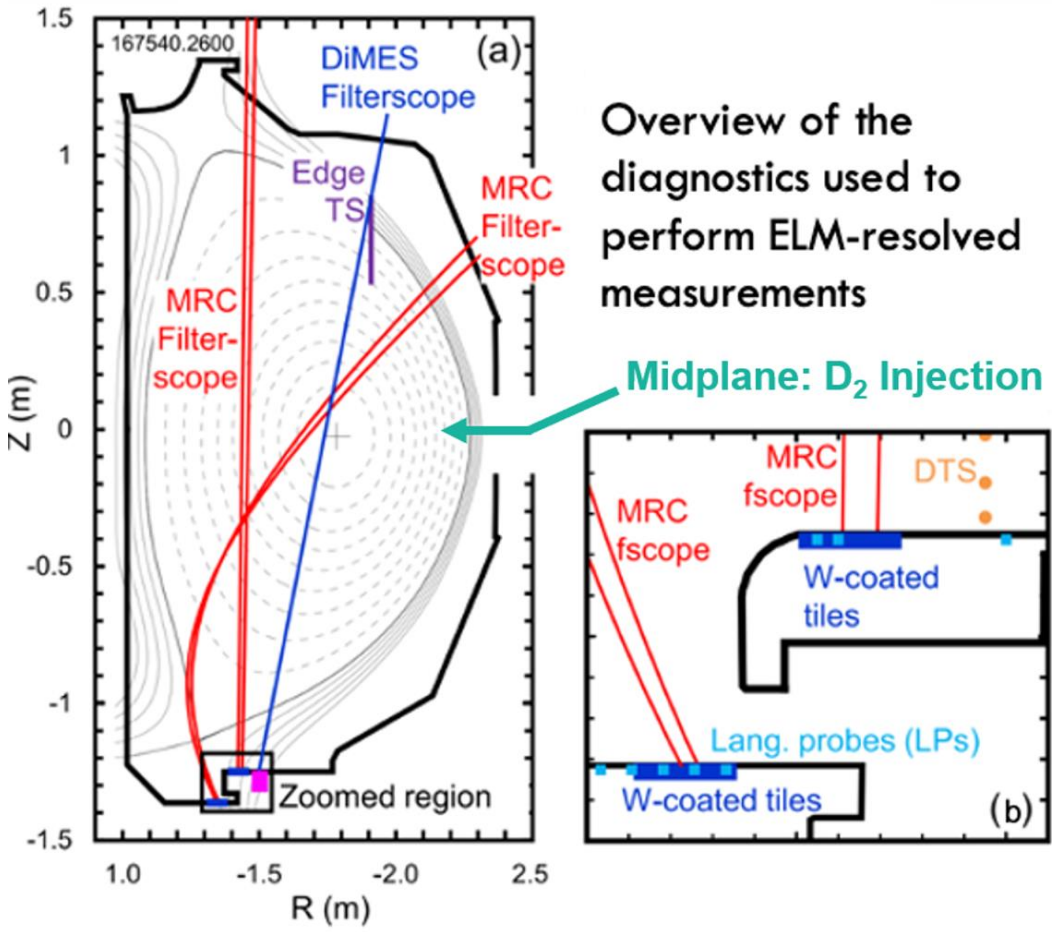



***Figure 13. Overview of the diagnostics used to perform ELM-resolved measurements during the MRC. Figure adapted from [8].***

shelf (opposed to the divertor floor below the shelf and at the bottom of the image), shown in the upper right portion of Figure 13b. The W photon emission signal obtained from the WI filterscope chord viewing the OSP position is then converted to gross W erosion using the ionization/photon (S/XB) method. The S/XB method essentially multiplies the measured photon emission rate by the atomic ionizations per photon, also known as the S/XB coefficient. The S/XB coefficient is a function of the divertor $T_e$ and $n_e$, where $n_e$ evolves significantly over the ELM cycle, making the S/XB coefficient time dependent. The S/XB coefficients for W atoms as a function of $T_e$ and $n_e$ are obtained via the open Atomic Data Analysis Structure (ADAS) [26]. Specifically, the characteristic $T_e$ and $n_e$ are averaged for the ELM duration and corresponding S/XB coefficient are considered for the intra-ELM S/XB coefficient. Then, $n_e$ is scaled directly to the photon intensity of the ELM with respect to the relative ELM start time, while $T_e$ is coherently averaged from numerous intra-ELM temperature inputs. Hence, Equation 5.1 below gives the calculation for the W gross erosion rate:

$$\Gamma = \frac{S}{XB} \int_0^\infty I \, \mathrm{dz} \qquad 5.1$$

Here $I$ is the photon intensity and dz is the integration of the W atoms along the line of sight of the WI filterscope chord. Langmuir probes were specifically installed on the W tiles to measure the relevant divertor $T_e$ and $n_e$ used to obtain the S/XB coefficient and W gross erosion rate. Lastly, $D_\alpha$ (656.19 nm) filterscopes were used to detect ELM start times to enable the analysis of W erosion relative to the ELM start time, enabling coherent averaging. The peak $D_\alpha$ filterscope signal determined the most significant ELMs worth measuring for this analysis. Thus, only ELMs that contain a peak intensity above some threshold fraction of the most intense ELM analyzed over the plasma discharge timeframe were included. In the Results section, **Table 1** shows this threshold

as a fraction of the most significant ELM for each shot and timeframe. Characteristically, there was generally a band of "large-sized", "mid-sized", and "small-sized" Type-I ELMs for each shot timeframe. For all shots, the "large-sized" and "mid-sized" ELMs were analyzed, as W erosion from the "small-sized" ELMs was negligible. The respective divertor $T_e$ and $n_e$ profiles used to obtain the S/XB coefficients differed for the "large-sized" and "mid-sized" ELMs as more intense ELMs contained slightly greater divertor $T_e$ and much greater divertor $n_e$. Since the divertor $n_e$ directly scales to the ELM intensity, the majority of the "mid-sized" ELMs resulted in a small contribution of erosion compared to the "large-sized" ELMs. On average, the mid-sized ELMs only contained about 3% of the total intra-ELM gross W erosion rate. In the no pellet pacing cases, this average contribution increased to around 10% of the total intra-ELM gross W erosion rate. Moreover, IR cameras were used to find the average peak intra-ELM heat flux for these MRC plasma discharges. More details on this analysis workflow can be found in previous papers on this topic [8, 27].

## 5.2 Small Angle Slot

This work analyzes intra-ELM W divertor erosion and heat flux under conditions similar to those from the 2016 Metal Rings Campaign (MRC) open divertor configuration, but with key diagnostic and result differences described in the Experimental Procedure section. Once again, experimental results are verified using the FSRM and an analytic steady-state near-surface C/W mixed-material layer model to correct FSRM intra-ELM W erosion predictions [22]. The 2022 Small Angle Slot V-shaped W (SAS-VW) campaign on the DIII-D tokamak featured a highly baffled closed divertor configuration designed to trap plasma impurities and achieve plasma detachment from the divertor target at lower main ion densities [13]. However, unmitigated edge-localized modes (ELMs) can "burn through" detachment and erode divertor material during

the intra-ELM phase [28]. For a set of H-mode attached plasma shots, we injected varying rates of $D_2$ gas and pellets at the outboard midplane of DIII-D to distinguish their impact on gross W erosion and divertor heat flux during and between ELMs. $D_2$ pellets injected at thermal velocities (approximately 100–200 m/s) near the low-field side midplane, where instabilities are significant, have been shown to mitigate ELM effects by triggering smaller, more frequent ELMs through pedestal destabilization and perturbation of the ballooning stability boundary [20]. The small angle slot was redesigned with a more V-shaped geometry, hence the "SAS-VW Divertor." Before the SAS-VW campaign, a 10 cm long, 10–15 μm thick W-coated region was installed along the outboard side of the divertor [13], similar to the MRC. For a series of plasma shots, we injected 1.3 mm × 0.9 mm cylindrical $D_2$ pellets at frequencies up to ~60 Hz near the low-field side midplane using two pellet guns capable of up to 30 Hz each [11]. In another series, we puffed $D_2$ gas at rates from 27 to 72 Torr-L/s. All plasma shots analyzed here were performed in H-mode with attached divertor plasmas showing strong W photon signals above background levels. Several discharges instead used $D_2$ gas with comparable mass injection rates at the same midplane position to distinguish pellet versus gas effects on W erosion and heat flux.

A diagnostic setup similar to the MRC measured pedestal and divertor plasma conditions and WI photon emission throughout the SAS-VW experiment. In-situ W erosion estimates were obtained via visible light spectroscopy. Dα (656 nm), CIII (465 nm), and WI (400.9 nm) filterscopes were used to detect ELM start times, C photon emission, and W photon emission, respectively. Langmuir probes (LP) and Thomson scattering (TS) measured $T_e$ and $n_e$ at the divertor surface and pedestal top. LP used I–V scanning with 4 mm wide tips to capture transient $T_e$ resolution during ELMs [25]. Surface eroding thermocouples (SETCs) with ELM-resolved time resolution were installed along the divertor surface to compensate for the limited view of

infrared (IR) cameras in the narrow SAS-VW slot [29]. Figure 14 summarizes the divertor diagnostics used in this study. The partly transparent orange bars represent filterscope chords viewing three regions of the SAS-VW divertor. The outer strike point (OSP) for the plasma shots discussed here is from the "view 2" position ($Z \approx 1.20$ m, $R \approx 1.49$ m). We analyze experimental data using LPs and SETCs (blue and red, respectively) along the W surface (gray). All LP and filterscope data were obtained from the view 2 line of sight. These diagnostics are located at distinct toroidal positions within the SAS divertor. Assuming a similar DIII-D poloidal diagnostic overlay as Figure 13 (for the upper divertor), Figure 14 shows the diagnostic setup used in the SAS-VW experiment. As seen, the SAS-VW diagnostic setup benefits from several WI (400.9 nm) spectral lines and a vast installment of LPs and SETCs to calculate divertor conditions, W erosion, and heat flux alike. Importantly, the IR cameras lacked line-of-sight of the SAS-VW divertor due to the tight baffling geometry compared to the MRC. Thus, SETCs provided crucial heat flux measurements in the absence of IR cameras for SAS-VW plasma discharges. Fortunately, past studies on the DIII-D lower divertor cross-calibrated IR camera and SETC measurements and confirmed accurate heat flux measurement agreement between the two methods [29-31]. Likewise, Figure 15 compares IR camera and SETC heat flux values in an ELMing H-mode shot from the lower divertor. Notably, the SETCs are capable of intra-ELM heat measurements, but the time resolution is not as sharp as the IR camera. Amongst other factors, this likely results in an underestimation of peak ELM heat flux values, especially for larger ELMs. However, SETCs still provide an accurate comparison of intra-ELM heat flux values within a set of experimental plasma discharges. The next section will compare experimental and modeling results from the MRC and SAS-VW experiments. Unlike the $D_\alpha$ and CIII filterscopes, the WI filterscope is characterized by a 'narrow' and 'medium' chord at each

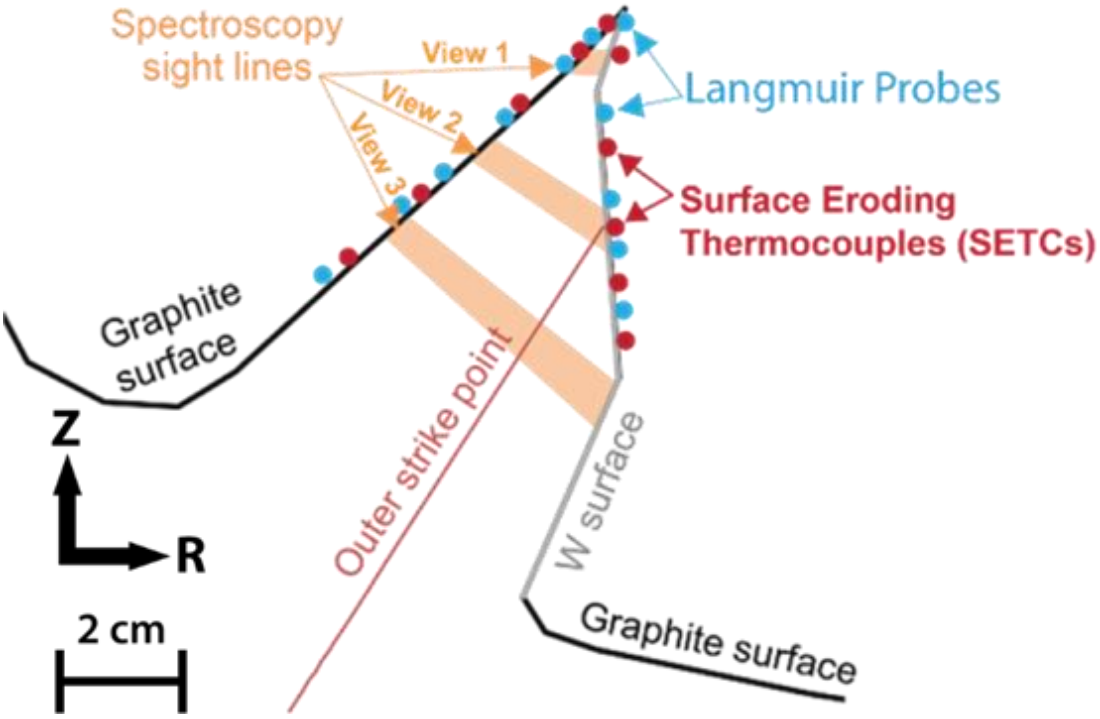



***Figure 14. Overview of the diagnostics used to perform ELM-resolved measurements during the SAS-VW campaign adapted from [13]. The red line indicates the outer strike point (OSP) position for the analyzed plasma shots. The orange spectroscopic lines of sight include the WI, $D_\alpha$, and CIII filterscopes. LP and SETCs indicated by blue and red dots, respectively, were installed along the W surface shown by the grey line. Spectroscopy, LPs, and SETCs are at different toroidal locations within the SAS divertor [14].***

viewpoint. The ‘narrow’ and ‘medium’ filterscopes integrate the measured WI photon emission spectra with a 10 Å and 15 Å full width half maximum transmission filter, respectively. The two-filter filterscope configuration permits subtraction of background continuum emissions after cross-calibration with the DIII-D Multichordal Divertor Spectrometer (MDS) [32]. Hence, Equation 5.2 gives the expression for the background subtracted line intensity to resolve intra-ELM measurements.

$$I_{f_{scope}} = \frac{I_N - R_{CC} * I_M}{1 - R} \tag{5.2}$$

$I_{fscope}$ refers to the background subtracted WI filterscope, $I_N$ refers to the ‘narrow’ filterscope, $I_M$ refers to the ‘medium’ filterscope, and $R_{CC}$ refers to the linear fit cross-calibration factor value between MDS and filterscope signals [32]. To compute $R_{CC}$, we perform a Levenberg-Marquardt least-squares fit between a matrix of the $I_N$ and $I_M$ signals and the MDS signal for WI photon emission [32]. Simply, $R_{CC}$ equals the $I_N$ transmission function ($T_N$) divided by the $I_M$ transmission function ($T_M$) as expressed below in Equation 5.3.

$$R_{CC} \equiv \frac{\int T_N(\lambda) d\lambda}{\int T_M(\lambda) d\lambda} < 1 \tag{5.3}$$

Importantly, λ represents the wavelength of the filterscope. $T_N$ contains a 10 FWHM λ Å and $T_M$ contains a 15 FWHM λ Å. The average $R_{CC}$ value for plasma shots analyzed during this experiment was 0.775 and an uncertainty range of $R_{CC}$ +/- 0.025 is accounted for in error propagation of the WI erosion results. Essentially, the filterscope time resolution is fast enough to resolve ELMs while the MDS data is not.

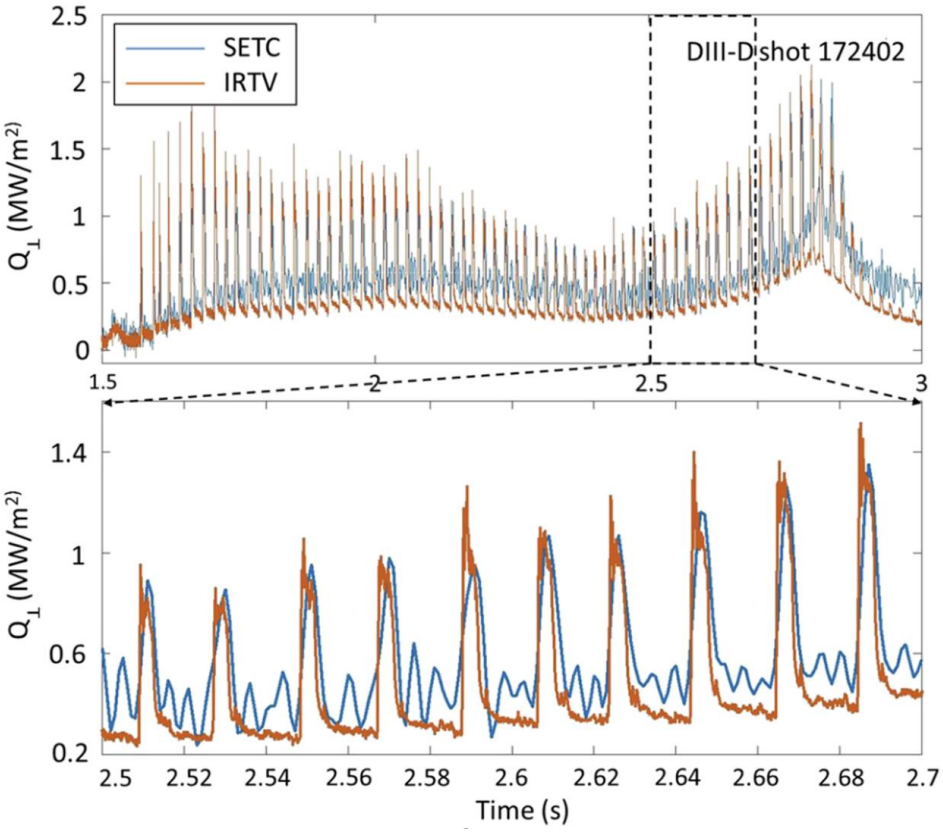



***Figure 15. Comparison between SETC and IR camera intra-ELM heat flux [30].***

Thus, the two-filterscope configuration is necessary to analyze ELMs and comparison to the MDS data ensures that the spectroscopically measured data is sensible. The calibrated filterscope photon emission is within reasonable comparison to the MDS photon emission. Though on average, the calibrated filterscope photon emission is larger than its MDS counterparts. The two-filter filterscope configuration requires a strong WI emission line distinguishable from impurity lines around the same light wavelength. Fortunately, the strongly attached H-mode plasma allowed adequate detection of W photon emission. The S/XB method multiplies the filterscope measured W photon emission rate by the atomic ionizations per photon, also known as the S/XB coefficient, to calculate W erosion. The S/XB coefficients are a function of $T_e$ and $n_e$ and are obtained via the open Atomic Data Analysis Structure [26]. Hence, Equation 5.4 gives the calculation to determine the experiment W erosion and the filterscope to MDS comparison is shown in Figure 16.

$$\Gamma_{W_{experiment}} = 4\pi \frac{S}{XB} \int_0^\infty I dz \tag{5.4}$$

Here, I is the two-filter filterscope photon intensity ($ph*cm^{-2}*s^{-1}*sr^{-1}$) and dz is the integration of the W atoms along the line of sight of the WI filterscope chord. Similarly, the same process is used to convert the D and C photon rates to D and C atoms, respectively. Thus, by dividing the C flux by the D flux, we obtain the C plasma impurity concentration ($f_C$) during ELMs, as expressed in Equation 5.5:

$$f_c = \frac{\Gamma_C}{\Gamma_D} \tag{5.5}$$

$f_C$ is used to find the concentration of C on the divertor surface ($\sigma_C$) to correct the FSRM predicted intra-ELM gross W erosion. Essentially, the FSRM predicted intra-ELM W erosion is

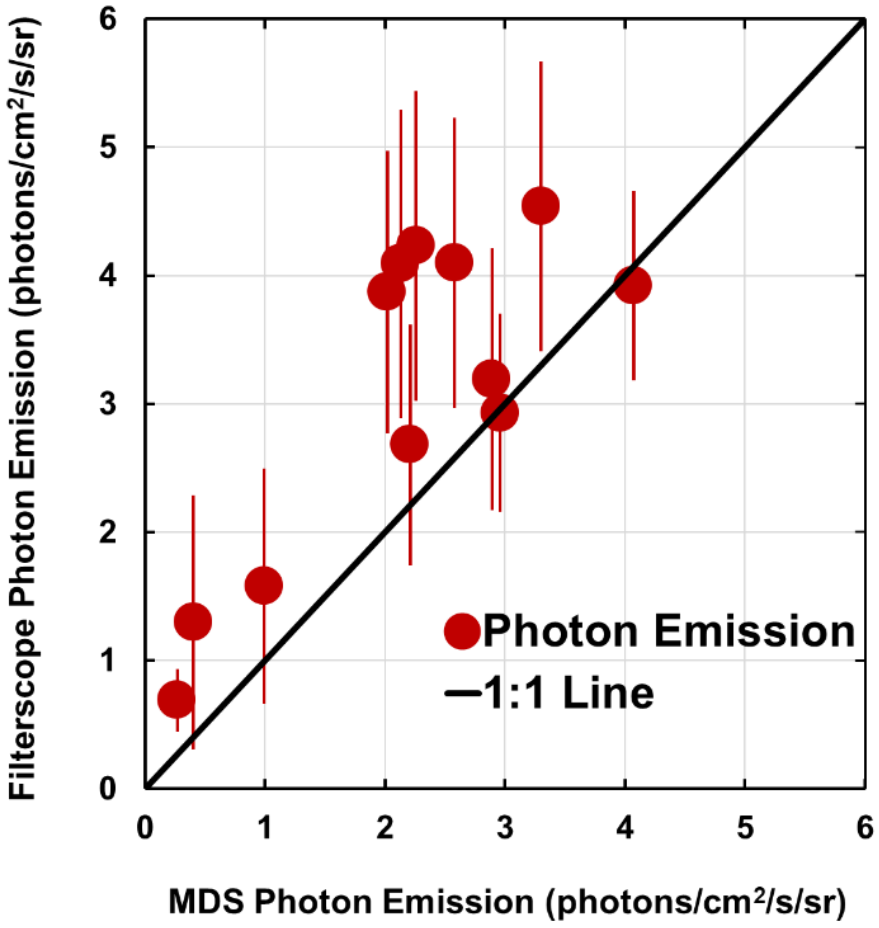



**Figure 16. Calibrated two-filter filterscope WI photon intensity versus the calibrated MDS WI photon intensity integrated for the analyzed time range of each plasma shot.**

multiplied by the concentration of W on the divertor surface ($\sigma_W$) to account for C deposition. Importantly, only recycling ion interactions within the near-surface material layer are considered. Importantly, only recycling ion interactions within the near-surface material layer are considered such that free-streaming ion effects are ignored.

# Chapter 6

# Experimental Results

## 6.1 Metal Rings Campaign

The Metal Rings Campaign (MRC) took place in the summer of 2016, and the analysis concluded with this work in 2022. Here, intra-ELM and inter-ELM W erosion rates have been analyzed for 9 different plasma shots over various time ranges with relatively constant input parameters for validation of the FSRM. **Table 1** lists the $D_2$ mass injection rate in arbitrary units (A.U.) and the analyzed plasma shot time ranges. Shot time ranges were selected after the OSP position settled within 1 cm of the nearest MRC Langmuir probe positions (R=1.41 - 1.42 m). Due to uncertainties in the number and size of the $D_2$ pellets injected over the course of each analyzed shot, the pellet masses are determined with a microwave cavity diagnostic [33]. However, an absolute calibration of the cavity signal for this dataset is unavailable, thus the technique only provides a relative comparison of pellet masses, and the total injected mass is given in A.U. For the majority of the shots and associated time ranges, the $D_2$ mass injection rate in A.U. has been determined by conducting a linear fit to the cumulative injected mass over time. Figure 17 shows the $D_2$ mass injection rates for each shot time range plotted as a function of nominal $D_2$ pellet injection frequency. Unfortunately, it is a time-consuming process to interpret the cumulative $D_2$ mass injection over a given time range. Thus, the shots with asterisks in **Table 1** were not mass calibrated. Instead, the linear trendline is applied to interpolate these data points, shown in red in Figure 17. For shot 167351, the $D_2$ injection rate was increased from a nominal pellet pacing injection frequency of 20 to 60 Hz in increments of 10 Hz. In actuality, the second $D_2$ pellet gun applied did not perform up to 30 Hz and the actual amount of $D_2$ injected at a given nominal injection frequency can vary as displayed in Figure 17. Consequently, the nominal $D_2$

**Table 1:** MRC Plasma Shot Summary

| Shot number 167xxx | $D_2$ mass injection rate (A.U.) | $F_{ELM}$ (Hz) | Threshold | Time range (ms) |
|---|---|---|---|---|
| 349 | 0 | 8 | 0.25 | 2200:3200 |
| 351 | 13.3 | 25.7 | 0.25 | 2150:2500 |
| 351 | 14.8 | 20 | 0.25 | 2550:3000 |
| 351 | 35.6 | 24.4 | 0.25 | 3050:3500 |
| 351 | 34.7 | 20 | 0.25 | 3550:4000 |
| 351 | 40.7 | 22.2 | 0.3 | 4050:4500 |
| 352 | 40.6* | 16 | 0.25 | 2550:3050 |
| 353 | 0 | 15 | 0.25 | 2100:2900 |
| 354 | 0 | 9.4 | 0.25 | 2600:4200 |
| 355 | 38 | 13.3 | 0.4 | 3900:4800 |
| 356 | 40.6* | 18.5 | 0.4 | 3400:4700 |
| 357 | 25 | 20 | 0.3 | 2600:3000 |
| 358 | 27* | 22.5 | 0.25 | 2600:3000 |
| 358 | 27* | 20 | 0.2 | 3200:3800 |

*Interpolated $D_2$ mass injection rates from Figure 17

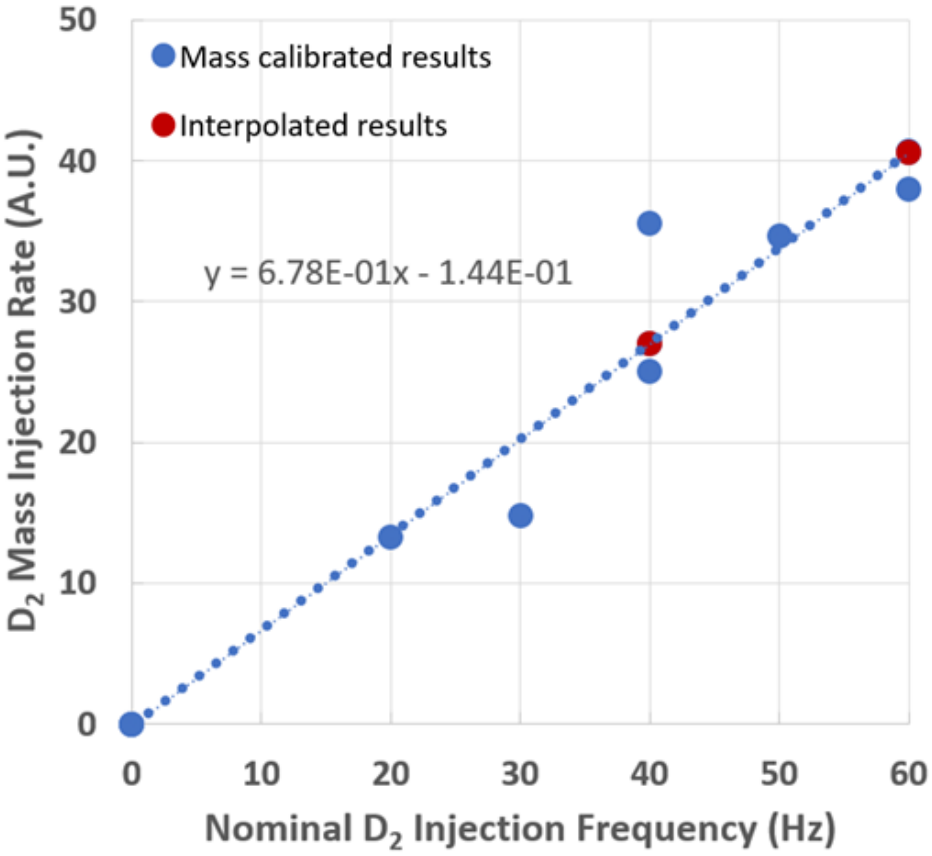



***Figure 17. Mass injection rate as a function of $D_2$ nominal injection frequency. Data interpolated by the linear trendline are shown in red.***

pellet injection frequency has been supplanted by the $D_2$ mass injection rate. Nonetheless, each nominal frequency lasted 500 ms and $D_2$ pellet injection started once a stable OSP position was obtained near R=1.42 m, around 2.1 seconds into the plasma shot. Figure 18 shows the measured divertor $T_e$ and $n_e$ and time range-average $D_2$ mass injection rate as a function of plasma shot time for shot 167351. Increasing frequency of injected $D_2$ pellets causes an increase in the divertor $n_e$ but a decrease in the divertor $T_e$. The increase of divertor $T_e$ just after 2 seconds into the plasma shot is the result of the stabilization of the OSP position. From here, the divertor $T_e$ steadily decreases with increasing $D_2$ mass injection rate while divertor $n_e$ steadily increases. Interestingly, for shot 167351, the ELM frequency ($F_{ELM}$) remained relatively constant as the $D_2$ mass injection rate increased. For this shot, there were about 10 "large-sized" ELMs for each $D_2$ mass injection rate time range. The divertor and pedestal $n_e$ and $T_e$ have been measured over the course of each plasma shot. As discussed previously, these parameters are direct inputs into the FSRM, helping predict average intra-ELM divertor erosion for current and future tokamak devices. Notably, plasma confinement parameters are largely unaltered by the changing $D_2$ mass injection rate in this shot. Figure 19 shows the characteristic peak intra-ELM $T_e$ and $n_e$ just before the ELM crash at the pedestal and divertor for each plasma shot. Similar to the divertor plasma conditions at the time just before the ELM crash, $n_e$ increased and $T_e$ decreased at the pedestal top with increasing $D_2$ mass injection rate. Notably, the divertor intra-ELM regime plasma conditions demonstrated a much larger fractional change in comparison to the pedestal plasma conditions. Changes in the pedestal $T_e$ just before the ELM crash showed the least correlation to the $D_2$ mass injection rate. When comparing the average divertor and pedestal $n_e$ and $T_e$ over the shot time (in inter or intra-ELM regime), similar trends for the divertor plasma conditions are seen while an increasing pedestal $n_e$ and decreasing pedestal $T_e$ correlates more

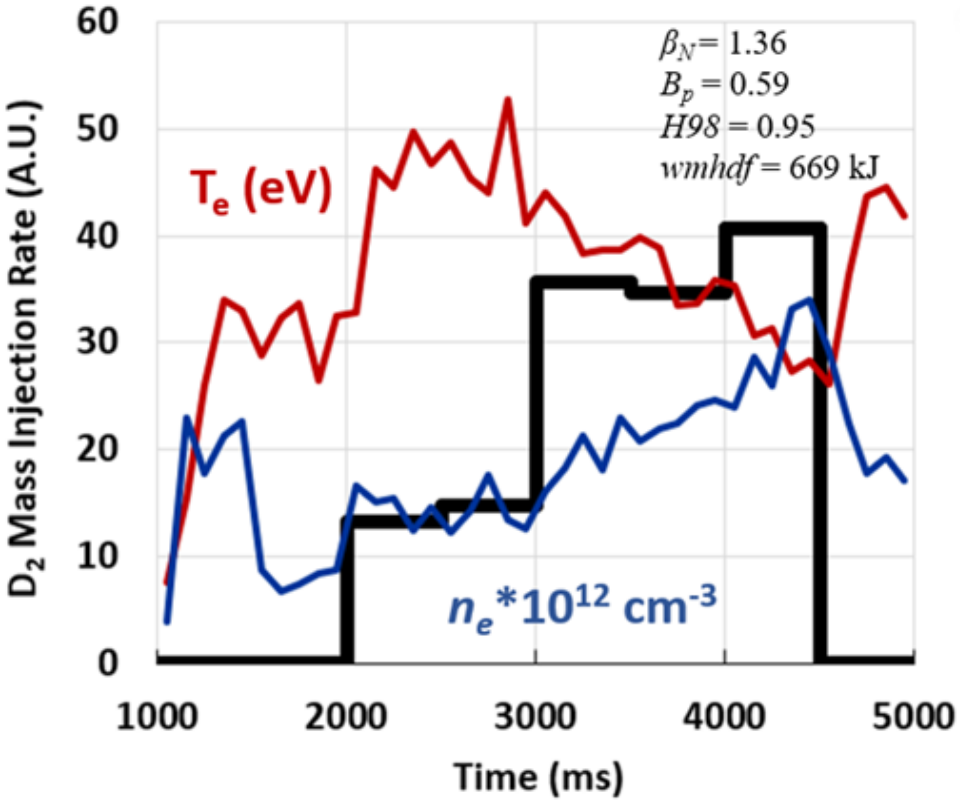



***Figure 18. Time history of the $D_2$ mass injection rate and divertor electron density and temperature in DIII-D discharge 167351. Y-axis values represent $D_2$ mass injection rate and divertor electron density and temperature. Normalized plasma pressure ($\beta_N$), the ratio of the plasma pressure to the poloidal magnetic pressure ($\beta_p$), the ratio of measured confinement time over predicted confinement time (H98), and the total plasma energy measured at a rapid frequency (wmhdf) plasma confinement are also overlaid.***

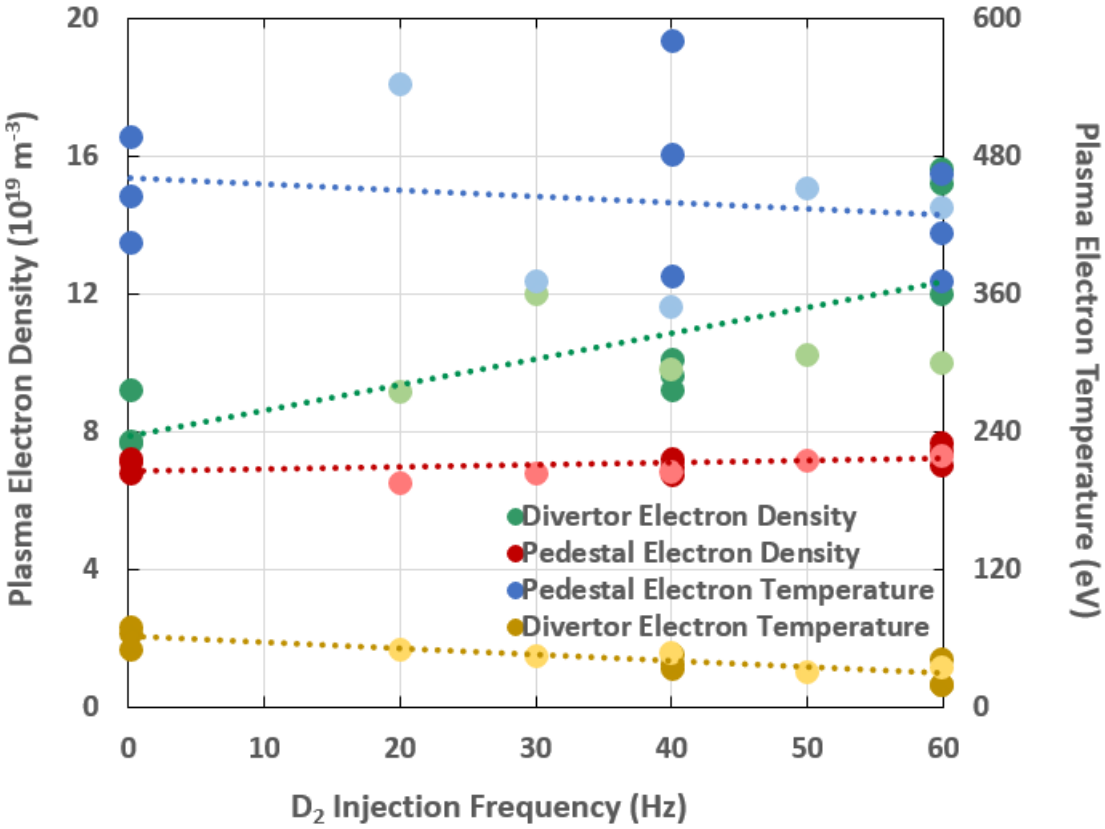



***Figure 19. Measured divertor and pedestal electron temperature and density just before the ELM crash as a function of $D_2$ mass injection rate for all cases listed in Table 1. The partially transparent data points represent the pellet pacing frequency sweep, shot 167351.***

strongly to an increasing nominal $D_2$ pellet injection frequency. In contrast, varying the $D_2$ mass injection rate resulted in inconclusive changes to the core plasma stored energy [27] and other plasma confinement parameters. Typically, the "large-sized" and "mid-sized" ELM bursts in this experiment lasted 1 to 4 ms before the W erosion returned to inter-ELM levels. Langmuir probes measured an accurate divertor $n_e$ profile as a function of time relative to the ELM start. Over the time course of each ELM, the spatiotemporal resolution of the LP was able to capture a few divertor $T_e$ measurements per ELM. Coherent averaging was then used to determine an appropriate divertor $T_e$ input, averaged from 0 to 1 ms relative to the ELM start time, for the S/XB coefficient and FSRM. Moreover, similar processes were used to estimate the divertor $n_e$ and $T_e$ in past MRC analyses involving $D_2$ pellet injection [8]. The average W gross erosion rate per ELM as a function of time relative to the ELM start is shown in Figure 20 for each $D_2$ mass injection rate in discharge 167351. Over the course of shot 167351, the peak intra-ELM W gross erosion rate was the greatest at the nominal 30 Hz pellet pacing frequency, corresponding to the $D_2$ mass injection rate of 14.8 A.U. The inter-ELM W gross erosion rate at 14.8 A.U. was similar to the 13.3 A.U. case, but greater than any of the higher injection frequencies. At injection frequencies higher than 14.8 A.U., both the intra-ELM and inter-ELM W erosion rates at the OSP position monotonically decreased. Unfortunately, the OSP position did not stabilize for this shot until the 20 Hz nominal pellet pacing frequency, corresponding to the $D_2$ mass injection rate of 13.3 A.U. This prevents comparing the W erosion rate to the no pellet case for this shot. The difference in W erosion for the various $D_2$ mass injection rates for shot 167351 is attributed to both changing divertor conditions and ELM amplitude, although the $F_{ELM}$ remained relatively unchanged. $D_2$ injection may have initially increased erosion due to increasing $n_e$ before a large enough amount of $D_2$ was injected to decrease $T_e$ sufficiently. When averaging the gross W

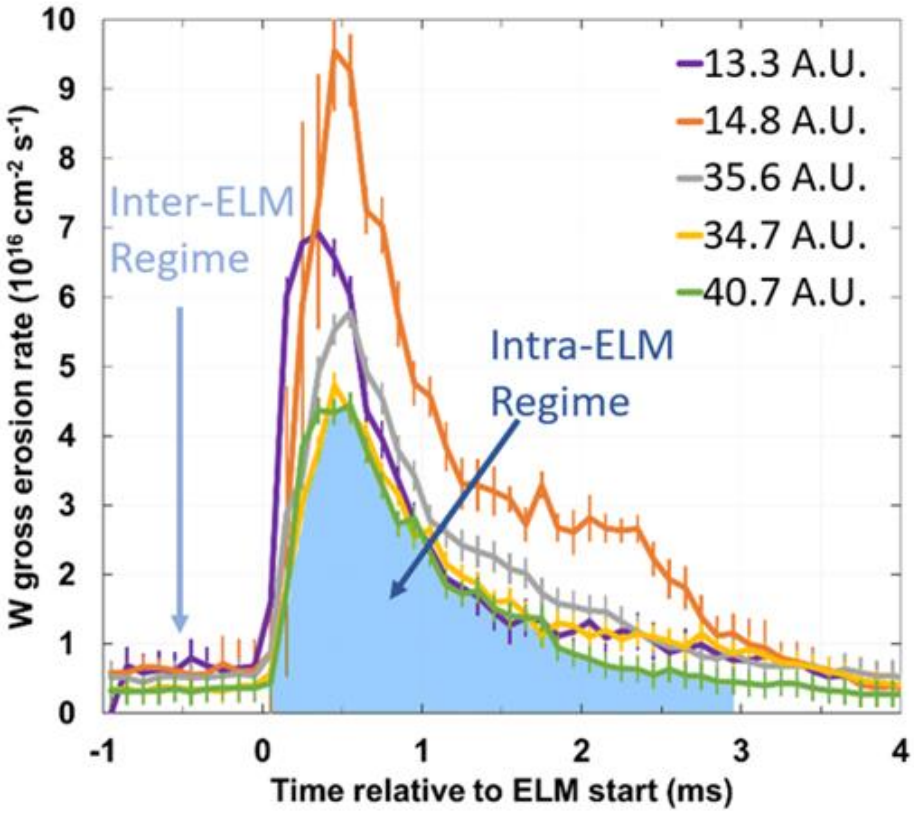



***Figure 20. Measured average W gross erosion rate per ELM during DIII-D discharge 167351 for the time ranges indicated in Table 1. Each time range corresponds to a $D_2$ mass injection rate averaged over the respective time range.***

erosion rate at the OSP position across the entire discharge, inter-ELM erosion exceeded intra-ELM erosion by approximately 150%. This is due to the plasma residing in the inter-ELM phase about 85% to 90% of the time. On average, an ELM resulted in transient W erosion, about 300% greater than the steady-state in the inter-ELM regime.

In this section, we compare the measured intra-ELM W erosion against the calculations of the FSRM as a function of increasing $D_2$ pellet injection frequencies. As discussed in Section 4.1, the FSRM provides a framework to calculate the average W erosion per ELM given the experimentally measured pedestal and divertor conditions. Figure 21 compares this average intra-ELM W erosion between the FSRM and experimental data. The standard deviation of the raw WI emission signals is considered as the error bar, shown for all measured average intra-ELM erosion shots. Thus, the error is considered on an ELM-by-ELM basis. The FSRM calculations both with and without the mixed-material model are shown in Figure 21. In general, increasing $D_2$ mass injection rates led to a decrease in the average intra-ELM erosion with little to no degradation of pedestal parameters and plasma confinement metrics. Figure 21 shows the average intra-ELM gross W erosion decreasing with increasing inter-ELM density and increasing with increasing inter-ELM temperature. Generally, an increasing divertor plasma density leads to greater W erosion due to a higher incident particle flux. However, increasing $D_2$ pellet injection frequencies also decreases the divertor $T_e$ and consequently the divertor $E_i$. Thus, the general trend supports decreasing erosion with increasing divertor $n_e$, rather. Usually, the shots with a higher $D_2$ mass injection rate contain a higher divertor inter-ELM density and lower inter-ELM temperature, supported by Figure 18 and Figure 19. The correlation between the average intra-ELM gross erosion and inter-ELM temperature is weaker than comparing the average intra-ELM gross erosion to inter-ELM density. In fact, the FSRM may suggest little to

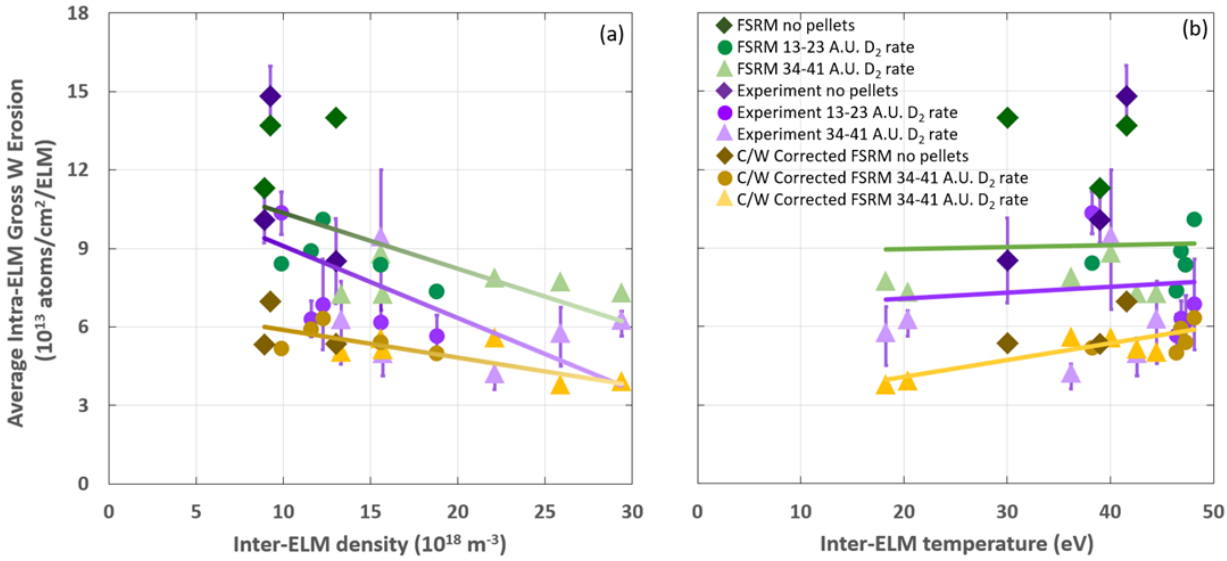



***Figure 21. Average gross W erosion rate per ELM measured experimentally (purple), calculated by the FSRM with no mixed-material model (green), and with the mixed-material model (gold), as a function of plasma electron inter-ELM (a) density and (b) temperature. Linear trendlines are overlaid in all cases.***

no W erosion correlation to the inter-ELM temperature before incorporating the C/W mixed material model. On average, the FSRM under-predicts the experimentally measured average intra-ELM W erosion by 28% when the mixed-material model is included. When mixed-material effects are neglected, the FSRM over-predicts the average intra-ELM W erosion by 24%. Thus, it is possible that W erosion may occur outside the C deposition layer. Next, we compare the predicted inter-ELM W erosion to the spectroscopically measured inter-ELM W erosion in Figure 22. This data was computed the same way as the SAS-VW inter-ELM W erosion; thus, the corresponding analytical methodology can be found in the discussion around Figure 33. Correspondingly, Figure 23 shows a comparison between the C/W FSRM predicted intra-ELM and spectroscopically measured intra-ELM W erosion in a similar manner as in Figure 21. The MRC inter-ELM W erosion is integrated over a 5 ms time range (the average characteristic MRC ELM time) and compared to the average W erosion spanning 5 ms before an ELM. As seen in Figure 22, the predicted inter-ELM W erosion generally exceeds the experimentally measured inter-ELM W erosion, though the large uncertainties complicate a larger conclusion. In this case, the predicted inter-ELM W erosion rate incorporates the mixed material surface concentration and measured ion flux profiles in the same manner as discussed with Figure 33. Unfortunately, the intra-ELM Langmuir Probe ion saturation current was uninterpretable during the MRC due to large noise signal uncertainty. As a result, the MRC FSRM intra-ELM ion flux verification cannot be achieved unlike in SAS-VW, where $D_\alpha$ filterscope chords were installed to readily infer intra-ELM ion flux quantities. MRC FSRM ion flux measurements assumed an effective recycling coefficient ($R_{eff}$) of 0.96, inferred from relevant past MRC data analysis. Basically, $R_{eff}$ is used to determine how much additional intra-ELM ion flux is due to recycling particles. Thus, the additional parallel ion flux to the target is described in Equation 6.1 below:

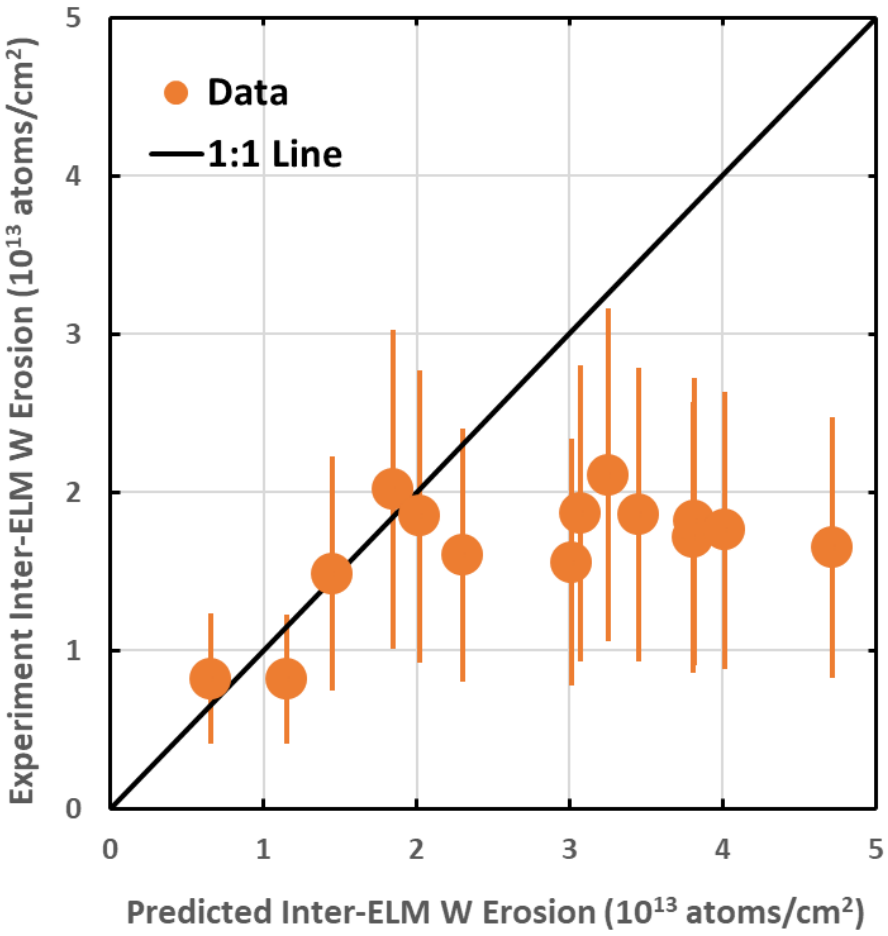



**Figure 22. MRC experiment vs. predicted inter-ELM W erosion.**

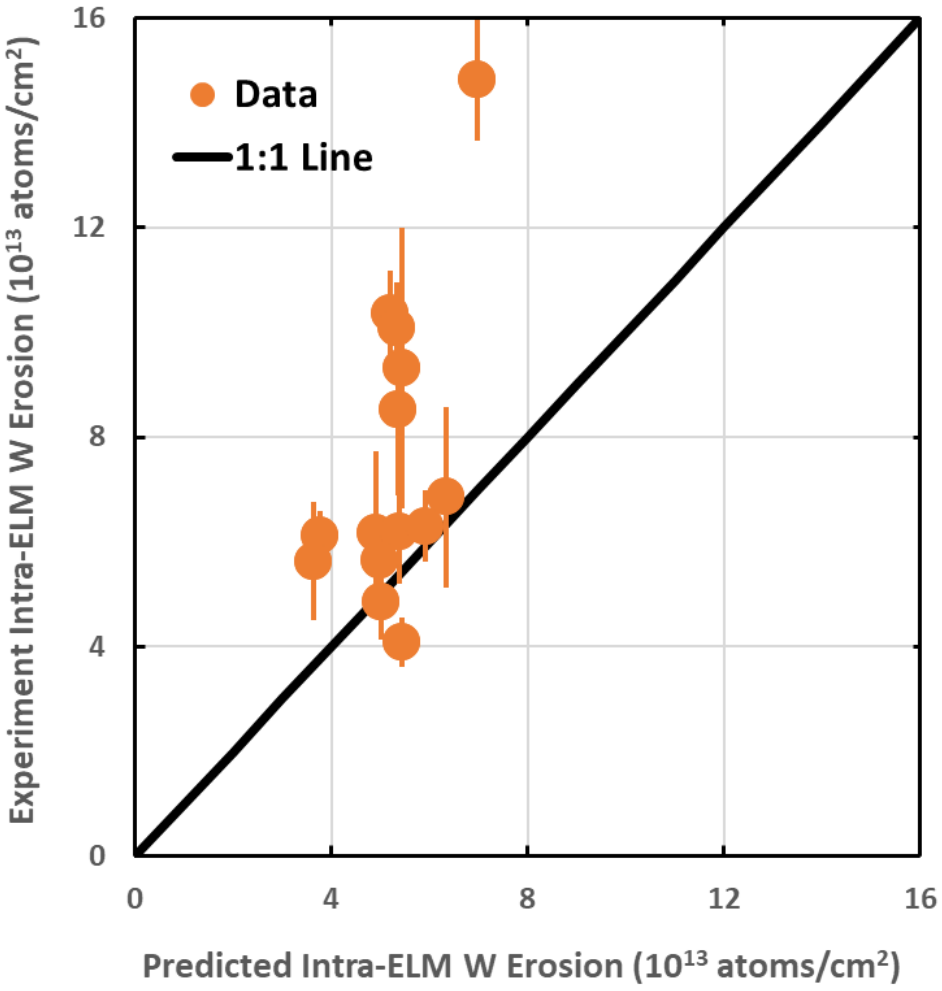



***Figure 23. MRC experiment vs. predicted inter-ELM W erosion.***

$$\Gamma_{||,REC} = \frac{R_{eff}}{1-R_{eff}} * \Gamma_{||,FS} * \sin(\alpha) \quad 6.1$$

$\Gamma_{||,FS}$ is the free streaming ion flux that strikes the divertor and α is the magnetic inclination angle measured from the surface, which averaged at 2 degrees for MRC shots. The $\sin(\alpha)$ multiplication represents the fraction of recycling ion flux that follow the grazing magnetic field line to strike the divertor surface whereas $\frac{R_{eff}}{1-R_{eff}}$ represents an empirical scaling factor. Plausibly, the LP ion saturation current used to infer to the experimental ion flux is oversaturated, resulting in an overestimation of the experimental ion flux. However, a slight increase in ion flux quantities in the FSRM would create more accurate C/W FSRM predictions. Perhaps a higher $R_{eff}$ value would be more accurate, but the additional recycling ion flux has a $T_i$ and corresponding $Y_W$ much lower than its ELMy counterpart. Thus, the additional predicted W erosion would be minimal.

Next, Figure 24 shows the predicted fractional concentration of W exposed at the divertor surface. Increasing $D_2$ mass injection rate increases the concentration of deuterium at the divertor and decreases the concentration of carbon at the divertor to expose more W. However, the increasing $D_2$ mass injection rate generally decreases the carbon $E_i$ at the W divertor to increase $\sigma_C$ as well. In this case, it appears that the reduction of carbon concentration has the bigger impact on carbon deposition than the lower C $E_i$. As a result, we see an increase in $\sigma_W$ with increasing $D_2$ mass injection rate. Plausibly, MRC $\sigma_C$ is more overestimated with lower $D_2$ mass injection rates, correlating to a higher plasma impurity concentration of C. This would explain the convergence of MRC C/W FSRM and experimental estimations with increasing $D_2$ injection rate seen in Figure 21. Once again, PYEAD and SDTrim.SP modelling can uncover more

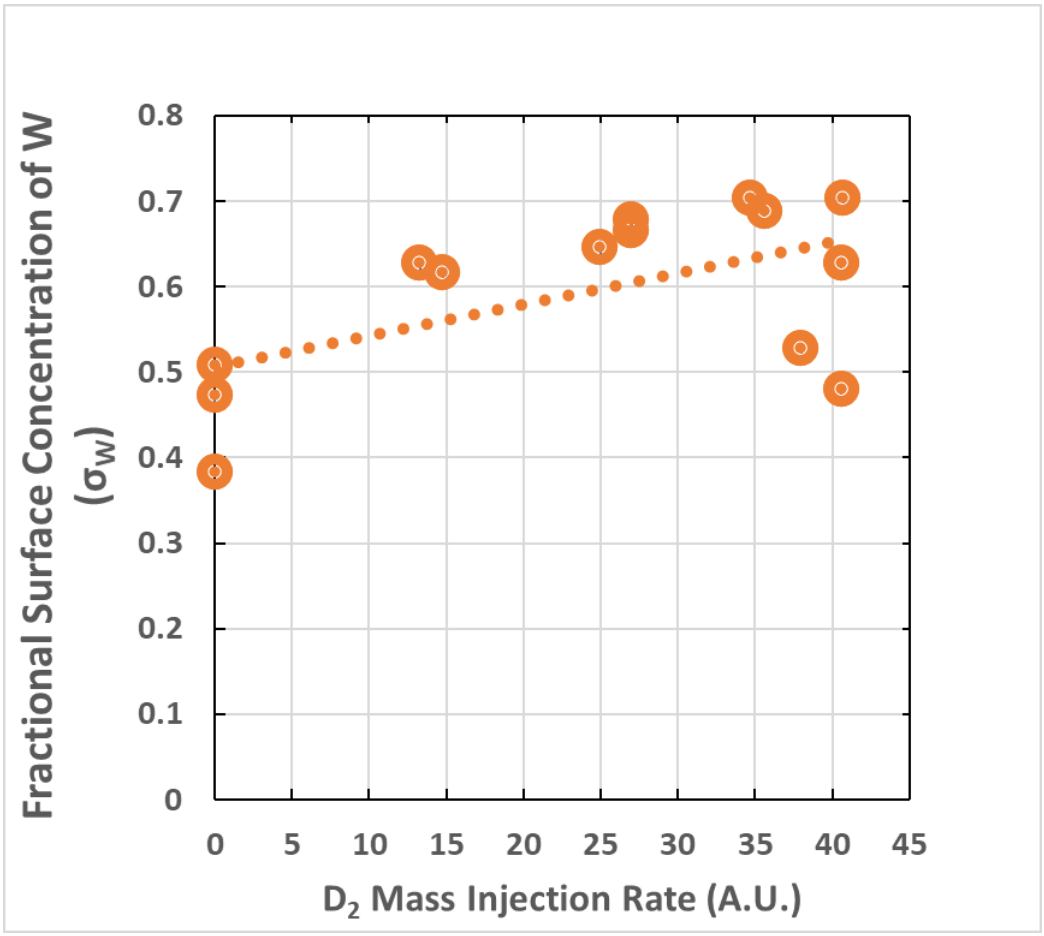



***Figure 24. Fractional concentration of W at the divertor surface during an ELM with respect to $D_2$ mass injection rate.***

accurate estimations and improvements to the C/W mixed material model will improve estimations. Next, Figure 25 shows the measured total gross intra-ELM W erosion rate for all ELMs occurring as a function of inter-ELM density and temperature for each plasma shot listed in **Table 1**. This rate is equal to the average erosion per ELM in Figure 21 multiplied by the $F_{ELM}$. Additionally, Figure 25 shows the predicted "C-free" total gross W erosion rate. This quantity is an extrapolation to the total gross W erosion rate that would be experimentally measured if there was no C deposition, i.e., if a mixed C/W layer did not exist. The predicted C-free total gross W erosion rate is obtained by dividing the measured experimental erosion by the calculated normalized surface concentration of W, $\sigma_W$, as discussed in Section 4.2 of Chapter 4. Of course, if C was not a part of the mixed material layer, one would assume a non-graphite first wall and divertor PMI to differ. Nonetheless, Figure 25 highlights this potential benefit of a low-Z first wall material. Similar to Figure 21, the total gross W erosion rate decreases with increasing inter-ELM density and increases with increasing inter-ELM temperature. Although, much weaker trends between the $D_2$ mass injection rate and total gross W erosion rate exist. The total gross W divertor erosion rate appears to be impacted more heavily by the divertor conditions than ELM amplitude or ELM triggering physics. The predicted C-free gross intra-ELM W erosion rate shows a similar trend compared to the inter-ELM density. Contrary, the relationship between the predicted “C free” total gross W erosion rate and inter-ELM temperature looks relatively inconclusive. Then, Figure 26 shows the $F_{ELM}$ and average pedestal stored energy drop associated with an ELM and Figure 27 shows the average peak intra-ELM heat flux, both as a function of $D_2$ mass injection rate. The $F_{ELM}$ and heat flux values correspond to the “large sized” Type-I ELMs discussed previously. The $F_{ELM}$ is lowest in the no $D_2$ pellet cases, but there is no clear distinction in the $F_{ELM}$ between the various $D_2$ mass injection rates.

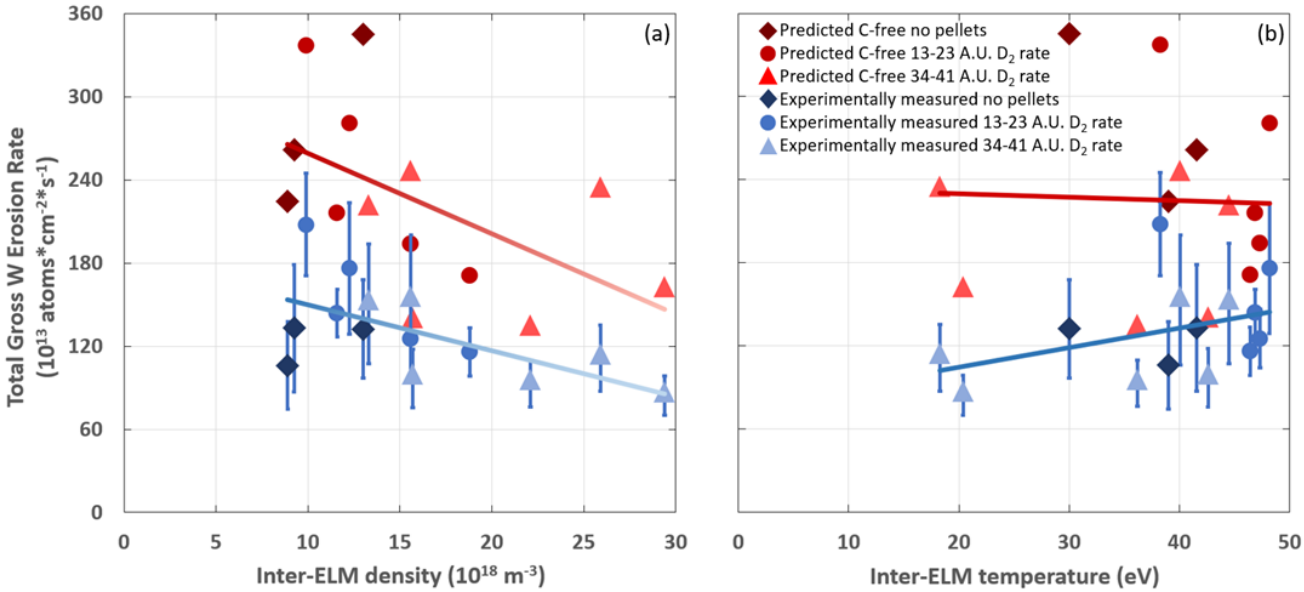



*Figure 25. Measured total intra-ELM gross W erosion rate (blue) and predicted gross W erosion rate in the absence of a C/W mixed material layer (red) vs. plasma electron inter-ELM (a) density and (b) temperature. Linear fits are overlaid in both cases.*

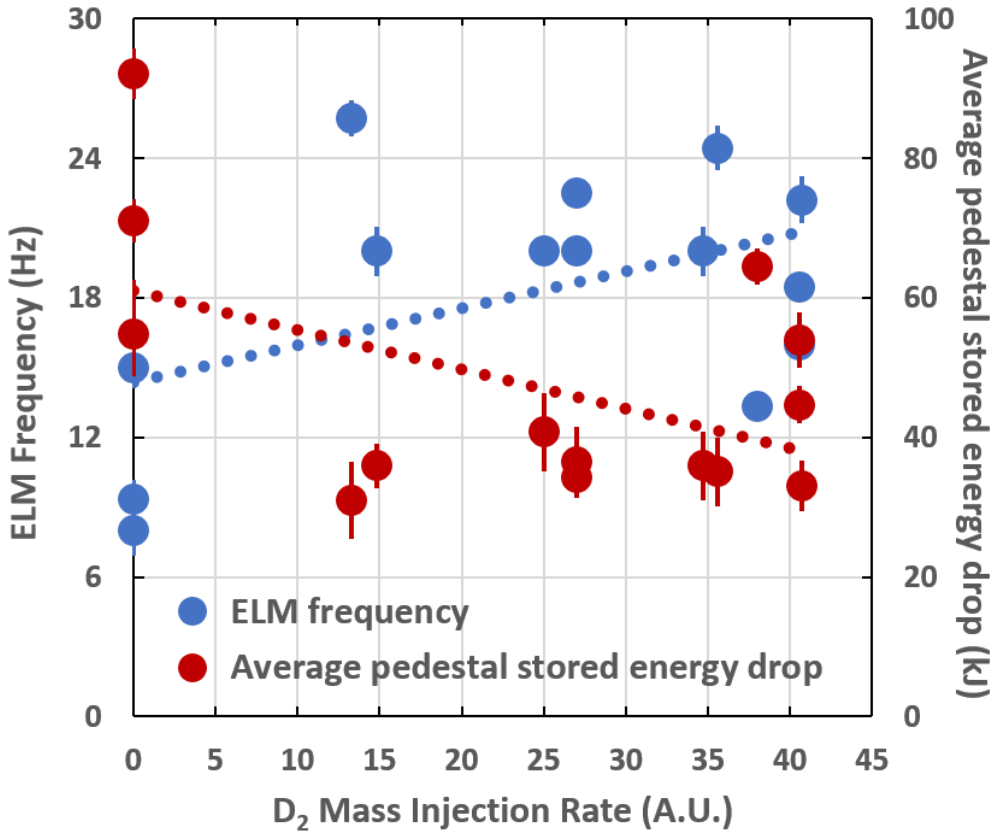



*Figure 26. ELM frequency and average pedestal stored energy drop per ELM as a function of $D_2$ mass injection rate.*

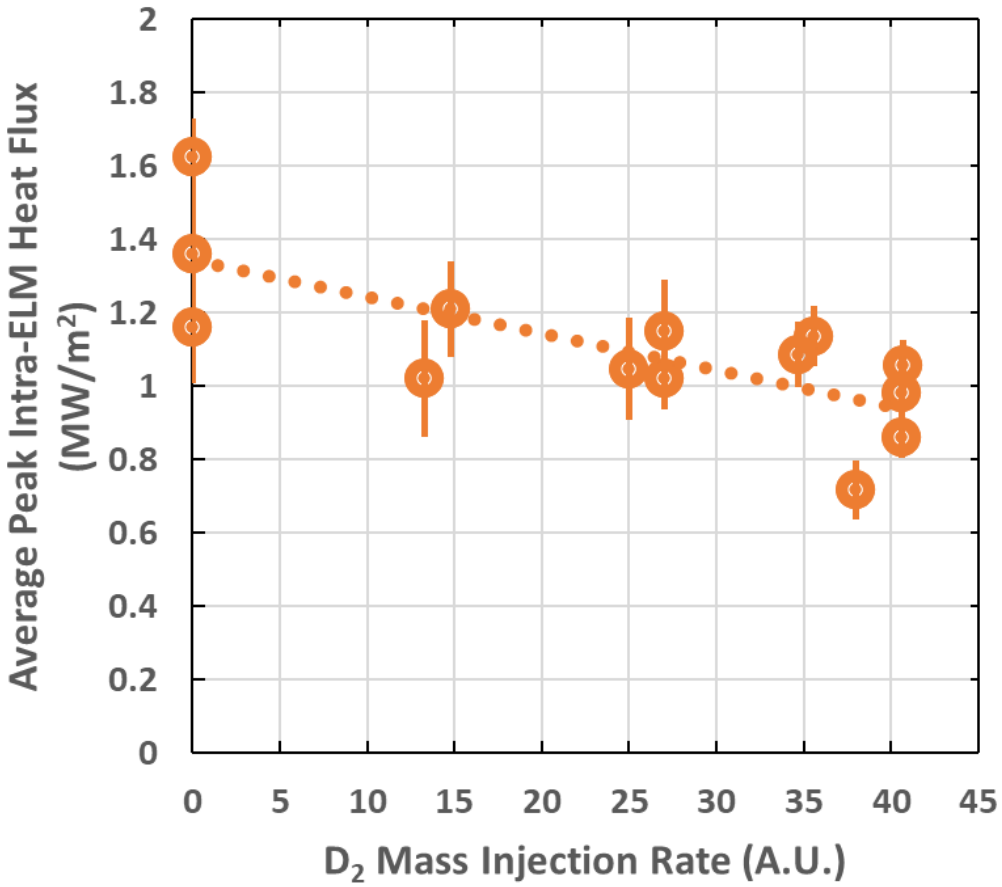



***Figure 27. Average peak intra-ELM heat flux vs. $D_2$ mass injection rate.***

Shots with $D_2$ mass injection may have had a higher $F_{ELM}$ due to a slightly higher pedestal density profile and/or infrequent triggering of ELMs, but the impact of $D_2$ pellet ELM triggering appears minimal. Contrary, the average pedestal stored energy drop is highest for the no pellet cases and is lower for the $D_2$ pellet injection cases. Once again, increasing the $D_2$ mass injection rate further has an inconclusive effect. The peak intra-ELM heat flux associated with the ELM decreased steadily with increasing $D_2$ mass injection. In past MRC and other DIII-D affiliated experiments, the peak intra-ELM heat flux and average pedestal stored energy drop monotonically decrease with increasing $D_2$ mass injection, while the $F_{ELM}$ increases [11]. In both Figure 26 and Figure 27, the error is considered the standard error of the mean of measurements associated with each ELM. We use experimental heat flux measured from the IR camera to validate FSRM heat flux estimations. Hence, Figure 28 shows the comparison between measured and predicted MRC heat flux values. The average heat flux values more or less match between the IR camera measurements and FSRM predictions, however the IR camera does not seem to show much of an increase in heat flux at the peak of the ELM signal, unlike the FSRM. This is likely due to ELM data signal oversaturation. Most notably, the average ELM erosion decreased steadily with increasing $D_2$ mass injection rate, which directly correlates to the higher inter-ELM densities shown in Figure 21. Intermediate $D_2$ mass injection rates (13-23 A.U.) seemed to result in a larger total gross W erosion rate and average W erosion per ELM (at the OSP) than the no pellet and 34-41 A.U. cases. This may be due to an increased $D^+$ ion flux to the divertor compared to the no pellet case without a substantially lowered plasma temperature to sufficiently decrease the Y of D and C on W. Contrary, it is hypothesised that the 34-41 A.U. $D_2$ mass injection rate reduced the divertor $T_e$ and $E_i$ significantly enough to overcome the increasing ion flux to the target. While $D_2$ pellet shots resulted in about twice the $F_{ELM}$ as no pellets shots, many

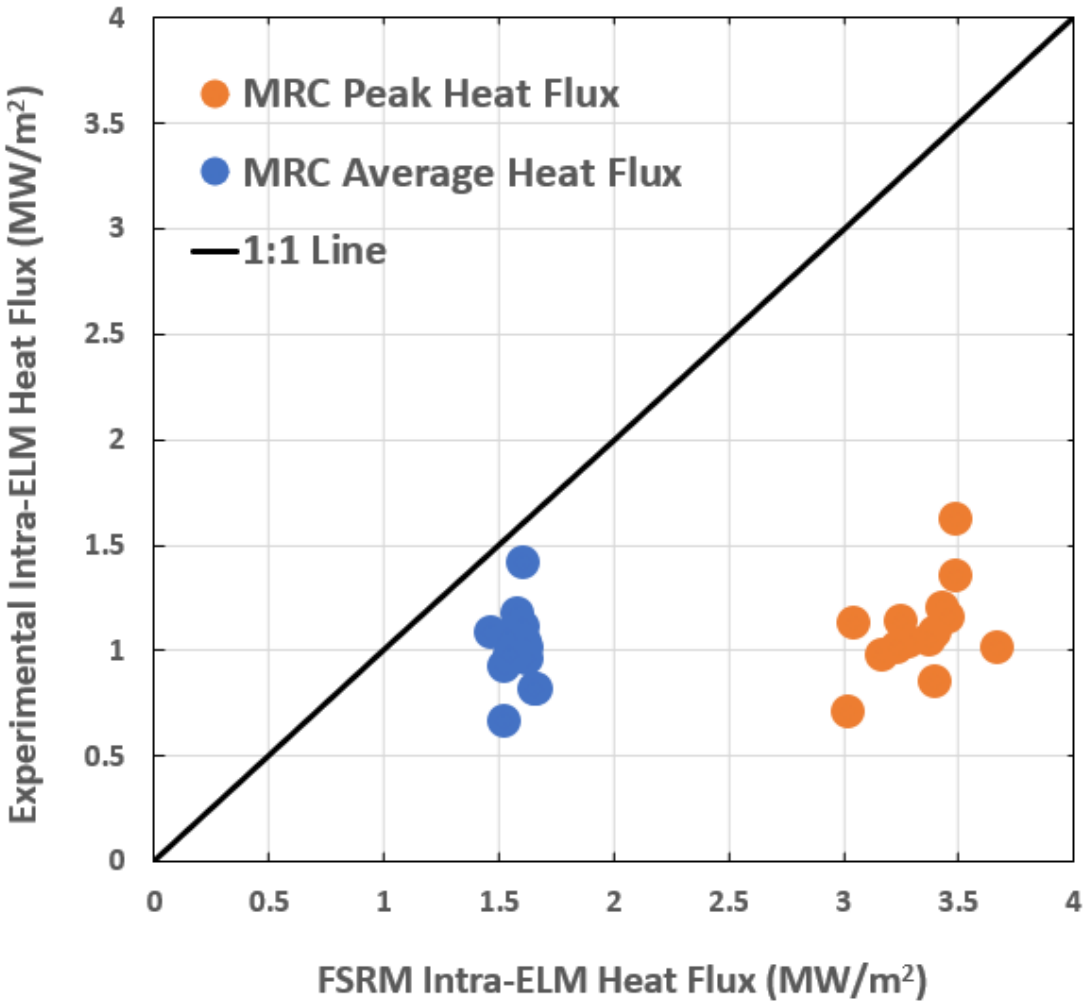



***Figure 28. MRC intra-ELM experimental heat flux as a function of FSRM heat flux.***

injection cases were not seen to pace the more numerous large ELMs above the threshold considered significant. Although, some of the "mid-sized" ELMs accounted for in the total gross W erosion rate analysis in Figure 25 were likely triggered. $D_2$ pellet injection led to relatively small changes in the pedestal plasma conditions, opposed to the divertor plasma conditions and in most cases did not trigger ELMs by reaching the associated ballooning-limited boundary. Thus, the $D_2$ pellet injection rate did not drastically impact the $F_{ELM}$. Besides the associated ELM triggering physics, there may exist an ideal pellet injection rate that lowers the $T_e$ and $E_i$ at the divertor substantially enough to overcome the increasing ion flux to the target without significantly increasing the collisionality of the pedestal. These assertions are primarily supported through the $D_2$ pellet injection rate sweep shot (167351) and trends between the average W erosion and inter-ELM density in Figure 21.

As expected, the divertor target and pedestal $T_e$ just before the ELM crash both decrease with $D_2$ mass injection rate while the divertor target and pedestal $n_e$ just before the ELM crash both increase. Commonly, a lower average gross W erosion per ELM also corresponds to a reduction in the peak heat flux deposited on the divertor with respect to time and an improvement in confinement performance [8, 11, 12]. Like in past MRC data analysis and other experiments, increasing the $D_2$ pellet injection rate decreased the peak intra-ELM heat flux [11, 12]. On future devices with much larger and less frequent expected ELMs like ITER, reducing the peak intra-ELM heat flux becomes far more significant to avoid material melting and cracking in addition to longer term erosion. Moreover, the total intra-ELM erosion to total inter-ELM erosion ratio is expected to be much larger on some future devices, making large ELM mitigation in terms of both heat flux and erosion of utmost importance.

It should also be noted that while this study is limited to W sputtering effects close to the strike-point, it was generally observed during the MRC that ELMs cause significantly more W erosion than the inter-ELM plasma when moving radially away from the OSP for attached divertor plasma shots [34]. This is due to a large decrease in the $T_e$ with increasing distance from the OSP, thus decreasing the $E_i$ to the divertor and Y of D and C on W. Likewise, past studies emphasize that larger ELMs will contain a wider heat flux footprint on the divertor than smaller ELMs [35, 36]. Additionally, higher $D_2$ mass injection rates further decrease the divertor $T_e$ and reduce the Y as the distance from the OSP position increases. Hence, smaller, more frequent ELMs emerging from perturbations in the pedestal initiated by faster $D_2$ pellet injection rates likely result in a smaller footprint on the divertor, also leading to a lower total W erosion rate. Therefore, it is likely that $D_2$ pellets with a mass injection rate of 34-41 A.U. resulted in lower total W erosion rates than no pellets. Unfortunately, hardware and diagnostic limitations prevent verification of lower intra-ELM and total intra-ELM W erosion rates with increasing distances from the OSP.

Overall, the FSRM provided reasonable estimations of the erosion per ELM given the various experimental input parameters. Some incorporation of the mixed C/W material layer is necessary to correct the overestimation, however. Likewise, refining the FSRM remains an ongoing effort, and incorporating the effects of a mixed material layer are one of many areas to improve upon. Incorporating the presence of a mixed material deposition layer enables far more accurate erosion estimations for current and future fusion devices with differing divertor and first wall materials and those utilizing impurity injection or wall conditioning. Moreover, mixed material models will help the fusion community understand the compatibility of various candidate divertor and first wall materials given various plasma conditions and operating scenarios.

## 6.2 Small Angle Slot

We present results from the SAS-VW campaign in a similar fashion to the MRC. **Table 2** overviews the plasma discharges analyzed from this experimental campaign. Shot time ranges were selected after the OSP position settled within 1 cm of the SAS-VW view 2 LP installed in the W tile (Z = 1.2 m). Seven plasma shots included $D_2$ pellet injection, seven employed $D_2$ gas puffing, and two involved neither within the time ranges of interest. Some plasma shots, however, experienced filterscope signal trips that rendered portions of the data uninterpretable. In such cases, the missing data were excluded from the relevant figures. Because of uncertainties in the number and size of $D_2$ pellets injected over the duration of each analyzed shot, pellet masses were determined using a microwave cavity diagnostic [33]. The $D_2$ mass injection rates for gas-puffing plasma shots were interpolated from the linear trendline between inter-ELM $n_e$ and $D_2$ mass injection rate obtained from the pellet injection shots, as shown in Figure 29. The 3 MW plasma shots were excluded from this mass calibration due to inherent differences in divertor inter-ELM $n_e$, resulting from the higher power injection level. Additionally, plasma shot 190999 was excluded because its $D_2$ mass injection rate and inter-ELM $n_e$ were significantly lower than those within the interpolation range, making it unsuitable for inclusion. Notably, SAS-VW graphs plot divertor inter-ELM $n_e$ on the X-axis since the gas puff shots are not calibrated to an arbitrary mass injection rate. Moreover, inter-ELM $n_e$ strongly correlates to the A.U. $D_2$ pellet injection frequencies and the gas puff rates in Torr-Liter/second (Torr-L/s). Likewise, Figure 30 and Figure 31 plot inter-ELM $n_e$ as a function of pellet $D_2$ mass injection rate and $D_2$ gas puff rate, respectively. As seen, inter-ELM $n_e$ strongly correlates with pellet $D_2$ mass injection rate and $D_2$ gas puff rate, making it a good proxy for $D_2$ mass injection rate. Importantly, we attempted to match each $D_2$ pellet shot with the same $D_2$ mass injection rate

**Table 2:** SAS-VW Plasma Shot Summary

| Shot Numbers 19XXXX | $D_2$ Mass Injection Rate | Injection Method | Large $F_{ELM}$ (Hz) | Threshold | Time ranges (ms) |
|---|---|---|---|---|---|
| **1002** | **0** | **None** | **32** | **0.4** | **2900:5200** |
| **0999** | **20 Hz** | **Pellets** | **37** | **0.55** | **2600:5200** |
| **1001** | **40 Hz** | **Pellets** | **40** | **0.55** | **3400:5200** |
| **1006** | **40 Hz** | **Pellets** | **33** | **0.6** | **3200:5200** |
| **1000** | **27 T-L/s** | **Gas** | **45** | **0.55** | **3000:5200** |
| **0994** | **27 T-L/s** | **Gas** | **40** | **0.55** | **3200:5200** |
| **1005** | **40 Hz** | **Pellets** | **44** | **0.6** | **3200:5200** |
| **0996** | **20 Hz** | **Pellets** | **48** | **0.55** | **3200:5200** |
| **0990** | **0** | **None** | **40** | **0.5** | **3000:3500** |
| **1009** | **54 T-L/s** | **Gas** | **53** | **0.55** | **3200:5200** |
| **1008** | **54 T-L/s** | **Gas** | **56** | **0.55** | **3200:5200** |
| **1016** | **60 Hz** | **Pellets** | **49** | **0.55** | **3200:5200** |
| **1017** | **60 Hz** | **Pellets** | **51** | **0.55** | **3200:5200** |
| **1013** | **72 T-L/s** | **Gas** | **54** | **0.55** | **3200:5200** |
| **1014** | **72 T-L/s** | **Gas** | **64** | **0.55** | **3200:5200** |
| **1015** | **72 T-L/s** | **Gas** | **64** | **0.55** | **3200:5200** |

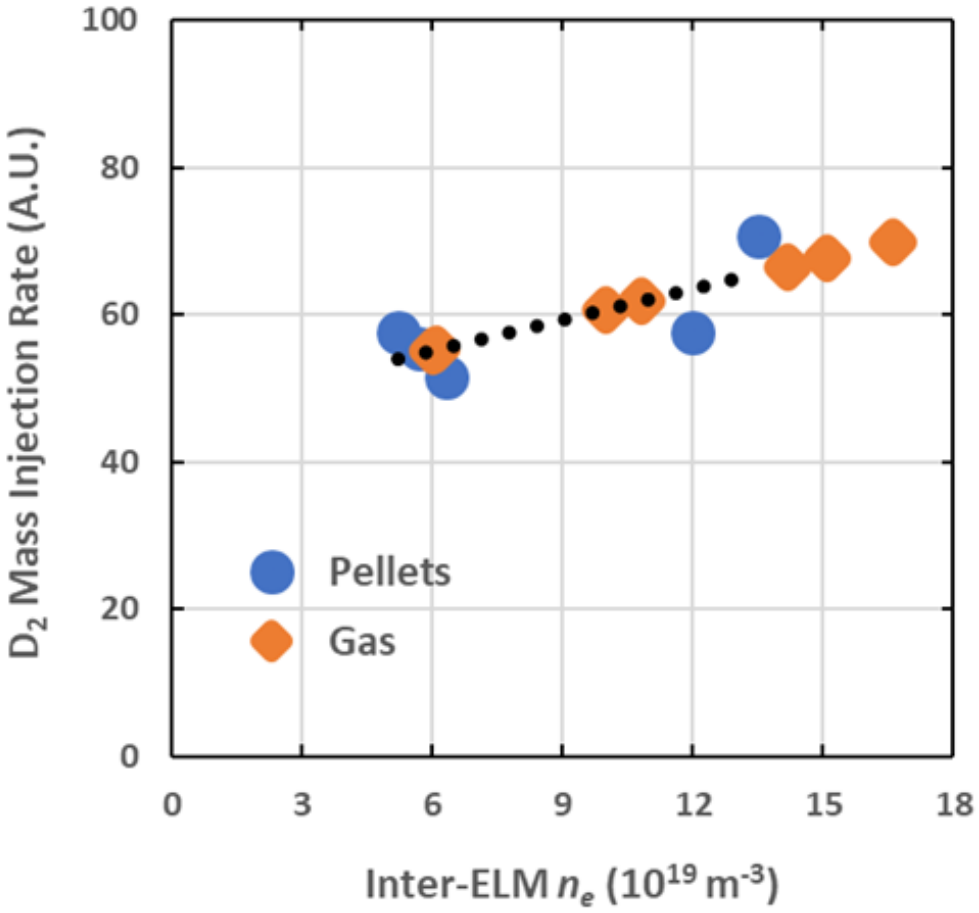



***Figure 29. Mass injection rate as a function of inter-ELM $n_e$ for shots at 2.6 MW of heating power. $D_2$ midplane gas puff plasma shot data points interpolated by the linear trendline are shown in orange diamonds while $D_2$ pellet injection plasma shots are displayed in blue circles. A black trendline for the data is displayed.***

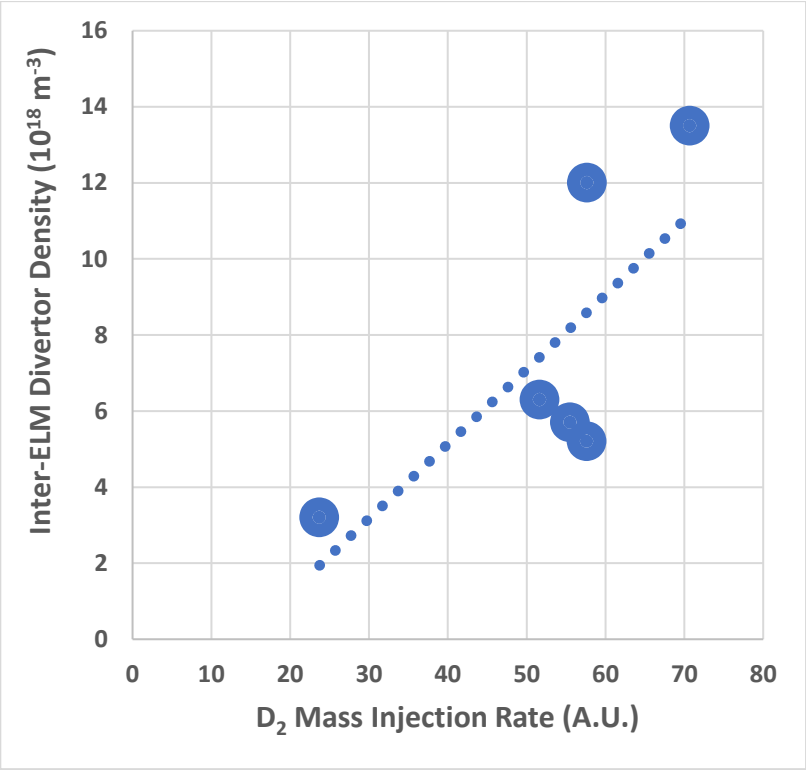



*Figure 30. $D_2$ pellet shots inter-ELM density as a function of $D_2$ mass injection rate.*

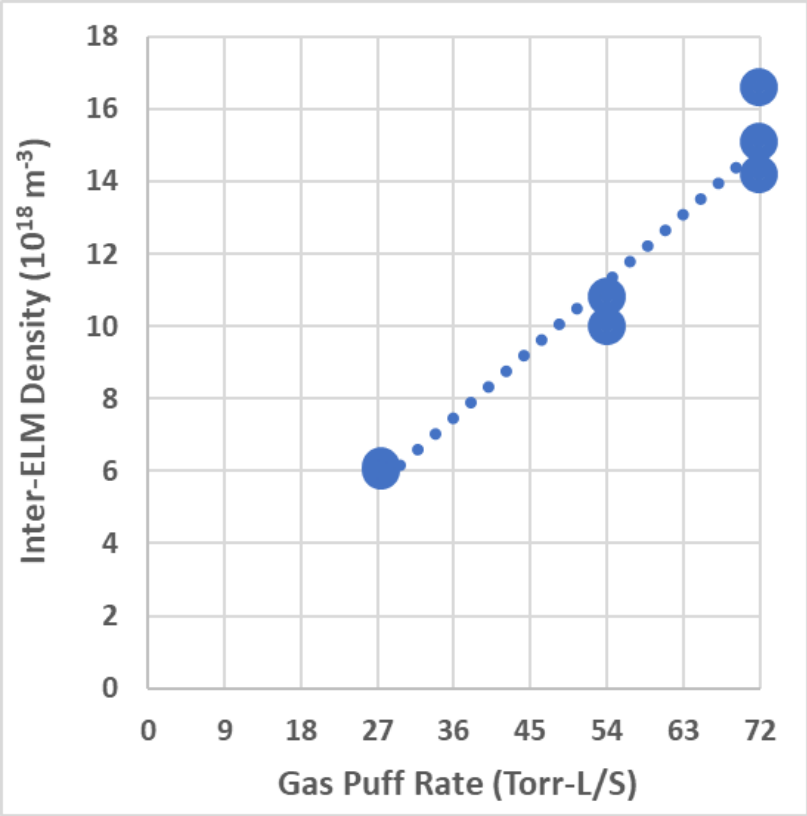



*Figure 31. $D_2$ gas shots inter-ELM density as a function of gas puff rate in Torr-L/s.*

of a corresponding $D_2$ gas shot. Hence, 20 Hz pellets were configured to match 27 T-L/s gas, 40 Hz to 54 T-L/s, and 60 Hz to 72 T-L/s. Unfortunately, higher nominal pellet injection frequencies injected less $D_2$ mass than expected. Underperformance of the pellet injection system was compensated for by reducing the high $D_2$ gas injection rate from 81 T-L/s to 72 T-L/s. However, based on inter-ELM $n_e$ profiles, 54 and 72 T-L/s gas shots likely still injected more $D_2$ mass than their $D_2$ gas equivalent shots.

Figure **32** shows the neutral beam injected power ($P_{NBI}$), $D_2$ midplane gas puffing rate, OSP position, line average density, and divertor $D_\alpha$ intensity for plasma shot 191009. In general, each plasma shot's outer strike point (OSP) position stabilized within approximately 2 seconds after the plasma shot begins. The midplane outboard $D_2$ injection began around 2.5 seconds into the shot. During the analyzed time frame, the injected neutral beam power ($P_{NBI}$), $D_2$ midplane gas puffing rate, and OSP position typically remained stable, although a gradual increase in line-averaged density and divertor $D_\alpha$ intensity was observed as the discharge progressed. Notably, the $P_{NBI}$ signal was smoothed by a factor of 1000, since the pulse power fluctuates with the sequencing of neutral beam sources. Additionally, the $D_2$ gas puffing rate was calibrated based on the output voltage signal. We attempted to match the $D_2$ mass injection rates between pellet and gas-puffing plasma shots: 20 Hz pellet shots were compared to 27 Torr·L/s gas-puffing shots, 40 Hz to 54 Torr·L/s, and 60 Hz to 72 Torr·L/s. The highest rate (81 Torr·L/s) was excluded due to known pellet gun performance degradation at elevated insertion frequencies. Notably, most gas-puffing plasma shots exhibited slightly higher inter-ELM electron densities ($n_e$), corresponding to higher effective $D_2$ mass injection rates than their pellet-injection counterparts. After calibrating the measured $D_2$ gas puffing voltages, we determined that the

actual gas puffing rates were approximately 33, 65, and 86 Torr·L/s, respectively, rather than the nominal 27, 54, and 72

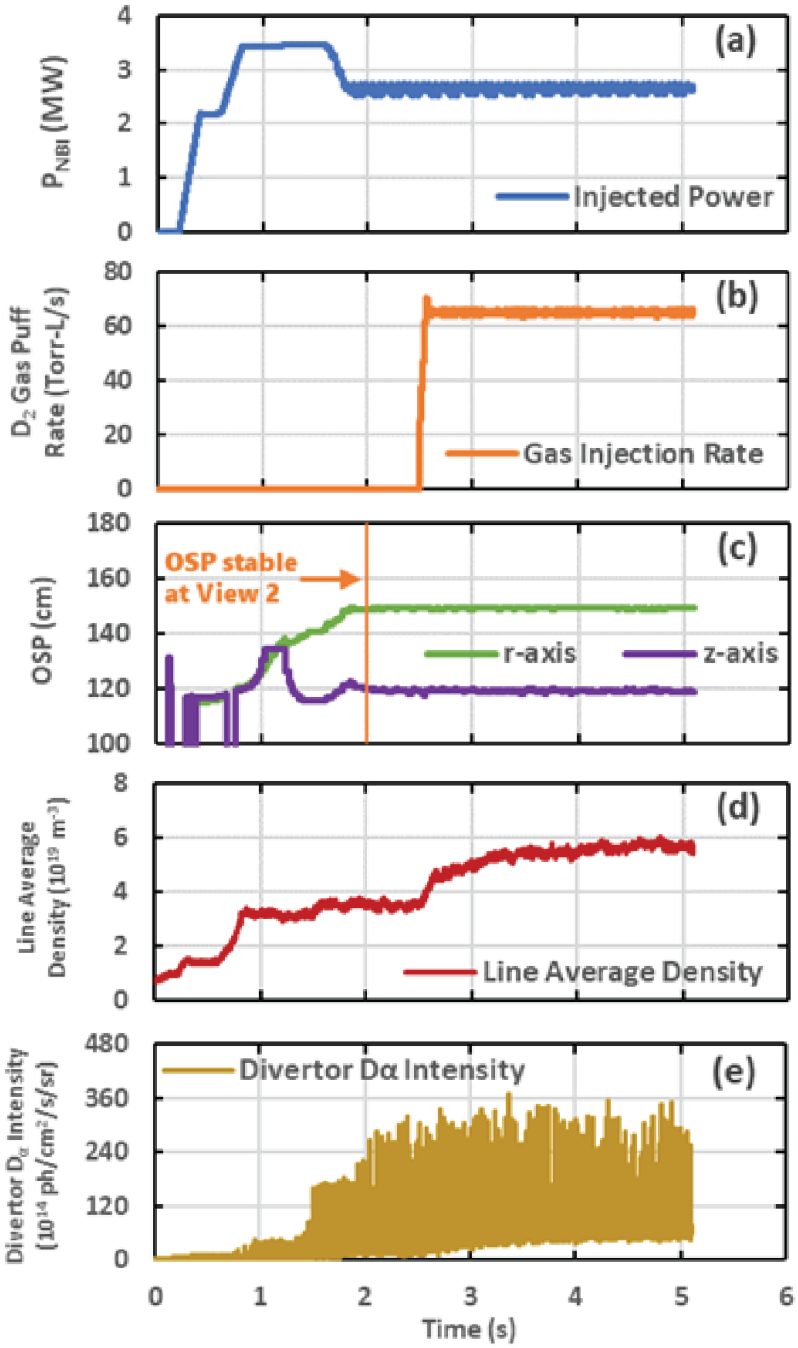



**Figure 32. Plasma shot 191009 parameters vs time for (a) Injected Power in blue, (b) $D_2$ Midplane Gas Puff Rate in orange, (c) OSP Position in green for r-axis and purple for z-axis, (d) Line Average Density in red, and (e) Divertor $D_\alpha$ Intensity in brown.**

Torr·L/s.

Despite these discrepancies, we obtained reasonably good agreement between the experimental data for $D_2$ pellet injection and gas-puffing plasma shots. Figure 33 compares the experimentally measured and predicted inter-ELM W erosion. The predicted inter-ELM W erosion is calculated by multiplying the spectroscopically measured C and D ion fluxes striking the divertor by their respective Y at the average θ and energy ($E_i$), along with the predicted $\sigma_W$ between ELMs within the C–W interaction layer. For these predictions, only the C–W interaction layer is considered, excluding contributions from free-streaming ions or neighboring regions. Accordingly, Equation 6.2 defines the predicted inter-ELM W erosion.

$$\Gamma_{W_{inter-ELM,predicted}} = \sigma_W * [(\Gamma_C * Y_{C-W}) + (\Gamma_D * Y_{D-W})] \quad 6.2$$

Importantly, $Y_{D-W}$ is negligible at inter-ELM ion impact energies ($E_i$) and the second term in the brackets is assumed to be zero. Moreover, W self-sputtering is considered negligible compared to C and D induced W sputtering during and between ELMs [8]. $Y_{C-W}$ and $Y_{D-W}$ values during and between ELMs are computed by RustBCA, a binary collision ion-material interaction code, at a fixed recycling θ of 45° relative to the divertor surface normal and $E_i$ based on the respective divertor electron temperature ($T_e$) for each plasma shot [5]. The inter-ELM and recycling C ion impact energy ($E_C$) and D ion impact energy ($E_D$) are a function of the $T_e$ as described in Equation 6.3 below [8].

$$E_i = 2 * T_i + 3 * Z * T_e \quad 6.3$$

Here, the charge state used for the C ions is Z=2, the charge state of most C ions striking the divertor. In Figure 33, $\sigma_W$ ranged from 0.65 to 0.8 during the inter-ELM regime. The filterscope signals used to calculate experimental and predicted W erosion spanning the three

milliseconds before a large Type-I ELM, resulting in many measurements over the course of a plasma shot that were averaged to obtain the calculation. In all cases, the error is considered the standard deviation of the average measurement value. For the experimental W erosion results, the error is propagated with a range of +/- 0.025 uncertainty in the MDS and filterscope calibration $R_{CC}$ value. In the case for intra-ELM results, the ELMy signal is subtracted by the background inter-ELM signal, and the error propagation is calculated accordingly. Notably, whether $D_2$ gas or pellets were injected, there did not seem to be a substantial impact on the agreement between the measured and predicted results. Just as the MRC, we assumed the same $\theta = 45°$ for the SAS-VW campaign [8, 27]. The consequent $\sigma_C$ resulted in an average predicted inter-ELM W erosion 42% higher than measured experimentally. $\theta = 45°$ is selected as the fitting value based on past literature, where surface roughness effects are considered [8]. This value shows reasonable agreement for the inter-ELM W erosion results but overpredicts the experimental intra-ELM W erosion. Though, preliminary GITR-RustBCA coupling results show that $\theta$ can vary by 1° to 2° between plasma shots depending on the plasma conditions [17]. In fact, at a higher $E_i$, higher $T_e$, and lower $n_e$, GITR-RustBCA calculates a larger $\theta$ and consequently, a smaller $\sigma_C$ and larger $\sigma_W$. Theoretically, this increases the predicted intra-ELM W erosion and brings the results closer to the 1:1 line. Additional details on plasma parameters and surface roughness effects on $\theta$ will be discussed in Section 7.2. Next, the impact of the various $D_2$ mass injection rates on pedestal and divertor plasma conditions have been monitored. Figure 34 shows the pedestal and divertor $T_e$ and $n_e$ input parameters for the FSRM as a function of the inter-ELM $n_e$. Unlike the MRC **Table 1** shots, pedestal $T_e$ and pedestal $n_e$ are average values from the inter-ELM regimes because the intra-ELM Thompson Scattering time resolution did not perform as well as it did during the MRC, unfortunately. In conjunction with lower

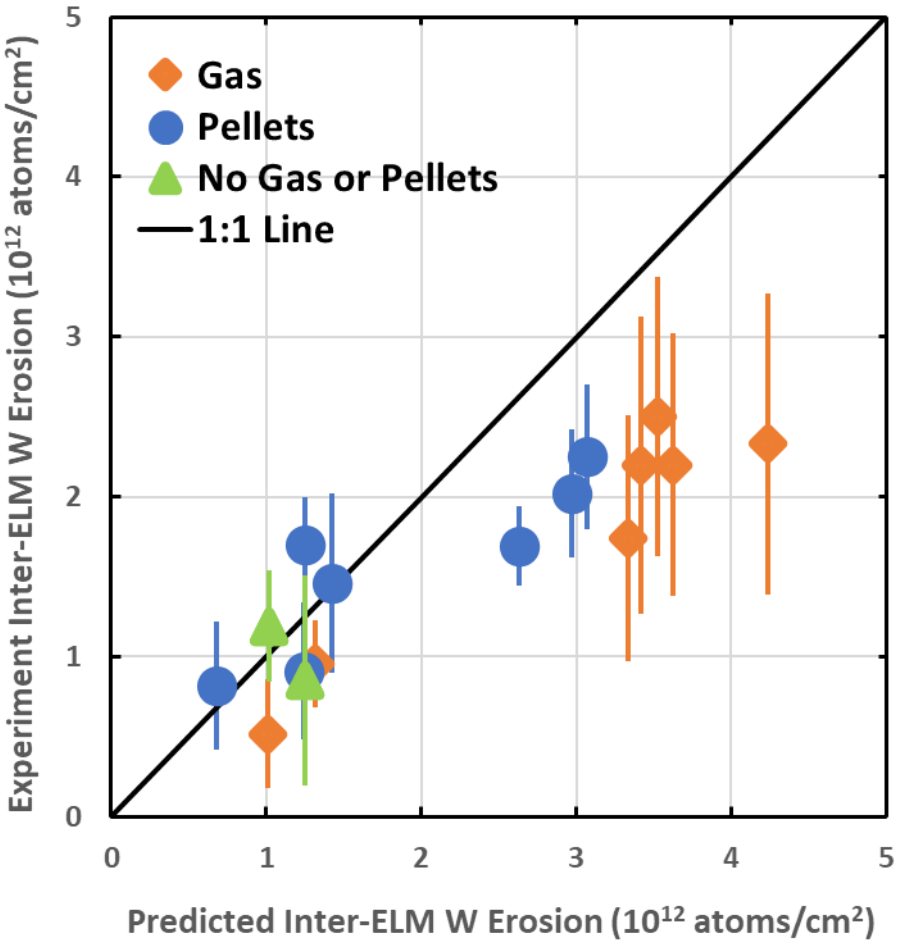



***Figure 33. Experiment vs. predicted inter-ELM W erosion at θ=45°. $D_2$ gas puffing plasma shots are displayed in orange diamonds, $D_2$ pellet injection plasma shots are displayed in blue circles, and plasma shots with neither are displayed in green triangles.***

energy ELM bursts compared to the MRC, SAS-VW large ELM emission showed little to no drop in the pedestal $T_e$ and $n_e$ at the time of an ELM. Hence, using mean rather than max pedestal $T_e$ and $n_e$ appears to be more accurate. Contrary, divertor $T_e$ and $n_e$ are still similarly coherently averaged from the intra-ELM regimes. In comparison to Figure 19's MRC data, a much more noticeable change in pedestal parameters results from $D_2$ mass injection. The lower collisionality plasma in the SAS-VW campaign results in $D_2$ mass injection causing a much greater increase in pedestal $n_e$ and consequent decrease in pedestal $T_e$. Comparatively, the intra-ELM divertor temperature does not decrease nearly as much with increasing inter-ELM density and the intra-ELM divertor density increases more profoundly with increasing inter-ELM density. As a result, the average gross intra-ELM W erosion at the view 2 OSP position from the SAS-VW campaign does not appear to be strongly affected by the $D_2$ mass injection rate as shown in Figure 35. Plausibly, there may be reduced W erosion when comparing the no gas or pellet shots to the shots with either $D_2$ gas or pellets of any injection rate. Interestingly, this difference is exacerbated when comparing the 3 MW shots rather than the 2.6 MW shots, although data are limited for the 3 MW case. The lower average intra-ELM W erosion for the 3 MW shots compared to the 2.6 MW shots is partly explained by the corresponding higher natural $F_{ELM}$ at higher power injection levels, although to what extent is unclear. All in all, intra-ELM W erosion from the SAS-VW campaign is almost an order of magnitude lower than the MRC while achieving higher pedestal temperatures and lower pedestal collisionality. Comparing experimental and FSRM ion flux profiles allows us to uncover key differences impacting intra-ELM W erosion estimations. Figure 36 shows these differences for the SAS-VW plasma discharges. Like the MRC, the SAS-VW experimental ion flux values exceed the FSRM ion flux values when using an effective recycling coefficient ($R_{eff}$) of 0.96. So, in Figure 36 we used

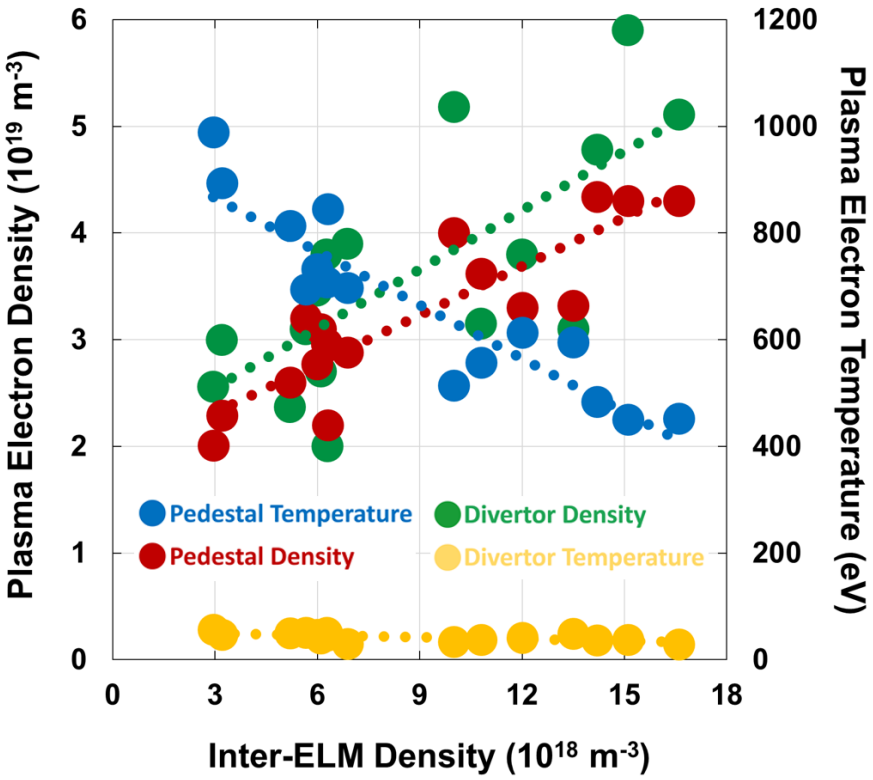



*Figure 34. Measured divertor and pedestal electron temperature and density just before the ELM crash as a function of $D_2$ injection frequency for all cases listed in Table 2. Linear trendlines are shown in all cases.*

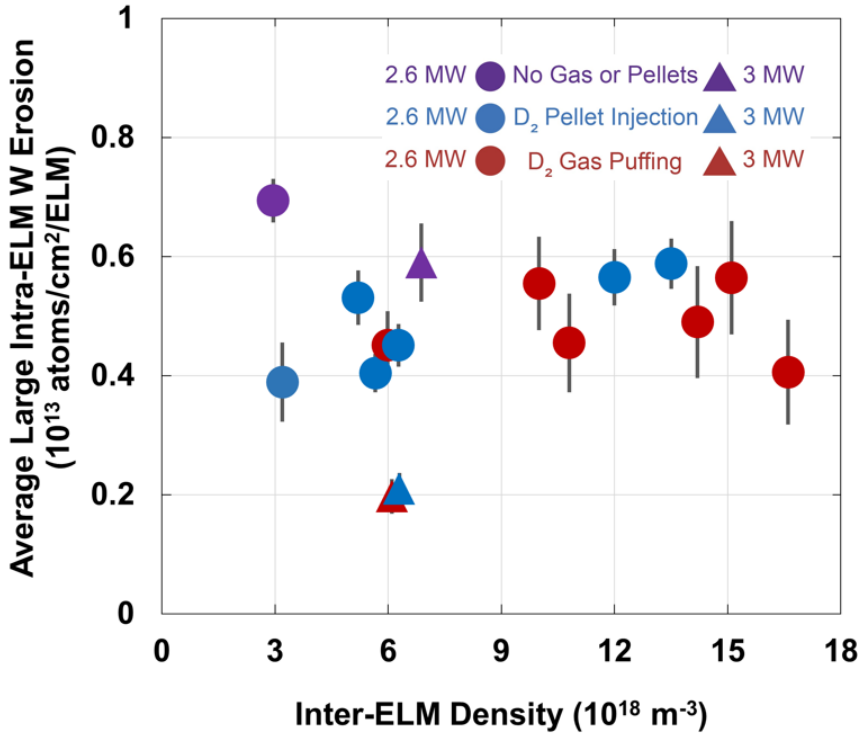



*Figure 35. Average large intra-ELM W erosion as a function of inter-ELM.*

$R_{eff} = 0.983$ to best match the experimental and FSRM ion flux profiles. Although FSRM W erosion exceeds experimental W erosion, it is postulated that LP ion saturation estimations are untrustworthy since the data are inherently noisy.

The predicted C/W mixed material adjusted FSRM intra-ELM W erosion at the view 2 OSP position has been analyzed for each plasma shot. Once again, the FSRM results are multiplied by $\sigma_W$ to account for the fraction of the W divertor surface exposed to incoming energetic ions. Figure 37 shows the predicted fractional concentration of W exposed on the divertor surface as a function of the inter-ELM density. Similar to the MRC results, $\sigma_W$ increases with increasing inter-ELM density. Interestingly, the opposite trend is seen for the three 3 MW plasma shots. The low $T_e$ of ~30 eV in the 3 MW no gas or pellet plasma shot decreased the deposition of carbon. This low $T_e$ is likely due to the OSP sweep occurring during this shot, although OSP is stable at the view 2 Z = 1.2 m position for the analyzed timeframe. $\sigma_W$ has little to no dependence on whether $D_2$ gas or pellets were injected. Thus, Figure 38 shows the predicted C/W adjusted FSRM intra-ELM W erosion results overlaid with partly transparent colored experimental results from Figure 35. Clearly, the C/W adjusted FSRM well overpredicts the experimental gross intra-ELM W erosion, contrary to the MRC. Like the MRC results, estimations are generally more accurate in higher $D_2$ mass injection rate plasma discharges with lower plasma fractional concentration of C impurities. Thus, it appears that $\sigma_C$ is inaccurately calculated once again. Unlike the MRC, $\sigma_C$ seems too small for lower $D_2$ mass injection rate SAS-VW plasma discharges. Detailed analysis on Y and R values and their impact on $\sigma_C$ are discussed alongside with RustBCA computations in Section 8 to better estimate W erosion during and between ELMs. $Y_{D-W}$ sputtering during ELMs had a substantially larger impact on W erosion than between ELMs, accounting for nearly half of the W erosion. The average amount of

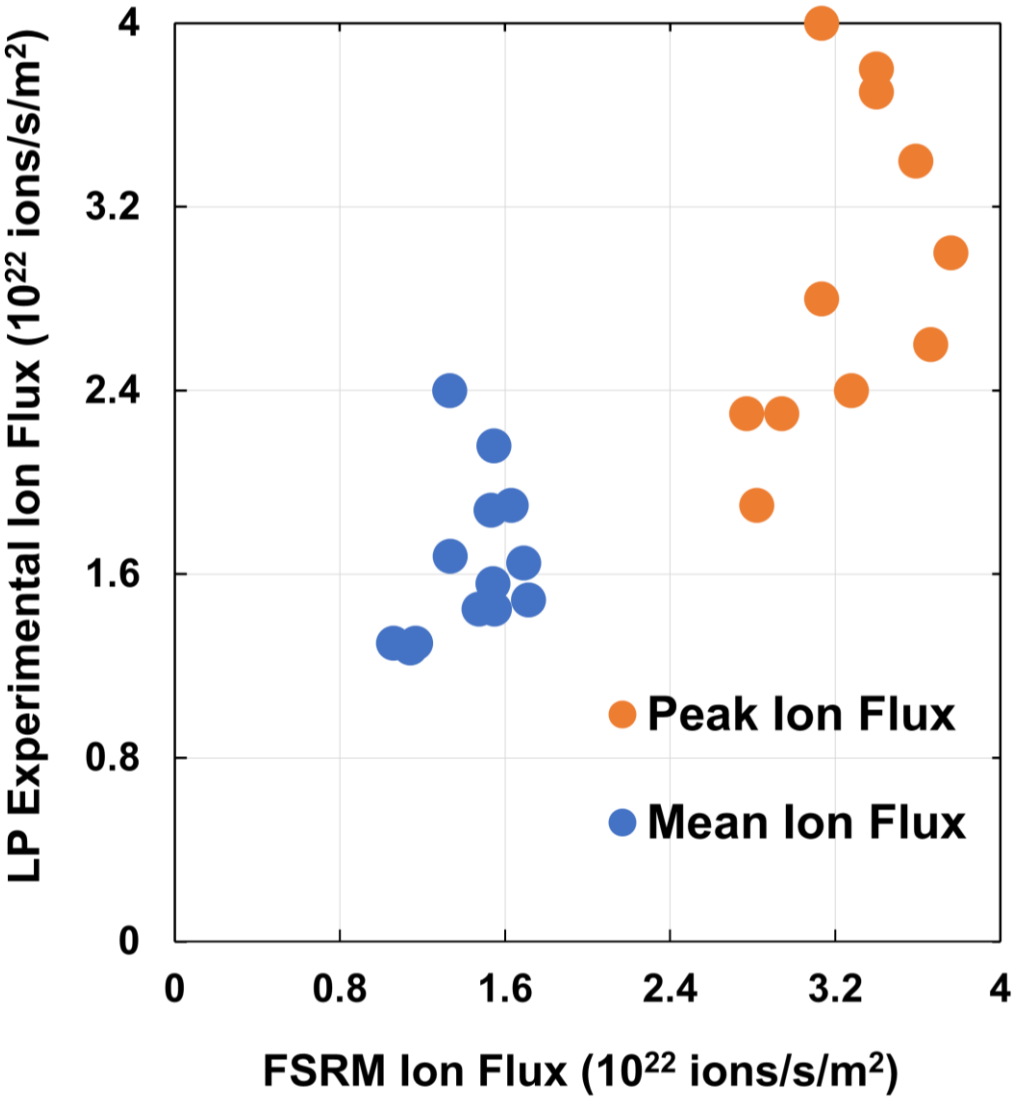



***Figure 36. SAS-VW intra-ELM experimental ion flux as a function of FSRM ion flux.***

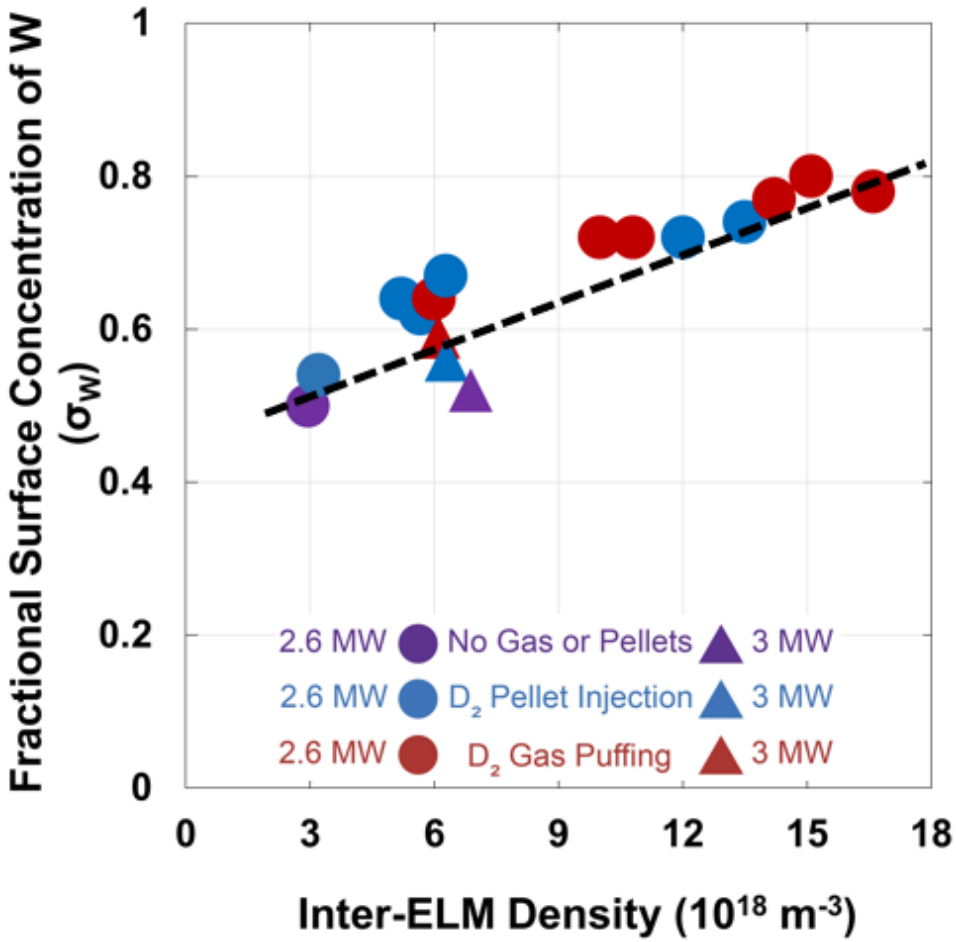



***Figure 37. Fractional surface concentration of W as a function of inter-ELM density.***

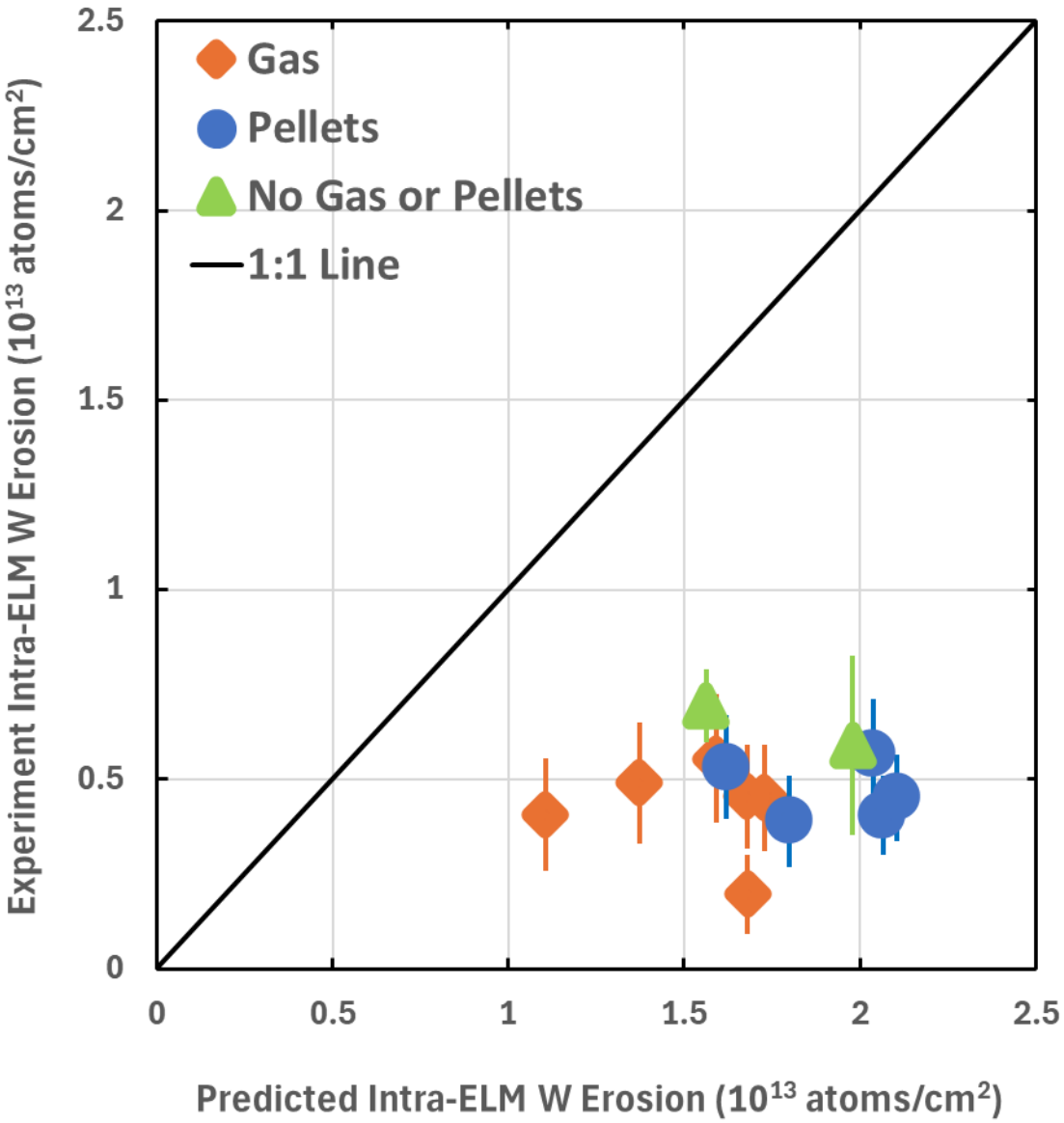



***Figure 38. Experiment vs. predicted intra-ELM W erosion at θ=45°. $D_2$ gas puffing plasma shots are displayed in orange diamonds, D2 pellet injection plasma shots are displayed in blue circles, and plasma shots with neither are displayed in green triangles.***

W erosion spanning ~ 3 ms large Type-I ELM times was about 3.5 times larger during ELMs than between ELMs. Also, other factors may contribute to the overprediction and are under investigation. These factors may include but are not limited, WI filterscopes not detecting some leading-edge tile erosion, oversimplifying assumptions regarding the divertor ion to electron temperature ratio, and lack of incorporating peak ELM $T_e$ reduction in the FSRM [37, 38]. Although, these factors are assumed to be small and do not explain discrepancies in FSRM intra-ELM W erosion estimations and are not the forefront of this dissertation work.

Likewise, Figure 39 shows the comparison between MRC and SAS-VW experimental intra-ELM W erosion as a function of inter-ELM $n_e$. The MRC plasma shots detailed here [27] are of similar attached divertor H-mode plasma parameters to the newly analyzed SAS-VW plasma shots. The average intra-ELM W erosion across all examined plasma shots was $4.75\times10^{12}$ atoms/cm$^2$ while the plasma shots without $D_2$ injection measured $6.42\times10^{12}$ W/cm$^2$. No noticeable difference in intra-ELM W erosion is seen between $D_2$ gas and pellets. Ongoing analysis regarding iterations to the near-surface mixed-material C/W layer model aims to improve predictions and uncover physics regarding C-W mixing. Without the incorporation of $\sigma_W$, the FSRM overpredicts intra-ELM W erosion on average by a factor of 5, worsening for plasma shots with lower $D_2$ insertion rates and $n_e$, and corresponding higher $f_c$. Also, unlike the MRC, no relation between the $D_2$ mass injection rate and experimentally measured intra-ELM W erosion is particularly evident. For the MRC, plasma shots with the largest intra-ELM W erosion contained the lowest inter-ELM $n_e$. The magnitude of erosion was much lower in the SAS-VW, attributed to the closed divertor geometry causing a lower $n_e$ in SAS-VW than the MRC [13]. On average, the intra-ELM SAS-VW $\sigma_W$ is predicted to be 0.58, while the intra-ELM MRC $\sigma_W$ is predicted to be 0.45. Notably, this difference is due to the lower C plasma impurity concentration

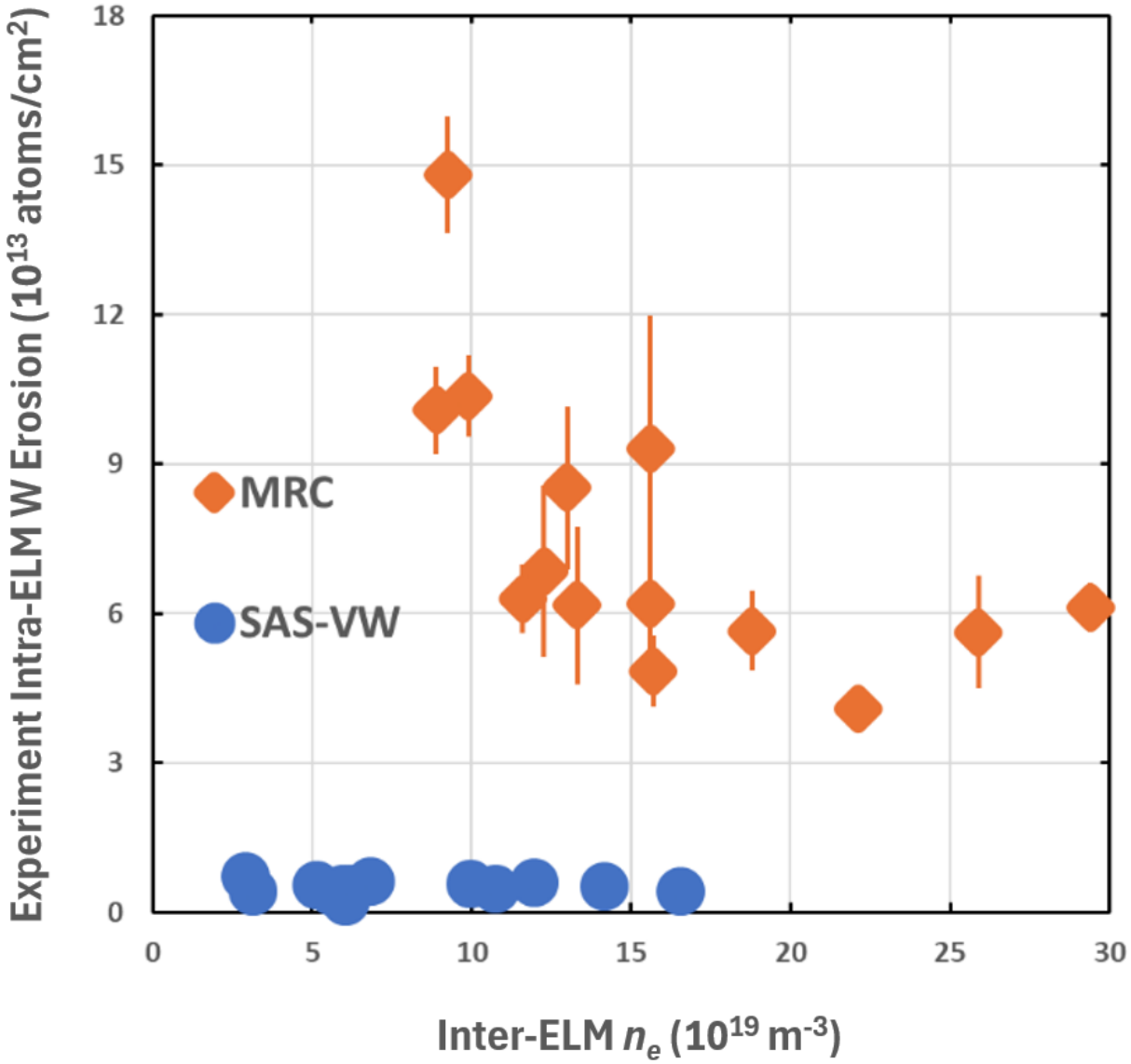



***Figure 39. Experiment intra-ELM W Erosion vs. inter-ELM $n_e$ shown in orange diamonds for the MRC and in blue circles for the SAS-VW campaign.***

in the SAS-VW plasma shots than the MRC plasma shots [8, 27]. Though, these measured differences are from the pedestal because the MRC did not contain CIII filterscopes at the divertor like SAS-VW did. The most accurate θ for the MRC W erosion results was reported to be 45° [8], while the most accurate SAS-VW θ for agreement between experimental and modelling results for plasma shots analyzed in this manuscript is 40° relative to the divertor surface normal. Though we lack concrete evidence to support the change in θ, so we have decided to keep θ = 45°. A decrease in θ towards the surface normal inherently causes a decrease in $R_{C-W}$, $R_{C-C}$, $Y_{C-W}$, and $Y_{C-C}$ [5], meaning more incoming C deposits on the C/W surface and less C erodes from it to increase C coverage of the divertor. In both campaigns, injecting $D_2$ caused a profound increase in inter-ELM $n_e$ and pedestal $n_e$. Moreover, **Table 4** shows average values of experimental data across all plasma shots analyzed in [27] and listed in **Table 3** for the MRC and SAS-VW campaigns, respectively. **Table 4** highlights a multitude of key differences between the MRC and SAS-VW campaign. Overall, the MRC experienced much more W erosion, and similar average ELM peak heat flux compared to the SAS-VW campaign. The difference in W erosion may partially be attributed to the difference in the two campaign's pedestal plasma parameters. The doubled MRC $n_{e,ped}$ and $n_{e,div}$ with only a ~25% reduction in $T_{e,div}$ explains an increase in W erosion, but not by over an order of magnitude like seen in comparison to the SAS-VW campaign. As mentioned previously, SETCs measured the heat flux during ELMs. The SETC time resolution is on the scale of milliseconds, just fast enough to measure the transient ELM profile, but not to the accuracy of a conventional IR camera. A

**Table 4**: MRC and SAS-VW Plasma Parameters

| Plasma shot number | $D_2$ mass injection rate (A.U.) | $F_{ELM}$ (Hz) | Type of $D_2$ injection | $P_{NBI}$ (MW) | Time range (ms) |
|---|---|---|---|---|---|
| 191002 | 0 | 32 | Neither | 2.6 | 2900:5200 |
| 190990 | 0 | 40 | Neither | 3 | 3000:3500 |
| 190996 | 21 | 48 | Pellets | 3 | 3200:5200 |
| 190999 | 24 | 37 | Pellets | 2.6 | 2600:5200 |
| 191000 | 48 | 45 | Gas | 2.6 | 3000:5200 |
| 190994 | 48 | 40 | Gas | 3 | 3200:5200 |
| 191005 | 52 | 44 | Pellets | 2.6 | 3200:5200 |
| 191006 | 56 | 33 | Pellets | 2.6 | 3200:5200 |
| 191016 | 58 | 49 | Pellets | 2.6 | 3200:5200 |
| 191001 | 58 | 40 | Pellets | 2.6 | 3400:5200 |
| 191009 | 59 | 53 | Gas | 2.6 | 3200:5200 |
| 191008 | 62 | 56 | Gas | 2.6 | 3200:5200 |
| 191017 | 71 | 51 | Pellets | 2.6 | 3200:5200 |
| 191013 | 71 | 54 | Gas | 2.6 | 3200:5200 |
| 191014 | 74 | 64 | Gas | 2.6 | 3200:5200 |
| 191015 | 78 | 64 | Gas | 2.6 | 3200:5200 |

median filter was applied to reduce noise in the SETC signal, and the heat flux was calculated using a two-dimensional finite difference thermal model in MATLAB. For more information regarding the heat flux data analysis, please see [30]. Figure 40 compares the experiment and FSRM predicted intra-ELM peak heat flux for the analyzed plasma shots. We find reasonable agreement between the SETC experimentally measured and FSRM predicted intra-ELM peak heat flux. The average experiment intra-ELM peak heat flux was 3 $MW/m^2$ while plasmas shots without $D_2$ injection had an average of 4.57 $MW/m^2$. Our FSRM predicted heat flux is a function of our pedestal $T_e$ and free streaming (FS) ion flux to the divertor. This provides us reassurance that the FSRM is modeling the FS component of our intra-ELM W erosion results accurately considering that the FS intra-ELM W erosion is also a function of the FS ion flux and the heat flux results are not convoluted by mixing C and W atoms deposited on the divertor surface. Interestingly, all $D_2$ gas puffing plasma shots lie above the 1:1 line while all but one $D_2$ pellet injection shot falls below the 1:1 line. Comparatively, the SAS-VW FSRM intra-ELM peak heat flux is about 0.3 $MW/m^2$ larger than the MRC FSRM intra-ELM peak heat flux. This is due to the slightly higher SAS-VW average intra-ELM $T_{e,div}$ of 42 eV compared to the MRC $T_{e,div}$ average intra-ELM $T_{e,div}$ of 39 eV. Despite the higher SAS-VW pedestal $T_e$, high neutral pressures near the target yielded significant radiative cooling [14]. In addition, the higher SAS-VW $F_{ELM}$ exhausts heat more frequently than during the MRC plasma shots analyzed here. Both mechanisms resulted in lower heat flux and temperature profiles at the divertor. Compared to the MRC, SAS-VW plasma shots show a larger drop in the pedestal $T_e$ with increasing inter-ELM $n_e$ [27]. While increasing amounts of $D_2$ insertion generally cools the $T_e$ and increases the $n_e$, physics regarding the triggering of ELMs has a substantial impact on the result [11, 12]. In comparison to the MRC, we see less of a decrease in the intra-ELM $T_e$ as the inter-ELM $n_e$

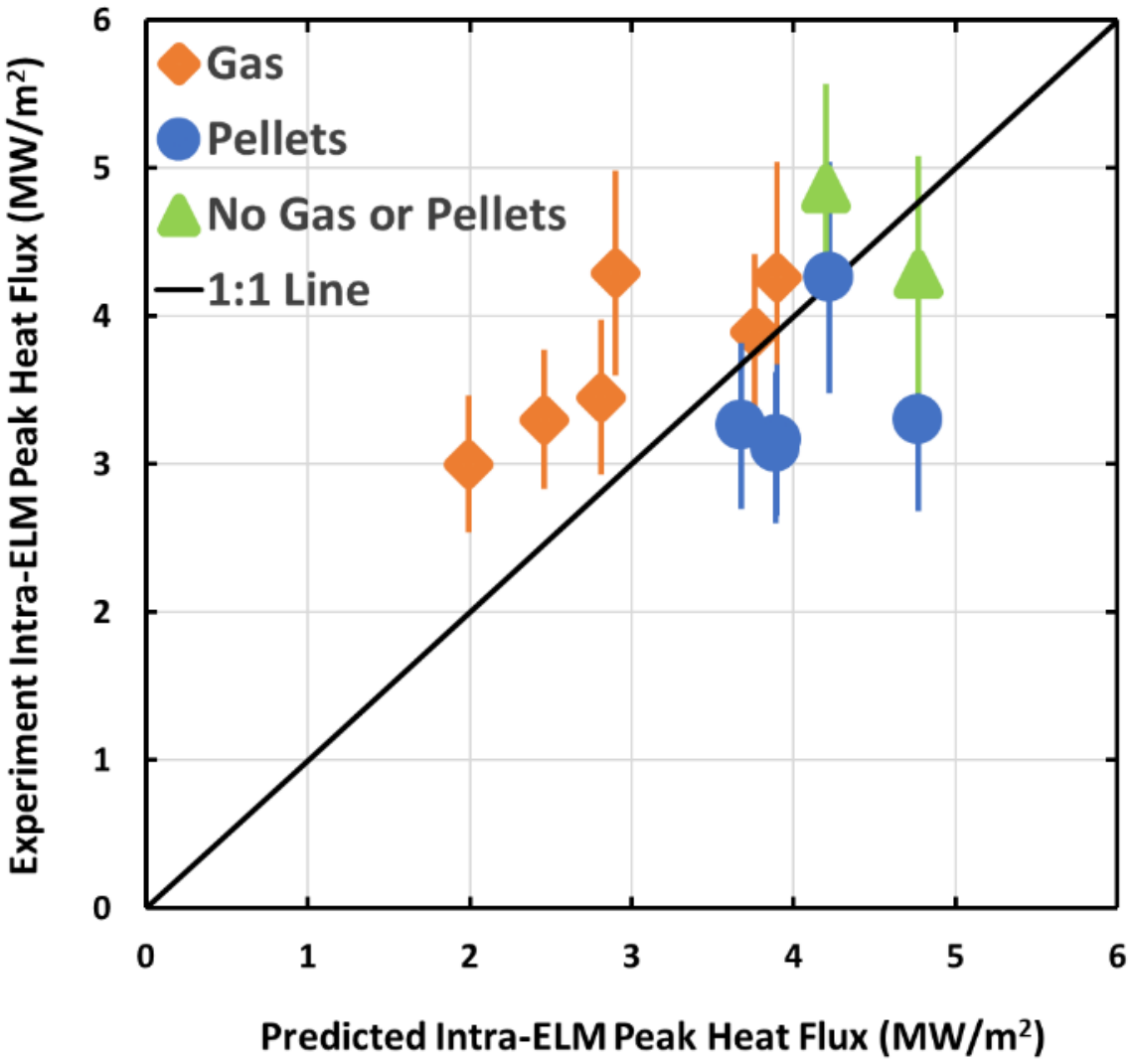



***Figure 40. Experiment (SETC) vs. predicted (FSRM) intra-ELM peak heat flux. $D_2$ gas puffing plasma shots are displayed in orange diamonds, $D_2$ pellet injection plasma shots are displayed in blue circles, and plasma shots with neither are displayed in green triangles.***

increases. In addition, $T_e$ decreases to below 10 eV in some plasma shots at the view 1 vertex location. This is likely due to SAS-VW's highly baffled closed divertor configuration and improved neutral confinement [12, 13, 15].

Contrary to the MRC, the SAS-VW total gross intra and inter-ELM W erosion rates both appear to increase with increasing $D_2$ mass injection rates. The total gross intra-ELM W erosion rate increases due to more numerous small ELMs while the large ELMs remain around the same size. Similarly, the larger divertor particle flux caused by an increased $D_2$ mass injection rate increases the inter-ELM erosion rate since the divertor $T_e$ does not significantly decrease with increased $D_2$ mass injection in these SAS-VW plasma shots. Figure 41 shows the sum of the intra-ELM and inter-ELM W erosion rates as a function of inter-ELM $n_e$ for each SAS-VW plasma shot analyzed. Past ~$10^{19}$ Divertor inter-ELM $n_e$, both the intra- and inter-ELM gross W erosion increases profoundly. However, it does not seem that low $D_2$ mass injection rates associated with low inter-ELM densities increased W erosion. Again, little difference in W erosion is seen between $D_2$ gas and pellet shots with similar inter-ELM density. Due to the strongly attached plasma divertor conditions, the inter-ELM W erosion exceeds the intra-ELM W erosion. While the W erosion is around 4 times greater during an ELM than between ELMs, approximately 85% of the shot time is spent in the inter-ELM regime which leads to more inter-ELM induced W erosion like the MRC results. Next, we discuss large ELM pedestal stored energy drop, frequency, and heat flux from the SAS-VW campaign. Figure 42 shows both the ELM pedestal stored energy drop and $F_{ELM}$ as a function of inter-ELM density. From Figure 42 we see a clear increase and decrease in the average large $F_{ELM}$ and pedestal stored energy drop with increasing inter-ELM $n_e$, respectively. However, several characteristics contrast the MRC. Thus, more frequent and lower energy ELMs are emitted from the pedestal in the SAS-VW

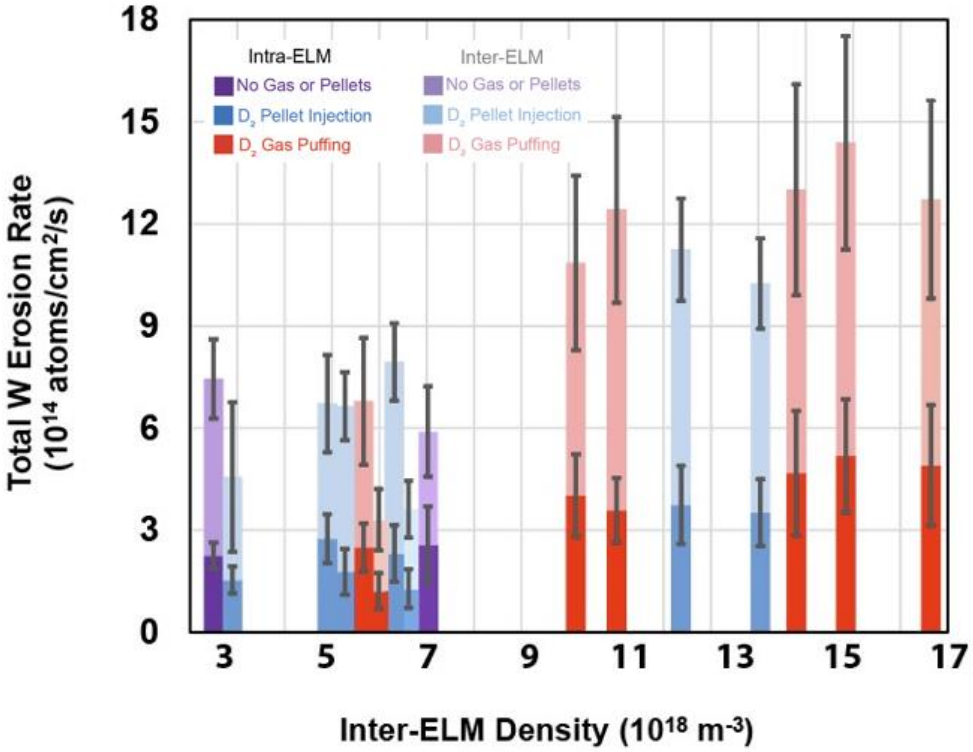



*Figure 41. Total W intra- and inter-ELM erosion rates shown in solid.*

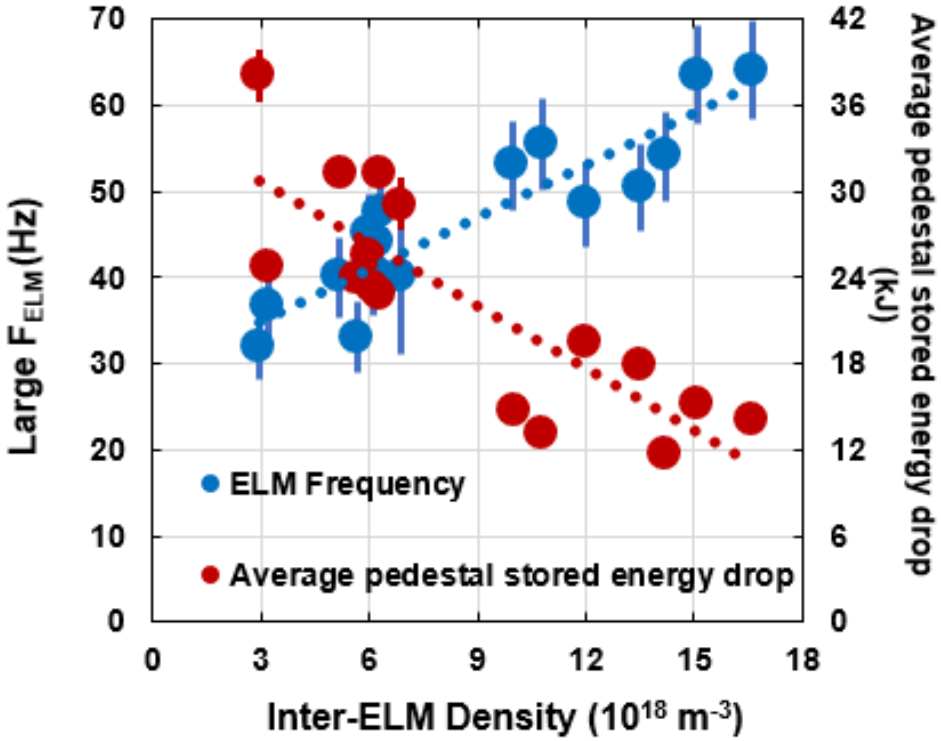



*Figure 42. Large ELM frequency and pedestal stored energy drop as a function of inter-ELM density with dashed linear trendlines.*

campaign than the MRC in shots with similar power levels and $D_2$ mass injection rate. Yet the divertor $T_e$ between the two campaigns are similar and less W erosion is seen in the SAS-VW campaign than the MRC. This further supports that the lower SAS-VW pedestal $n_e$ compared to the MRC is the driving factor controlling W erosion. The lower $n_e$ profiles lead to less $\Gamma_{||,FS}$ to the divertor in the SAS-VW campaign than the MRC to reduce W erosion. Although increasing $D_2$ mass injection rates did not reduce the W divertor erosion in the SAS-VW campaign and increased W divertor erosion at high $D_2$ mass injection rates, several positive effects of $D_2$ mass injection still exist. As seen, the large reduction in average pedestal stored energy drop associated with an ELM benefits plasma confinement and releases less energy towards the divertor. Although, the positive confinement impact is undermined by the large decrease in pedestal $T_e$ with higher $D_2$ mass injection. Even so, the average peak ELM heat flux noticeably decreases with increases in $D_2$ mass injection rate. Likewise, Figure 43 shows the average intra-ELM peak heat flux with respect to inter-ELM $n_e$. As seen in Figure 43, the average large ELM peak heat flux decreases with increasing inter-ELM density. Interestingly, a dip below the trendline is seen for shots around 6E18 $m^{-3}$ inter-ELM $n_e$. Once again, $D_2$ gas and pellet shots with around the same inter-ELM density show comparable values. In terms of inter and intra-ELM W erosion, ELM peak heat flux and energy reduction, and minimal pedestal plasma degradation, the relatively low $D_2$ mass injection rate proves beneficial in the SAS-VW campaign. In the MRC, this is not the case. Plausibly, the low $D_2$ mass injection rates increased W intra- and inter-ELM erosion while more certainly decreasing ELM energy and heat flux. This difference in MRC and SAS-VW W erosion trend is thought to be due to the larger reduction in $T_e$ with relatively high $D_2$ mass injection in the MRC than the SAS-VW campaign. Last of all, the SAS-VW divertor heat flux exceeds the MRC heat flux due to a larger $T_{e,ped}$ although

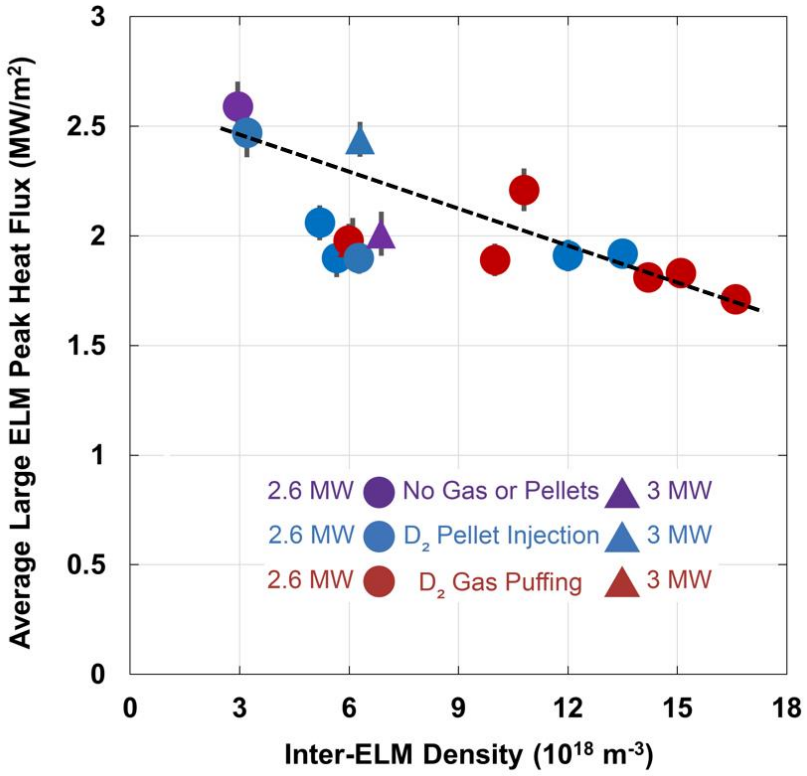



*Figure 43. Average large ELM peak heat flux as a function of inter-ELM density with a linear dashed trendline.*

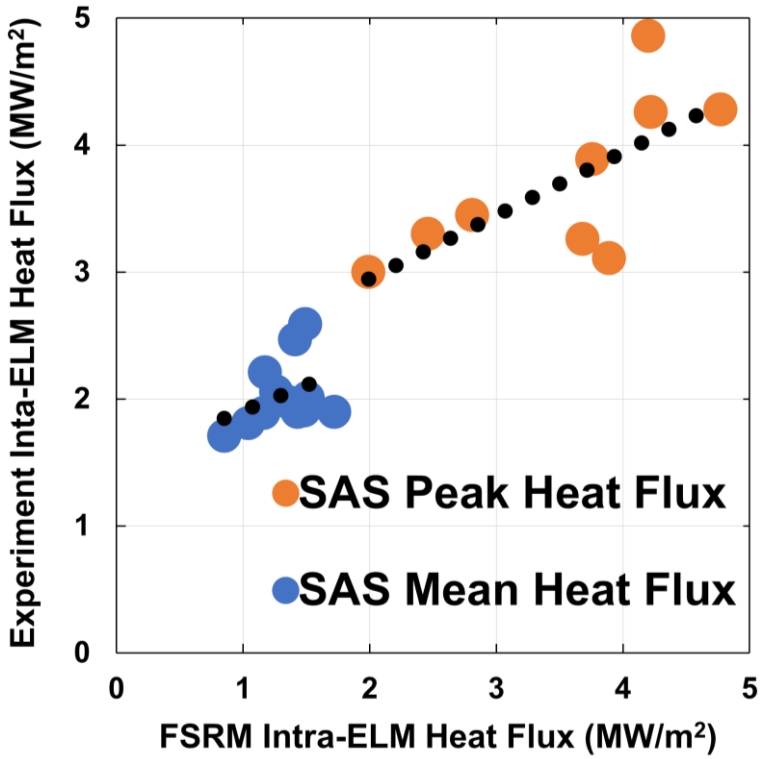



*Figure 44. SAS-VW intra-ELM experimental heat flux as a function of FSRM heat flux.*

containing a lower $n_{e,ped}$, stemming from Equation 3. Figure 44 compares the experimental and FSRM SAS-VW heat flux profiles. The experimental SETC measurements FSRM predictions seem to match close. Since FSRM heat flux is proportionate to FSRM ion flux, it is unlikely that FRSM ion flux values are underestimated. FSRM heat flux quantities should be similar between MRC and SAS-VW shots, given that the tradeoff in $n_{e,ped}$ and $T_{e,ped}$ parameters and roughly equivalent $T_{e,div}$. Though, diagnostic signals tend oversaturate during transient events such as ELMs. Unfortunately, this makes a direct comparison between the MRC and SAS-VW experimental intra-ELM heat flux values unachievable.

# Chapter 7

## SAS-VW Surface Analysis

### 7.1 Energy Dispersive X-ray Spectroscopy

Energy dispersive x-ray spectroscopy (EDS) was performed for the SAS-VW tiles to assess elemental composition and uniformity. Two SAS-VW tiles were analyzed; one tile was exposed to the plasma under experimental operation whereas the other was not. Several samples were cut from each tile, as shown below in Figure 45. All samples were taken from the middle of the SAS-VW tile from a region known as the progressive slant, as indicated in Figure 45. For the SAS-VW plasma shots analyzed in this study, the OSP position fluctuated in this region of interest. The white boxes in Figure 45 were one-inch square samples we designated as “large” whereas the black boxes were half-inch square samples we designated as “small”. Notably, the small sample locations were much closer to SAS-VW’s vertex than the large sample locations. Likewise, we noticed a less homogeneous mixture of W and C for the exposed small sample locations closer to the SAS-VW vertex. Figure 46 shows the comparison between the large and small sample locations and their EDS profiles. Most obviously, the C-W mixture is much less uniform closer to the vertex. Plausibly, this could be a sign of thick C deposition in the vertex that is broken off as chunks to reveal the barren W surface. Afterall, the SAS-VW V shaped closed divertor configuration was designed to trap impurities [13] . Interestingly, large sample 3 showed the most C deposition of the 3 large samples. Relatively, this large sample was further down the progressive slant and closer to the vertex. The reasoning for large sample 3’s increased C composition is not clear but could have something to do with this. Surprisingly, the patchier C deposition shown for the small samples can reach thickness on the scale of 1-10 μm. Figure 47 shows a secondary electron image of a section taken from small sample 1 displaying the C layer

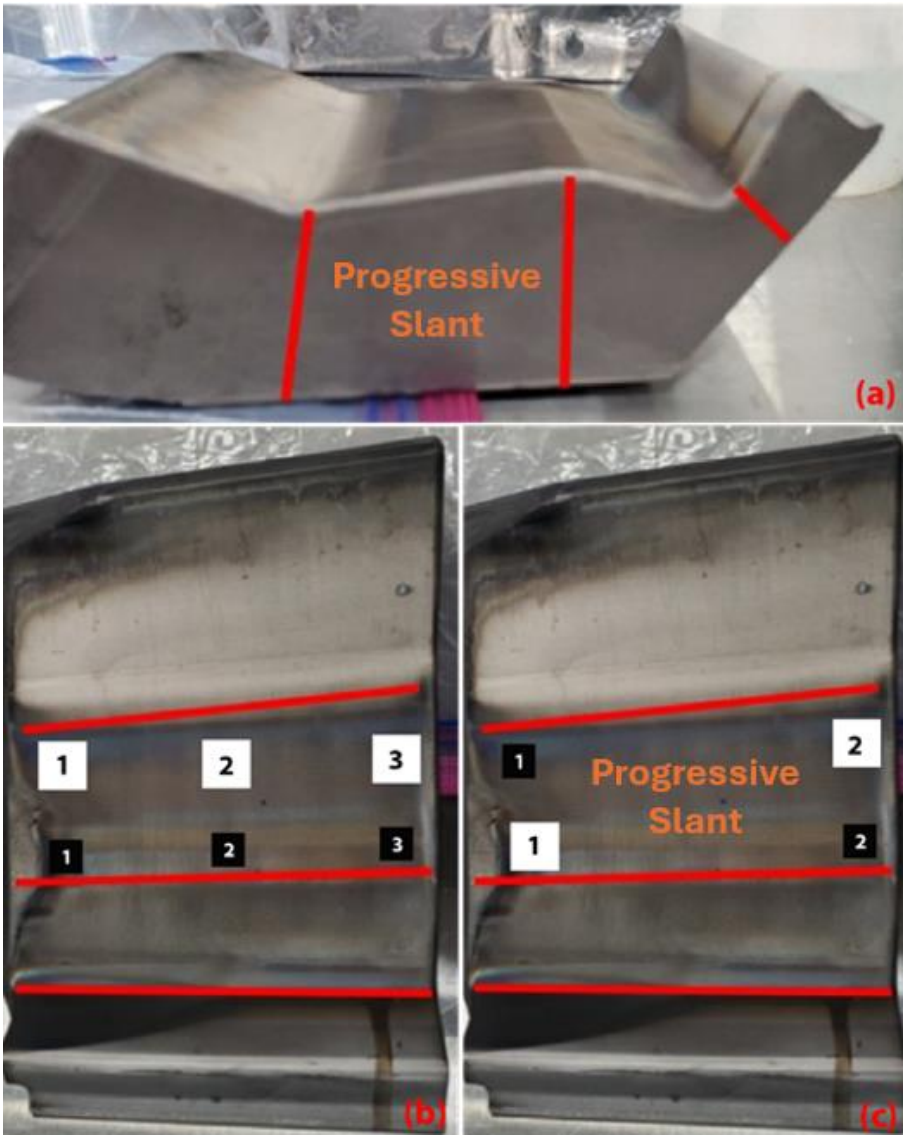



***Figure 45. SAS-VW tile cut positions are indicated by the red lines (a) side view of entire tile (b) exposed tile sample positions (c) unexposed tile sample positions.***

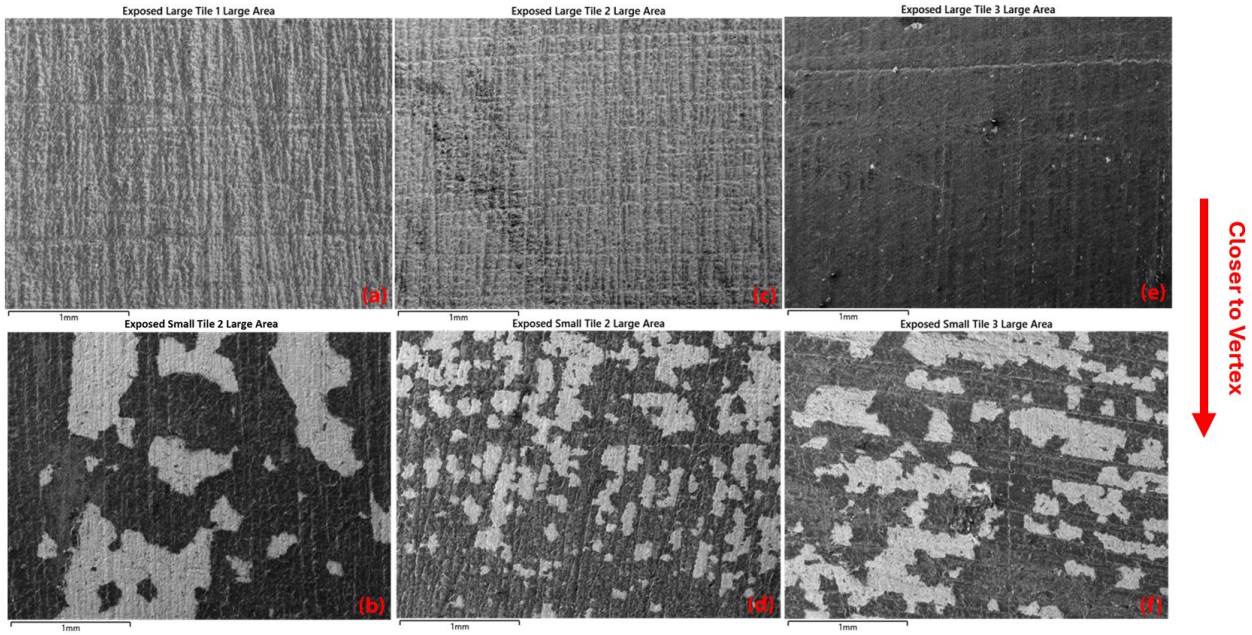



*Figure 46. EDS profiles for exposed tiles. Dark colored areas represent C concentration while light colored areas represent W concentration. (a) large sample 1 (b) small sample 1 (c) large sample 2 (d) small sample 2 (e) large sample 3 (f) small sample 3.*

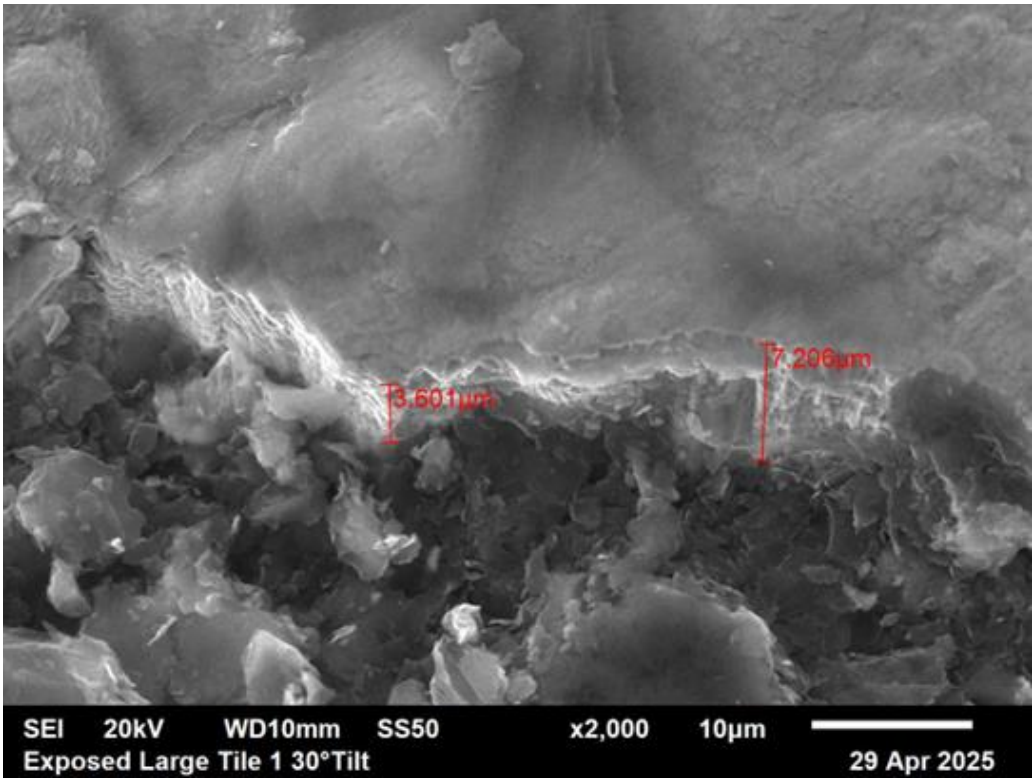



*Figure 47. Secondary electron image scan taken from sample 1. The lighter color represents C while the darker color represents W, contrary to the EDS profile. The C layer thicknesses are approximated in red.*

thickness. The secondary electron image scan was taken at a 30° tilt into the surface to approximate the C thickness layer. Additional information regarding the secondary electron image scan can be found here. Unfortunately, the EDS system was unable to be calibrated to determine an accurate quantitative comparison between C and W. Though, we can compare the elemental concentration of the unexposed tile samples to the exposed tile samples. In Figure 48, a representative average of the elemental concentration is compared between the unexposed and exposed tile samples. The unexposed representative sample had a considerable amount of C on the surface due to the smudgy nature of graphite. The average atomic concentration of the exposed tile was about 30% higher than the unexposed tile for the same probing 5 kV x-ray energy, supporting that there was significant C coverage of the SAS-VW divertor during operation. The material depth at which the x-ray energy penetrates and analyzes is estimated by the exponential attenuation law. Likewise, Equation 7.1 shows the exponential attenuation law equation for x-rays in an elemental media such as C or W.

$$\frac{I}{I_0} = \exp\left[-\left(\frac{\mu}{\rho}\right) * x\right] \tag{7.1}$$

The NIST X-Ray Mass Attenuation Coefficients $\left(\frac{\mu}{\rho}\right)$ for C and W are 19.12 $cm^2/g$ and 553.4 $cm^2/g$, respectively, at 5 keV x-ray energy. The attenuation length of x-rays into the material degrades to 1/e of its surface value, so $\frac{I}{I_0} = \frac{1}{e}$. x represents the material mass thickness and is equivalent to the product of the material density (ρ) and the thickness to which the x-rays penetrate (t). Thus, the x-ray's penetration depth, t, is expressed in Equation 7.2 below.

$$t = -\frac{\ln\left(\frac{I_0}{I}\right)}{\left(\frac{\mu}{\rho}\right)*\rho} \tag{7.2}$$

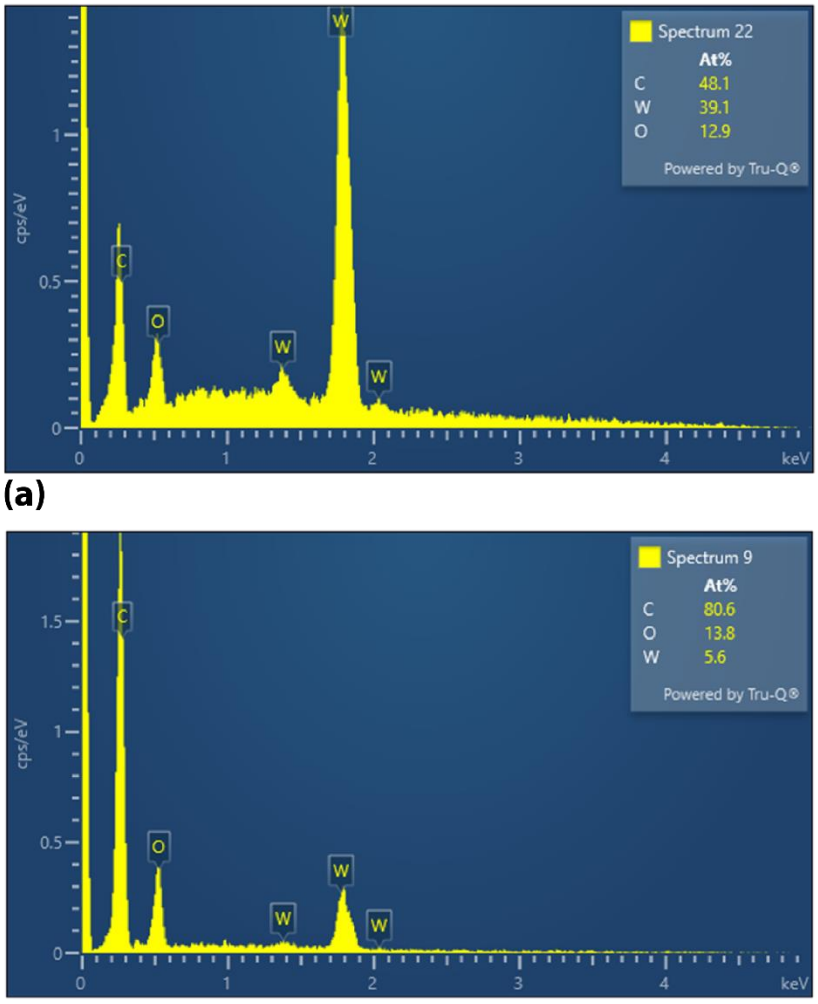



***Figure 48. 5 kV EDS spectrum for (a) Unexposed representative large sample 1 (b) Exposed representative large sample 1.***

Here, $\rho_C = 1.7 \frac{g}{cm^3}$ and $\rho_W = 19.3 \frac{g}{cm^3}$ and t calculates to $t_C = 307.7$ μm and $t_W = 0.94$ μm. The SAS-VW graphite tiles were coated with 10-15 μm thick W and on top of this layer we observed layers of C on the scale of 1-10 μm. While the x-ray attenuation depth falls drastically short of penetrating the entirety of the W coated surface, it is still difficult to assess the tile surface elemental composition given the inconsistent tile surface uniformity and uncalibrated EDS spectrum. Though speculative, it seems likely that a significant portion, perhaps half or more, of the SAS-VW coated W surface is covered in C during DIII-D exposed plasma operation. This resides in the ballpark of the predicted C and W surface concentration values.

## 7.2 Profilometer Topographical Data

WYKO profilometry scans were performed in attempt to characterize surface roughness effects on θ [39]. Essentially, a rougher surface makes incoming ions strike at a more normally distributed spectrum from $0° < \theta < 90°$, as depicted in Figure 49 below. As seen, the target's surface normal is at an incline, thereby reducing the angle at which the ion strikes the surface relative to the normal by ε, as described by Equation 7.3 below.

$$\theta' = \theta - \varepsilon \tag{7.3}$$

θ' is referred to as the "local" θ. Once topographic data of the SAS-VW tile sample is found using profilometer optical scanning and input into micro pattern roughness computations along with the theoretically smooth surface ion angle distribution (IAD), we can obtain a local θ distribution (LIAD) [39]. Thus, Figure 49 shows an example of an exposed SAS-VW tile sample LIAD. As seen, the LIAD average for the exposed tile sample is ~73° for D ions. Although, C ions from the same sample were found to be on average a few degrees closer to normal incidence

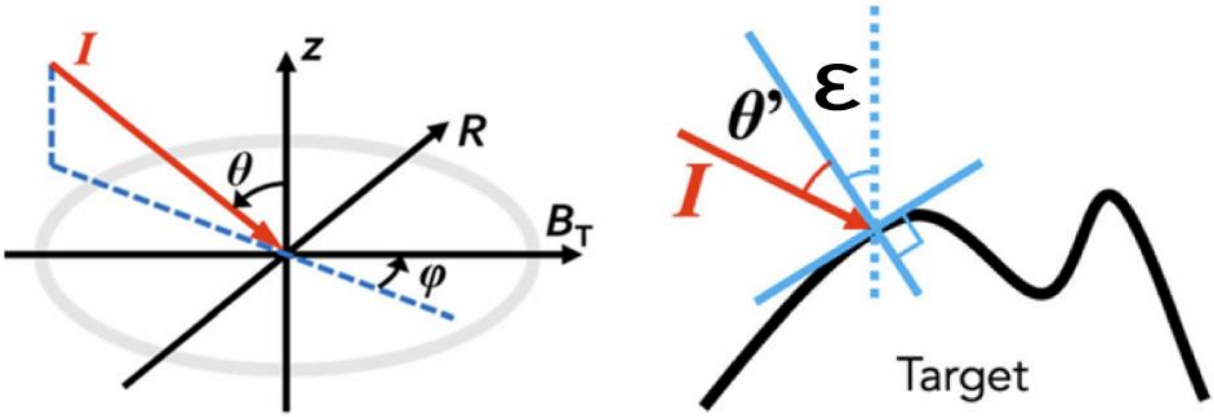



***Figure 49. Schematic of how surface roughness affects ion impact angle (θ) on the target. θ' represents the rough surface θ [39].***

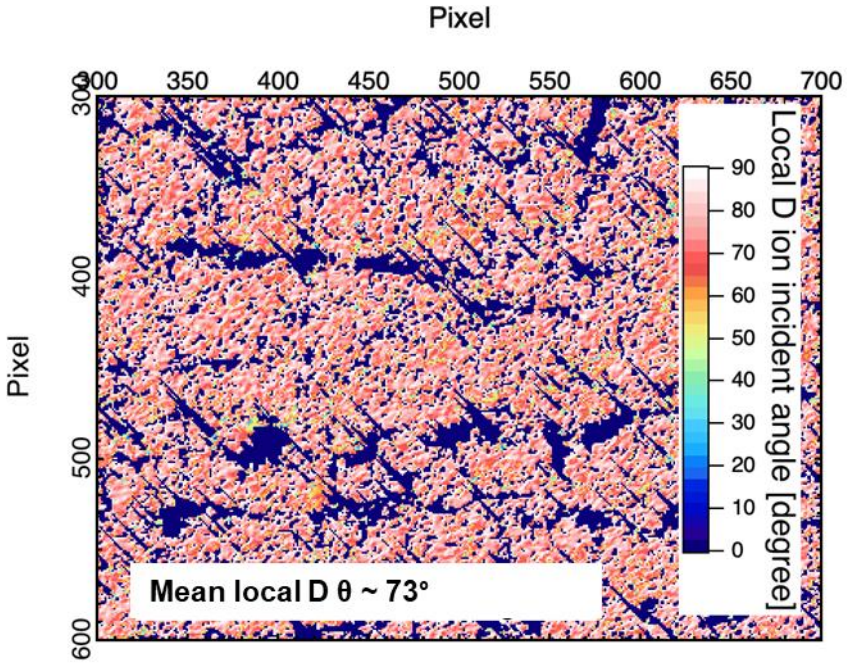



***Figure 50. LIAD for exposed SAS-VW tile sample.***

with a similar LIAD. Interestingly, a number of ions were found to be incident at angles so grazing that W and C Y would significantly decrease, indicated by the pale while color. On the contrary, a decent portion of the LIAD is a dark blue color, indicating near normal angle of incidence, associated with low probability of particle reflection and significantly increased C deposition, in addition to reduced W and C erosion compared to a 45° θ. The original theoretically smooth surface IAD is seen in Figure 51. IADs (regarding only the poloidal angle of incidence) for high energy ions relevant to intra-ELM conditions were computed with a sheath model called LPTMC, similar to [40]. LPTMC uses free-streaming approximations and produces IAD trends with the double linear approximation of electric potential, a shifted Maxwellian distribution ($\overline{v_{\parallel}} = c_s$) in parallel-to-B direction sampled at a distance perpendicular to the wall and a centered Maxwellian in perpendicular-to-B direction. LPTMC assumes no perpendicular diffusion or surface roughness, uniform plasma background and magnetic field close to the wall, and a 1-dimensional sheath electric-potential drop. Though, the models may not fully capture gyro-orbit effects during ELMs very effectively and should be taken with a grain of salt. Relevantly, C IADs are predicted to redeposit much more normal to the surface, though the exact magnitude of the predictions has differed [17, 18, 41, 42]. Accordingly, Figure 52 shows a smooth surface C redeposition IAD determined by LPTMC. Notably, the redeposited C IAD is much more normal compared to initially incident C ions, reducing $R_C$ and contributing to significant C implantation to reduce W erosion. Sadly, redeposition processes of low-Z ions are convoluted and it is difficult to gauge how much C is redepositing between incident C ions, eroding C atoms, and C sourcing from nearby graphite surfaces. For any given set of plasma parameters, it is difficult to pin the exact IADs. In combination with the surface roughness effects, it is nearly impossible to prove or disprove if the past assumption of an average θ of 45°

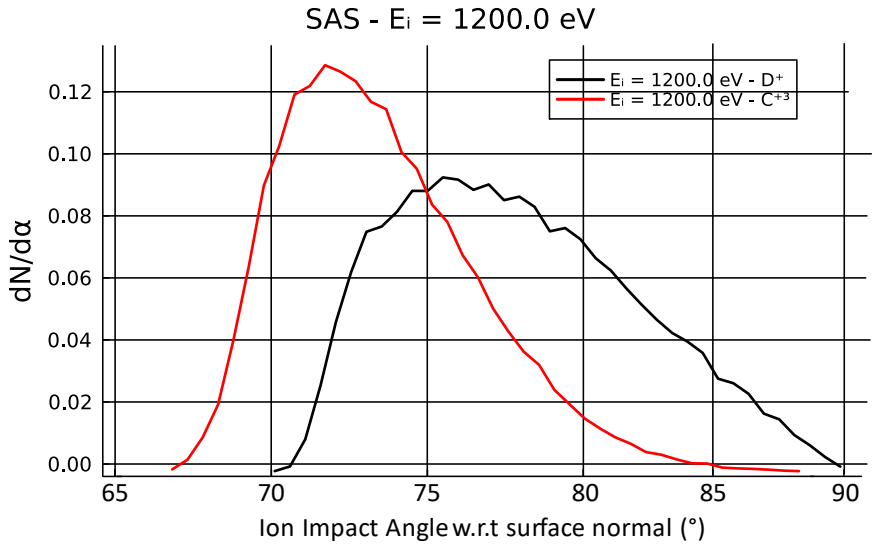



***Figure 51. Theoretically smooth surface IAD at $E_i$ = 1200 eV determined by LPTMC.***

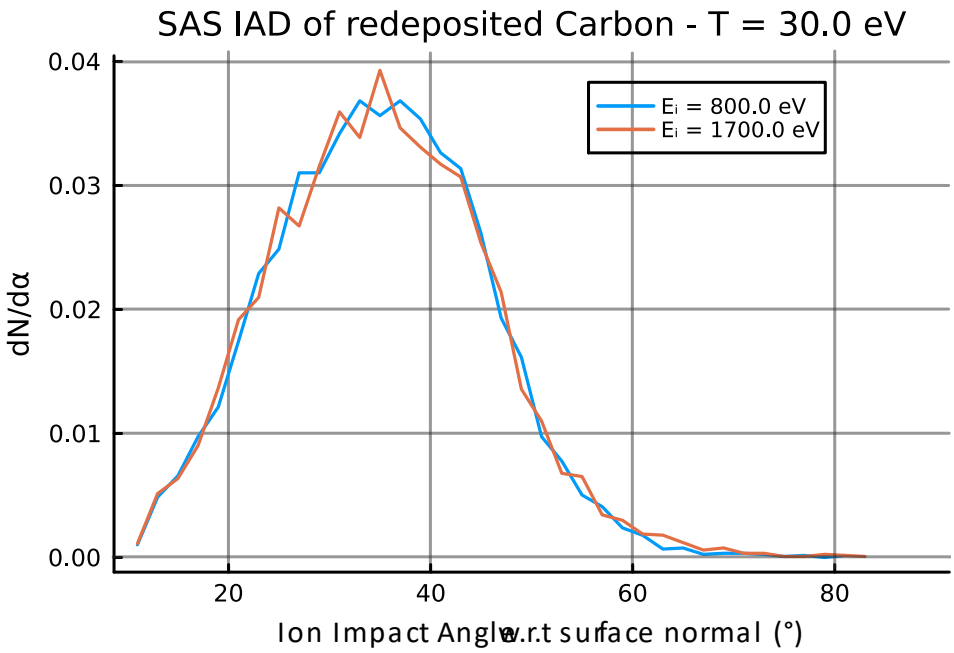



***Figure 52. Theoretically smooth surface IAD at $E_C$ = 800 eV (blue) and $E_C$ = 1700 eV (orange) determined by LPTMC.***

is correct or not. Thus, we continue to use 45° as our assumption, as providing full IADs for all calculations is time extensive and not necessarily more accurate since we cannot certainly prove or disprove the IAD. Lastly, it should be noted that the LIAD calculation from Figure 50 is only from one tile sample that was analyzed many plasma shots after the ones studied here were experimented. Thus, the data is unreliable for quantitative purposes because the surface roughness could have been very different at the time of these plasma shots.

# Chapter 8

# RustBCA Modelling

## 8.1 Single Ion-Target Sputtering Yields and Reflection Coefficients

In this section, I discuss using RustBCA to better understand and estimate the R and Y values associated with D, C, and W, in order to determine W erosion rates and provide insight into future physical sputtering analyses in mixed-material environments. RustBCA can compute R and Y for both simple single-ion/single-target interactions (e.g., C on W) and more complex cases. The latter may include mixed ion concentrations (such as a typical DIII-D plasma of 97% deuterium and 3% carbon) or layered target materials, where each layer has a distinct elemental composition (e.g., a homogeneous layer containing 47% atomic W, 47% atomic C, and 6% atomic O). RustBCA can compute Y and R values at various $E_i$ and $\theta$. In most cases we have selected $\theta = 45°$ as the best representative $\theta$ on the material target given surface roughness and gyro orbit effects. In these simulations, $E_i$ ranges up to 1.6 keV to give insight into not only inter-ELM and intra-ELM associated $E_i$ with DIII-D, but also potentially larger $E_i$. We are primarily interested in sputtering of the W divertor and any C deposited on the surface. So, we have benchmarked $Y_{D\text{-}C}$, $Y_{C\text{-}C}$, $Y_{D\text{-}W}$, and $Y_{C\text{-}W}$ computations from RustBCA to Eckstein 2002 values in Figure 53 to ensure our calculations align with past literature. All values are at an $\theta$ of 45° except for $Y_{C\text{-}W}$, which is at normal (perpendicular) incidence due to lack of available data. Overall, we find that RustBCA computes Y values that align with the past Eckstein literature. Importantly, we used the bulk binding energy (BBE) of the target as a free parameter in RustBCA to obtain values that coincide with Eckstein Y. Specifically, we used the default $BBE_W$ and $BBE_C$ of 0.0 eV, but increased the $BBE_C$ to 1.0 eV for $Y_{D\text{-}C}$ and $BBE_C$ to 2.0 eV for $Y_{C\text{-}C}$. Contrary, the RustBCA BBE parameter has no effect on R. Likewise, the comparison between

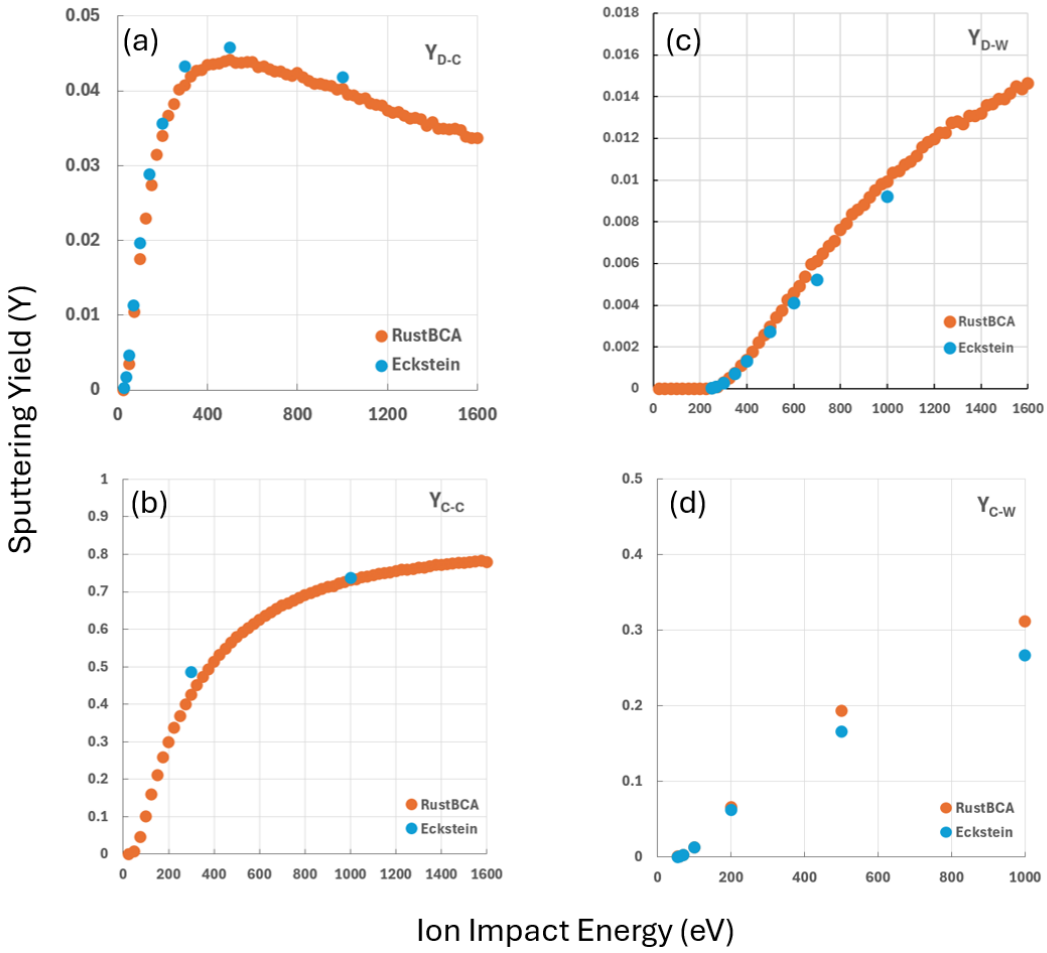



***Figure 53. Sputtering Yield (Y) vs. Ion Impact Energy ($E_i$) for RustBCA and 2002 Eckstein (a) $Y_{D-C}$ (b) $Y_{C-C}$ (c) $Y_{D-W}$ (d) $Y_{C-W}$.***

RustBCA and Eckstein $R_{C-C}$ and $R_{C-W}$ can be found in Figure 54. Once again, very limited data exists for Eckstein C-W interaction, so we benchmarked $R_{C-W}$ using a normal ion angle incidence for $R_{C-W}$ and 45° θ for $R_{C-C}$. We find that RustBCA slightly underestimates R in comparison to the Eckstein values but find the impact on W erosion and C deposition to be negligible. Currently, our FSRM intra-ELM W erosion predictions use SDTrim.SP calculations at 45° θ. So, we have compared the $Y_W$ to those computed by RustBCA in Figure 55. As seen in Figure 55, RustBCA slightly underestimates $Y_W$ compared to SDTrim.SP, whereas RustBCA slightly overestimates $Y_W$ compared to Eckstein in relation to Figure 53. Overall, RustBCA predicts very similar sputtering Yand R values compared to Eckstein's 2002 data and SDTrim.SP. Though, it is worth noting that I use RustBCA's preset surface binding energy (SBE) for both C and W, 7.37 eV and 8.9 eV, respectively. The SBE is calculated as the minimum energy required, at a given surface, for a recoil atom moving perpendicular to that surface to cause a sputtering event. It is postulated that using the RustBCA presets is a reasonable assumption in this particular case due to the inherently similar SBE values for C and W. Whereas for elements with much different SBE values, the appropriate SBE model requires closer consideration [43]. As mentioned previously, Y and R values are taken at a 45° θ, assumed to be an appropriate average after incorporating surface roughness, sheath, and ion gyro-orbit effects [37]. A more detailed post-mortem analysis could be used to estimate θ from plasma parameters and surface topography [39]. However, many subsequent plasma shots with varying plasma parameters occurred after the shots studied here, so any surface roughness measurements from available tile samples would not represent the plasma shots studied in these experiments. Yet, it is still important to discuss Y and R values at varying θ, due to the impact on C deposition and W erosion. Thus, Figures 56-61 show R and Y values as a function of θ at

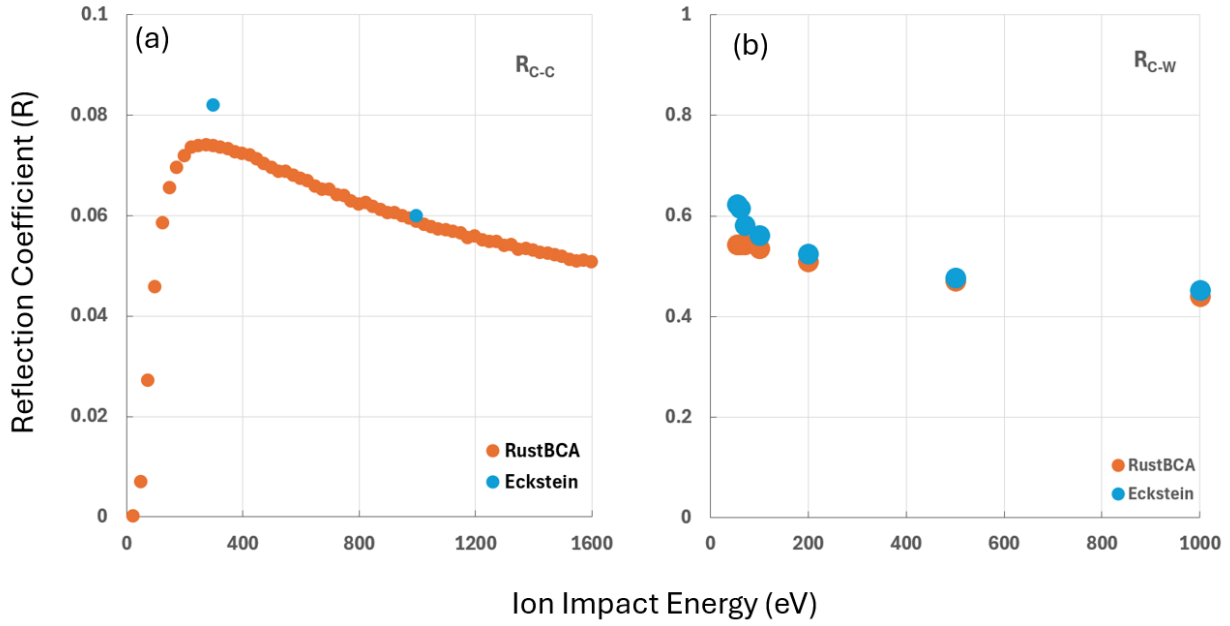



***Figure 54. Reflection Coefficient (R) vs. Ion Impact Energy ($E_i$) for RustBCA and 2002 Eckstein (a) $R_{C-C}$ and (b) $R_{C-W}$.***

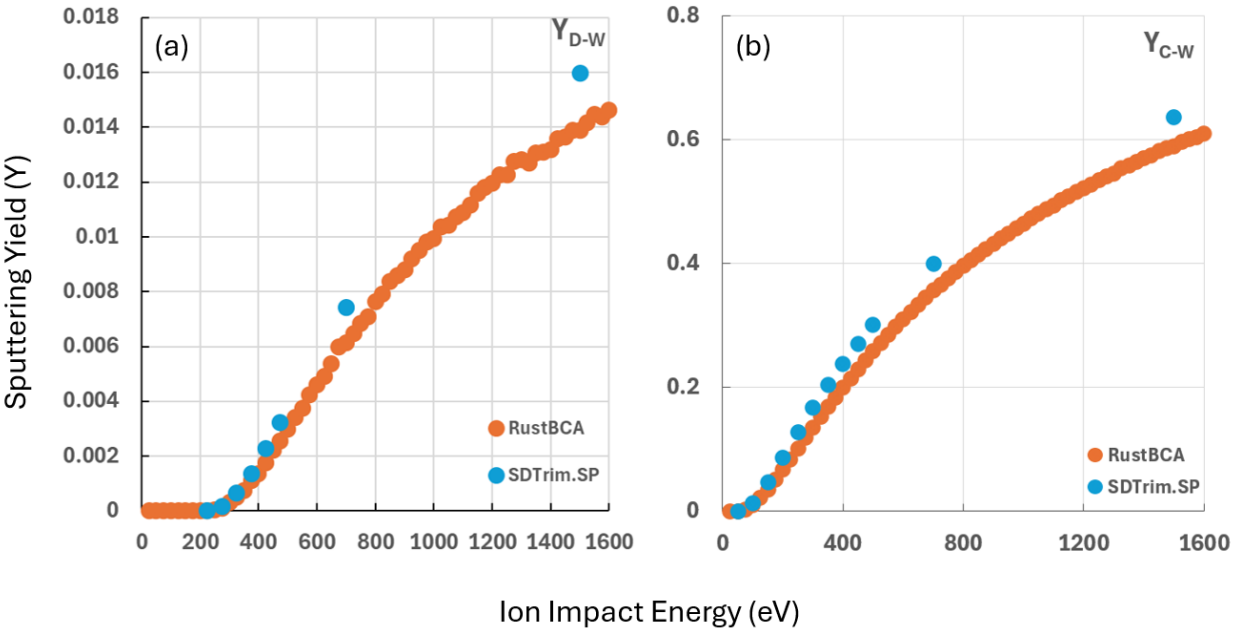



***Figure 55. Sputtering Yield (Y) vs. Ion Impact Energy ($E_i$) for RustBCA and 2002 Eckstein (a) $Y_{D-W}$ (b) $Y_{C-W}$.***

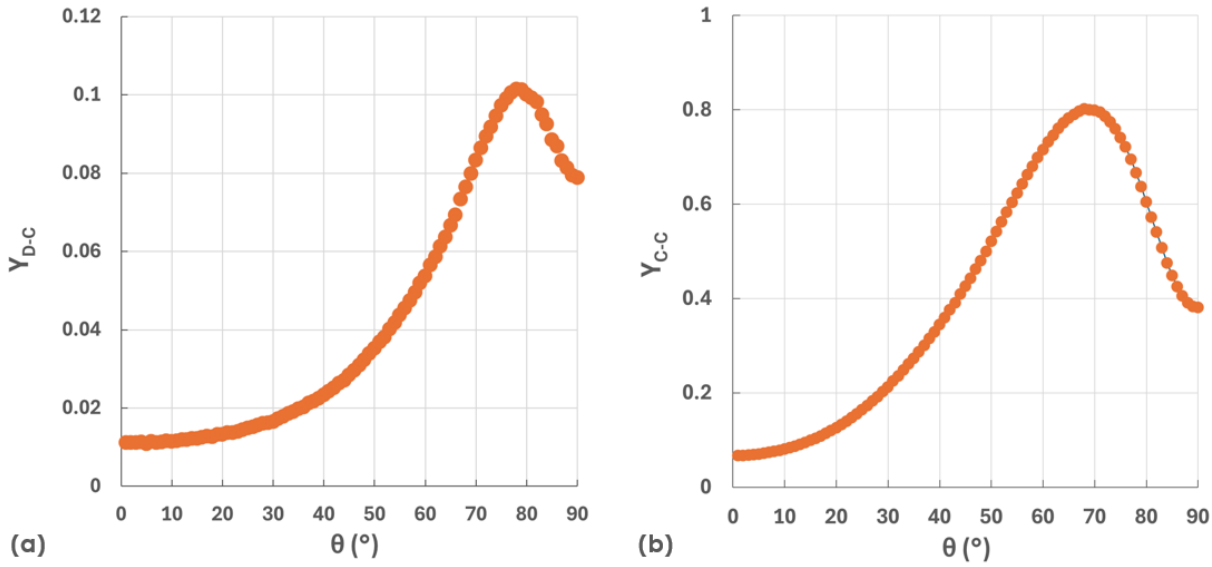



***Figure 56. (a) $Y_{D-C}$ at $E_D$ = 200 eV and (b) $Y_{C-C}$ at $E_C$ = 300 eV.***

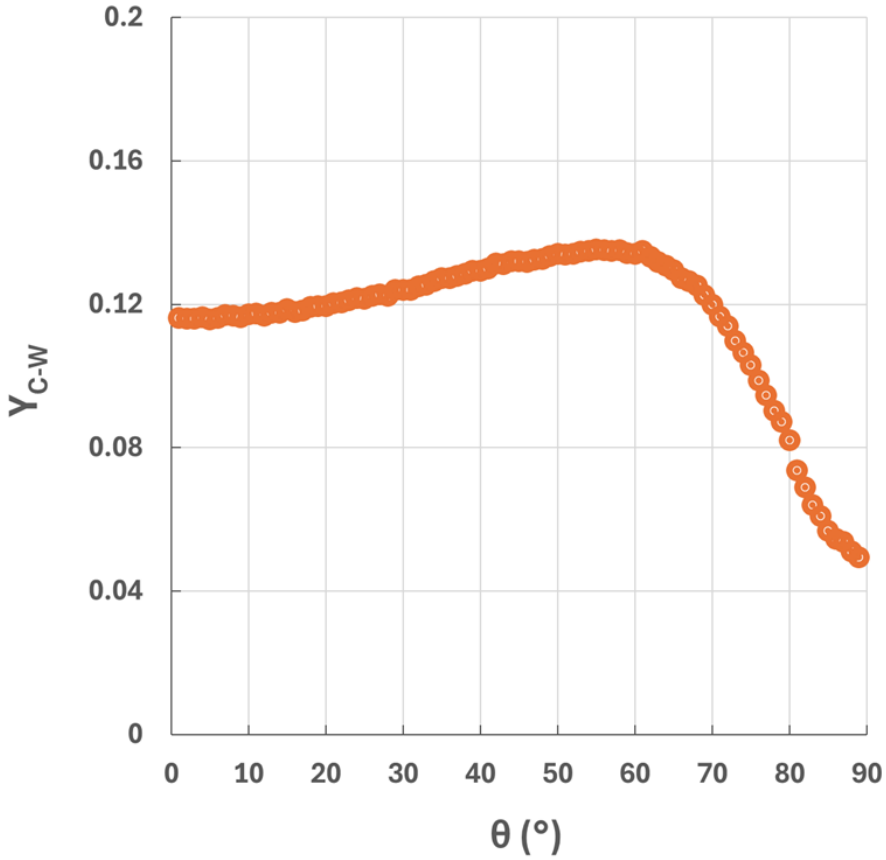



***Figure 57. $Y_{C-W}$ at $E_C$ = 300 eV.***

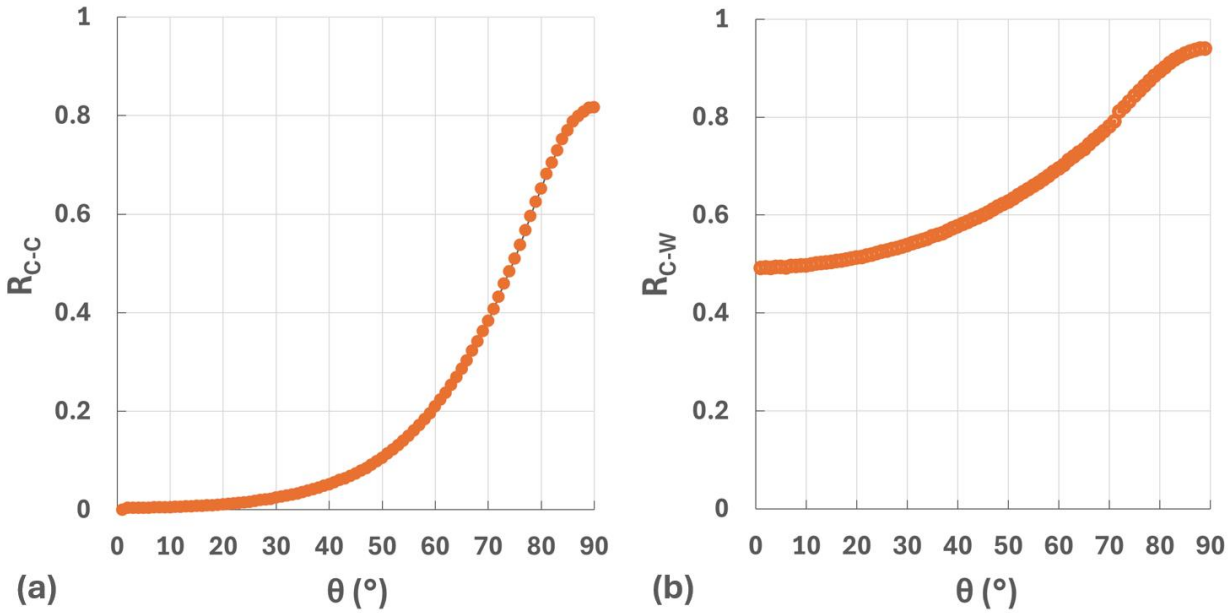



***Figure 58. (a) $R_{C-C}$ and (b) $R_{C-W}$ at $E_C$ = 300 eV.***

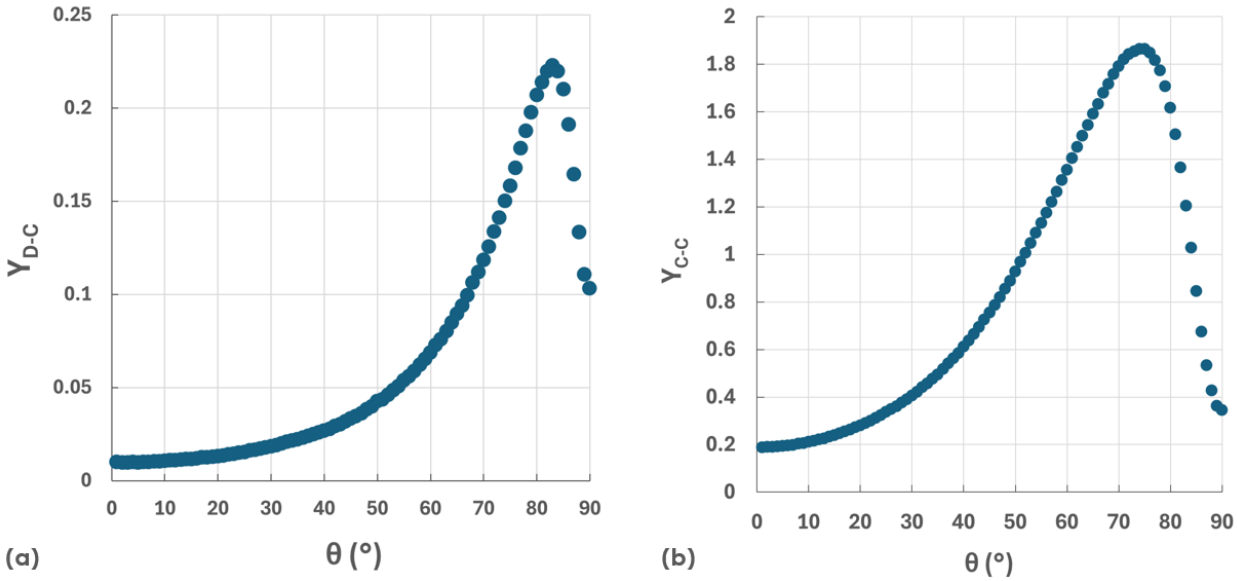



***Figure 59. (a) $Y_{D-C}$ and (b) $Y_{C-C}$ at $E_i$ = 1200 eV.***

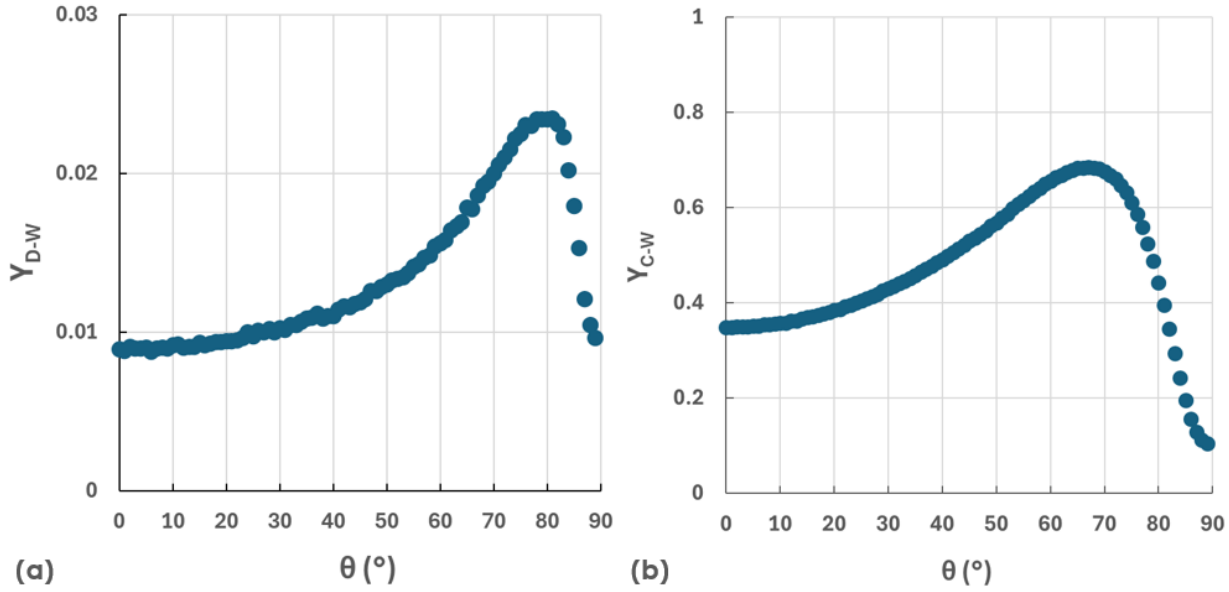



***Figure 60. (a) $Y_{D-W}$ and (b) $Y_{C-W}$ at $E_i$ = 1200 eV.***

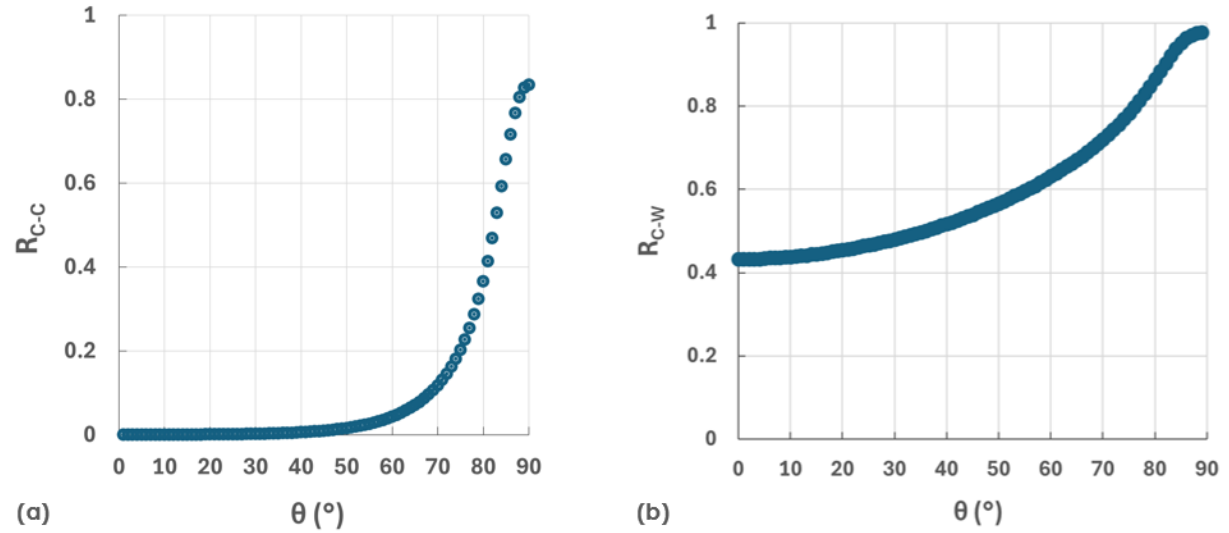



***Figure 61. (a) $R_{C-C}$ and (b) $R_{C-W}$ at $E_i$ = 1200 eV.***

relevant $E_i$ values for the plasma shots studied here. Once again, all θ values are with respect to the surface normal such that θ = 0° is perpendicular ion incidence to the divertor surface and θ = 90° is parallel ion incidence to the divertor surface. Figure 56 shows $Y_{D-C}$ at $E_D$ = 200 eV and $Y_{C-C}$ at $E_C$ = 300 eV as relevant inter-ELM $Y_C$. Figure 57 shows $Y_{C-W}$ at $E_C$ = 300 eV as relevant inter-ELM $Y_W$. Figure 58 shows $R_{C-C}$ and $R_{C-W}$ at $E_C$ = 300 eV at relevant inter-ELM C R. Figure 59 shows $Y_{D-C}$ and $Y_{C-C}$ at $E_i$ = 1200 eV at relevant intra-ELM $Y_C$. Figure 61 shows $R_{C-C}$ and $R_{C-W}$ at $E_i$ = 1200 eV at relevant intra-ELM $R_C$. Figure 56 shows that at θ = 45°, $Y_{D-C}$ and $Y_{C-C}$ have values of 0.028 and 0.426 at $E_D$ = 200 eV and $E_C$ = 300 eV, respectively. For $Y_{C-C}$, this value is pretty close to the spectrum average of 0.41 and the average value at θ = 45° is a good representation of the normally distributed θ spectrum. For $Y_{D-C}$, this is not the case, as the average value across the θ spectrum is 0.043. This could lead to an underestimation of C erosion between ELMs, thereby decreasing $\sigma_C$ and increasing W erosion. On the contrary, Figure 57 shows that the inter-ELM relevant $E_C$ = 300 eV at θ = 45° is above the spectrum average, resulting in an overestimation of W erosion between ELMs. At the relatively low $E_i$, relatively light C ions are less likely to transfer sufficient energy at a glancing incidence angle to breach the physical sputtering threshold required to sputter a relatively heavy W target. $Y_{C-W}$ is estimated to peak around θ = 58°. When comparing $Y_{D-C}$, $Y_{C-C}$, and $Y_{C-W}$ for a relatively high $E_i$ of 1200 eV, the Y distributions in Figure 59 and Figure 60 have shifted to the right towards increased Y at more glancing angles before the Y plummets at too sharp of ion incidence relative to the surface. In all cases, an initial increase in Y is seen as you move away from normal incidence of θ = 0° and toward a more grazing angle of incidence. This is because the grazing angle of incidence increases the probability that the recoil atom scatters out and away from the surface material and the collision cascade is more near-surface than a more normal angle of

incidence collision cascade. Moreover, as the collision cascade depth increases for the more glancing ion incidence, these relatively more near-surface displaced atoms have less material to travel through to escape the material, effectively being sputter rather than trapped within the material where they can recombine. This also alludes to the more drastic spread in Y with changes in θ for higher $E_i$. From Figure 58, we see the drastic increase of particle reflection for a light C atom on a heavy W atom as opposed to C on C since the C atom contains less sufficient energy to embed in the heavy W surface as opposed to the light C surface. For higher $E_i$ as shown in Figure 61, R decreases due to increased $E_i$ and ion embedding, except at very glancing ion incidence. At very glancing ion incidence, the higher energy ions have sufficient energy to recoil from the surface whereas lower energy ions are more likely to slow down and deposit on the surface. Likewise, we can generally take away that lower $E_i$ and more normal θ (perpendicular, closer to 0°), leads to more C embedding, characteristic of increased C deposition.

## 8.2 Multi Ion-Target Sputtering Yields and Reflection Coefficients

This section aims to decouple the effects of mixed material environments on W erosion predictions in a different manner than the C/W mixed material model. Y from single element material target interactions are compared to Y from a material target with a homogenous mixture of C and W, along with Y from a monolayer C deposition on top of a homogenous mixture of C and W. Afterall, C is expected to implant at high concentrations up to 10 nm below the W surface [44]. For $Y_W$ computations, we consider an ion flux composed of 97% D and 3% C as a realistic scenario for ions bombarding the DIII-D divertor. Likewise, Figure 62 shows RustBCA computed $Y_W$ results using this ion flux concentration for a 1:1 homogenous ratio of C:W compared to a solid W target. Obviously, one would expect the homogenous 1:1 C:W target

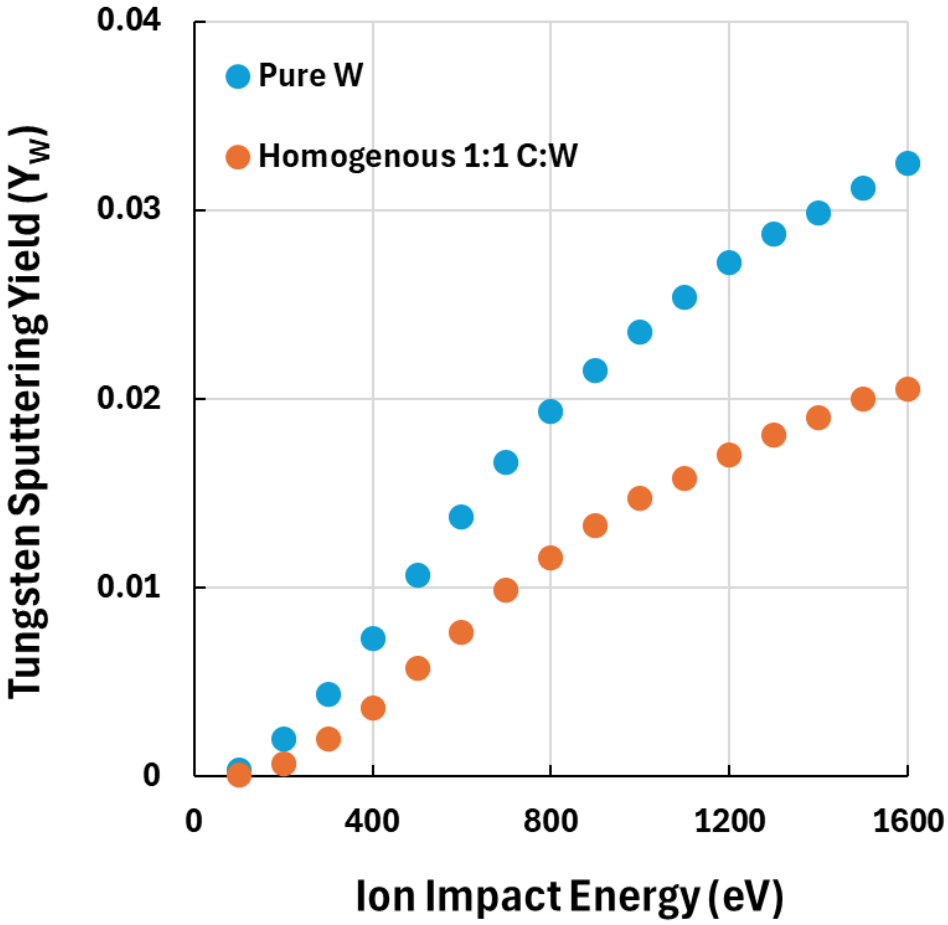



***Figure 62. RustBCA $Y_W$ comparison between W and homogenous 1:1 C:W targets for a 97% D and 3% C ion flux at $\theta$ = 45°.***

layer to have a significantly lower $Y_W$ than pure W. One would logically think that a half C and half W surface would yield half the $Y_W$. This seems to hold true at an $E_i$ of 400 eV, but the ratio varies with change in $E_i$. Thus, we compare the ratio of the homogenous 1:1 C:W $Y_W$ to pure W $Y_W$ in Figure 63. For simplicity, we define the variable Q in Equation 8.1 below and set this as the y-axis in comparison to $E_i$ on the x-axis.

$$\boldsymbol{Q} = \frac{\textit{1:1 C:W } Y_W}{\textit{Pure Tungsten } Y_W} \qquad 8.1$$

Notably, the ratio between the homogenous 1:1 C:W $Y_W$ to pure W $Y_W$ approaches 0.5 as $E_i$ increases. At divertor detachment relevant low $E_i$, we find that the homogenous 1:1 C:W $Y_W$ is considerably lower than pure W $Y_W$*0.5. Whereas at intra-ELM relevant $E_i$, the homogenous 1:1 C:W $Y_W$ is about 30% larger than pure W $Y_W$*0.5. Accordingly, applying this at our inter-ELM relevant $T_i$ gives slightly better agreement between predicted and experimental inter-ELM W erosion for both MRC and SAS-VW results, while the agreement between predicted and experimental intra-ELM W erosion worsens. However, it is plausible that C deposition accumulates between ELMs due to lower $E_i$ and greatly reduced $Y_C$ as seen in Figure 56 [41]. Though C deposition may only cover a portion of the W divertor surface by the time an ELM filament reaches the divertor, C will implant up to a few nm below the surface as well. Thus, we compute and compare $Y_W$ for the homogenous 1:1 C:W layer to $Y_W$ for a monolayer of C deposition on top of the homogenous 1:1 C:W layer. Hence, Figure 64 shows the comparison in the same manner as in Figure 62 and Figure 63. We define the variable P in Equation 8.2 and set this mathematical expression as the y-axis in Figure 64b. In Figure 64, we see that adding just 1 monolayer of C atop the homogenous 1:1 C:W target considerably reduces $Y_W$, especially at lower $E_i$.

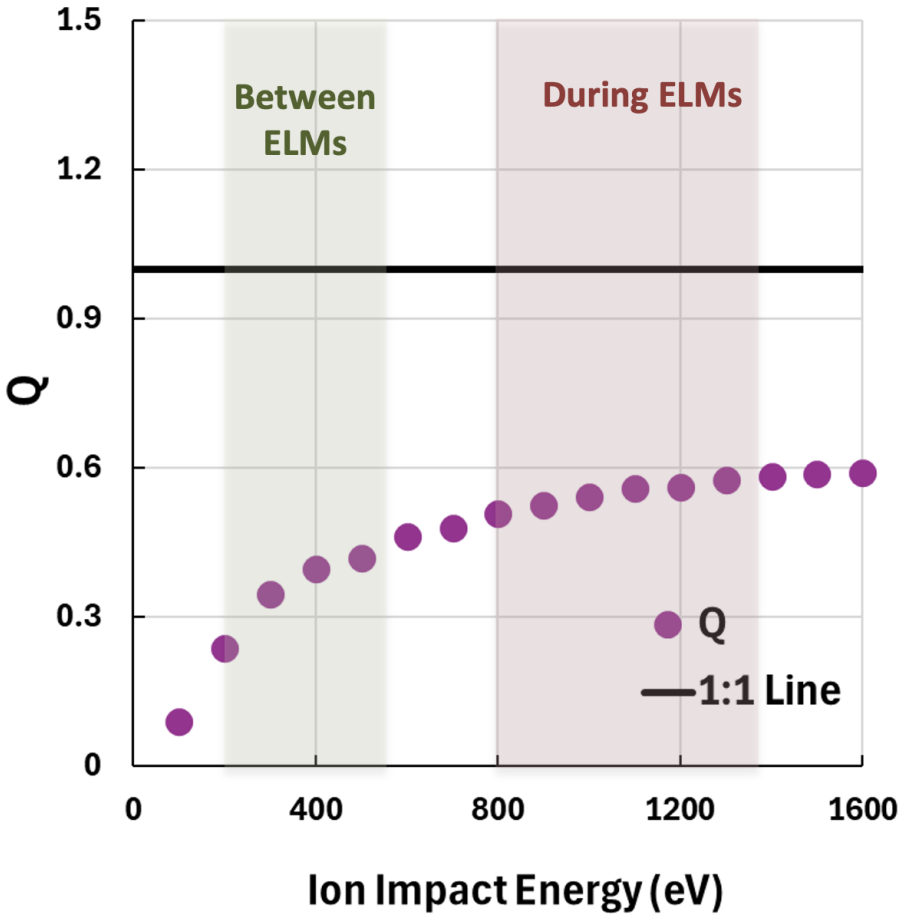



*Figure 63. The ratio of 0.5*$Y_W$ to the homogenous 1:1 C:W $Y_W$ vs. Ion Impact Energy ($E_i$).*

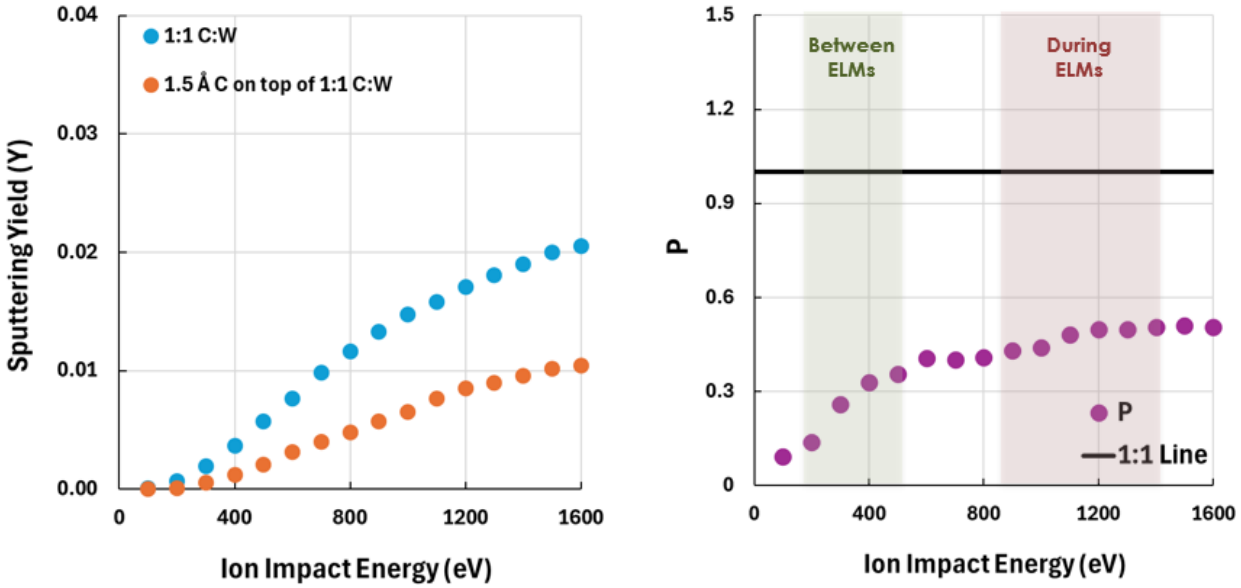



*Figure 64. (a) RustBCA $Y_W$ comparison between homogenous 1:1 C:W and a monolayer of C atop homogenous 1:1 C:W for a 97% D and 3% C ion flux at $\theta = 45°$ (b) The ratio of $Y_W$ for a monolayer of C atop homogenous 1:1 C:W to homogenous 1:1 C:W vs. Ion Impact Energy ($E_i$).*

$$P = \frac{1.5\ \text{Å on top of 1:1 C:W } Y_W}{1\text{:}1\ C\text{:}W\ Y_W} \qquad 8.2$$

In Figure 64, we see that adding just 1 monolayer of C atop the homogenous 1:1 C:W target considerably reduces $Y_W$, especially at lower $E_i$. Considering that a monolayer of C is only about 1.5 Å thick, while EDS measurements back in Figure 47 show C deposition layers up to 10 µm thick, it is plausible that such layers can completely inhibit W erosion. Thus, incorporating the effects of a C deposition layer build up between ELMs seems realistic and would substantially reduce intra-ELM W erosion predictions to give a better agreement compared to experimentally measured values for the SAS-VW campaign. Depending on the thickness, near-surface deposited C layer could be entirely eroded during an ELM event due to the large particle flux at high $E_i$. Unfortunately, pinpointing the exact proportion of the W divertor C deposition covers and its thickness real time is infeasible. It is plausible that the closed SAS-VW divertor resulted in more significant C deposition compared to the open MRC divertor due to its intrinsic nature of high impurity recycling and trapping thanks to the V-shaped geometry and large graphite surface across the V-shaped slot. CIII filterscopes viewing the large graphite surface across the V-shaped slot would have given crucial information regarding C sourcing. LPs were installed at such locations, thus a better understanding of C charge states and associated impact angle reaching the divertor could have been more understood as well [17, 45].

# Chapter 9

# Conclusions and Key Takeaways

## 9.1 Overview

This dissertation set out to resolve one of the largest uncertainties obstructing reliable lifetime predictions of plasma-facing components (PFCs) in present and future tokamak reactors: the accurate quantification of W divertor erosion in mixed-material, ELMy H-mode plasmas. Through two major experimental campaigns on DIII-D (MRC and SAS-VW), we spectroscopically obtained real and meaningful intra- and inter-ELM W erosion results across a range of plasma parameters such as $T_e$, $n_e$, and $f_c$. Combined with mixed-material steady-state C/W layer modelling and RustBCA sputtering calculations, this work provides new insight into the ion-material interactions that govern intra- and inter-ELM erosion. The results clarify the dominant physics controlling erosion in intra- and inter-ELM regimes, reveal the limitations of existing models and data uncertainties, and identify critical knowledge for more predictive divertor lifetime estimates and considerations for reactors like ITER, SPARC, and DEMO. While the scope of this work focuses on divertor erosion, it also concludes with insight into relevant topics such as divertor heat flux and core W contamination mitigation. Ultimately, next step devices seek to operate at longer times and higher temperatures, greatly jeopardizing the structural integrity of PFCs.

## 9.2 Key Findings from Experimental Campaigns

### 9.2.1 ELM-resolved tungsten erosion trends

Across both the MRC and SAS-VW experiments, several robust trends emerged: $D_2$ mass injection consistently reduces large Type-I intra-ELM W erosion once the injection rate is high

enough to significantly lower $T_{e,div}$ and associated $E_i$. Though, W erosion from smaller, "grassy", ELMs generally increased with $T_{e,div}$ with more $D_2$ mass injection. Intermediate injection rates can increase W erosion, producing a non-monotonic dependence. This arises when $D_2$ raises divertor electron plasma density ($n_{e,div}$) and ion flux before $T_{e,div}$ decreases sufficiently to reduce Y. Inter-ELM erosion frequently exceeds intra-ELM erosion in total contribution, despite lower instantaneous values, due to the large fraction of time spent in the inter-ELM state. ELM amplitude and peak heat flux footprints associated with melting concerns shrink with higher $D_2$ mass injection, consistent with prior DIII-D pellet pacing studies, but the specific scaling differs between open and closed divertor configurations. These observations reinforce that fueling-driven mitigation strategies must be tuned carefully, as divertor response is governed by competing changes in $n_e$, $T_e$, ELM structure, and impurity transport. However, it is imperative to keep factors such as plasma shaping and collisionality into account as well. If the design parameters allow divertor detachment relevant temperatures, intra-ELM W erosion would exceed inter-ELM W erosion for instance. Moreover, in this case, one could not indefinitely increase $D_2$ mass injection to combat ELMs due to potential rising plasma collisionality and density limit concerns.

### 9.2.2 Influence of divertor geometry (open vs. closed configurations)

When comparing the open MRC divertor and the highly baffled SAS-VW divertor, we found that the FSRM underpredicted intra-ELM W erosion for the MRC and overpredicted intra-ELM W erosion for the SAS-VW after incorporating the steady-state C/W mixed material model. A plausible explanation may be due to the intrinsic impurity trapping nature of the physical V-shaped geometry of the SAS-VW divertor, leading to increased C deposition and decreased W erosion. Unfortunately, the MRC divertor was not as well diagnosed compared to the SAS-VW

divertor at the time, complicating comparison. Most prominently, SAS-VW contained $D_\alpha$ and CIII filterscopes installed at the divertor while the MRC did not. This allowed for more accurate determination of D and C ion fluxes for purposes of W erosion and C deposition estimations. Future fusion tokamaks concerned with divertor erosion and deposition would greatly benefit from these diagnostics to implement real-time control mechanisms such as strike point sweeps and divertor impurity injection. Notably, the magnetic field inclination angle ($\alpha$) relative to the divertor surface averaged around 1° for the SAS-VW and 2° for the MRC. Though due to surface roughness and ion gyro-orbit effects, the $\theta$ is thought to be largely unaffected, especially for redepositing particles. Considering this, the sharper $\alpha$ for the SAS-VW is better in terms of reducing impinging heat flux. The SAS-VW pedestal operates significantly hotter temperature than the MRC's (denoted by the higher $T_{e,ped}$), but resulted in similar divertor temperature, and substantially reduced W erosion due to lower $n_{e,div}$ and impinging ion fluxes. One would also want to consider the impact of divertor baffling on W leakage from the divertor as well, but this is largely outside the scope of this study.

### 9.2.3 Carbon-induced erosion, deposition, and mixed-material layer formation

A central part of this work is that the presence of C strongly modulates erosion. Without the presence of C, we would expect virtually no inter-ELM W erosion due to D $E_i$ residing below the W sputtering threshold. Additionally, just a 3% C ion flux results in about half of the intra-ELM W erosion from the plasma shots studied here. Although, C deposition helps reduce gross W erosion by shielding the W from incoming ions, regardless of the ELM regime. It is postulated that C deposition accumulates between ELMs due to significantly reduced $Y_C$ at lower $E_i$ relative to intra-ELM conditions. Such phenomena would help explain SAS-VW intra-ELM W erosion overprediction but is not entirely understood. EDS analyses from the SAS-VW tiles showed that

C deposition layers can reach thicknesses on the scale of 1–10 μm, more than sufficient to inhibit W divertor erosion. Importantly, C not only deposits on the W divertor surface, but will embed several nanometers below the surface as well. Thus, this would effectively reduce W erosion even if C was not necessarily on top of the W surface. We find that the current steady-state C/W mixed-material model provides a good quick proxy to more accurately determine inter- and intra-ELM W erosion. It would be advantageous to incorporate C redeposition effects into the C/W mixed material model, but the local redeposition of low-Z impurities is tricky by nature. While the vast majority of W is expected to redeposit on the divertor (though impacted by plasma parameters, shaping, and divertor geometry and outside the scope of this study), C eroded from the divertor has a much longer ionization path than W and comparatively less C is expected to redeposit locally. Several past studies have estimated that anywhere from 10-40% of gross C erosion from the DIII-D Divertor Material Exposure Stage (DiMES), based on ERO and SOLPS-ITER simulations, is expected to redeposit within 2-10 cm from the eroded location, a scale relevant to the MRC and SAS-VW divertors [41]. This quantity is non-negligible and contributes to increased C deposition and reduced W erosion. Notably, the OSP position from the SAS-VW plasma discharges studied here have considerably more surface area within proximity than the MRC shelf plasma discharges. Logically, this would greatly increase the local C redeposition, but it is difficult to quantify specifics to include for a redeposition term in the steady-state C/W mixed material model since it relies on nearby geometries. Likewise, a hotter, denser plasma would lead to quicker C ionization with less distance traveled, resulting in increased local C deposition. A more detailed analysis is required, which may be computationally time-consuming and expensive. Additionally, it is important to understand the C ion charge state distribution when comparing spectroscopically measured C quantities to predicted amounts. For example, the

SAS-VW CIII filterscopes only measure $C^{2+}$ ions and higher charge states (because C will have to ionize twice to transition into $C^{2+}$ before ionizing to higher charge states such that $C^{3+}$ and higher charge states are captured). Thus, $C^0$ and $C^{1+}$ charge states are not measured by the CIII filterscopes. Instead, they are estimated using OEDGE calculations and we approximate that around 20% of the C flux incident to the divertor is not captured due to $C^{1+}$ flux, and we incorporate this increased C concentration fudge factor into our analysis [45]. Although, C eroding from across the V-shape slot may contribute more $C^0$ and $C^{1+}$ unaccounted for. CIII filterscopes viewing the graphite surface across the V-shaped slot in conjunction with the LPs installed there could have theoretically provided this additional C sourcing information. Evidently, plasma parameters such as $T_e$, $n_e$, and $f_c$ at the pedestal and divertor result in large differences for ELM regime W sputtering and C deposition. These observations reveal that the mixed-material correction must evolve beyond a simple near-surface steady-state model. It is imperative to compare more complex simulations to experimentally measured data to unravel complex particle physics interactions, but computationally expensive.

### 9.2.4 Heat flux measurements and implications for melting risk

Through SETC and IR camera comparisons, this work aligned heat-flux measurements across campaigns and confirmed: Peak intra-ELM heat flux monotonically decreases with $D_2$ mass injection, consistent with reduced ELM size. SAS-VW heat flux measurements, though broadened by instrument response, exhibit a clear reduction in peak transients relative to the open-divertor MRC configuration. The relevance of ELM-induced heat flux mitigation strategies will depend on the future operating scenario. With the substantial startup and operating costs associated with fusion devices, energy output will need to be maximized to return a profit. Plausibly, this may depend on confinement regimes that operate with ELMy H-mode plasmas.

While grazing magnetic field lines minimize peak heat flux profiles, such acute angles may increase gross and/or net erosion after incorporating effects like surface roughness and ion gyro-orbit effects in addition to plasma parameters.

### 9.2.5 Other sources of uncertainty

Unfortunately, several other sources of error relevant to the work conducted here exist. First, LPs may underpredict $T_{e,div}$ measurements during ELMs. The fast, transient nature of ELMs may have oversaturated the LP current, leading to missing data and underpredicted $T_{e,div}$. Though, significantly increased W and C erosion during ELMs also cools the surrounding $T_{e,div}$ through particle recycling. S/XB coefficients that determine the photon emission rates to atom conversion through ADAS physics are currently under investigation, but this report utilizes the most up to date and published values. Lastly, the ion to electron temperature ratio ($\tau$) is assumed to be equal to 1, but several studies have inconsistently shown otherwise. Thus far, our $T_i$ values are assumed to be equal to the LP $T_e$ measurements. Variations in $\tau$ are not well understood and can have a large effect on determining $E_i$, especially between ELMs as described in Equation 6.3. Moreover, changes to $\tau$ affect $\theta$. For instance, consider the IADs at various $\tau$ values shown in Figure 65. As seen, a reduction of $\tau$ shifts $\theta$ more normal, increasing C deposition and reducing W erosion, which may partially explain SAS-VW intra-ELM W erosion underpredictions [44].

## 9.3 Modeling Insights and Validation

### 9.3.1 FSRM performance and limitations

The FSRM generally captured the qualitative erosion trends with varying $D_2$ injection and pedestal/divertor plasma conditions, but several discrepancies emerged: In the MRC, the uncorrected FSRM overpredicted erosion by ~24% on average. When incorporating the C/W

mixed-material correction, the FSRM underpredicted erosion by ~28%. In SAS-VW conditions, agreement worsened plausibly due to stronger C trapping, altered θ, and modified recycling physics. More robust, full kinetic physics models are continuously under development to more closely analyze these effects.

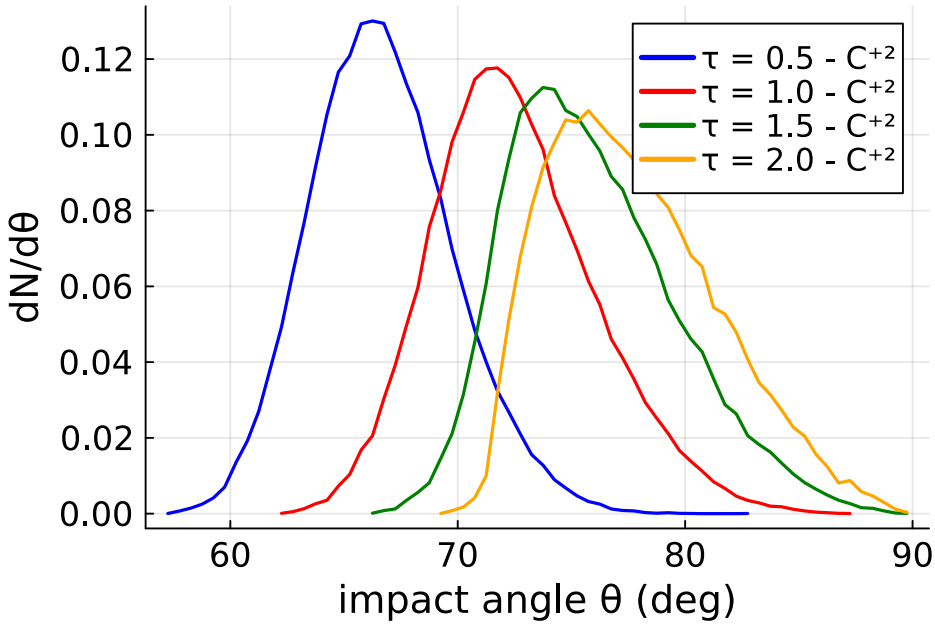



***Figure 65. $C^{2+}$ distribution probability at $T_e$ = 20 eV and $E_C$ = 1 keV as a function of θ for τ = 0.5 (blue), τ = 1.0 (red), τ = 1.5 (green), and τ = 2.0 (orange) determined by LPTMC.***

### 9.3.2 RustBCA contributions

RustBCA simulations were essential for calculating Y and R values used for the steady-state mixed material C/W model during and between ELMs. Though computational software like SDTrim.SP exist and perform similar calculations, RustBCA's open-source system allows for more continuous usage and open community feedback and support. Moreover, RustBCA results have been benchmarked to find good agreement with relevant SDTrim.SP and Eckstein Y and R values. Imperatively, RustBCA simulations show considerably different $Y_W$ for a homogeneous 1:1 C:W surface than pure W $0.5*Y_W$ for a DIII-D relevant intra-ELM combined ion flux of 97% D and 3% C at $\theta = 45°$ with respect to $E_i$. At divertor detachment relevant $E_i$, results show that $Y_W$ is greatly reduced for the homogeneous 1:1 C:W surface compared to the pure W $0.5*Y_W$ (which assumes $\sigma_W = 0.5$). Contrary, $Y_W$ for a homogeneous 1:1 C:W surface is approximately 25% higher than pure W $0.5*Y_W$ at intra-ELM relevant $E_i$. The differences in gross W erosion estimations are substantial for predicting divertor lifetime in a fusion device. It is postulated that implanted C interstitials in the W divertor increase the W sputtering threshold to lower $Y_W$, but at higher $E_i$ C atoms will have sufficient recoil energy to increase W sputtering instead. These accommodations would inherently increase our intra-ELM W erosion predictions but insignificantly alter the inter-ELM W erosion predictions due to strongly attached divertor relevant $E_i$. A larger influence on intra-ELM W erosion predictions is due to the likelihood of C deposition accumulation between ELMs. Although C deposition accumulation may only cover a fraction of the W divertor by the time an ELM strikes, RustBCA simulates a substantial decrease in $Y_W$ with a mere monolayer of C atop the homogenous 1:1 C:W surface. At intra-ELM relevant $E_i$ for this study, 1.5Å of C on top of the W surface reduces $Y_W$ by ~50%. This likely explains the disagreement between FSRM intra-ELM W erosion predictions between the SAS-VW and

the MRC, as the SAS-VW divertor baffling likely increases C deposition relative to the MRC. Unfortunately, CIII filterscopes were not available for the MRC divertor, so those results were inferred with upstream pedestal $f_c$, plausibly a source of error that inhibits closer comparison between the two campaigns. These results support the argument that erosion models used in reactor design must couple binary-collision modeling with surface-composition evolution. RustBCA or other similar models may provide substantial benefit to modelling the next generation of fusion test reactors like SPARC or ITER. Computations must consider many aspects, including but not limited to mixed material and ion concentrations, $\theta$, $E_i$, and surface and BBE.

### 9.3.3 Predictive limits of current erosion models

FSRM-style models are attractive for their speed, but this dissertation shows they require substantial refinement to remain relevant for reactor design. Key missing pieces include time-dependent mixed-material evolution, coupled sheath-edge kinetic modeling, explicit IADs tied to magnetic geometry, divertor-specific neutral trapping physics in closed configurations, and self-consistent recycling particle energy distributions. Thus, next-generation erosion models must integrate binary-collision physics (RustBCA, SDTrim.SP), gyrokinetic-informed ion distributions, geometry (PFC shaping, tile leading edges), impurity transport, and deposition codes (ERO, DIVIMP).

## 9.4 Future Work

Based on the findings of this dissertation, several paths for strengthening erosion prediction capability are recommended. Enhanced C/W mixed-material models that include time evolution, layer thickness effects, and multi-ion implantation profiles are key. Full integration of

RustBCA-based Y and R values across $T_{e,div}$-dependent energy distributions will enhance W sputtering predictabilities in addition to improved measurements of $\theta$ and $E_i$ distributions using fast-framing spectroscopy or synthetic diagnostics. The use of ERO for cross-validation of mixed-material surface evolution during and between ELMs is missing and must be coupled with FSRM with SOLPS-ITER or UEDGE simulations to produce self-consistent divertor boundary conditions. Expansion to reactor-relevant transients, including larger Type-I ELMs and ELM-free regimes. Lastly, the associated modelling and experimental validation should substitute C with other more relevant future fusion impurities like boron, lithium, or beryllium for a multitude of benefits outside the scope of this thesis.

## 9.5 Final Remarks

The path to commercial fusion energy depends critically on understanding and ultimately controlling divertor material response to high-power plasmas. This dissertation contributes a clarified physics basis for mixed-material tungsten erosion, validated across two distinct geometric divertor configurations. Through combined experimental insight and modeling development, the work strengthens the predictive foundation required to design durable PFCs for next-step tokamaks.

The overarching message of this research is that mixed-material physics, impurity deposition, and ELM-resolved ion–surface interactions cannot be overlooked. Ensuring future divertors survive decades of operation requires the integrated, multi-physics modeling approach demonstrated herein. This work provides essential steps toward that goal and establishes a framework for continued progress as fusion devices move toward ignition and sustained power production.

# References


1. Clifford, C.C.a.H. *World electricity generation since 1900*. 2023; Available from: https://visualizingenergy.org/world-electricity-generation-since-1900/.
2. Mueller, M. *Nuclear Power is the Most Reliable Energy Source and It's Not Even Close*. 2021; Available from: https://www.energy.gov/ne/articles/nuclear-power-most-reliable-energy-source-and-its-not-even-close.
3. Lanctot, M. *DOE Explains...Tokamaks*. Available from: https://www.energy.gov/science/doe-explainstokamaks.
4. Stacey, W., *Fusion Plasma Physics.* 2005.
5. Drobny, J. and D. Curreli, *RustBCA: A High-Performance Binary-Collision-Approximation Code for Ion-Material Interactions.* Journal of open source software, 2021. **6**(64): p. 3298.
6. Wirth, B., *Fusion materials modeling: Challenges and opportunities.* MRS Bulletin, 2011. **36**(3): p. 216-222.
7. Abrams, T., et al., *Advances in Low-Temperature Tungsten Spectroscopy Capability to Quantify DIII-D Divertor Erosion.* IEEE transactions on plasma science, 2018. **46**(5): p. 1298-1305.
8. Abrams, T., et al., *Impact of ELM control techniques on tungsten sputtering in the DIII-D divertor and extrapolations to ITER.* Physics of plasmas, 2019. **26**(6): p. 062504.
9. Abrams, T., et al., *Experimental validation of a model for particle recycling and tungsten erosion during ELMs in the DIII-D divertor.* Nuclear Materials and Energy, 2018. **17**: p. 164-173.

10. Xu, G.L., et al., *Study of DIII-D tungsten erosion processes by using a carbon–tungsten mixed material model.* Nuclear materials and energy, 2019. **18**(C): p. 141-146.

11. Baylor, L.R., et al., *Reduction of edge localized mode intensity on DIII-D by on-demand triggering with high frequency pellet injection and implications for ITERa).* Physics of Plasmas, 2013. **20**(8): p. 082513.

12. Wilcox, R.S., et al., *Pellet triggering of edge localized modes in low collisionality pedestals at DIII-D.* Nuclear fusion, 2021. **62**(2): p. 26017.

13. Abrams, T., et al., *Design and physics basis for the upcoming DIII-D SAS-VW campaign to quantify tungsten leakage and transport in a new slot divertor geometry*. Physica scripta, 2021. **96**(12): p. 124073.

14. Moser, A.L., et al., *Separating divertor closure effects on divertor detachment and pedestal shape in DIII-D.* Physics of plasmas, 2020. **27**(3): p. 032506.

15. Moser, A.L., et al., *The effect of divertor closure on detachment onset in DIII-D.* Nuclear Materials and Energy, 2019. **19**: p. 67-71.

16. Si, H., et al., *Modeling of combined effects of divertor closure and advanced magnetic configuration on detachment in DIII-D by SOLPS.* 2018. **58**.

17. Easley, D.C., et al., *Dependence of high-Z redeposition on the field-to-surface pitch angle and other sheath parameters in tokamaks.* Physics of plasmas, 2024. **31**(5).

18. Stangeby, P.C., *The Chodura sheath for angles of a few degrees between the magnetic field and the surface of divertor targets and limiters.* Nuclear Fusion, 2012. **52**(8): p. 083012.

19. Moulton, D., et al., *Quasineutral plasma expansion into infinite vacuum as a model for parallel ELM transport.* Plasma physics and controlled fusion, 2013. **55**(8): p. 85003-21.

20. Fundamenski, W., R.A. Pitts, and J.E. contributors, *A model of ELM filament energy evolution due to parallel losses.* Plasma Physics and Controlled Fusion, 2006. **48**(1): p. 109.

21. Ding, R., et al., *Simulation of gross and net erosion of high-Z materials in the DIII-D divertor.* Nuclear Fusion, 2016. **56**(1): p. 016021.

22. Abrams, T., et al., *Evaluation of silicon carbide as a divertor armor material in DIII-D H-mode discharges.* Nuclear Fusion, 2021. **61**(6): p. 066005.

23. Chrystal, C., et al., *Improved edge charge exchange recombination spectroscopy in DIII-D.* Review of scientific instruments, 2016. **87**(11): p. 11E512-11E512.

24. Holtrop, K., et al., *The Design and Use of Tungsten Coated TZM Molybdenum Tile Inserts in the DIII-D Tokamak Divertor.* Fusion Science and Technology, 2017. **72**(4): p. 634-639.

25. Watkins, J.G., et al., *High heat flux Langmuir probe array for the DIII-D divertor plates.* Review of scientific instruments, 2008. **79**(10): p. 10F125-10F125-4.

26. *ADAS: Atomic Data and Analysis Structure*. Available from: https://open.adas.ac.uk/.

27. Cacheris, A., et al., *The effectiveness of D2 pellet injection in reducing intra-ELM and inter-ELM tungsten divertor erosion rates in DIII-D during the Metal Rings Campaign.* Plasma Physics and Controlled Fusion, 2023. **65**(8): p. 085010.

28. Adamek, J., et al., *Temporal characteristics of ELMs on the COMPASS divertor.* Nuclear fusion, 2023. **63**(8): p. 86009.

29. Ren, J., et al., *Development of Surface Eroding Thermocouples in Small Angle Slot Divertor in DIII-D.* IEEE transactions on plasma science, 2020. **48**(6): p. 1804-1809.

30. Ren, J., et al., *The surface eroding thermocouple for fast heat flux measurement in DIII-D.* Review of scientific instruments, 2018. **89**(10): p. 10J122-10J122.

31. Ren, J., et al., *Measurements of multiple heat flux components at the divertor target by using surface eroding thermocouples (invited).* Review of scientific instruments, 2022. **93**(10): p. 103541-103541.

32. Herfindal, J.L., et al., *Calibration improvements expand filterscope diagnostic use.* Review of scientific instruments, 2024. **95**(2).

33. Gouge, M.J., S.K. Combs, and S.L. Milora, *A combined microwave cavity and photographic diagnostic for high-speed projectiles.* Review of scientific instruments, 1990. **61**(8): p. 2102-2105.

34. Unterberg, E.A., et al., *Localized divertor leakage measurements using isotopic tungsten sources during edge-localized mode-y H-mode discharges on DIII-D.* Nuclear fusion, 2019. **60**(1): p. 16028.

35. Eich, T., et al., *Type-I ELM power deposition profile width and temporal shape in JET.* Journal of nuclear materials, 2011. **415**(1): p. S856-S859.

36. Jakubowski, M.W., et al., *Overview of the results on divertor heat loads in RMP controlled H-mode plasmas on DIII-D.* Nuclear fusion, 2009. **49**(9): p. 095013.

37. Schmid, K., et al., *Impact of gyro-motion and sheath acceleration on the flux distribution on rough surfaces.* Nuclear Fusion, 2010. **50**(10): p. 105004.

38. Zhao, B., et al., *Novel data interpretation method for DIII-D divertor retarding field energy analyzer with 3-D particle-in-cell simulations.* Review of scientific instruments, 2024. **95**(7).

39. Abe, S., et al., *Computational investigation of incident ion angles and material erosion at rough graphite and silicon carbide divertor surfaces.* Physics of plasmas, 2022. **29**(10).

40. Guillemaut, C., et al., *Experimental estimation of tungsten impurity sputtering due to Type I ELMs in JET-ITER-like wall using pedestal electron cyclotron emission and target Langmuir probe measurements.* Physica Scripta, 2016. **2016**(T167): p. 014005.

41. Guterl, J., et al., *Dynamic control of low-Z material deposition and tungsten erosion by strike point sweeping on DIII-D.* Nuclear Materials and Energy, 2017. **12**: p. 392-398.

42. Hua, T.Q. and J.N. Brooks, *Erosion/redeposition analysis of the DIII-D divertor.* Journal of nuclear materials, 1995. **220**(1-3): p. 342-346.

43. Nichols, J.H., M.A. Jaworski, and K. Schmid, *Sensitivity of WallDYN material migration modeling to uncertainties in mixed-material surface binding energies.* Nuclear materials and energy, 2017. **12**: p. 513-517.

44. Brooks, J.N., et al., *Tungsten–carbon surface evolution and erosion modeling for a small angle slot divertor in DIII-D.* Nuclear fusion, 2021. **61**(12): p. 126071.

45. Abrams, T., et al., *The inter-ELM tungsten erosion profile in DIII-D H-mode discharges and benchmarking with ERO+OEDGE modeling.* Nuclear Fusion, 2017. **57**(5): p. 056034.

# Appendix

## A C/W steady-state mixed material model revision for C redeposition

Adjust the $\sigma_C$ calculation by incorporating C redeposition factors *Z* and *A*. *Z* represents a fractional increase in C striking the divertor due to redeposition of C ions that initially impact the divertor. *A* represents the fractional decrease in C erosion from the mixed material interaction layer due to redeposition of eroded C back onto the divertor. For example, *Z* = 1.1 equates to 10% of initially incident C ions restriking the divertor and Equation A.1 expresses *A*:

$$A = [1 - X * (1 - R_C)] \quad \text{A.1}$$

*X* represents the fraction of eroding C atoms that restrike the divertor and $R_C$ is necessary to calculate the probabity if they reflect off the divertor surface or not. Likewise, Equations 4.5, 4.9, and 4.11 are refined as Equations A.2, A.3, and A.4, respectively.

$$Y_{C,tot} = \Gamma_D \sigma_C (Z * f_C Y_{C\to C} + (Y_{D\to C} + X_{D\to C})) \quad \text{A.2}$$

$$Z * f_C \Gamma_D = \mathrm{A} * \Gamma_{C,out,tot} \quad \text{A.3}$$

$$\sigma_C = \frac{Z * f_C (1 - R_{C\to W})}{A * [(Y_{D\to C} + X_{D\to C}) + Z * Y_{C\to C} f_c + R_{C\to C} f_c - R_{C\to W} f_c]} \quad \text{A.4}$$

## B RustBCA Python Y & R Computational Setup for C/W Mixed Material

```
Cd RustBCA
Py
from libRustBCA import *; from scripts.materials import *
from scripts.materials import *
carbon['Z'] = 6.0 #Change Z from integer to floating point number
import sys
```

```
import numpy as np

np.set_printoptions(linewidth=np.inf)

np.set_printoptions(threshold=sys.maxsize)

angle = 45.0 # deg

carbon['Eb'] = 0.0

number_ions=1000000

import time

target = tungsten

ion1 = deuterium

carbon2 = carbon.copy()

carbon2['Z'] = carbon['Z'] + 1e-6

ion2 = carbon2

Z1 = [ion1["Z"]]*(number_ions*97//100) + [ion2["Z"]]*(number_ions*3//100)

m1 = [ion1["m"]]*(number_ions*97//100) + [ion2["m"]]*(number_ions*3//100)

Ec1 = [ion1["Ec"]]*(number_ions*97//100) + [ion2["Ec"]]*(number_ions*3//100)

Es1 = [ion1["Es"]]*(number_ions*97//100) + [ion2["Es"]]*(number_ions*3//100)

energies_eV = 25.0*np.ones(number_ions)

ux = np.cos(angle*np.pi/180.)*np.ones(number_ions)

uy = np.sin(angle*np.pi/180.)*np.ones(number_ions)

uz = np.zeros(number_ions)

output, incident, stopped = compound_bca_list_1D_py(ux, uy, uz, energies_eV, Z1, m1, Ec1, Es1,
[target['Z'], 6.0], [target['m'], 12.011], [target['Ec'], 1.0], [target['Es'], 7.37], [target['Eb'], 0.0], [[0.066142,
0.066142]], [1000.0])

output = np.array(output)

content = str(output)

file = open("C_W.txt", "w+")

file.write(content)

Z = output[:, 0]

m = output[:, 1]
```

```
E = output[:, 2]
x = output[:, 3]
y = output[:, 4]
z = output[:, 5]
ux = output[:, 6]
uy = output[:, 7]
uz = output[:, 8]
sputtered_W = output[np.logical_and(Z == target['Z'], E > 0), :]
sputtered_C = output[np.logical_and(Z == 6.0, E > 0), :]
reflected = output[np.logical_and(Z == 6.0, x < 0), :]
implanted = output[np.logical_and(Z == 6.0, x > 0), :]
num_reflected = np.shape(reflected)[0]
energy_reflected = np.sum(reflected[:, 2])
num_reflected/number_ions
energy_reflected/number_ions
num_sputtered_W = np.shape(sputtered_W)[0]
energy_sputtered_W = np.sum(sputtered_W[:, 2])
num_sputtered_W/number_ions
energy_sputtered_W/number_ions
num_sputtered_C = np.shape(sputtered_C)[0]
energy_sputtered_C = np.sum(sputtered_C[:, 2])
num_sputtered_C/number_ions
energy_sputtered_C/number_ions
num_implanted = np.shape(implanted)[0]
energy_implanted = np.sum(implanted[:, 2])
num_implanted/number_ions
energy_implanted/number_ions
energies_eV = 50.0*np.ones(number_ions)
ux = np.cos(angle*np.pi/180.)*np.ones(number_ions)
```

```
uy = np.sin(angle*np.pi/180.)*np.ones(number_ions)

uz = np.zeros(number_ions)

output, incident, stopped = compound_bca_list_1D_py(ux, uy, uz, energies_eV, Z1, m1, Ec1, Es1,
[target['Z'], 6.0], [target['m'], 12.011], [target['Ec'], 1.0], [target['Es'], 7.37], [target['Eb'], 0.0], [[0.066142,
0.066142]], [1000.0])

output = np.array(output)

content = str(output)

file = open("C_W.txt", "w+")

file.write(content)

Z = output[:, 0]

m = output[:, 1]

E = output[:, 2]

x = output[:, 3]

y = output[:, 4]

z = output[:, 5]

ux = output[:, 6]

uy = output[:, 7]

uz = output[:, 8]

sputtered_W = output[np.logical_and(Z == target['Z'], E > 0), :]

sputtered_C = output[np.logical_and(Z == 6.0, E > 0), :]

reflected = output[np.logical_and(Z == 6.0, x < 0), :]

implanted = output[np.logical_and(Z == 6.0, x > 0), :]

num_reflected = np.shape(reflected)[0]

energy_reflected = np.sum(reflected[:, 2])

num_reflected/number_ions

energy_reflected/number_ions

num_sputtered_W = np.shape(sputtered_W)[0]

energy_sputtered_W = np.sum(sputtered_W[:, 2])

num_sputtered_W/number_ions
```

```
energy_sputtered_W/number_ions

num_sputtered_C = np.shape(sputtered_C)[0]

energy_sputtered_C = np.sum(sputtered_C[:, 2])

num_sputtered_C/number_ions

energy_sputtered_C/number_ions

num_implanted = np.shape(implanted)[0]

energy_implanted = np.sum(implanted[:, 2])

num_implanted/number_ions

energy_implanted/number_ions

energies_eV = 100.0*np.ones(number_ions)

ux = np.cos(angle*np.pi/180.)*np.ones(number_ions)

uy = np.sin(angle*np.pi/180.)*np.ones(number_ions)

uz = np.zeros(number_ions)

output, incident, stopped = compound_bca_list_1D_py(ux, uy, uz, energies_eV, Z1, m1, Ec1, Es1,
[target['Z'], 6.0], [target['m'], 12.011], [target['Ec'], 1.0], [target['Es'], 7.37], [target['Eb'], 0.0], [[0.066142,
0.066142]], [1000.0])

output = np.array(output)

content = str(output)

file = open("C_W.txt", "w+")

file.write(content)

Z = output[:, 0]

m = output[:, 1]

E = output[:, 2]

x = output[:, 3]

y = output[:, 4]

z = output[:, 5]

ux = output[:, 6]

uy = output[:, 7]

uz = output[:, 8]
```

```
sputtered_W = output[np.logical_and(Z == target['Z'], E > 0), :]

sputtered_C = output[np.logical_and(Z == 6.0, E > 0), :]

reflected = output[np.logical_and(Z == 6.0, x < 0), :]

implanted = output[np.logical_and(Z == 6.0, x > 0), :]

num_reflected = np.shape(reflected)[0]

energy_reflected = np.sum(reflected[:, 2])

num_reflected/number_ions

energy_reflected/number_ions

num_sputtered_W = np.shape(sputtered_W)[0]

energy_sputtered_W = np.sum(sputtered_W[:, 2])

num_sputtered_W/number_ions

energy_sputtered_W/number_ions

num_sputtered_C = np.shape(sputtered_C)[0]

energy_sputtered_C = np.sum(sputtered_C[:, 2])

num_sputtered_C/number_ions

energy_sputtered_C/number_ions

num_implanted = np.shape(implanted)[0]

energy_implanted = np.sum(implanted[:, 2])

num_implanted/number_ions

energy_implanted/number_ions

energies_eV = 200.0*np.ones(number_ions)

ux = np.cos(angle*np.pi/180.)*np.ones(number_ions)

uy = np.sin(angle*np.pi/180.)*np.ones(number_ions)

uz = np.zeros(number_ions)

output, incident, stopped = compound_bca_list_1D_py(ux, uy, uz, energies_eV, Z1, m1, Ec1, Es1,
[target['Z'], 6.0], [target['m'], 12.011], [target['Ec'], 1.0], [target['Es'], 7.37], [target['Eb'], 0.0], [[0.066142,
0.066142]], [1000.0])

output = np.array(output)

content = str(output)
```

```
file = open("C_W.txt", "w+")
file.write(content)
Z = output[:, 0]
m = output[:, 1]
E = output[:, 2]
x = output[:, 3]
y = output[:, 4]
z = output[:, 5]
ux = output[:, 6]
uy = output[:, 7]
uz = output[:, 8]
sputtered_W = output[np.logical_and(Z == target['Z'], E > 0), :]
sputtered_C = output[np.logical_and(Z == 6.0, E > 0), :]
reflected = output[np.logical_and(Z == 6.0, x < 0), :]
implanted = output[np.logical_and(Z == 6.0, x > 0), :]
num_reflected = np.shape(reflected)[0]
energy_reflected = np.sum(reflected[:, 2])
num_reflected/number_ions
energy_reflected/number_ions
num_sputtered_W = np.shape(sputtered_W)[0]
energy_sputtered_W = np.sum(sputtered_W[:, 2])
num_sputtered_W/number_ions
energy_sputtered_W/number_ions
num_sputtered_C = np.shape(sputtered_C)[0]
energy_sputtered_C = np.sum(sputtered_C[:, 2])
num_sputtered_C/number_ions
energy_sputtered_C/number_ions
num_implanted = np.shape(implanted)[0]
energy_implanted = np.sum(implanted[:, 2])
```

```
num_implanted/number_ions

energy_implanted/number_ions

energies_eV = 300.0*np.ones(number_ions)

ux = np.cos(angle*np.pi/180.)*np.ones(number_ions)

uy = np.sin(angle*np.pi/180.)*np.ones(number_ions)

uz = np.zeros(number_ions)

output, incident, stopped = compound_bca_list_1D_py(ux, uy, uz, energies_eV, Z1, m1, Ec1, Es1,
[target['Z'], 6.0], [target['m'], 12.011], [target['Ec'], 1.0], [target['Es'], 7.37], [target['Eb'], 0.0], [[0.066142,
0.066142]], [1000.0])

output = np.array(output)

content = str(output)

file = open("C_W.txt", "w+")

file.write(content)

Z = output[:, 0]

m = output[:, 1]

E = output[:, 2]

x = output[:, 3]

y = output[:, 4]

z = output[:, 5]

ux = output[:, 6]

uy = output[:, 7]

uz = output[:, 8]

sputtered_W = output[np.logical_and(Z == target['Z'], E > 0), :]

sputtered_C = output[np.logical_and(Z == 6.0, E > 0), :]

reflected = output[np.logical_and(Z == 6.0, x < 0), :]

implanted = output[np.logical_and(Z == 6.0, x > 0), :]

num_reflected = np.shape(reflected)[0]

energy_reflected = np.sum(reflected[:, 2])

num_reflected/number_ions
```

```
energy_reflected/number_ions

num_sputtered_W = np.shape(sputtered_W)[0]

energy_sputtered_W = np.sum(sputtered_W[:, 2])

num_sputtered_W/number_ions

energy_sputtered_W/number_ions

num_sputtered_C = np.shape(sputtered_C)[0]

energy_sputtered_C = np.sum(sputtered_C[:, 2])

num_sputtered_C/number_ions

energy_sputtered_C/number_ions

num_implanted = np.shape(implanted)[0]

energy_implanted = np.sum(implanted[:, 2])

num_implanted/number_ions

energy_implanted/number_ions

energies_eV = 400.0*np.ones(number_ions)

ux = np.cos(angle*np.pi/180.)*np.ones(number_ions)

uy = np.sin(angle*np.pi/180.)*np.ones(number_ions)

uz = np.zeros(number_ions)

output, incident, stopped = compound_bca_list_1D_py(ux, uy, uz, energies_eV, Z1, m1, Ec1, Es1,
[target['Z'], 6.0], [target['m'], 12.011], [target['Ec'], 1.0], [target['Es'], 7.37], [target['Eb'], 0.0], [[0.066142,
0.066142]], [1000.0])

output = np.array(output)

content = str(output)

file = open("C_W.txt", "w+")

file.write(content)

Z = output[:, 0]

m = output[:, 1]

E = output[:, 2]

x = output[:, 3]

y = output[:, 4]
```

```
z = output[:, 5]
ux = output[:, 6]
uy = output[:, 7]
uz = output[:, 8]
sputtered_W = output[np.logical_and(Z == target['Z'], E > 0), :]
sputtered_C = output[np.logical_and(Z == 6.0, E > 0), :]
reflected = output[np.logical_and(Z == 6.0, x < 0), :]
implanted = output[np.logical_and(Z == 6.0, x > 0), :]
num_reflected = np.shape(reflected)[0]
energy_reflected = np.sum(reflected[:, 2])
num_reflected/number_ions
energy_reflected/number_ions
num_sputtered_W = np.shape(sputtered_W)[0]
energy_sputtered_W = np.sum(sputtered_W[:, 2])
num_sputtered_W/number_ions
energy_sputtered_W/number_ions
num_sputtered_C = np.shape(sputtered_C)[0]
energy_sputtered_C = np.sum(sputtered_C[:, 2])
num_sputtered_C/number_ions
energy_sputtered_C/number_ions
num_implanted = np.shape(implanted)[0]
energy_implanted = np.sum(implanted[:, 2])
num_implanted/number_ions
energy_implanted/number_ions
energies_eV = 500.0*np.ones(number_ions)
ux = np.cos(angle*np.pi/180.)*np.ones(number_ions)
uy = np.sin(angle*np.pi/180.)*np.ones(number_ions)
uz = np.zeros(number_ions)
```

```
output, incident, stopped = compound_bca_list_1D_py(ux, uy, uz, energies_eV, Z1, m1, Ec1, Es1, [target['Z'], 6.0], [target['m'], 12.011], [target['Ec'], 1.0], [target['Es'], 7.37], [target['Eb'], 0.0], [[0.066142, 0.066142]], [1000.0])

output = np.array(output)

content = str(output)

file = open("C_W.txt", "w+")

file.write(content)

Z = output[:, 0]

m = output[:, 1]

E = output[:, 2]

x = output[:, 3]

y = output[:, 4]

z = output[:, 5]

ux = output[:, 6]

uy = output[:, 7]

uz = output[:, 8]

sputtered_W = output[np.logical_and(Z == target['Z'], E > 0), :]

sputtered_C = output[np.logical_and(Z == 6.0, E > 0), :]

reflected = output[np.logical_and(Z == 6.0, x < 0), :]

implanted = output[np.logical_and(Z == 6.0, x > 0), :]

num_reflected = np.shape(reflected)[0]

energy_reflected = np.sum(reflected[:, 2])

num_reflected/number_ions

energy_reflected/number_ions

num_sputtered_W = np.shape(sputtered_W)[0]

energy_sputtered_W = np.sum(sputtered_W[:, 2])

num_sputtered_W/number_ions

energy_sputtered_W/number_ions

num_sputtered_C = np.shape(sputtered_C)[0]
```

```
energy_sputtered_C = np.sum(sputtered_C[:, 2])

num_sputtered_C/number_ions

energy_sputtered_C/number_ions

num_implanted = np.shape(implanted)[0]

energy_implanted = np.sum(implanted[:, 2])

num_implanted/number_ions

energy_implanted/number_ions

energies_eV = 600.0*np.ones(number_ions)

ux = np.cos(angle*np.pi/180.)*np.ones(number_ions)

uy = np.sin(angle*np.pi/180.)*np.ones(number_ions)

uz = np.zeros(number_ions)

output, incident, stopped = compound_bca_list_1D_py(ux, uy, uz, energies_eV, Z1, m1, Ec1, Es1,
[target['Z'], 6.0], [target['m'], 12.011], [target['Ec'], 1.0], [target['Es'], 7.37], [target['Eb'], 0.0], [[0.066142,
0.066142]], [1000.0])

output = np.array(output)

content = str(output)

file = open("C_W.txt", "w+")

file.write(content)

Z = output[:, 0]

m = output[:, 1]

E = output[:, 2]

x = output[:, 3]

y = output[:, 4]

z = output[:, 5]

ux = output[:, 6]

uy = output[:, 7]

uz = output[:, 8]

sputtered_W = output[np.logical_and(Z == target['Z'], E > 0), :]

sputtered_C = output[np.logical_and(Z == 6.0, E > 0), :]
```

```
reflected = output[np.logical_and(Z == 6.0, x < 0), :]

implanted = output[np.logical_and(Z == 6.0, x > 0), :]

num_reflected = np.shape(reflected)[0]

energy_reflected = np.sum(reflected[:, 2])

num_reflected/number_ions

energy_reflected/number_ions

num_sputtered_W = np.shape(sputtered_W)[0]

energy_sputtered_W = np.sum(sputtered_W[:, 2])

num_sputtered_W/number_ions

energy_sputtered_W/number_ions

num_sputtered_C = np.shape(sputtered_C)[0]

energy_sputtered_C = np.sum(sputtered_C[:, 2])

num_sputtered_C/number_ions

energy_sputtered_C/number_ions

num_implanted = np.shape(implanted)[0]

energy_implanted = np.sum(implanted[:, 2])

num_implanted/number_ions

energy_implanted/number_ions

energies_eV = 700.0*np.ones(number_ions)

ux = np.cos(angle*np.pi/180.)*np.ones(number_ions)

uy = np.sin(angle*np.pi/180.)*np.ones(number_ions)

uz = np.zeros(number_ions)

output, incident, stopped = compound_bca_list_1D_py(ux, uy, uz, energies_eV, Z1, m1, Ec1, Es1,
[target['Z'], 6.0], [target['m'], 12.011], [target['Ec'], 1.0], [target['Es'], 7.37], [target['Eb'], 0.0], [[0.066142,
0.066142]], [1000.0])

output = np.array(output)

content = str(output)

file = open("C_W.txt", "w+")

file.write(content)
```

```
Z = output[:, 0]
m = output[:, 1]
E = output[:, 2]
x = output[:, 3]
y = output[:, 4]
z = output[:, 5]
ux = output[:, 6]
uy = output[:, 7]
uz = output[:, 8]
sputtered_W = output[np.logical_and(Z == target['Z'], E > 0), :]
sputtered_C = output[np.logical_and(Z == 6.0, E > 0), :]
reflected = output[np.logical_and(Z == 6.0, x < 0), :]
implanted = output[np.logical_and(Z == 6.0, x > 0), :]
num_reflected = np.shape(reflected)[0]
energy_reflected = np.sum(reflected[:, 2])
num_reflected/number_ions
energy_reflected/number_ions
num_sputtered_W = np.shape(sputtered_W)[0]
energy_sputtered_W = np.sum(sputtered_W[:, 2])
num_sputtered_W/number_ions
energy_sputtered_W/number_ions
num_sputtered_C = np.shape(sputtered_C)[0]
energy_sputtered_C = np.sum(sputtered_C[:, 2])
num_sputtered_C/number_ions
energy_sputtered_C/number_ions
num_implanted = np.shape(implanted)[0]
energy_implanted = np.sum(implanted[:, 2])
num_implanted/number_ions
energy_implanted/number_ions
```

```
energies_eV = 800.0*np.ones(number_ions)

ux = np.cos(angle*np.pi/180.)*np.ones(number_ions)

uy = np.sin(angle*np.pi/180.)*np.ones(number_ions)

uz = np.zeros(number_ions)

output, incident, stopped = compound_bca_list_1D_py(ux, uy, uz, energies_eV, Z1, m1, Ec1, Es1,
[target['Z'], 6.0], [target['m'], 12.011], [target['Ec'], 1.0], [target['Es'], 7.37], [target['Eb'], 0.0], [[0.066142,
0.066142]], [1000.0])

output = np.array(output)

content = str(output)

file = open("C_W.txt", "w+")

file.write(content)

Z = output[:, 0]

m = output[:, 1]

E = output[:, 2]

x = output[:, 3]

y = output[:, 4]

z = output[:, 5]

ux = output[:, 6]

uy = output[:, 7]

uz = output[:, 8]

sputtered_W = output[np.logical_and(Z == target['Z'], E > 0), :]

sputtered_C = output[np.logical_and(Z == 6.0, E > 0), :]

reflected = output[np.logical_and(Z == 6.0, x < 0), :]

implanted = output[np.logical_and(Z == 6.0, x > 0), :]

num_reflected = np.shape(reflected)[0]

energy_reflected = np.sum(reflected[:, 2])

num_reflected/number_ions

energy_reflected/number_ions

num_sputtered_W = np.shape(sputtered_W)[0]
```

```
energy_sputtered_W = np.sum(sputtered_W[:, 2])

num_sputtered_W/number_ions

energy_sputtered_W/number_ions

num_sputtered_C = np.shape(sputtered_C)[0]

energy_sputtered_C = np.sum(sputtered_C[:, 2])

num_sputtered_C/number_ions

energy_sputtered_C/number_ions

num_implanted = np.shape(implanted)[0]

energy_implanted = np.sum(implanted[:, 2])

num_implanted/number_ions

energy_implanted/number_ions

energies_eV = 900.0*np.ones(number_ions)

ux = np.cos(angle*np.pi/180.)*np.ones(number_ions)

uy = np.sin(angle*np.pi/180.)*np.ones(number_ions)

uz = np.zeros(number_ions)

output, incident, stopped = compound_bca_list_1D_py(ux, uy, uz, energies_eV, Z1, m1, Ec1, Es1,
[target['Z'], 6.0], [target['m'], 12.011], [target['Ec'], 1.0], [target['Es'], 7.37], [target['Eb'], 0.0], [[0.066142,
0.066142]], [1000.0])

output = np.array(output)

content = str(output)

file = open("C_W.txt", "w+")

file.write(content)

Z = output[:, 0]

m = output[:, 1]

E = output[:, 2]

x = output[:, 3]

y = output[:, 4]

z = output[:, 5]

ux = output[:, 6]
```

```
uy = output[:, 7]

uz = output[:, 8]

sputtered_W = output[np.logical_and(Z == target['Z'], E > 0), :]

sputtered_C = output[np.logical_and(Z == 6.0, E > 0), :]

reflected = output[np.logical_and(Z == 6.0, x < 0), :]

implanted = output[np.logical_and(Z == 6.0, x > 0), :]

num_reflected = np.shape(reflected)[0]

energy_reflected = np.sum(reflected[:, 2])

num_reflected/number_ions

energy_reflected/number_ions

num_sputtered_W = np.shape(sputtered_W)[0]

energy_sputtered_W = np.sum(sputtered_W[:, 2])

num_sputtered_W/number_ions

energy_sputtered_W/number_ions

num_sputtered_C = np.shape(sputtered_C)[0]

energy_sputtered_C = np.sum(sputtered_C[:, 2])

num_sputtered_C/number_ions

energy_sputtered_C/number_ions

num_implanted = np.shape(implanted)[0]

energy_implanted = np.sum(implanted[:, 2])

num_implanted/number_ions

energy_implanted/number_ions

energies_eV = 1000.0*np.ones(number_ions)

ux = np.cos(angle*np.pi/180.)*np.ones(number_ions)

uy = np.sin(angle*np.pi/180.)*np.ones(number_ions)

uz = np.zeros(number_ions)

output, incident, stopped = compound_bca_list_1D_py(ux, uy, uz, energies_eV, Z1, m1, Ec1, Es1,
[target['Z'], 6.0], [target['m'], 12.011], [target['Ec'], 1.0], [target['Es'], 7.37], [target['Eb'], 0.0], [[0.066142,
0.066142]], [1000.0])
```

```
output = np.array(output)
content = str(output)
file = open("C_W.txt", "w+")
file.write(content)
Z = output[:, 0]
m = output[:, 1]
E = output[:, 2]
x = output[:, 3]
y = output[:, 4]
z = output[:, 5]
ux = output[:, 6]
uy = output[:, 7]
uz = output[:, 8]
sputtered_W = output[np.logical_and(Z == target['Z'], E > 0), :]
sputtered_C = output[np.logical_and(Z == 6.0, E > 0), :]
reflected = output[np.logical_and(Z == 6.0, x < 0), :]
implanted = output[np.logical_and(Z == 6.0, x > 0), :]
num_reflected = np.shape(reflected)[0]
energy_reflected = np.sum(reflected[:, 2])
num_reflected/number_ions
energy_reflected/number_ions
num_sputtered_W = np.shape(sputtered_W)[0]
energy_sputtered_W = np.sum(sputtered_W[:, 2])
num_sputtered_W/number_ions
energy_sputtered_W/number_ions
num_sputtered_C = np.shape(sputtered_C)[0]
energy_sputtered_C = np.sum(sputtered_C[:, 2])
num_sputtered_C/number_ions
energy_sputtered_C/number_ions
```

```
num_implanted = np.shape(implanted)[0]

energy_implanted = np.sum(implanted[:, 2])

num_implanted/number_ions

energy_implanted/number_ions

energies_eV = 1100.0*np.ones(number_ions)

ux = np.cos(angle*np.pi/180.)*np.ones(number_ions)

uy = np.sin(angle*np.pi/180.)*np.ones(number_ions)

uz = np.zeros(number_ions)

output, incident, stopped = compound_bca_list_1D_py(ux, uy, uz, energies_eV, Z1, m1, Ec1, Es1,
[target['Z'], 6.0], [target['m'], 12.011], [target['Ec'], 1.0], [target['Es'], 7.37], [target['Eb'], 0.0], [[0.066142,
0.066142]], [1000.0])

output = np.array(output)

content = str(output)

file = open("C_W.txt", "w+")

file.write(content)

Z = output[:, 0]

m = output[:, 1]

E = output[:, 2]

x = output[:, 3]

y = output[:, 4]

z = output[:, 5]

ux = output[:, 6]

uy = output[:, 7]

uz = output[:, 8]

sputtered_W = output[np.logical_and(Z == target['Z'], E > 0), :]

sputtered_C = output[np.logical_and(Z == 6.0, E > 0), :]

reflected = output[np.logical_and(Z == 6.0, x < 0), :]

implanted = output[np.logical_and(Z == 6.0, x > 0), :]

num_reflected = np.shape(reflected)[0]
```

```
energy_reflected = np.sum(reflected[:, 2])

num_reflected/number_ions

energy_reflected/number_ions

num_sputtered_W = np.shape(sputtered_W)[0]

energy_sputtered_W = np.sum(sputtered_W[:, 2])

num_sputtered_W/number_ions

energy_sputtered_W/number_ions

num_sputtered_C = np.shape(sputtered_C)[0]

energy_sputtered_C = np.sum(sputtered_C[:, 2])

num_sputtered_C/number_ions

energy_sputtered_C/number_ions

num_implanted = np.shape(implanted)[0]

energy_implanted = np.sum(implanted[:, 2])

num_implanted/number_ions

energy_implanted/number_ions

energies_eV = 1200.0*np.ones(number_ions)

ux = np.cos(angle*np.pi/180.)*np.ones(number_ions)

uy = np.sin(angle*np.pi/180.)*np.ones(number_ions)

uz = np.zeros(number_ions)

output, incident, stopped = compound_bca_list_1D_py(ux, uy, uz, energies_eV, Z1, m1, Ec1, Es1,
[target['Z'], 6.0], [target['m'], 12.011], [target['Ec'], 1.0], [target['Es'], 7.37], [target['Eb'], 0.0], [[0.066142,
0.066142]], [1000.0])

output = np.array(output)

content = str(output)

file = open("C_W.txt", "w+")

file.write(content)

Z = output[:, 0]

m = output[:, 1]

E = output[:, 2]
```

```
x = output[:, 3]
y = output[:, 4]
z = output[:, 5]
ux = output[:, 6]
uy = output[:, 7]
uz = output[:, 8]
sputtered_W = output[np.logical_and(Z == target['Z'], E > 0), :]
sputtered_C = output[np.logical_and(Z == 6.0, E > 0), :]
reflected = output[np.logical_and(Z == 6.0, x < 0), :]
implanted = output[np.logical_and(Z == 6.0, x > 0), :]
num_reflected = np.shape(reflected)[0]
energy_reflected = np.sum(reflected[:, 2])
num_reflected/number_ions
energy_reflected/number_ions
num_sputtered_W = np.shape(sputtered_W)[0]
energy_sputtered_W = np.sum(sputtered_W[:, 2])
num_sputtered_W/number_ions
energy_sputtered_W/number_ions
num_sputtered_C = np.shape(sputtered_C)[0]
energy_sputtered_C = np.sum(sputtered_C[:, 2])
num_sputtered_C/number_ions
energy_sputtered_C/number_ions
num_implanted = np.shape(implanted)[0]
energy_implanted = np.sum(implanted[:, 2])
num_implanted/number_ions
energy_implanted/number_ions
energies_eV = 1300.0*np.ones(number_ions)
ux = np.cos(angle*np.pi/180.)*np.ones(number_ions)
uy = np.sin(angle*np.pi/180.)*np.ones(number_ions)
```

```
uz = np.zeros(number_ions)

output, incident, stopped = compound_bca_list_1D_py(ux, uy, uz, energies_eV, Z1, m1, Ec1, Es1, [target['Z'], 6.0], [target['m'], 12.011], [target['Ec'], 1.0], [target['Es'], 7.37], [target['Eb'], 0.0], [[0.066142, 0.066142]], [1000.0])

output = np.array(output)

content = str(output)

file = open("C_W.txt", "w+")

file.write(content)

Z = output[:, 0]

m = output[:, 1]

E = output[:, 2]

x = output[:, 3]

y = output[:, 4]

z = output[:, 5]

ux = output[:, 6]

uy = output[:, 7]

uz = output[:, 8]

sputtered_W = output[np.logical_and(Z == target['Z'], E > 0), :]

sputtered_C = output[np.logical_and(Z == 6.0, E > 0), :]

reflected = output[np.logical_and(Z == 6.0, x < 0), :]

implanted = output[np.logical_and(Z == 6.0, x > 0), :]

num_reflected = np.shape(reflected)[0]

energy_reflected = np.sum(reflected[:, 2])

num_reflected/number_ions

energy_reflected/number_ions

num_sputtered_W = np.shape(sputtered_W)[0]

energy_sputtered_W = np.sum(sputtered_W[:, 2])

num_sputtered_W/number_ions

energy_sputtered_W/number_ions
```

```
num_sputtered_C = np.shape(sputtered_C)[0]

energy_sputtered_C = np.sum(sputtered_C[:, 2])

num_sputtered_C/number_ions

energy_sputtered_C/number_ions

num_implanted = np.shape(implanted)[0]

energy_implanted = np.sum(implanted[:, 2])

num_implanted/number_ions

energy_implanted/number_ions

energies_eV = 1400.0*np.ones(number_ions)

ux = np.cos(angle*np.pi/180.)*np.ones(number_ions)

uy = np.sin(angle*np.pi/180.)*np.ones(number_ions)

uz = np.zeros(number_ions)

output, incident, stopped = compound_bca_list_1D_py(ux, uy, uz, energies_eV, Z1, m1, Ec1, Es1,
[target['Z'], 6.0], [target['m'], 12.011], [target['Ec'], 1.0], [target['Es'], 7.37], [target['Eb'], 0.0], [[0.066142,
0.066142]], [1000.0])

output = np.array(output)

content = str(output)

file = open("C_W.txt", "w+")

file.write(content)

Z = output[:, 0]

m = output[:, 1]

E = output[:, 2]

x = output[:, 3]

y = output[:, 4]

z = output[:, 5]

ux = output[:, 6]

uy = output[:, 7]

uz = output[:, 8]

sputtered_W = output[np.logical_and(Z == target['Z'], E > 0), :]
```

```
sputtered_C = output[np.logical_and(Z == 6.0, E > 0), :]

reflected = output[np.logical_and(Z == 6.0, x < 0), :]

implanted = output[np.logical_and(Z == 6.0, x > 0), :]

num_reflected = np.shape(reflected)[0]

energy_reflected = np.sum(reflected[:, 2])

num_reflected/number_ions

energy_reflected/number_ions

num_sputtered_W = np.shape(sputtered_W)[0]

energy_sputtered_W = np.sum(sputtered_W[:, 2])

num_sputtered_W/number_ions

energy_sputtered_W/number_ions

num_sputtered_C = np.shape(sputtered_C)[0]

energy_sputtered_C = np.sum(sputtered_C[:, 2])

num_sputtered_C/number_ions

energy_sputtered_C/number_ions

num_implanted = np.shape(implanted)[0]

energy_implanted = np.sum(implanted[:, 2])

num_implanted/number_ions

energy_implanted/number_ions

energies_eV = 1500.0*np.ones(number_ions)

ux = np.cos(angle*np.pi/180.)*np.ones(number_ions)

uy = np.sin(angle*np.pi/180.)*np.ones(number_ions)

uz = np.zeros(number_ions)

output, incident, stopped = compound_bca_list_1D_py(ux, uy, uz, energies_eV, Z1, m1, Ec1, Es1,
[target['Z'], 6.0], [target['m'], 12.011], [target['Ec'], 1.0], [target['Es'], 7.37], [target['Eb'], 0.0], [[0.066142,
0.066142]], [1000.0])

output = np.array(output)

content = str(output)

file = open("C_W.txt", "w+")
```

```
file.write(content)
Z = output[:, 0]
m = output[:, 1]
E = output[:, 2]
x = output[:, 3]
y = output[:, 4]
z = output[:, 5]
ux = output[:, 6]
uy = output[:, 7]
uz = output[:, 8]
sputtered_W = output[np.logical_and(Z == target['Z'], E > 0), :]
sputtered_C = output[np.logical_and(Z == 6.0, E > 0), :]
reflected = output[np.logical_and(Z == 6.0, x < 0), :]
implanted = output[np.logical_and(Z == 6.0, x > 0), :]
num_reflected = np.shape(reflected)[0]
energy_reflected = np.sum(reflected[:, 2])
num_reflected/number_ions
energy_reflected/number_ions
num_sputtered_W = np.shape(sputtered_W)[0]
energy_sputtered_W = np.sum(sputtered_W[:, 2])
num_sputtered_W/number_ions
energy_sputtered_W/number_ions
num_sputtered_C = np.shape(sputtered_C)[0]
energy_sputtered_C = np.sum(sputtered_C[:, 2])
num_sputtered_C/number_ions
energy_sputtered_C/number_ions
num_implanted = np.shape(implanted)[0]
energy_implanted = np.sum(implanted[:, 2])
num_implanted/number_ions
```

```
energy_implanted/number_ions

energies_eV = 1600.0*np.ones(number_ions)

ux = np.cos(angle*np.pi/180.)*np.ones(number_ions)

uy = np.sin(angle*np.pi/180.)*np.ones(number_ions)

uz = np.zeros(number_ions)

output, incident, stopped = compound_bca_list_1D_py(ux, uy, uz, energies_eV, Z1, m1, Ec1, Es1,
[target['Z'], 6.0], [target['m'], 12.011], [target['Ec'], 1.0], [target['Es'], 7.37], [target['Eb'], 0.0], [[0.066142,
0.066142]], [1000.0])

output = np.array(output)

content = str(output)

file = open("C_W.txt", "w+")

file.write(content)

Z = output[:, 0]

m = output[:, 1]

E = output[:, 2]

x = output[:, 3]

y = output[:, 4]

z = output[:, 5]

ux = output[:, 6]

uy = output[:, 7]

uz = output[:, 8]

sputtered_W = output[np.logical_and(Z == target['Z'], E > 0), :]

sputtered_C = output[np.logical_and(Z == 6.0, E > 0), :]

reflected = output[np.logical_and(Z == 6.0, x < 0), :]

implanted = output[np.logical_and(Z == 6.0, x > 0), :]

num_reflected = np.shape(reflected)[0]

energy_reflected = np.sum(reflected[:, 2])

num_reflected/number_ions

energy_reflected/number_ions
```

```
num_sputtered_W = np.shape(sputtered_W)[0]

energy_sputtered_W = np.sum(sputtered_W[:, 2])

num_sputtered_W/number_ions

energy_sputtered_W/number_ions

num_sputtered_C = np.shape(sputtered_C)[0]

energy_sputtered_C = np.sum(sputtered_C[:, 2])

num_sputtered_C/number_ions

energy_sputtered_C/number_ions

num_implanted = np.shape(implanted)[0]

energy_implanted = np.sum(implanted[:, 2])

num_implanted/number_ions

energy_implanted/number_ions

energies_eV = 1700.0*np.ones(number_ions)

ux = np.cos(angle*np.pi/180.)*np.ones(number_ions)

uy = np.sin(angle*np.pi/180.)*np.ones(number_ions)

uz = np.zeros(number_ions)

output, incident, stopped = compound_bca_list_1D_py(ux, uy, uz, energies_eV, Z1, m1, Ec1, Es1,
[target['Z'], 6.0], [target['m'], 12.011], [target['Ec'], 1.0], [target['Es'], 7.37], [target['Eb'], 0.0], [[0.066142,
0.066142]], [1000.0])

output = np.array(output)

content = str(output)

file = open("C_W.txt", "w+")

file.write(content)

Z = output[:, 0]

m = output[:, 1]

E = output[:, 2]

x = output[:, 3]

y = output[:, 4]

z = output[:, 5]
```

```
ux = output[:, 6]
uy = output[:, 7]
uz = output[:, 8]
sputtered_W = output[np.logical_and(Z == target['Z'], E > 0), :]
sputtered_C = output[np.logical_and(Z == 6.0, E > 0), :]
reflected = output[np.logical_and(Z == 6.0, x < 0), :]
implanted = output[np.logical_and(Z == 6.0, x > 0), :]
num_reflected = np.shape(reflected)[0]
energy_reflected = np.sum(reflected[:, 2])
num_reflected/number_ions
energy_reflected/number_ions
num_sputtered_W = np.shape(sputtered_W)[0]
energy_sputtered_W = np.sum(sputtered_W[:, 2])
num_sputtered_W/number_ions
energy_sputtered_W/number_ions
num_sputtered_C = np.shape(sputtered_C)[0]
energy_sputtered_C = np.sum(sputtered_C[:, 2])
num_sputtered_C/number_ions
energy_sputtered_C/number_ions
num_implanted = np.shape(implanted)[0]
energy_implanted = np.sum(implanted[:, 2])
num_implanted/number_ions
energy_implanted/number_ions
energies_eV = 1800.0*np.ones(number_ions)
ux = np.cos(angle*np.pi/180.)*np.ones(number_ions)
uy = np.sin(angle*np.pi/180.)*np.ones(number_ions)
uz = np.zeros(number_ions)
```

```
output, incident, stopped = compound_bca_list_1D_py(ux, uy, uz, energies_eV, Z1, m1, Ec1, Es1, [target['Z'], 6.0], [target['m'], 12.011], [target['Ec'], 1.0], [target['Es'], 7.37], [target['Eb'], 0.0], [[0.066142, 0.066142]], [1000.0])

output = np.array(output)

content = str(output)

file = open("C_W.txt", "w+")

file.write(content)

Z = output[:, 0]

m = output[:, 1]

E = output[:, 2]

x = output[:, 3]

y = output[:, 4]

z = output[:, 5]

ux = output[:, 6]

uy = output[:, 7]

uz = output[:, 8]

sputtered_W = output[np.logical_and(Z == target['Z'], E > 0), :]

sputtered_C = output[np.logical_and(Z == 6.0, E > 0), :]

reflected = output[np.logical_and(Z == 6.0, x < 0), :]

implanted = output[np.logical_and(Z == 6.0, x > 0), :]

num_reflected = np.shape(reflected)[0]

energy_reflected = np.sum(reflected[:, 2])

num_reflected/number_ions

energy_reflected/number_ions

num_sputtered_W = np.shape(sputtered_W)[0]

energy_sputtered_W = np.sum(sputtered_W[:, 2])

num_sputtered_W/number_ions

energy_sputtered_W/number_ions

num_sputtered_C = np.shape(sputtered_C)[0]
```

```
energy_sputtered_C = np.sum(sputtered_C[:, 2])

num_sputtered_C/number_ions

energy_sputtered_C/number_ions

num_implanted = np.shape(implanted)[0]

energy_implanted = np.sum(implanted[:, 2])

num_implanted/number_ions

energy_implanted/number_ions

energies_eV = 1900.0*np.ones(number_ions)

ux = np.cos(angle*np.pi/180.)*np.ones(number_ions)

uy = np.sin(angle*np.pi/180.)*np.ones(number_ions)

uz = np.zeros(number_ions)

output, incident, stopped = compound_bca_list_1D_py(ux, uy, uz, energies_eV, Z1, m1, Ec1, Es1,
[target['Z'], 6.0], [target['m'], 12.011], [target['Ec'], 1.0], [target['Es'], 7.37], [target['Eb'], 0.0], [[0.066142,
0.066142]], [1000.0])

output = np.array(output)

content = str(output)

file = open("C_W.txt", "w+")

file.write(content)

Z = output[:, 0]

m = output[:, 1]

E = output[:, 2]

x = output[:, 3]

y = output[:, 4]

z = output[:, 5]

ux = output[:, 6]

uy = output[:, 7]

uz = output[:, 8]

sputtered_W = output[np.logical_and(Z == target['Z'], E > 0), :]

sputtered_C = output[np.logical_and(Z == 6.0, E > 0), :]
```

```
reflected = output[np.logical_and(Z == 6.0, x < 0), :]

implanted = output[np.logical_and(Z == 6.0, x > 0), :]

num_reflected = np.shape(reflected)[0]

energy_reflected = np.sum(reflected[:, 2])

num_reflected/number_ions

energy_reflected/number_ions

num_sputtered_W = np.shape(sputtered_W)[0]

energy_sputtered_W = np.sum(sputtered_W[:, 2])

num_sputtered_W/number_ions

energy_sputtered_W/number_ions

num_sputtered_C = np.shape(sputtered_C)[0]

energy_sputtered_C = np.sum(sputtered_C[:, 2])

num_sputtered_C/number_ions

energy_sputtered_C/number_ions

num_implanted = np.shape(implanted)[0]

energy_implanted = np.sum(implanted[:, 2])

num_implanted/number_ions

energy_implanted/number_ions

energies_eV = 2000.0*np.ones(number_ions)

ux = np.cos(angle*np.pi/180.)*np.ones(number_ions)

uy = np.sin(angle*np.pi/180.)*np.ones(number_ions)

uz = np.zeros(number_ions)

output, incident, stopped = compound_bca_list_1D_py(ux, uy, uz, energies_eV, Z1, m1, Ec1, Es1,
[target['Z'], 6.0], [target['m'], 12.011], [target['Ec'], 1.0], [target['Es'], 7.37], [target['Eb'], 0.0], [[0.066142,
0.066142]], [1000.0])

output = np.array(output)

content = str(output)

file = open("C_W.txt", "w+")

file.write(content)
```

```
Z = output[:, 0]
m = output[:, 1]
E = output[:, 2]
x = output[:, 3]
y = output[:, 4]
z = output[:, 5]
ux = output[:, 6]
uy = output[:, 7]
uz = output[:, 8]
sputtered_W = output[np.logical_and(Z == target['Z'], E > 0), :]
sputtered_C = output[np.logical_and(Z == 6.0, E > 0), :]
reflected = output[np.logical_and(Z == 6.0, x < 0), :]
implanted = output[np.logical_and(Z == 6.0, x > 0), :]
num_reflected = np.shape(reflected)[0]
energy_reflected = np.sum(reflected[:, 2])
num_reflected/number_ions
energy_reflected/number_ions
num_sputtered_W = np.shape(sputtered_W)[0]
energy_sputtered_W = np.sum(sputtered_W[:, 2])
num_sputtered_W/number_ions
energy_sputtered_W/number_ions
num_sputtered_C = np.shape(sputtered_C)[0]
energy_sputtered_C = np.sum(sputtered_C[:, 2])
num_sputtered_C/number_ions
energy_sputtered_C/number_ions
num_implanted = np.shape(implanted)[0]
energy_implanted = np.sum(implanted[:, 2])
num_implanted/number_ions
energy_implanted/number_ions
```

# C DIII-D IDL Experimental Analysis and FSRM Computations

```
pro cacherisphddissertationappendix.pro, shot, trange, tcyclerange, sxb, elms=elms,
errorbars=errorbars, q, tfactor, uptfactor, fscope, inter_ELMs=inter_ELMs, Carbon=Carbon,
FSRM=FSRM, intra_ELMs=intra_ELMs, Energy=Energy, D_intra_ELMs=D_intra_ELMs,
D_inter_ELMs=D_inter_ELMs, Deuterium=Deuterium, ion=ion, ang=ang, lep=lep, dachan,
pedestal=pedestal, plottempdens=plottempdens, werror=werror, wmhdf=wmhdf, setc=setc,
saselm=saselm, mrchf=mrchf, lmode=lmode, confinement=confinement, mds=mds,
mdswi=mdswi, intersub=intersub, TIME=TIME, view=view, da=da, c3=c3, DTS=DTS ;add
view l8er, add view and filter to assess gain gn and gm if needed, add fscope after uptfactor


close,/all


if keyword_set (DTS) then begin

d=get_lp(shot)

;d=get_mds_active_probes(shot)

help, d

print, d.chan.r

print, d.chan.z


;SAS DIVERTOR TEMPERATURE


dt=get_ptname_elm(shot,'divtemp',trange=trange,times=d.chan[q].time,signal=d.chan[q].temp,tc
yclerange=tcyclerange,tfactor=0.3, uptfactor=uptfactor, dachan=fs06F)

;print, 'divertor temperature', dt.divtemp

;print,dt.time

plot,dt.time,dt.divtemp,psym=4,symsize=2,yrange=[0,100]

Intradivtemp=mean(dt.divtemp[where(dt.time gt 0 and dt.time lt 1 and dt.divtemp gt 10 and
dt.divtemp lt 100)]) ;for Intra-ELM, 0 to 1.5 for SAS V1

Interdivtemp=mean(dt.divtemp[where(dt.time gt -4 and dt.time lt -1 and dt.divtemp gt 5 and
dt.divtemp lt 80)]) ;for Inter-ELM

;STDtemp=mean(dt.error[where(dt.time gt -4 and dt.time lt -1)]) ;for Inter-ELM
```

```
print, 'Intra-ELM temperature', Intradivtemp

print, 'Inter-ELM temperature', Interdivtemp

;print, 'Inter-ELM temp error', dt.error


endif


;ELM FREQUENCY

c=get_felm(shot, trange[0], trange[-1], /plot, tfactor=tfactor, uptfactor=uptfactor,
dachan=dachan) ;fscope=fscope

print, 'FELM', c

;print, stddev(c)


;TIME STARTS & ENDS

tstart=trange[0]

tend=trange[-1]

tcycstart=tcyclerange[0]

tcycend=tcyclerange[-1]


;CONFINEMENT PARAMETERS

if keyword_set (confinement) then begin


gadat,x,y,'pinj',shot

pinj = y[where(x gt 0 and x lt tend)]

pinj = smooth(pinj, 1000)

;print,'pinj', pinj


Time = x[where(x gt 0 and x lt tend)]


gadat,x,y,'lob2',shot
```

```
gas_rate = y[where(x gt 0 and x lt tend)]
gas_rate=CONGRID(gas_rate, N_ELEMENTS(Time))
;print,'gas rate', gas_rate

gadat,x,y,'fssasda',shot
fssasda = y[where(x gt 0 and x lt tend)]
fssasda=CONGRID(fssasda, N_ELEMENTS(Time))
;print,'fssasda', fssasda

gadat,x,y,'density',shot
density = y[where(x gt 0 and x lt tend)]
density=CONGRID(density, N_ELEMENTS(Time))
;print, 'density', density

gadat,x,y,'zvsout',shot
zvsout = y[where(x gt 0 and x lt tend)]
zvsout=CONGRID(zvsout, N_ELEMENTS(Time))
;print,'zvsout', zvsout

gadat,x,y,'rvsout',shot
rvsout = y[where(x gt 0 and x lt tend)]
rvsout=CONGRID(rvsout, N_ELEMENTS(Time))
;print,'rvsout', rvsout

WRITE_CSV, '191009_Time', Time, HEADER=['Time (ms)']
WRITE_CSV, '191009_pinj', pinj, HEADER=['pinj (kW)']
WRITE_CSV, '191009_gas_rate', gas_rate, HEADER=['gas_rate (Torr-L/s)']
WRITE_CSV, '191009_fssasda', fssasda, HEADER=['fssasda (ph/sr/cm^2/s']
```

```
WRITE_CSV, '191009_density', density, HEADER=['density (cm^-3)']
WRITE_CSV, '191009_zvsout', zvsout, HEADER=['zvsout (m)']
WRITE_CSV, '191009_rvsout', rvsout, HEADER=['rvsout (m)']

;H98
gadat,x,y,'h_thh98y2',shot
H98 = mean(y[where(x gt trange[0] and x lt trange[-1])])
print,'H98:', H98

;BN
gadat,x,y,'betan',shot
BetaN = mean(y[where(x gt trange[0] and x lt trange[-1])])
print,'BetaN:', BetaN

;Bp
gadat,x,y,'betap',shot
Betap = mean(y[where(x gt trange[0] and x lt trange[-1])])
print,'Betap:', Betap

;wmhdf
gadat,x,y,'wmhdf',shot
wmhdf = mean(y[where(x gt trange[0] and x lt trange[-1])])
print,'wmhdf average:', wmhdf
;print, 'STD', stddev(wmhdf)
;help, wmhdf

;wmhd
gadat,x,y,'wmhd',shot
```

```
wmhd = mean(y[where(x gt trange[0] and x lt trange[-1])])
print,'mean wmhd:', wmhd
;print, 'STD', stddev(wmhdf)
;help, wmhd

stop
endif

;PEDESTAL CONDITIONS
if keyword_set (pedestal) then begin

;Pedestal temperature average over whole shot
gadat,x,y,'prmtan_teped',shot
teped=mean(y[where(x gt trange[0] and x lt trange[-1])])
STD_teped=stddev((y[where(x gt trange[0] and x lt trange[-1])]))/sqrt(n_elements(y))
print,'pedestal temperature', teped
;print,'teped STD', STD_teped

;Pedestal density average over whole shot
gadat,x,y,'prmtan_neped',shot
neped=mean(y[where(x gt trange[0] and x lt trange[-1])])
STD_neped=stddev((y[where(x gt trange[0] and x lt trange[-1])]))/sqrt(n_elements(y))/1e19
print,'pedestal density', neped
;print,'neped STD', STD_neped


;CARBON (PEDESTAL) - QUICK OVERVIEW
```

```
;Average Carbon impurity percentage just outside of SOL

gadat,x,y,'cerafzt7',shot ;use cerafzt10 for MRC, cerafzt7 for SAS

cerafzt7=mean(y[where(x gt tstart and x lt tend)])

print,'carbon impurity % Unresolved', cerafzt7


car=get_ptname_elm(shot,'cerafzt10',trange=[tstart,tend],tcyclerange=tcyclerange,
tfactor=tfactor, uptfactor=uptfactor) ;use cerafzt10 for MRC, cerafzt7 for SAS

plot,car.time,car.cerafzt10,psym=5,symsize=2

cerafzt10=mean(car.cerafzt10[where(car.time lt tcyclerange[-1] and car.time gt tcyclerange[0]
and car.cerafzt10)])

print,'carbon impurity % ELM-resolved', cerafzt10


;stop

endif


;CORE PLASMA STORED ENERGY

if keyword_set (Energy) then begin

gadat,x,y,'wmhd',shot

Energy=mean(y[where(x gt trange[0] and x lt trange[-1])])

print, 'stored energy', Energy

endif


;TEMP/DENS DIVERTOR - QUICK PLOT

if keyword_set (plottempdens) then begin

d=get_lp(shot)

ww=plot(d.chan[q].time, smooth(d.chan[q].dens,2), xra=trange, yra=[0,8e13],
window_title='density')

rr=plot(d.chan[q].time, smooth(d.chan[q].temp,2), xra=trange, yra=[0,100]
,window_title='temperature')

;stop
```

```
endif

;MAGNETIC FIELD INCLINATION ANGLE
if keyword_set (ang) then begin
;ang=calc_angle_actual(shot, tstart, tend, r=1.601, z=-1.251) ;1.601 near fs06f
;ang=calc_angle_actual(shot, tstart, tend, r=1.42, z=-1.251) ; near fs04f (MRC W
;tile)r=1.45, z=-1.251
ang=calc_angle_actual(shot, tstart, tend) ;1.601 (1.61 to match LP) near fs06f
print, 'angle', ang
endif

;SETC
if keyword_set (setc) then begin
;setc=get_ptname_elm(shot,'SETC008_Q',trange=trange,tcyclerange=[-20,20])
;plot,setc.time,setc.setc008_q,psym=5,symsize=2,yrange=[0,3e6]
;heatflux=mean(setc.setc008_q[where(setc.time gt -1 and setc.time lt 1 and setc.setc008_q gt 1e5
and setc.setc008_q lt 5e6)])/1e6
;peakheatflux=max(setc.setc008_q[where(setc.time gt -10 and setc.time
;lt 10 and setc.setc008_q gt 1e5 and setc.setc008_q lt 5e6)])/1e6

;Heat flux over whole shot
gadat,x,y,'SETC009_Q',shot
heatflux=mean(y[where(x gt trange[0] and x lt trange[-1])])
peakheatflux=max(y[where(x gt trange[0] and x lt trange[-1])])

print,'mean heat flux', heatflux/1e6
print, 'peak heat flux', peakheatflux/1e6
endif
```

```
;-------------------------------------------------------------;

;SAS-VW INTRA-ELM ANALYSIS
if keyword_set (saselm) then begin

;Filterscope data
an=get_sasvw_fscope(shot, 2, 'W1N')
am=get_sasvw_fscope(shot, 2, 'W1M')

;Retrieve R value for calibration:
R=sasvw_crosscal([shot], 2)
;print, 'R', R.RFIT
;R1=R.RFIT ;.775 for V2, .18 for V1
R1=0.775
R2=.75 ;.75 for V2, .175 for V1
R3=.8 ;.8 for V2, .185 for V1

if keyword_set (mdswi) then begin

;MDS data
;.r /fusion/projects/boundary/abramst/sasvw_analysis.pro
;.r /fusion/projects/boundary/abramst/atomic_phys.pro
;module load mdspec
b=get_sasvw_mds_wi(shot, 2,/calibrate)
;help, b
MDS_Photons=b.int_wi[where(b.time gt tstart and b.time lt tend)]
;mdsnewsxbintra=fltarr(n_elements(b.time))
;for n=0,n_elements(mdsnewsxbintra)-1 do
mdsnewsxbintra[n]=get_sxb_wi(maxdensity[n],Intradivtemp)
```

```
;mdsWI=mdsnewsxbintra*b.int_wi

Filterscope_Photons=(an.cali-R1*am.cali)/(1-R1)

FR2=(an.cali-R2*am.cali)/(1-R2)

FR3=(an.cali-R3*am.cali)/(1-R3)

FP=Filterscope_Photons[where(an.time gt tstart and an.time lt tend)]

FP2=FR2[where(an.time gt tstart and an.time lt tend)]

FP3=FR3[where(an.time gt tstart and an.time lt tend)]

MP=CONGRID(MDS_Photons, N_ELEMENTS(FP))

;WI=CONGRID(b.int_wi, N_ELEMENTS((an.cali-am.cali*R1)/(1-R1)))

MDS_integrated = TOTAL(MP)

print, 'MDS_Integrated', MDS_integrated/1e17

Filterscope_integrated = TOTAL(FP)

print, 'Filterscope_Integrated', Filterscope_integrated/1e17

FR2I=TOTAL(FP2)

FR3I=TOTAL(FP3)

ERROR=FR2I-FR3I

ERROR_integrated=TOTAL(ERROR)

print,'ERROR', ERROR_integrated/1e17

;Units of photons/cm2/sr/s

;plot, an.time, WI, yrange=[1,5e12]

;oplot, an.time, smooth((an.cali-am.cali*R1)/(1-R1),5000), color=60

;j=plot(b.time, b.int_wi, ytitle='WI intensity (ph*cm-2*s-1/sr)', xtitle='Time (ms)',
xrange=trange, window_title='correctelms')

;oplot, an.time, an.cali

;j=oplot(an.time, an.cali, "r4-", ytitle='WI intensity (ph*cm-2*s-1/sr)', xtitle='Time (ms)',
xrange=tcyclerange, yrange=[0,1e14], window_title='correctelms')

stop

endif
```

str1=get_ptname_elm(shot, 'int_wi_fscope1', trange=trange,tcyclerange=tcyclerange, signal=(an.cali-R1*am.cali)/(1-R1),times=an.time, dachan=dachan, tfactor=tfactor, uptfactor=uptfactor, elmtimes=elmtimes) ;-0.5-1.5 for small ELMs, -0.5-2.5 for large | alter to tcyclerange=[-0.5, 2.5] for W erosion

str6=get_ptname_elm(shot, 'int_wi_fscope6', trange=trange,tcyclerange=[-0.5, 2.5], signal=(an.cali-R2*am.cali)/(1-R2),times=an.time, dachan=dachan, tfactor=tfactor, uptfactor=uptfactor, elmtimes=elmtimes)

str7=get_ptname_elm(shot, 'int_wi_fscope7', trange=trange,tcyclerange=[-0.5, 2.5], signal=(an.cali-R3*am.cali)/(1-R3),times=an.time, dachan=dachan, tfactor=tfactor, uptfactor=uptfactor, elmtimes=elmtimes)

str2=get_ptname_elm(shot, 'int_wi_fscope2', trange=trange, tcyclerange=[-4, -1], signal=(an.cali-R1*am.cali)/(1-R1), times=an.time, dachan=dachan, tfactor=tfactor, uptfactor=uptfactor)

str3=get_ptname_elm(shot, 'int_wi_fscope3', trange=trange, tcyclerange=[-4, -1], signal=(an.cali-R2*am.cali)/(1-R2), times=an.time, dachan=dachan, tfactor=tfactor, uptfactor=uptfactor)

str4=get_ptname_elm(shot, 'int_wi_fscope4', trange=trange, tcyclerange=[-4, -1], signal=(an.cali-R3*am.cali)/(1-R3), times=an.time, dachan=dachan, tfactor=tfactor, uptfactor=uptfactor)

;SMALL ELMS

;str1=get_ptname_elm(shot, 'int_wi_fscope1', trange=trange,tcyclerange=[-0.5, 2.5], signal=WI, times=an.time, dachan=dachan, tfactor=tfactor, uptfactor=uptfactor, elmtimes=elmtimes) ;-0.5-1.5 for small ELMs, -0.5-2.5 for large

;USE THESE FOR AM.CALI FILTERSCOPE TRIPS

;str1=get_ptname_elm(shot, 'int_wi_fscope1', trange=trange, tcyclerange=[-0.5, 2.5], signal=an.cali*0.5, times=an.time, dachan=dachan, tfactor=tfactor, uptfactor=uptfactor); for shots 161016-7, 191005-6 only

;str2=get_ptname_elm(shot, 'int_wi_fscope2', trange=trange, tcyclerange=[-4, -1], signal=an.cali*0.5, times=an.time, dachan=dachan, tfactor=tfactor, uptfactor=uptfactor); for shots 161016-7, 191005-6 only

;str3=get_ptname_elm(shot, 'int_wi_fscope3', trange=trange, tcyclerange=[-4, -1], signal=an.cali*0.55, times=an.time, dachan=dachan, tfactor=tfactor, uptfactor=uptfactor); for shots 161016-7, 191005-6 only

;str4=get_ptname_elm(shot, 'int_wi_fscope4', trange=trange, tcyclerange=[-4, -1], signal=an.cali*0.45, times=an.time, dachan=dachan, tfactor=tfactor, uptfactor=uptfactor); for shots 161016-7, 191005-6 only

;str2=get_ptname_elm(shot, 'int_wi_fscope2', trange=trange, tcyclerange=[-4, -1], signal=WI, times=an.time, dachan=dachan, tfactor=tfactor, uptfactor=uptfactor)

;str3=get_ptname_elm(shot, 'int_wi_fscope3', trange=trange, tcyclerange=[-4, -1], signal=WI, times=an.time, dachan=dachan, tfactor=tfactor, uptfactor=uptfactor)

;str4=get_ptname_elm(shot, 'int_wi_fscope4', trange=trange, tcyclerange=[-4, -1], signal=WI, times=an.time, dachan=dachan, tfactor=tfactor, uptfactor=uptfactor)

;str6=get_ptname_elm(shot, 'int_wi_fscope6', trange=trange,tcyclerange=[-0.5, 2.5], signal=WI,times=an.time, dachan=dachan, tfactor=tfactor, uptfactor=uptfactor, elmtimes=elmtimes)

;str7=get_ptname_elm(shot, 'int_wi_fscope7', trange=trange,tcyclerange=[-0.5, 2.5], signal=WI,times=an.time, dachan=dachan, tfactor=tfactor, uptfactor=uptfactor, elmtimes=elmtimes)

;RETRIEVE LANGMUIR PROBE DATA

;***q=13 for 163 A-12 Langmuir probe for view 2***

;q=11 for 159 A-10 Langmuir probe for view 1

;q=15 for 167 A-14 Langmuir probe for view 3

;q=11,12,13,14,15 (whole slant)

d=get_lp(shot)

help, d

;d=get_mds_active_probes(shot)

;print, d.chan[*]

;stop

;restore,'sasvw_pmt_info.sav'

;g=get_sasvw_fscope(shot, view, filter)

;SAS DIVERTOR DENSITY

dd=get_ptname_elm(shot,'divdens',trange=trange,times=d.chan[q].time,signal=d.chan[q].dens,tcyclerange=[-4,4],tfactor=tfactor, uptfactor=uptfactor, dachan=dachan, elmtimes=elmtimes)

```
print, 'divertor density', dd.divdens

print, 'time', dd.time

;print, 'divertor density error', dd.error

plot,dd.time,dd.divdens,psym=4,symsize=2,yrange=[0,1e14]

;stop

maxdivdens=max(dd.divdens[where(dd.time gt 0 and dd.time lt 1 and dd.divdens gt 5e12 and dd.divdens lt 6e13)]) ;for intra-ELM erosion, lower bound of 1e13 for large ELMs, 1e12 for small, 0 to 1.5 for SAS V1

avgdivdens=mean(dd.divdens[where(dd.time gt -4 and dd.time lt -1 and dd.divdens lt 3e13)]) ; for inter-ELM erosion

;maxdivdens=3.8e13 ;for manual: 3e13 for 0999 v2, 3.8e13 for 1005 v2

print, 'Intra-ELM density', maxdivdens

print, 'Inter-ELM density', avgdivdens

maxdensity=((str1.int_wi_fscope1)/max(str1.int_wi_fscope1))*maxdivdens*1e6 ;scale divertor density to the WI filterscope signal

;print, 'maxdensity', maxdensity

;stop

avgdensity2=((str2.int_wi_fscope2)/max(str2.int_wi_fscope2))*avgdivdens*1e6 ;scale divertor density to the WI filterscope signal

avgdensity3=((str3.int_wi_fscope3)/max(str3.int_wi_fscope3))*avgdivdens*1e6 ;scale divertor density to the WI filterscope signal

avgdensity4=((str4.int_wi_fscope4)/max(str4.int_wi_fscope4))*avgdivdens*1e6 ;scale divertor density to the WI filterscope signal

;print, dd.error

;stop


;SAS DIVERTOR TEMPERATURE


dt=get_ptname_elm(shot,'divtemp',trange=trange,times=d.chan[q].time,signal=d.chan[q].temp,tcyclerange=tcyclerange,tfactor=tfactor, uptfactor=uptfactor, dachan=dachan)

;print, 'divertor temperature', dt.divtemp
```

```
;print,dt.time

plot,dt.time,dt.divtemp,psym=4,symsize=2,yrange=[0,100]

Intradivtemp=mean(dt.divtemp[where(dt.time gt 0 and dt.time lt 1 and dt.divtemp gt 10 and
dt.divtemp lt 100)]) ;for Intra-ELM, 0 to 1.5 for SAS V1

Interdivtemp=mean(dt.divtemp[where(dt.time gt -100 and dt.time lt 0 and dt.divtemp gt 5 and
dt.divtemp lt 80)]) ;for Inter-ELM

;STDtemp=mean(dt.error[where(dt.time gt -4 and dt.time lt -1)]) ;for Inter-ELM

print, 'Intra-ELM temperature', Intradivtemp

print, 'Inter-ELM temperature', Interdivtemp

;Intradivtemp = 80

;print, 'Inter-ELM temp error', dt.error

;help, dt

;avgdivtemp=25 ;for inter-ELM erosion

;stop



;A-5

q6=get_ptname_elm(shot,'divtemp',trange=trange,times=d.chan[6].time,signal=d.chan[6].temp,tc
yclerange=tcyclerange,tfactor=tfactor, uptfactor=uptfactor, dachan=dachan)

Inter_Te_6=mean(q6.divtemp[where(q6.time gt -4 and q6.time lt -1 and q6.divtemp gt 5 and
q6.divtemp lt 80)]) ;for Inter-ELM

Intra_Te_6=mean(q6.divtemp[where(q6.time gt 0 and q6.time lt 1 and q6.divtemp gt 10 and
q6.divtemp lt 100)]) ;for Intra-ELM, 0 to 1.5 for SAS V1


;A-6

q7=get_ptname_elm(shot,'divtemp',trange=trange,times=d.chan[7].time,signal=d.chan[7].temp,tc
yclerange=tcyclerange,tfactor=tfactor, uptfactor=uptfactor, dachan=dachan)

Inter_Te_7=mean(q7.divtemp[where(q7.time gt -4 and q7.time lt -1 and q7.divtemp gt 5 and
q7.divtemp lt 80)]) ;for Inter-ELM

Intra_Te_7=mean(q7.divtemp[where(q7.time gt 0 and q7.time lt 1 and q7.divtemp gt 10 and
q7.divtemp lt 100)]) ;for Intra-ELM, 0 to 1.5 for SAS V1
```

;A-7

q8=get_ptname_elm(shot,'divtemp',trange=trange,times=d.chan[8].time,signal=d.chan[8].temp,tcyclerange=tcyclerange,tfactor=tfactor, uptfactor=uptfactor, dachan=dachan)

Inter_Te_8=mean(q8.divtemp[where(q8.time gt -4 and q8.time lt -1 and q8.divtemp gt 5 and q8.divtemp lt 80)]) ;for Inter-ELM

Intra_Te_8=mean(q8.divtemp[where(q8.time gt 0 and q8.time lt 1 and q8.divtemp gt 10 and q8.divtemp lt 100)]) ;for Intra-ELM, 0 to 1.5 for SAS V1

;A-8

q9=get_ptname_elm(shot,'divtemp',trange=trange,times=d.chan[9].time,signal=d.chan[9].temp,tcyclerange=tcyclerange,tfactor=tfactor, uptfactor=uptfactor, dachan=dachan)

Inter_Te_9=mean(q9.divtemp[where(q9.time gt -4 and q9.time lt -1 and q9.divtemp gt 5 and q9.divtemp lt 80)]) ;for Inter-ELM

Intra_Te_9=mean(q9.divtemp[where(q9.time gt 0 and q9.time lt 1 and q9.divtemp gt 10 and q9.divtemp lt 100)]) ;for Intra-ELM, 0 to 1.5 for SAS V1

;A-9

q10=get_ptname_elm(shot,'divtemp',trange=trange,times=d.chan[10].time,signal=d.chan[10].temp,tcyclerange=tcyclerange,tfactor=tfactor, uptfactor=uptfactor, dachan=dachan)

Inter_Te_10=mean(q10.divtemp[where(q10.time gt -4 and q10.time lt -1 and q10.divtemp gt 5 and q10.divtemp lt 80)]) ;for Inter-ELM

Intra_Te_10=mean(q10.divtemp[where(q10.time gt 0 and q10.time lt 1 and q10.divtemp gt 10 and q10.divtemp lt 100)]) ;for Intra-ELM, 0 to 1.5 for SAS V1

;A-10 (Vertex)

q11=get_ptname_elm(shot,'divtemp',trange=trange,times=d.chan[11].time,signal=d.chan[11].temp,tcyclerange=tcyclerange,tfactor=tfactor, uptfactor=uptfactor, dachan=dachan)

Inter_Te_11=mean(q11.divtemp[where(q11.time gt -4 and q11.time lt -1 and q11.divtemp gt 5 and q11.divtemp lt 80)]) ;for Inter-ELM

Intra_Te_11=mean(q11.divtemp[where(q11.time gt 0 and q11.time lt 1 and q11.divtemp gt 10 and q11.divtemp lt 100)]) ;for Intra-ELM, 0 to 1.5 for SAS V1

;A-11

q12=get_ptname_elm(shot,'divtemp',trange=trange,times=d.chan[12].time,signal=d.chan[12].temp,tcyclerange=tcyclerange,tfactor=tfactor, uptfactor=uptfactor, dachan=dachan)

Inter_Te_12=mean(q12.divtemp[where(q12.time gt -4 and q12.time lt -1 and q12.divtemp gt 5 and q12.divtemp lt 80)]) ;for Inter-ELM

Intra_Te_12=mean(q12.divtemp[where(q12.time gt 0 and q12.time lt 1 and q12.divtemp gt 10 and q12.divtemp lt 100)]) ;for Intra-ELM, 0 to 1.5 for SAS V1

;A-12 (OSP)

q13=get_ptname_elm(shot,'divtemp',trange=trange,times=d.chan[13].time,signal=d.chan[13].temp,tcyclerange=tcyclerange,tfactor=tfactor, uptfactor=uptfactor, dachan=dachan)

Inter_Te_13=mean(q13.divtemp[where(q13.time gt -4 and q13.time lt -1 and q13.divtemp gt 5 and q13.divtemp lt 80)]) ;for Inter-ELM

Intra_Te_13=mean(q13.divtemp[where(q13.time gt 0 and q13.time lt 1 and q13.divtemp gt 10 and q13.divtemp lt 100)]) ;for Intra-ELM, 0 to 1.5 for SAS V1

;A-13

q14=get_ptname_elm(shot,'divtemp',trange=trange,times=d.chan[14].time,signal=d.chan[14].temp,tcyclerange=tcyclerange,tfactor=tfactor, uptfactor=uptfactor, dachan=dachan)

Inter_Te_14=mean(q14.divtemp[where(q14.time gt -4 and q14.time lt -1 and q14.divtemp gt 5 and q14.divtemp lt 80)]) ;for Inter-ELM

Intra_Te_14=mean(q14.divtemp[where(q14.time gt 0 and q14.time lt 1 and q14.divtemp gt 10 and q14.divtemp lt 100)]) ;for Intra-ELM, 0 to 1.5 for SAS V1

;A-14 (View 1)

q15=get_ptname_elm(shot,'divtemp',trange=trange,times=d.chan[15].time,signal=d.chan[15].temp,tcyclerange=tcyclerange,tfactor=tfactor, uptfactor=uptfactor, dachan=dachan)

Inter_Te_15=mean(q15.divtemp[where(q15.time gt -4 and q15.time lt -1 and q15.divtemp gt 5 and q15.divtemp lt 80)]) ;for Inter-ELM

Intra_Te_15=mean(q15.divtemp[where(q15.time gt 0 and q15.time lt 1 and q15.divtemp gt 10 and q15.divtemp lt 100)]) ;for Intra-ELM, 0 to 1.5 for SAS V1

```
Inter_temp = [Inter_Te_6, Inter_Te_7, Inter_Te_8, Inter_Te_9, Inter_Te_10, Inter_Te_11,
Inter_Te_12, Inter_Te_13, Inter_Te_14, Inter_Te_15]

Intra_temp = [Intra_Te_6, Intra_Te_7, Intra_Te_8, Intra_Te_9, Intra_Te_10, Intra_Te_11,
Intra_Te_12, Intra_Te_13, Intra_Te_14, Intra_Te_15]


print, 'Inter-ELM Electron Temperature', Inter_temp

print, 'Intra-ELM Electron Temperature', Intra_temp


;stop

;---------------------------------------------------------------------


;DEUTERIUM

if keyword_set (DA) then begin

d_alpha=get_sasvw_fscope(shot, 2, 'DA')

da=get_ptname_elm(shot, 'da', trange=trange,tcyclerange=tcyclerange,
signal=d_alpha.cali,times=d_alpha.time, dachan=dachan, tfactor=tfactor, uptfactor=uptfactor,
elmtimes=elmtimes)

print, 'D_Alpha', da.da

print, 'time', da.time

;print, 'D_Alpha Error', da.error


damaxdensity=((da.da)/max(da.da))*maxdivdens*1e6


DA_SXB=fltarr(n_elements(da.time))

for n=0,n_elements(DA_SXB)-1 do DA_SXB[n]=get_sxb_da(damaxdensity[n],Intradivtemp)

print, 'da sxb', DA_SXB

;stop

j=plot(da.time,da.da*DA_SXB*4*!pi,"r4-",ytitle='D_Alpha (atoms*cm-2*s-1)', xtitle='Time
(ms)', xrange=tcyclerange, yrange=[0,5e18], window_title='D_Alpha inferred Ion Flux')
```

```
;j=errorplot(da.time, da.da*DA_SXB*4*!pi, fltarr(n_elements(da.time)),
da.error*DA_SXB*4*!pi, "m4", overplot=1)

;print, 'Intra D_Alpha Error', DaIntraError


;Intra-ELM Deuterium

DA_Intra = INT_TABULATED(da.time[where(da.time gt 0 and da.time lt
2.5)],da.da[where(da.time gt 0 and da.time lt 2.5)]*DA_SXB[where(da.time gt 0 and da.time lt
2.5)])*0.001*4*!pi

print,'DA INTRA', DA_Intra


;stop

;Inter-ELM Deuterium

;DA_Inter = INT_TABULATED(da.time[where(da.time gt -4 and da.time lt -
1)],da.da[where(da.time gt -4 and da.time lt -1)]*DA_SXB[where(da.time gt -4 and da.time lt -
1)])*0.001*4*!pi

;print, 'DA INTER', DA_Inter


;Intra-ELM Deuterium Error

DA_Intra_Error = INT_TABULATED(da.time[where(da.time gt 0 and da.time lt
2.5)],da.error[where(da.time gt 0 and da.time lt 2.5)]*DA_SXB[where(da.time gt 0 and da.time
lt 2.5)])*0.001*4*!pi

print,'DA INTRA Error', DA_Intra_Error


;Inter-ELM Deuterium Error

;DA_Inter_Error = INT_TABULATED(da.time[where(da.time gt -4 and da.time lt -
1)],da.error[where(da.time gt -4 and da.time lt -1)]*DA_SXB[where(da.time gt -4 and da.time lt
-1)])*0.001*4*!pi

;print, 'DA INTER Error', DA_Inter_Error


;stop

endif
```

```
;-------------------------------------------------------------------------------------------------------------------------------------------------------

;CARBON

if keyword_set (C3) then begin

carbon_3=get_sasvw_fscope(shot, 2, 'C3')

c3=get_ptname_elm(shot, 'c3', trange=trange,tcyclerange=tcyclerange,
signal=carbon_3.cali,times=carbon_3.time, dachan=dachan, tfactor=tfactor, uptfactor=uptfactor,
elmtimes=elmtimes)

;print, 'Carbon III', c3.c3

;print, 'time', c3.time

;print, 'Carbon III Error', c3.error


c3maxdensity=((c3.c3)/max(c3.c3))*maxdivdens*1e6


C3_SXB=fltarr(n_elements(c3.time))

for n=0,n_elements(C3_SXB)-1 do C3_SXB[n]=get_sxb_ciii(c3maxdensity[n],Intradivtemp)


print, 'c3 sxb', C3_SXB

;print, c3.c3


;C_DURING_ELMS=plot(c3.time,c3.c3*C3_SXB*4*!pi,"r4-",ytitle='CIII (atoms*cm-2*s-1)',
xtitle='Time (ms)', xrange=tcyclerange, yrange=[0,1e17], window_title='CIII Ion Flux')

;C_BETWEEN_ELMS=plot(carbon_3.time,smooth(carbon_3.cali,5000),"r4-",ytitle='CIII
(atoms*cm-2*s-1)', xtitle='Time (ms)', xrange=trange, yrange=[0,1e15], window_title='CIII Ion
Flux')


;Dalpha=plot(d_alpha.time,smooth(d_alpha.cali,5000),"r4-",ytitle='DA (atoms*cm-2*s-1)',
xtitle='Time (ms)', xrange=trange, yrange=[0,1e17], window_title='DA inferred Ion Flux')

;help, d.chan[q].dens
```

```
;help, carbon_3.cali

;help, d_alpha.cali

;help, (an.cali-R1*am.cali)/(1-R1)


;stop


DENS=CONGRID(d.chan[q].dens, N_ELEMENTS(d_alpha.cali))

;help, DENS


;stop


;DA_SXB2=fltarr(n_elements(d_alpha.time))

;for n=0,n_elements(DA_SXB2)-1 do DA_SXB2[n]=get_sxb_da(DENS[n]*1e6,Interdivtemp)

DA_SXB2=get_sxb_da(avgdivdens*1e6,Interdivtemp)


;C3_SXB2=fltarr(n_elements(carbon_3.time))

;for n=0,n_elements(C3_SXB2)-1 do C3_SXB2[n]=get_sxb_ciii(DENS[n]*1e6,Interdivtemp)

C3_SXB2=get_sxb_ciii(avgdivdens*1e6,Interdivtemp)


WI_SXB2=get_sxb_wi(avgdivdens*1e6,Interdivtemp)


;C=plot(carbon_3.time,smooth((carbon_3.cali*C3_SXB2),5000),"r4-", ytitle='C', xtitle='Time
(ms)', xrange=trange, yrange=[0,2e15], window_title='C')

;W=plot(an.time,smooth((an.cali-R1*am.cali)/(1-R1)*(WI_SXB2),2000),"r4-", ytitle='W',
xtitle='Time (ms)', xrange=trange, yrange=[0,2e14], window_title='W')

;stop


C_flux = mean(smooth((carbon_3.cali[where(carbon_3.time gt trange[0] and carbon_3.time lt
trange[-1])]*C3_SXB2),10000))
```

```
;print, 'C flux', C_flux


W_flux = mean((smooth((an.cali[where(an.time gt trange[0] and an.time lt trange[-1])]-
R1*am.cali[where(am.time gt trange[0] and am.time lt trange[-1])]),2000)/(1-R1)))*WI_SXB2

;print, 'W flux', W_flux


C_W = W_flux/C_flux

;print, 'W/C', W_flux/C_flux

;W_C=plot(carbon_3.time, smooth((an.cali-R1*am.cali)/(1-
R1)*(WI_SXB2),2000)/smooth((carbon_3.cali*C3_SXB2),10000),"r4-", ytitle='W/C',
xtitle='Time (ms)', xrange=trange, yrange=[0,0.2], window_title='W/C')


;stop


;C_W_ratio=plot(carbon_3.time,smooth((carbon_3.cali*C3_SXB2)/(((an.cali-R1*am.cali)/(1-
R1))*WI_SXB2),2000),"r4-", ytitle='C%', xtitle='Time (ms)', xrange=trange, yrange=[0,1],
window_title='C%')

;stop


;C_percentage=plot(carbon_3.time,smooth(((carbon_3.cali*C3_SXB2)/(d_alpha.cali*DA_SXB2
)),2000),"r4-", ytitle='C%', xtitle='Time (ms)', xrange=trange, yrange=[0,0.1],
window_title='C%')

;stop


C_D_INTRA=plot(c3.time,((c3.c3*C3_SXB)/((da.da*DA_SXB)+(c3.c3*C3_SXB))*100),"r4-
",ytitle='C Plasma Impurity Percentage (%)', xtitle='Time Relative to ELM Start (ms)',
xrange=tcyclerange, yrange=[0,10], window_title='C Plasma Impurity Percentage')

;stop

fc = (c3.c3*C3_SXB)/((da.da*DA_SXB)+(c3.c3*C3_SXB))


Inter_fc=mean(fc[where(c3.time gt -5 and c3.time lt -2)])*100
```

```
;print, 'Inter-ELM C3', Inter_fc

Intra_fc=mean(fc[where(c3.time gt 0 and c3.time lt 2.5)])*100

;print, 'Intra-ELM C3', Intra_fc


C3_Intra = INT_TABULATED(c3.time[where(c3.time gt 0 and c3.time lt
2.5)],c3.c3[where(c3.time gt 0 and c3.time lt 2.5)]*C3_SXB[where(c3.time gt 0 and c3.time lt
2.5)])*0.001*4*!pi ;Intra-ELM Carbon

;print,'C3 INTRA', C3_Intra


;C3_Inter = INT_TABULATED(c3.time[where(c3.time gt -4 and c3.time lt -
1)],c3.c3[where(c3.time gt -4 and c3.time lt -1)]*C3_SXB[where(c3.time gt -4 and c3.time lt -
1)])*0.001*4*!pi ;Inter-ELM Carbon

;print, 'C3 INTER', C3_Inter


C3_Intra_Error = INT_TABULATED(c3.time[where(c3.time gt 0 and c3.time lt
2.5)],c3.error[where(c3.time gt 0 and c3.time lt 2.5)]*C3_SXB[where(c3.time gt 0 and c3.time lt
2.5)])*0.001*4*!pi ;Intra-ELM Carbon

;print,'C3 INTRA Error', C3_Intra_Error


;C3_Inter_Error = INT_TABULATED(c3.time[where(c3.time gt -4 and c3.time lt -
1)],c3.error[where(c3.time gt -4 and c3.time lt -1)]*C3_SXB[where(c3.time gt -4 and c3.time lt -
1)])*0.001*4*!pi ;Inter-ELM Carbon

;print, 'C3 INTER Error', C3_Inter_Error


;stop

endif


;---------------------------------------------------------------------


;SAS SXB COEFFICIENTS
```

```
;INTRA-ELM

newsxbintra=fltarr(n_elements(str1.time))

;for n=0,n_elements(newsxb)-1 do print,'sxb',

;get_sxb_wi(density[n],avgdivtemp)

;Intradivtemp = 34.5

for n=0,n_elements(newsxbintra)-1 do
newsxbintra[n]=get_new_sxb_wi(maxdensity[n],Intradivtemp)

;help, newsxbintra

print,'Wi SXB', newsxbintra

;stop


I1=str1.int_wi_fscope1 ;photons

I6=str6.int_wi_fscope6 ;photons

I7=str7.int_wi_fscope7 ;photons

IE67 = I6-I7

;IE1=sqrt((str1.error)^2 + ((IE67)^2)) ; photons STD

;print, 'ERROR', IE1

;IE1=str1.error ;W error for shots 191005-6 & 191016-7 only

;print, 'I1', I1

;print, 'IE1', IE1

;print, 'error %', IE1/I1


W1 = INT_TABULATED(str1.time[where(str1.time gt -0.5 and str1.time lt
2.5)],I1[where(str1.time gt -0.5 and str1.time lt 2.5)]*newsxbintra[where(str1.time gt -0.5 and
str1.time lt 2.5)])*0.001*4*!pi ;W atoms per ELM per cm^2

;WE1 = INT_TABULATED(str1.time,IE1*newsxbintra)*0.001*4*!pi ;W atoms

;error per ELM


print,'Intra-ELM Erosion:', W1, 'atoms/ELM/cm^2'
```

```
;print,'Intra-ELM Erosion ERROR:', WE1, 'atoms/ELM/cm^2'

;stop


;help, str1.time

;help, c3.time


W_INTRA=plot(str1.time,I1*newsxbintra,"r4-",ytitle='Intra-ELM W erosion (atoms*cm-2*s-1)',
xtitle='Time (ms)', xrange=[-50,0], yrange=[0,4e13], window_title='correctelms')

;stop

;W_C_INTRA=plot(c3.time,(I1*newsxbintra/(c3.c3*C3_SXB)),"r4-",ytitle='W/C Ratio',
xtitle='Time (ms)', xrange=[-4,4], yrange=[0,1], window_title='W/C Ratio')


;stop


;INTER-ELM

I2=str2.int_wi_fscope2

print, 'inter-ELM photon intensity', I2

I3=str3.int_wi_fscope3

I4=str4.int_wi_fscope4

I5=sqrt((str3.error)^2 + (str4.error)^2)

newsxbinter2=fltarr(n_elements(str2.time))

for n=0,n_elements(newsxbinter2)-1 do
newsxbinter2[n]=get_new_sxb_wi(avgdensity2[n],Interdivtemp)


Inter_Summed = INT_TABULATED(str2.time,I2*newsxbinter2)*0.001*4*!pi ;W atoms per
ELM

print, 'Inter-ELM EROSION', Inter_Summed

;stop


newsxbinter3=fltarr(n_elements(str3.time))
```

```
for n=0,n_elements(newsxbinter3)-1 do
newsxbinter3[n]=get_sxb_wi(avgdensity3[n],Interdivtemp)


newsxbinter4=fltarr(n_elements(str4.time))

for n=0,n_elements(newsxbinter4)-1 do
newsxbinter4[n]=get_sxb_wi(avgdensity4[n],Interdivtemp)


;W2 = INT_TABULATED(str2.time,I2*newsxbinter2)*0.001*4*!pi

;W3 = INT_TABULATED(str3.time,I3*newsxbinter3)*0.001*4*!pi

;W4 = INT_TABULATED(str4.time,I4*newsxbinter4)*0.001*4*!pi

W5 = INT_TABULATED(str2.time,I5*newsxbinter4)*0.001*4*!pi

;print,'Inter-ELM Erosion 1:', W2, 'atoms/ELM/cm^2'

;print,'Inter-ELM Erosion 2:', W3, 'atoms/ELM/cm^2'

;print,'Inter-ELM Erosion 3:', W4, 'atoms/ELM/cm^2'

;print,'Inter-ELM Erosion Error:', W5, 'atoms/ELM/cm^2'

;print, 'FELM', c

;for i=0,nelms-1 do print, INT_TABULATED(a.time,a.GAMMA_W_all[*,i]*newsxb)*0.001

;totparticlescm2selm = avgparticlescm2elm*c

;print,'total W erosion rate (atoms/cm2/s)', totparticlescm2selm


endif


;-------------------------------------------------------------;



;METAL RINGS CAMPAIGN CODE


;INTRA-ELM ANALYSIS

if keyword_set (intra_ELMs) then begin
```

```
d=get_lp(shot)

a=get_wi_elm(shot, trange=trange, elmtimes=elmtimes, view=view, tcyclerange=tcyclerange,
sxb=sxb, tfactor=tfactor, dachan=fs06)


;Divertor density just before ELM crash

ned=get_ptname_elm(shot,'divdens',trange=trange,times=d.chan[6].time,signal=d.chan[6].dens,t
cyclerange=[-1,4],tfactor=tfactor) ;for mid inlcude upfactor=upfactor

plot,ned.time,ned.divdens,psym=5,symsize=2,yra=[0,2e14]

;l=plot(ned.time,ned.divdens,yra=[0,1.5e12],"r4-",ytitle='Divertor

;Density', xtitle='Time (ms)', overplot=1, xrange=tcyclerange, window_title='Divertor Density')

avgdivdens=mean(ned.divdens[where(ned.time gt 0 and ned.time lt 5 and ned.divdens gt 2e13
and ned.divdens lt 1.6e14)])

maxdivdens=max(ned.divdens[where(ned.time gt 0 and ned.time lt 2 and ned.divdens gt 2e13
and ned.divdens lt 1.6e14)])

meandivdens=mean(ned.divdens[where(ned.time gt 0 and ned.time lt 2 and ned.divdens gt 2e13
and ned.divdens lt 1.6e14)])

;avgdivdens=1.6e14

print,'average divertor density', avgdivdens

print,'max ELM divertor density', maxdivdens

print, 'mean ELM divertor desnity', meandivdens


maxdensity=(a.GAMMA_W)/max(a.GAMMA_W)*maxdivdens*1e6


;w=plot(d.chan[q].time, d.chan[q].dens,xra=trange,yra=[0,1e14],window_title='density')

;stop


;Divertor temperature just before ELM crash

ted=get_ptname_elm(shot,'divtemp',trange=trange,times=d.chan[6].time,signal=d.chan[6].temp,t
cyclerange=[-1,4],tfactor=tfactor);for mid inlcude upfactor=upfactor
```

```
plot,ted.time,ted.divtemp,psym=5,symsize=2,yra=[0,120]

avgdivtemp=mean(ted.divtemp[where(ted.time gt 0 and ted.time lt 5.0 and ted.divtemp gt 5 and ted.divtemp lt 80)])

maxdivtemp=max(ted.divtemp[where(ted.time gt 0 and ted.time lt 2 and ted.divtemp gt 5 and ted.divtemp lt 80)])

meandivtemp=mean(ted.divtemp[where(ted.time gt 0 and ted.time lt 2 and ted.divtemp gt 5 and ted.divtemp lt 80)])

Intradivtemp=meandivtemp

;maxdivtemp=20

print, 'average divertor temperature', avgdivtemp

print, 'max ELM divertor temperature', maxdivtemp

print, 'mean ELM divertor temperature', meandivtemp

;stop


;print, 'D_Alpha Error', da.error


;DA_SXB=fltarr(n_elements(a.time))

for n=0,n_elements(DA_SXB)-1 do DA_SXB[n]=get_sxb_da(density[n],Intradivtemp)

;stop


endif


;-------------------------------------------------------------;



if keyword_set (FSRM) then begin


;PEDESTAL BEFORE CRASH
```

```
;Density
nep=get_ptname_elm(shot,'prmtan_neped',trange=trange,tcyclerange=[-10,10])
plot,nep.time,nep.prmtan_neped,psym=5,symsize=2
neped=mean(nep.prmtan_neped[where(nep.time gt -2 and nep.time lt 1 and nep.prmtan_neped gt 6e19 and nep.prmtan_neped lt 9e19)]) ;6-9e19 and max for MRC, 2e19 to 4e19 and mean for SAS
print,'pedestal density', neped

;stop

;Temperature
tep=get_ptname_elm(shot,'prmtan_teped',trange=trange,tcyclerange=[-10,10])
plot,tep.time,tep.prmtan_teped,psym=5,symsize=2
teped=mean(tep.prmtan_teped[where(tep.time gt -2 and tep.time lt 1 and tep.prmtan_teped gt 200 and tep.prmtan_teped lt 400)]) ;200-400 and max for MRC, 300 to 1300 and mean for SAS
print,'pedestal temperature', teped

;stop

;ANGLE
;ang=calc_angle_actual(shot, tstart, tend) ;/SAS for SAS
ang=calc_angle_lp(shot, tstart, tend)
help, ang
print,'ang', ang
;ang=0.9
; 0.9 for sas, 2 for mrc
;cerafzt7=2.8 ;for shot 191016

;FC
```

```
;Intradivtemp = 45

;For MRC:
gadat,x,y,'cerafzt10',shot ;use cerafzt10 for MRC, cerafzt7 for SAS
cerafzt7=mean(y[where(x gt tstart and x lt tend)])
intra_fc = cerafzt7

;intra_fc = 4.5 ;use manual input if CIII filterscope tripped
print, 'intra_fc', intra_fc
print, 'divtemp', intradivtemp

;FSRM W EROSION
graph=elm_werosion_moulton(neped,teped,clstar=18*!pi,theta0=2*!pi,divtemp=Intradivtemp,
divdens=maxdensity,angle=ang,fc=intra_fc/100,reff=0.96)
print, maxdensity

;fc =cerafxt10 for MRC, fc=cerafzt7 for SAS, divtemp=Intradivtemp, 0.96 for MRC, 0.983
seems most accurate for SAS
;print, "Time Array", graph.time[where(graph.time gt 0 and graph.time lt 0.0025)]

;avgpcm2elm=INT_TABULATED(graph.time[where(graph.time gt -0.0005 and graph.time lt
0.0025)],graph.gamma_w[where(graph.time gt -0.0005 and graph.time lt 0.0025)])*0.0001
;SAS-VW

avgpcm2elm=INT_TABULATED(graph.time[where(graph.time gt 0.0 and graph.time lt
0.004)],graph.gamma_w[where(graph.time gt 0.0 and graph.time lt 0.004)])*0.0001
;MRC

;avgpscm2elm=avgpcm2elm/((trange[-1]-trange[0])*0.001)
print,'FSRM average erosion per ELM (atoms/cm2)', avgpcm2elm
```

```
;stop


f=plot(graph.time*1e3,graph.gamma_w/1e4, xrange=[-0.5,2.5],xtitle='ELM time (ms)',ytitle='W
erosion (cm-2 s-1)') ;-1 to 4 for MRC, -0.5 to 2.5 for SAS


;FSRM Te & Ti

T_e=plot(graph.time*1e3,graph.temp_e, xrange=[-0.5,2.5],xtitle='ELM time
(ms)',ytitle='electron temperature') ;-1 to 4 for MRC, -0.5 to 2.5 for SAS

T_i=plot(graph.time*1e3,graph.temp_i, xrange=[-0.5,2.5],xtitle='ELM time (ms)',ytitle='ion
temperature') ;-1 to 4 for MRC, -0.5 to 2.5 for SAS


Te_avg = mean(graph.temp_e[where(graph.time gt 0 and graph.time lt 0.0025)])

print, 'Te_avg', Te_avg


Ti_avg = mean(graph.temp_i[where(graph.time gt 0 and graph.time lt 0.0025)])

print, 'Ti_avg', Te_avg


;stop


;ION FLUXES

ionfluxgraph=plot(graph.time*1e3,graph.total_ionflux_perp,
xrange=[tcyclerange[0],tcyclerange[-1]],xtitle='ELM time (ms)',ytitle='ion flux') ;-1 to 4 for
MRC, -0.5 to 2.5 for SAS

;stop

;ionfluxgraph=plot(graph.time*1e3,(graph.density + graph.ne_extra), xrange=[-
0.5,2.5],xtitle='ELM time (ms)',ytitle='density') ;0 to 4 for MRC, 0 to 2.5 for SAS


print, 'mean ion flux (ions/cm2)', INT_TABULATED(graph.time[where(graph.time gt 0.0 and
graph.time lt 0.004)],graph.total_ionflux_perp[where(graph.time gt 0.0 and graph.time lt
0.004)])*0.0001
```

```
print, 'max ion flux rate (ions/cm2/s)', max(graph.total_ionflux_perp[where(graph.time gt tcyclerange[0] and graph.time lt tcyclerange[-1])])*0.0001

;stop

recycled_d_flux = INT_TABULATED(graph.time[where(graph.time gt 0 and graph.time lt tcyclerange[-1]*0.001)],graph.recycled_d_flux[where(graph.time gt 0 and graph.time lt tcyclerange[-1]*0.001)])

recycled_c_flux = INT_TABULATED(graph.time[where(graph.time gt 0 and graph.time lt tcyclerange[-1]*0.001)],graph.recycled_c_flux[where(graph.time gt 0 and graph.time lt tcyclerange[-1]*0.001)])

print, 'reycled D flux', recycled_d_flux

print, 'recycled C flux', recycled_c_flux

;stop

ionflux_c_perp = INT_TABULATED(graph.time[where(graph.time gt tcyclerange[0]*0.001 and graph.time lt tcyclerange[-1]*0.001)],graph.ionflux_c_perp[where(graph.time gt tcyclerange[0]*0.001 and graph.time lt tcyclerange[-1]*0.001)])

ionflux_d_perp = INT_TABULATED(graph.time[where(graph.time gt tcyclerange[0]*0.001 and graph.time lt tcyclerange[-1]*0.001)],graph.ionflux_perp[where(graph.time gt tcyclerange[0]*0.001 and graph.time lt tcyclerange[-1]*0.001)]) - ionflux_c_perp

print, 'free stream D flux', ionflux_d_perp

print, 'free stream C flux', ionflux_c_perp

ionflux_perp = INT_TABULATED(graph.time[where(graph.time gt tcyclerange[0]*0.001 and graph.time lt tcyclerange[-1]*0.001)],graph.ionflux_perp[where(graph.time gt tcyclerange[0]*0.001 and graph.time lt tcyclerange[-1]*0.001)])

recyc_ionflux_perp = INT_TABULATED(graph.time[where(graph.time gt tcyclerange[0]*0.001 and graph.time lt tcyclerange[-1]*0.001)],graph.recyc_ionflux_perp[where(graph.time gt tcyclerange[0]*0.001 and graph.time lt tcyclerange[-1]*0.001)])
```

```
print, 'recycle : free streaming ratio', recyc_ionflux_perp/ionflux_perp


;stop


recyc_fraction = (INT_TABULATED(graph.time[where(graph.time gt tcyclerange[0]*0.001 and
graph.time lt tcyclerange[-1]*0.001)],graph.recyc_ionflux_perp[where(graph.time gt
tcyclerange[0]*0.001 and graph.time lt tcyclerange[-
1]*0.001)]))/(INT_TABULATED(graph.time[where(graph.time gt tcyclerange[0]*0.001 and
graph.time lt tcyclerange[-1]*0.001)],graph.total_ionflux_perp[where(graph.time gt
tcyclerange[0]*0.001 and graph.time lt tcyclerange[-1]*0.001)]))


;print, 'recyc_fraction', recyc_fraction


FD_recyc = recycled_d_flux/(recycled_d_flux + ionflux_d_perp)

;print, 'FD_recyc', FD_recyc


FC_recyc = recycled_c_flux/(recycled_c_flux + ionflux_c_perp)

;print, 'FC_recyc', FC_recyc



;ION ENERGIES



;Deuterium Ei

Ei =  graph.Ei[where(graph.time gt 0 and graph.time lt 0.0025)]

;print, "Ei Array", Ei


D_flux = (graph.ionflux_perp[where(graph.time gt 0 and graph.time lt 0.0025)] -
graph.ionflux_c_perp[where(graph.time gt 0 and graph.time lt 0.0025)])

;print, "D Array", D_flux
```

```
Ed_int = INT_TABULATED(graph.time[where(graph.time gt -0.0005 and graph.time lt 0.0025)],Ei*D_flux)

D_int = INT_TABULATED(graph.time[where(graph.time gt -0.0005 and graph.time lt 0.0025)],D_flux)


;print, "FSRM Deuterium Flux", D_int


Ei_avg = mean(Ed_int/D_int)

;print, "Ed avg", Ei_avg



;Carbon Ei

Ec = graph.Ec[where(graph.time gt 0 and graph.time lt 0.0025)]

;print, "Ec Array", Ec


C_flux =  graph.ionflux_c_perp[where(graph.time gt 0 and graph.time lt 0.0025)]

;print, "C Array", C_flux


Ec_int = INT_TABULATED(graph.time[where(graph.time gt -0.0005 and graph.time lt 0.0025)],Ec*C_flux)

C_int = INT_TABULATED(graph.time[where(graph.time gt -0.0005 and graph.time lt 0.0025)],C_flux)


;print, "FSRM Carbon Flux", C_int


Ec_avg = mean(Ec_int/C_int)

;print, "Ec avg", Ec_avg


;FSRM mean and peak ELM HEAT FLUX values (not integrated)
```

```
;print, 'mean heat flux', mean(graph.total_heatflux_perp[where(graph.time gt -0.0005 and graph.time lt 0.0025)])

;print, 'peak heat flux', max(graph.total_heatflux_perp[where(graph.time gt -0.0005 and graph.time lt 0.0025)])

;stop


;WMHDF

if keyword_set (wmhdf) then begin

wmhdf=get_ptname_elm(shot, 'wmhdf', trange=trange, tcyclerange=[-5,5], tfactor=tfactor, uptfactor=uptfactor,  elmtimes=elmtimes, times=times, signal=signal, /intersub) ;/inersub

;print, wmhdf.wmhdf

;print, wmhdf.time

;print, wmhdf.error


ELM_Energy = INT_TABULATED(wmhdf.time[where(wmhdf.time gt 0 and wmhdf.time lt 2.5)],wmhdf.wmhdf[where(wmhdf.time gt 0 and wmhdf.time lt 2.5)])

ELM_Energy_Error = INT_TABULATED(wmhdf.time[where(wmhdf.time gt 0 and wmhdf.time lt 2.5)],wmhdf.error[where(wmhdf.time gt 0 and wmhdf.time lt 2.5)])


;print, 'Experiment ELM Energy(J)', ELM_Energy

;print, 'Experiment ELM Energy Error (J)', ELM_Energy_Error


wmhdf_perp = INT_TABULATED(graph.time[where(graph.time gt 0 and graph.time lt 0.0025)],graph.wmhdf_perp[where(graph.time gt 0 and graph.time lt 0.0025)])

;print, 'energy fluence (J)', wmhdf_perp


;stop


;FSRM PREDICTED INTER-ELM DENSITY
```

```
print, 'inter-ELM density', mean(graph.density[where(graph.time gt -0.0005 and graph.time lt 0)]) + mean(graph.ne_extra[where(graph.time gt -0.0005 and graph.time lt 0)]) ;do not include *sin(ang*!pi/180.)

print, 'mean density', mean(graph.density[where(graph.time gt -0.0005 and graph.time lt 0.0025)]) + mean(graph.ne_extra[where(graph.time gt -0.0005 and graph.time lt 0.0025)]) ;do not include *sin(ang*!pi/180.)

print, 'max density', max(graph.density[where(graph.time gt -0.0005 and graph.time lt 0.0025)]) + max(graph.ne_extra[where(graph.time gt -0.0005 and graph.time lt 0.0025)]) ;do not include*sin(ang*!pi/180.)


stop

endif


endif


;-------------------------------------------------------------;


;EXPERIMENTAL ION FLUX


if keyword_set (ion) then begin


d=get_lp(shot)

;help, d.chan[13]

;6 refers to the R=1.42 m | Z=-1.25 m LP position for MRC

;13 refers to SAS-VW R=1.49 m | Z=1.20 m V2 position


;Magnetic Field Inclination Angle

;ang=calc_angle_actual(shot, tstart, tend, /SAS) ;/SAS for SAS

ang=calc_angle_lp(shot, tstart, tend)

help, ang
```

```
print,'ang', ang

;print,'lp_ang', lp_ang

;ang=0.9


jed=get_ptname_elm(shot,'jsat',trange=trange,times=d.chan[13].time,signal=d.chan[13].jsat,tcyclerange=[-4,4],tfactor=tfactor)


inter_mean=mean(jed.jsat[where(jed.time gt -4 and jed.time lt -1 and jed.jsat gt 0 and jed.jsat lt 20)])

inter_mean_ionflux = (inter_mean*sin(ang*!PI/180)/(1.602e-19))

print, 'inter-ELM Ion Flux (ions/cm2/s)', inter_mean_ionflux


intra_max=max(jed.jsat[where(jed.time gt 0 and jed.time lt 2 and jed.jsat gt 5 and jed.jsat lt 100)])

intra_max_ionflux = (intra_max*sin(ang*!PI/180)/(1.602e-19))

print, 'max intra-ELM Ion Flux (ion/cm2/s)', intra_max_ionflux


intra_mean = mean(jed.jsat[where(jed.time gt 0 and jed.time lt 2.5 and jed.jsat gt 5 and jed.jsat lt 100)])

intra_mean_ionflux = (intra_mean*sin(ang*!PI/180)/(1.602e-19))

print, 'mean intra-ELM Ion Flux (ions/cm2)', (intra_mean_ionflux-inter_mean_ionflux)*0.001*2.5


;intra_mean = INT_TABULATED(jed.time[where(jed.time gt 0 and jed.time lt 4)],jed.jsat[where(jed.time gt 0 and jed.time lt 4.0)]


h=plot(jed.time, jed.jsat, xra=[-4,4], yra=[0,50], window_title='OSP ion saturation current')

plot,jed.time,jed.jsat,psym=5,symsize=2

stop
```

```
;jsat in units of A/cm^2

;=ions/cm^2/s


;Retrieve ELM-resolved ion saturation current

jed6=get_ptname_elm(shot,'jsat',trange=trange,times=d.chan[6].time,signal=d.chan[6].jsat,tcyclerange=[-1,4],tfactor=tfactor)

jed7=get_ptname_elm(shot,'jsat',trange=trange,times=d.chan[7].time,signal=d.chan[7].jsat,tcyclerange=[-1,4],tfactor=tfactor)

jed8=get_ptname_elm(shot,'jsat',trange=trange,times=d.chan[8].time,signal=d.chan[8].jsat,tcyclerange=[-1,4],tfactor=tfactor)

jed9=get_ptname_elm(shot,'jsat',trange=trange,times=d.chan[9].time,signal=d.chan[9].jsat,tcyclerange=[-1,4],tfactor=tfactor)

jed10=get_ptname_elm(shot,'jsat',trange=trange,times=d.chan[10].time,signal=d.chan[10].jsat,tcyclerange=[-1,4],tfactor=tfactor)

jed11=get_ptname_elm(shot,'jsat',trange=trange,times=d.chan[11].time,signal=d.chan[11].jsat,tcyclerange=[-1,4],tfactor=tfactor)

jed12=get_ptname_elm(shot,'jsat',trange=trange,times=d.chan[12].time,signal=d.chan[12].jsat,tcyclerange=[-1,4],tfactor=tfactor)

jed13=get_ptname_elm(shot,'jsat',trange=trange,times=d.chan[13].time,signal=d.chan[13].jsat,tcyclerange=[-1,4],tfactor=tfactor)

jed14=get_ptname_elm(shot,'jsat',trange=trange,times=d.chan[14].time,signal=d.chan[14].jsat,tcyclerange=[-1,4],tfactor=tfactor)

jed15=get_ptname_elm(shot,'jsat',trange=trange,times=d.chan[15].time,signal=d.chan[15].jsat,tcyclerange=[-1,4],tfactor=tfactor)


h=plot(jed13.time, jed13.jsat, xra=[-0.5,2.5], yra=[0,50], window_title='OSP ion saturation current')

;stop

;plot,jed.time,jed.jsat,psym=5,symsize=2

;print, 'jsat', jed.jsat

;print, 'time', jed.time

;print, 'error', jed.error
```

;print, 'Ion STD', stddev(jed.jsat[where(jed.time gt -1 and jed.time lt 2 and jed.jsat gt 5 and jed.jsat lt 100)])*(sin(ang*!PI/180)/(1.602e-19))

;jsat in units of A/cm^2

;=ions/cm^2/s

;Intra-ELM

intra_max_6=max(jed6.jsat[where(jed6.time gt -1 and jed6.time lt 2 and jed6.jsat gt 5 and jed6.jsat lt 100)]) ; upper bounder of 100 or MRC, 50 for SAS

intra_max_7=max(jed7.jsat[where(jed7.time gt -1 and jed7.time lt 2 and jed7.jsat gt 5 and jed7.jsat lt 100)]) ; upper bounder of 100 or MRC, 50 for SAS

intra_max_8=max(jed8.jsat[where(jed8.time gt -1 and jed8.time lt 2 and jed8.jsat gt 5 and jed8.jsat lt 100)]) ; upper bounder of 100 or MRC, 50 for SAS

intra_max_9=max(jed9.jsat[where(jed9.time gt -1 and jed9.time lt 2 and jed9.jsat gt 5 and jed9.jsat lt 100)]) ; upper bounder of 100 or MRC, 50 for SAS

intra_max_10=max(jed10.jsat[where(jed10.time gt -1 and jed10.time lt 2 and jed10.jsat gt 5 and jed10.jsat lt 100)]) ; upper bounder of 100 or MRC, 50 for SAS

intra_max_11=max(jed11.jsat[where(jed11.time gt -1 and jed11.time lt 2 and jed11.jsat gt 5 and jed11.jsat lt 100)]) ; upper bounder of 100 or MRC, 50 for SAS

intra_max_12=max(jed12.jsat[where(jed12.time gt -1 and jed12.time lt 2 and jed12.jsat gt 5 and jed12.jsat lt 100)]) ; upper bounder of 100 or MRC, 50 for SAS

intra_max_13=max(jed13.jsat[where(jed13.time gt -1 and jed13.time lt 2 and jed13.jsat gt 5 and jed13.jsat lt 100)]) ; upper bounder of 100 or MRC, 50 for SAS

intra_max_14=max(jed14.jsat[where(jed14.time gt -1 and jed14.time lt 2 and jed14.jsat gt 5 and jed14.jsat lt 100)]) ; upper bounder of 100 or MRC, 50 for SAS

intra_max_15=max(jed15.jsat[where(jed15.time gt -1 and jed15.time lt 2 and jed15.jsat gt 5 and jed15.jsat lt 100)]) ; upper bounder of 100 or MRC, 50 for SAS

;print, 'peak intra-ELM jsat', intra_max_11, intra_max_12, intra_max_13, intra_max_14, intra_max_15

intra_mean_6=mean(jed6.jsat[where(jed6.time gt -0.5 and jed6.time lt 2.5 and jed6.jsat gt 5 and jed6.jsat lt 100)]) ; upper bounder of 10 for MRC, 50 for SAS

intra_mean_7=mean(jed7.jsat[where(jed7.time gt -0.5 and jed7.time lt 2.5 and jed7.jsat gt 5 and jed7.jsat lt 100)]) ; upper bounder of 10 for MRC, 50 for SAS

intra_mean_8=mean(jed8.jsat[where(jed8.time gt -0.5 and jed8.time lt 2.5 and jed8.jsat gt 5 and jed8.jsat lt 100)]) ; upper bounder of 10 for MRC, 50 for SAS

intra_mean_9=mean(jed9.jsat[where(jed9.time gt -0.5 and jed9.time lt 2.5 and jed9.jsat gt 5 and jed9.jsat lt 100)]) ; upper bounder of 10 for MRC, 50 for SAS

intra_mean_10=mean(jed10.jsat[where(jed10.time gt -0.5 and jed10.time lt 2.5 and jed10.jsat gt 5 and jed10.jsat lt 100)]) ; upper bounder of 10 for MRC, 50 for SAS

intra_mean_11=mean(jed11.jsat[where(jed11.time gt -0.5 and jed11.time lt 2.5 and jed11.jsat gt 5 and jed11.jsat lt 100)]) ; upper bounder of 10 for MRC, 50 for SAS

intra_mean_12=mean(jed12.jsat[where(jed12.time gt -0.5 and jed12.time lt 2.5 and jed12.jsat gt 5 and jed12.jsat lt 100)]) ; upper bounder of 10 for MRC, 50 for SAS

intra_mean_13=mean(jed13.jsat[where(jed13.time gt -0.5 and jed13.time lt 2.5 and jed13.jsat gt 5 and jed13.jsat lt 100)]) ; upper bounder of 10 for MRC, 50 for SAS

intra_mean_14=mean(jed14.jsat[where(jed14.time gt -0.5 and jed14.time lt 2.5 and jed14.jsat gt 5 and jed14.jsat lt 100)]) ; upper bounder of 10 for MRC, 50 for SAS

intra_mean_15=mean(jed15.jsat[where(jed15.time gt -0.5 and jed15.time lt 2.5 and jed15.jsat gt 5 and jed15.jsat lt 100)]) ; upper bounder of 10 for MRC, 50 for SAS

;print, 'mean intra-ELM jsat', intra_mean_11, intra_mean_12, intra_mean_13, intra_mean_14, intra_mean_15

intra_max_6_ionflux = (intra_max_6*sin(ang*!PI/180)/(1.602e-19))

intra_max_7_ionflux = (intra_max_7*sin(ang*!PI/180)/(1.602e-19))

intra_max_8_ionflux = (intra_max_8*sin(ang*!PI/180)/(1.602e-19))

intra_max_9_ionflux = (intra_max_9*sin(ang*!PI/180)/(1.602e-19))

intra_max_10_ionflux = (intra_max_10*sin(ang*!PI/180)/(1.602e-19))

intra_max_11_ionflux = (intra_max_11*sin(ang*!PI/180)/(1.602e-19))

intra_max_12_ionflux = (intra_max_12*sin(ang*!PI/180)/(1.602e-19))

intra_max_13_ionflux = (intra_max_13*sin(ang*!PI/180)/(1.602e-19))

print, 'intra_max_ion_flux', intra_max_13_ionflux

intra_max_14_ionflux = (intra_max_14*sin(ang*!PI/180)/(1.602e-19))

intra_max_15_ionflux = (intra_max_15*sin(ang*!PI/180)/(1.602e-19))

```
max_intra_ion_saturation_flux = [intra_max_6_ionflux, intra_max_7_ionflux,
intra_max_8_ionflux, intra_max_9_ionflux, intra_max_10_ionflux, intra_max_11_ionflux,
intra_max_12_ionflux, intra_max_13_ionflux, intra_max_14_ionflux, intra_max_15_ionflux]

print,'max intra-ELM ion saturation flux', max_intra_ion_saturation_flux


intra_mean_6_ionflux = (intra_mean_6*sin(ang*!PI/180)/(1.602e-19))

intra_mean_7_ionflux = (intra_mean_7*sin(ang*!PI/180)/(1.602e-19))

intra_mean_8_ionflux = (intra_mean_8*sin(ang*!PI/180)/(1.602e-19))

intra_mean_9_ionflux = (intra_mean_9*sin(ang*!PI/180)/(1.602e-19))

intra_mean_10_ionflux = (intra_mean_10*sin(ang*!PI/180)/(1.602e-19))

intra_mean_11_ionflux = (intra_mean_11*sin(ang*!PI/180)/(1.602e-19))

intra_mean_12_ionflux = (intra_mean_12*sin(ang*!PI/180)/(1.602e-19))

intra_mean_13_ionflux = (intra_mean_13*sin(ang*!PI/180)/(1.602e-19))

print, 'intra_mean_ion_flux', intra_mean_13_ionflux

intra_mean_14_ionflux = (intra_mean_14*sin(ang*!PI/180)/(1.602e-19))

intra_mean_15_ionflux = (intra_mean_15*sin(ang*!PI/180)/(1.602e-19))


;stop


mean_intra_ion_saturation_flux = [intra_mean_6_ionflux, intra_mean_7_ionflux,
intra_mean_8_ionflux, intra_mean_9_ionflux, intra_mean_10_ionflux, intra_mean_11_ionflux,
intra_mean_12_ionflux, intra_mean_13_ionflux, intra_mean_14_ionflux,
intra_mean_15_ionflux]

print,'mean intra-ELM ion saturation current', mean_intra_ion_saturation_flux


;Inter-ELM

inter_mean_6=mean(jed6.jsat[where(jed6.time gt -3 and jed6.time lt -0.5 and jed6.jsat gt 5 and
jed6.jsat lt 100)]) ; upper bounder of 10 for MRC, 50 for SAS

inter_mean_7=mean(jed7.jsat[where(jed7.time gt -3 and jed7.time lt -0.5 and jed7.jsat gt 5 and
jed7.jsat lt 100)]) ; upper bounder of 10 for MRC, 50 for SAS
```

inter_mean_8=mean(jed8.jsat[where(jed8.time gt -3 and jed8.time lt -0.5 and jed8.jsat gt 5 and jed8.jsat lt 100)]) ; upper bounder of 10 for MRC, 50 for SAS

inter_mean_9=mean(jed9.jsat[where(jed9.time gt -3 and jed9.time lt -0.5 and jed9.jsat gt 5 and jed9.jsat lt 100)]) ; upper bounder of 10 for MRC, 50 for SAS

inter_mean_10=mean(jed10.jsat[where(jed10.time gt -3 and jed10.time lt -0.5 and jed10.jsat gt 5 and jed10.jsat lt 100)]) ; upper bounder of 10 for MRC, 50 for SAS

inter_mean_11=mean(jed11.jsat[where(jed11.time gt -3 and jed11.time lt -0.5 and jed11.jsat gt 5 and jed11.jsat lt 100)]) ; upper bounder of 10 for MRC, 50 for SAS

inter_mean_12=mean(jed12.jsat[where(jed12.time gt -3 and jed12.time lt -0.5 and jed12.jsat gt 5 and jed12.jsat lt 100)]) ; upper bounder of 10 for MRC, 50 for SAS

inter_mean_13=mean(jed13.jsat[where(jed13.time gt -3 and jed13.time lt -0.5 and jed13.jsat gt 5 and jed13.jsat lt 100)]) ; upper bounder of 10 for MRC, 50 for SAS

inter_mean_14=mean(jed14.jsat[where(jed14.time gt -3 and jed14.time lt -0.5 and jed14.jsat gt 5 and jed14.jsat lt 100)]) ; upper bounder of 10 for MRC, 50 for SAS

inter_mean_15=mean(jed15.jsat[where(jed15.time gt -3 and jed15.time lt -0.5 and jed15.jsat gt 5 and jed15.jsat lt 100)]) ; upper bounder of 10 for MRC, 50 for SAS

;print, 'mean inter-ELM jsat', inter_mean_11, inter_mean_12, inter_mean_13, inter_mean_14, inter_mean_15

inter_mean_6_ionflux = (inter_mean_6*sin(ang*!PI/180)/(1.602e-19))

inter_mean_7_ionflux = (inter_mean_7*sin(ang*!PI/180)/(1.602e-19))

inter_mean_8_ionflux = (inter_mean_8*sin(ang*!PI/180)/(1.602e-19))

inter_mean_9_ionflux = (inter_mean_9*sin(ang*!PI/180)/(1.602e-19))

inter_mean_10_ionflux = (inter_mean_10*sin(ang*!PI/180)/(1.602e-19))

inter_mean_11_ionflux = (inter_mean_11*sin(ang*!PI/180)/(1.602e-19))

inter_mean_12_ionflux = (inter_mean_12*sin(ang*!PI/180)/(1.602e-19))

inter_mean_13_ionflux = (inter_mean_13*sin(ang*!PI/180)/(1.602e-19))

inter_mean_14_ionflux = (inter_mean_14*sin(ang*!PI/180)/(1.602e-19))

inter_mean_15_ionflux = (inter_mean_15*sin(ang*!PI/180)/(1.602e-19))

```
mean_inter_ion_saturation_flux = [inter_mean_6_ionflux, inter_mean_7_ionflux,
inter_mean_8_ionflux, inter_mean_9_ionflux, inter_mean_10_ionflux, inter_mean_11_ionflux,
inter_mean_12_ionflux, inter_mean_13_ionflux, inter_mean_14_ionflux,
inter_mean_15_ionflux]

print,'mean inter-ELM ion saturation flux', mean_inter_ion_saturation_flux


WRITE_CSV, STRING(shot), [Inter_temp, Intra_temp, max_intra_ion_saturation_flux,
mean_intra_ion_saturation_flux, mean_inter_ion_saturation_flux]


;HEADER = ['Inter-ELM Temperature', 'Intra-ELM Temperature', 'Max Intra-ELM Ion
Saturation Flux', 'Mean Intra-ELM Ion Saturation Flux', 'Mean Inter-ELM Ion Saturation Flux']


;print, 'Mean Ion STD', stddev(inter_mean)*sin(ang*!PI/180)/(1.602e-19))


endif


;MRC Code Analysis from this point and on

if keyword_set (Deuterium) then begin


a=get_wi_elm(shot, trange=trange, elmtimes=elmtimes, view=view, tcyclerange=tcyclerange,
sxb=sxb, tfactor=tfactor, dachan=fs06)

;help,a

nelms=n_elements(a.DA[0,*])


density=(a.DA)/max(a.DA)*divdens*1e6


divtemp2=divtemp/4


temperature=((a.DA)/max(a.DA)*divtemp2)+(3*divtemp2)
```

```
newsxb=fltarr(n_elements(a.time))
;print,newsxb

if keyword_set (D_intra_ELMs) then begin
for n=0,n_elements(newsxb)-1 do print, get_sxb_da(density[n],divtemp)
for n=0,n_elements(newsxb)-1 do newsxb[n]=get_sxb_da(density[n],divtemp)
endif

if keyword_set (D_inter_ELMs) then begin
for n=0,n_elements(newsxb)-1 do print, get_sxb_da(density[n],temperature[n])
for n=0,n_elements(newsxb)-1 do newsxb[n]=get_sxb_da(density[n],temperature[n])
endif

k=plot(a.time,a.DA*newsxb,"r4-",ytitle='D recycling (atoms*cm-2*s-1)', xtitle='Time (ms)',
xrange=tcyclerange, yrange=[0,1E22], window_title='Deuterium Recycling')
;stop
;if keyword_set (elms) then begin
for i=0,nelms-1 do k=plot(a.time,a.DA[*,i]*newsxb,ytitle='D Recycing (atoms*cm-2*s-1)'$
,xtitle='Time(ms)',xrange=tcyclerange, overplot=1)
;endif
k=plot(a.time,a.DA*newsxb,"r4-",ytitle='D Recycling (atoms*cm-2*s-1)', xtitle='Time (ms)',
xrange=tcyclerange,yra=[0,1e17],window_title='SXB corrected D Recycling',overplot=1)
print,'time', a.time
;print, 'D no SXB', a.DA
print, 'D recycling', a.DA*newsxb
print, 'newsxb', newsxb

;stop
```

```
avgparticlescm2elm = INT_TABULATED(a.time,a.DA*newsxb)*0.001
avgparticlescm2selm = avgparticlescm2elm/((trange[-1]-trange[0])*0.001)
totparticlescm2elm = avgparticlescm2elm*nelms
totparticlescm2selm = avgparticlescm2selm*nelms
;print,'average D Reycling during ELM', avgparticlescm2elm
;print,'average D Recycling rate during ELM', avgparticlescm2selm
;print,'total D recycling during ELMs', totparticlescm2elm
;print,'total D Recycling during ELMs', totparticlescm2selm

;stop
endif
;-------------------------------------------------------------------------------------------------------------------------------------------

if keyword_set (errorbars) then begin
p=errorplot(a.time, a.GAMMA_W, a.GAMMA_W_E, "m4", overplot=1)
print, 'error bars', a.gamma_W_E
endif

if keyword_set (QH_mode) then begin

h=plot(d.chan[q].time, d.chan[q].dens, xra=trange, yra=[0,1e14], window_title='INTER-ELM
DENSITY')

b=plot(d.chan[q].time, d.chan[q].temp, xra=trange, yra=[0,200], window_title='INTER-ELM
TEMPERATURE')

divdens=mean(d.chan[q].dens(where(d.chan[q].time gt trange[0] and d.chan[q].time lt trange[-1]
and d.chan[q].dens lt 1e14 and d.chan[q].dens gt 2.5e10 and d.chan[q].temp lt 100 and
d.chan[q].temp gt 3)))
```

```
print, 'divertor density:', divdens

divtemp=mean(d.chan[q].temp(where(d.chan[q].time gt trange[0] and d.chan[q].time lt trange[-1] and d.chan[q].dens lt 1e14 and d.chan[q].dens gt 2.5e10 and d.chan[q].temp lt 100 and d.chan[q].temp gt 3)))

print, 'divertor temperature', divtemp

endif

;For Calculating erosion between ELMs
if keyword_set (inter_ELMs) then begin

;density=smooth(a.GAMMA_W,2)/max(a.GAMMA_W)*divdens*1e6
;rint,'final density', density
;SXB COEEFICIENTS

;INTER-ELM:
if keyword_set (inter_ELMs) then begin
for n=0,n_elements(newsxb)-1 do print, get_sxb_wi(density[n],avgdivtemp)
for n=0,n_elements(newsxb)-1 do newsxb[n]=get_sxb_wi(density[n],avgdivtemp)
endif

;INTRA-ELM
if keyword_set (intra_ELMs) then begin
;for n=0,n_elements(newsxb)-1 do print, get_sxb_wi(density[n],divtemp) ;for 167355 and 167356
;for n=0,n_elements(newsxb)-1 do newsxb[n]=get_sxb_wi(density[n],divtemp) ;for 167355 and 167356
```

```
for n=0,n_elements(newsxb)-1 do print, get_sxb_wi(density[n],temperature[n])
for n=0,n_elements(newsxb)-1 do newsxb[n]=get_sxb_wi(density[n],temperature[n])
endif

endif


if keyword_set (lep) then begin
;da signal just before ELM crash
lep=get_ptname_elm(shot,'fs06f',trange=trange,tcyclerange=[-100,100])
plot,lep.time,lep.fs06f,psym=5,symsize=2
fs06f=mean(lep.fs06f[where(lep.time lt 1 and lep.time gt 0 and lep.fs06f gt 1e14)])
print,'da recycling', fs06f
stop
endif

;PLOT MRC EROSION
;j=plot(a.time,a.GAMMA_W*newsxb,"r4-",ytitle='W erosion (atoms*cm-2*s-1)', xtitle='Time (ms)', xrange=tcyclerange, yrange=[0,1E17], window_title='correctelms')

;stop

if keyword_set (errorbars) then begin
j=errorplot(a.time, a.GAMMA_W*newsxb,fltarr(n_elements(a.time)), a.GAMMA_W_E*newsxb, overplot=1)
endif
if keyword_set (elms) then begin
for i=0,nelms-1 do j=plot(a.time,a.GAMMA_W_all[*,i]*newsxb,ytitle='W erosion (atoms*cm-2*s-1)'$
```

```
,xtitle='Time(ms)',xrange=tcyclerange,overplot=1)

endif

;j=plot(a.time,a.GAMMA_W*newsxb,''r4-'',ytitle='W erosion (atoms*cm-2*s-1)', xtitle='Time
(ms)', xrange=tcyclerange,yra=[0,1.4e17],window_title='correctelms',overplot=1)

;print,'time', a.time

;PRINT MRC EROSION

;print, 'erosion', a.GAMMA_W*newsxb


;SXB coefficient plot

;sxb=plot(a.time,newsxb,''r4-'',ytitle='(W atoms/photon)', xtitle='Time (ms)',
xrange=tcyclerange,window_title='SXB coefficients')

;print, 'sxb', newsxb


;stop


;MRC W EROSION

;avgparticlescm2elm = INT_TABULATED(a.time,noRMP*10000000000000000)*0.001

;avgparticlescm2elm = INT_TABULATED(a.time,a.GAMMA_W*newsxb)*0.001

;print,'average erosion per ELM', avgparticlescm2elm

;for i=0,nelms-1 do print, INT_TABULATED(a.time,a.GAMMA_W_all[*,i]*newsxb)*0.001

;stop


if keyword_set (werror) then begin


;W Error

lower_error = INT_TABULATED(a.time,(a.GAMMA_W-a.GAMMA_W_E)*newsxb)*0.001

upper_error = INT_TABULATED(a.time,(a.GAMMA_W+a.GAMMA_W_E)*newsxb)*0.001

print, 'integrated average LOWER error', lower_error

print, 'integrated averager UPPER error', upper_error
```

```
endif

;stop
;Unsupress next lines for MRC data
;avgparticlescm2selm = avgparticlescm2elm/((trange[-1]-trange[0])*0.001)
;totparticlescm2elm = avgparticlescm2elm*nelms
;totparticlescm2selm = avgparticlescm2selm*nelms
;print,'average erosion per ELM', avgparticlescm2elm
;print,'average erosion rate per ELM', avgparticlescm2selm
;print,'total erosion', totparticlescm2elm
;print,'total erosion rate', totparticlescm2selm
;print,a.GAMMA_W_ALL[*,0]
;print,a.time
;print,a.GAMMA_W
;print,max(a.GAMMA_W)
;print,'inter-ELM divertor density', divdens
;print,'inter-ELM divertor temperature', divtemp
;a=get_wi_elm(shot, trange=trange, elmtimes=elmtimes,
;tcyclerange=tcyclerange, sxb=sxb, tfactor=tfactor,
;uptfactor=uptfactor, view=view)

;RETURNS MRC INTRA-ELM HEAT FLUX
if keyword_set (mrchf) then begin
alpha_top_in=75000
alpha_top_out=75000
hf=get_heatflux_elm(shot, elmtimes=elmtimes, tcyclerange=tcyclerange,
trange=trange,thresh=tfactor, num=3, dachan=dachan)
;'167349 digital_cam, dig_cam_01'
```

```
;elmtimes=elmtimes,tcyclerange=tcyclerange,$thresh=thresh,trange=trange,num=num,rrange=rr
ange,$ plot=plot,save=save,dachan=dachan

help, hf

print, hf.heatflux

z=plot(hf.time, hf.heatflux,"r4-",ytitle='Heat Flux (MW/m^2)', xtitle='Time (ms)',
xrange=tcyclerange, yra=[0,2e6],window_title='MRC Heat Flux')

peakhf=max(hf.heatflux[where(hf.time gt -1 and hf.time lt 2)])

meanhf=mean(hf.heatflux[where(hf.time gt -0.5 and hf.time lt 2.5)])

print, 'peak heat flux', peakhf

print, 'mean heat flux', meanhf

e=plot(hf.time, hf.heatflux_e,"r4-",ytitle='Heat Flux Error (MW/m^2)', xtitle='Time (ms)',
xrange=tcyclerange, yra=[0,1e6],window_title='MRC Heat Flux Error')

peakhf_error=max(hf.heatflux_e[where(hf.time gt -1 and hf.time lt 2)])

print, 'peak heat flux error', peakhf_error


endif


;stop
;EROSION PER ELM



;Average Carbon impurity percentage just outside of SOL

gadat,x,y,'cerafzt10',shot

cerafzt10=mean(y[where(x gt trange[0] and x lt trange[-1])])/100

print,'carbon impurity %', cerafzt10


;Average Carbon impurity percentage just outside of SOL during intra-ELM

;gadat,x,z, 'fs06', shot

;cerafzt10=mean(y[where(z gt 2e15)])/100
```

```
;print,'carbon impurity %', cerafzt10

;Neutral beam injection power
gadat,x,y,'pinj',shot
IP=mean(y[where(x gt trange[0] and x lt trange[-1])])
print, 'injected power', IP

;Stored core plasma energy
gadat,x,y,'wmhd',shot
Energy=mean(y[where(x gt trange[0] and x lt trange[-1])])
print, 'stored energy', Energy

;Pedestal density just before ELM crash
nep=get_ptname_elm(shot,'prmtan_neped',trange=trange,tcyclerange=[-100,100])
plot,nep.time,nep.prmtan_neped,psym=5,symsize=2
prmtan_neped=mean(nep.prmtan_neped[where(nep.time lt -0.5 and nep.prmtan_neped gt 5e19)])
print,'pedestal density', prmtan_neped

;stop

;Pedestal temperature just before ELM crash
tep=get_ptname_elm(shot,'prmtan_teped',trange=trange,tcyclerange=[-100,100])
plot,tep.time,tep.prmtan_teped,psym=5,symsize=2
prmtan_teped=mean(tep.prmtan_teped[where(tep.time lt -0.5 and tep.prmtan_teped gt 200)])
print,'pedestal temperature', prmtan_teped

;stop
```

```
;Pedestal temperature average over whole shot
;gadat,x,y,'prmtan_teped',shot
;prmtan_teped=mean(y[where(x gt trange[0] and x lt trange[-1])])
;print,'pedestal temperature', prmtan_teped

;Pedestal density average over whole shot
;gadat,x,y,'prmtan_neped',shot
;prmtan_neped=mean(y[where(x gt trange[0] and x lt trange[-1])])
;print,'pedestal density', prmtan_neped

;gadat,x,y,'pciu30',shot
;print,mean(y[where(x gt trange[0] and x lt trange[-1])])

;MR factors
;print, get_metalrings_factors(shot, view, trange[0], trange[-1])

;-------------------------------------------------------------------------------------------------------------------
-------------------------------------------------------------

;L-MODE EROSION FOR SETH
if keyword_set (lmode) then begin

;MDS Quick plot
;mdswi=get_sasvw_mds_wi(shot, 2, /calibrate)
;plot, mdswi.time, mdswi.int_wi

;offset = get_mds_offset(shot,2,plot=mdstr,mdstr=mdstr)
;print, offset, 'nm'
```

```
;Filterscope data
In=get_sasvw_fscope(shot, 2, 'W1N')
;gadat,x,In,'fssasvw2w1n',shot ;narrow filterscope
;IN=(In[where(In.time gt tstart and In.time lt tend)])
;plot, x, In

IN=In.cali
;Time=fltarr(n_elements(In.time))
;time=In.time
;Time=(time[where(time gt tstart and time lt tend)])

Im=get_sasvw_fscope(shot, 2, 'W1M')
;gadat,x,Im,'fssasvw2w1m',shot ;wide filterscope
;IM=(Im[where(Im.time gt tstart and Im.time lt tend)])
;plot, x, Im

IM=Im.cali

;W Spectroscopy Calibration Equation and Coefficients
;I=(In-R*Im)/(1-R)
;[Gn, Gm] values:
;[0.6, 0.6] for Seth 190XXX 405-431 SAS shots: R=0.7595 right values
;for V1?
;[0.7, 0.7] for Seth 190XXX 437-461 & 480-502 SAS shots: R=0.78

;R=0.6595
;print, 'I size', N_ELEMENTS(I)
```

```
;RETRIEVE LANGMUIR PROBE DATA
;***q=13 for 163 A-12 Langmuir probe for view 2***
;q=11 for 159 A-10 Langmuir probe for view 1 (vertex)
;q=15 for 167 A-14 Langmuir probe for view 3

d=get_lp(shot)
;use d.chan[q].dens for divertor density
;use d.chan[q].temp for divertor temperature

;SAS DIVERTOR DENSITY
density = d.chan[q].dens*1e6
time = d.chan[q].time

Density=(density[where(time gt tstart and time lt tend)])
;Time=(time[where(time gt tstart and time lt tend)])
;Density=CONGRID(Density, N_ELEMENTS(In))
;Time=CONGRID(Time, N_ELEMENTS(In))
plot, Time, Density

;SAS DIVERTOR TEMPERATURE
temperature = d.chan[q].temp
time = d.chan[q].time
Temperature=(temperature[where(time gt tstart and time lt tend and temperature lt 100)])
Mean_Temperature = mean(temperature[where(time gt tstart and time lt tend)])
print, 'mean temperature', Mean_Temperature
Time=(time[where(time gt tstart and time lt tend)])
;Temperature=CONGRID(Temperature, N_ELEMENTS(In))
;Time=CONGRID(Time, N_ELEMENTS(In))
```

```
plot, Time, Temperature
stop

;SAS SXB COEFFICIENTS
sxb=fltarr(n_elements(time))
for n=0,n_elements(sxb)-1 do sxb[n] = get_sxb_wi(Density[n],Temperature[n])
;sxb=CONGRID(SXB, N_ELEMENTS(In))
plot, Time, sxb

R=[0.55, 0.6, 0.65, 0.7, 0.75, 0.8]
;I=fltarr(n_elements(R))
;print, R[5]
;stop
;for n=0,5 do I=smooth((In-R[n]*Im)/(1-R[n]), 1000)

I0=CONGRID(smooth((In-R[0]*Im)/(1-R[0]), 1000), N_ELEMENTS(Time))
I1=CONGRID(smooth((In-R[1]*Im)/(1-R[1]), 1000), N_ELEMENTS(Time))
I2=CONGRID(smooth((In-R[2]*Im)/(1-R[2]), 1000), N_ELEMENTS(Time))
I3=CONGRID(smooth((In-R[3]*Im)/(1-R[3]), 1000), N_ELEMENTS(Time))
I4=CONGRID(smooth((In-R[4]*Im)/(1-R[4]), 1000), N_ELEMENTS(Time))
I5=CONGRID(smooth((In-R[5]*Im)/(1-R[5]), 1000), N_ELEMENTS(Time))

;W Source Erosion
W55=I0*sxb
W60=I1*sxb
W65=I2*sxb
W70=I3*sxb
W75=I4*sxb
```

```
W80=I5*sxb


plot, Time, W55
oplot, Time, W60, color=40
oplot, Time, W65, color=3
oplot, Time, W70, color=27
oplot, Time, W75, color=120
oplot, Time, W80, color=73

WRITE_CSV, '492', Time, W55, W60, W65, W70, W75, W80, HEADER=['Time (ms)', 'W55',
'W60', 'W65', 'W70', 'W75', 'W80']

stop
endif



end
```

# Vita

Alec was born and raised in the western suburbs of Saint Louis County. After graduating from Marquette High School, he earned his bachelor's degree in nuclear engineering with a minor concentration in material science engineering from the University of Tennessee at Knoxville (UTK). He graduated *cum laude* and completed three undergraduate internships before pursuing his Ph.D. in Nuclear Engineering at UTK with a focus on plasma-material interactions. Throughout his graduate career, he collaborated closely with DIII-D National Fusion Facility and scientists in Oak Ridge National Laboratory and Princeton Plasma Physics Laboratory. Apart from work, Alec enjoys gaming and the outdoors across a multitude of hobbies with many everlasting friends.